2022

Minimizing Cr-evaporation from Balance of Plant Components by Utilizing Cost-Effective Alumina-Forming Austenitic Steels

Lingfeng Zhou
West Virginia University, lz0019@mix.wvu.edu

Minimizing Cr-evaporation from Balance of Plant Components by Utilizing Cost-Effective Alumina-Forming Austenitic Steels

Lingfeng Zhou

Dissertation submitted to

Benjamin M. Statler College of Engineering and Mineral Resources

at West Virginia University

in partial fulfillment of the requirements

for the degree of

Doctor of Philosophy

In

Material Science and Engineering

Approved by

Xingbo Liu, Ph.D., Committee Chairperson

Konstantinos A. Sierros, Ph.D.

Terence Musho, Ph.D.

Wenyuan Li, Ph.D.

Harry Finklea, Ph.D.

Mike Brady, Ph.D.

Department of Mechanical and Aerospace Engineering

Morgantown, West Virginia

2022

Keywords: Alumina-forming austenitic (AFA) stainless steels, oxidation, solid oxide fuel cells, chromium deposition and poisoning, cathodes

ABSTRACT

Minimizing Cr-evaporation from Balance of Plant Components by Utilizing Cost-Effective Alumina-Forming Austenitic Steels

A solid oxide fuel cell (SOFC) is a clean and efficient energy conversion device. The development of intermediate-temperature SOFCs has made it preferable to use metallic interconnects (MICs) to greatly reduce the cost and significantly increase the efficiency compared to ceramic interconnect materials. However, gaseous chromium species will evaporate from the chromium-containing layer formed on the surface of commonly used MICs and balance of plant (BoP) components. Volatile chromium species have been shown to form solid deposits which poison the cathodes of SOFCs, causing drastic cell performance degradation and thereby limiting commercialization. In order to alleviate the Cr poisoning and achieve long-term high performance of SOFC stacks, various Al_2O_3-forming austenitic (AFA) stainless steels applied at different temperatures are evaluated in this work.

It is shown that on the AFAs, an alumina-based protective layer forms under high temperature that is invulnerable to water vapor effects and suppresses the diffusion of chromium and manganese which can prevent the generation of spinels on the alloy surface. The chromium (Cr) evaporation behavior of several different types of iron (Fe)-based AFA alloys and benchmark Cr_2O_3-forming Fe-based 310 and Ni-based 625 alloys was investigated for 500 h exposures at 800 °C to 900 °C in air with 10% H_2O. The Cr evaporation rates from alumina-forming austenitic (AFA) alloys were ~5 to 35 times lower than that of the Cr_2O_3-forming alloys depending on alloy and temperature. The Cr evaporation behavior was correlated with extensive characterization of the chemistry and microstructure of the oxide scales, which also revealed a degree of quartz tube Si contamination during the test. Long-term oxidation kinetics were also assessed at 800 to 1000 °C for up to 10,000 h in air with 10% H_2O to provide further guidance for SOFC BOP component alloy selection.

Besides the lower Cr evaporation rates and better oxidation resistance of AFAs than benchmark alloys after short-term (500 h) operation, AFAs also possess the sturdy and compact alumina layer after a long-term operation (5000 h). The Cr evaporation and high-temperature oxidation behaviors of AFA alloys are systematically investigated in air + 10% H_2O at 800 °C after various durations compared to commercial alloy 310S. The Cr evaporation rates of 310S are about 35 times higher than the AFA alloys after the entire test. Breakaway oxidation and spallation are observed on 310S after only one cycle, while the AFA alloys show high oxidation resistance. It is found that there are no voids formation, and the formation of a continuous alumina layer stays compact and stable during the entire test which greatly reduces the Cr

evaporation. The long-term oxidation and chromium evaporation behaviors of chromia-forming alloy 625 and AFA alloys were evaluated by transpiration tests, weight gain tests, X-ray diffraction technique, scanning electron microscopy coupled with energy dispersive X-ray analysis, and scanning transmission electron microscopy coupled with energy dispersive X-ray analysis. Results indicated that the 625 exhibits a 28-and 56-times higher evaporated Cr amounts than OC11 and OC11LZ, respectively. Different behaviors between OC11 and OC11LZ are resulted from the formed oxides scale variation during the long-term operation. Moreover, the effect of reactive elements on the long-term oxidation and chromium evaporation behaviors was discussed.

Cr evaporation from BoP components in high-temperature environment could severely deteriorate the electrochemical performance of SOFC. Several methods were applied to evaluate the Cr evaporation rates of BoP components after 500 h exposure at 800 °C to 900 °C in air with 10% H_2O. An optimal method was designed to exclude the effect of silicon (Si) deposits from quartz tube and sodium (Na) deposits from the sodium carbonate on the oxidation process and the chemical interaction between Cr gaseous species and alumina tube which could provide further quantitative correlation of the evaporated Cr species quantities and degradation rates of SOFC.

Based on the great performance of AFAs after long-term operation, AFAs are assembled with Anode-supported cells (ASC) to investigate the the Cr deposition of anode-supported cell under a constant current density of 0.5 A cm^{-2} at 800 °C with AFA alloys compared with commercial alloys which was analyzed by the distribution of relaxation times (DRT) and different equivalent circuit model methods. The performance deterioration of ASCs was mainly attributed to the increased polarization resistances of oxygen surface exchange and diffusion processes in the cathode region. The superior performance of ASC coupled with AFA alloys was due to the formed continuous alumina layer which can vastly decrease the evaporated gaseous Cr species, thus alleviating the Cr poisoning on the cathode region.

ACKNOWLEDGEMENTS

I would love to express my sincere gratitude to my advisor, **Dr Xingbo Liu**, for his patient guidance and intellectual support during my time at West Virginia University. I would like to thank my co-advisor **Dr Mike Brady**, for his patience, motivation, and immense knowledge. I am always enjoying receiving emails from him and absorbing a huge number of knowledges from those exciting suggestions. You are the best critic I can ever have. I would like to thank **Dr Wenyuan Li** for his continuous encouragement and organization on my research, meticulous suggestions on my papers and thoughtful kindness on my life. His guidance helped me in all the time of research and writing of this dissertation. I express my warm and sincere thanks to **Dr Harry Finklea** for his patient guidance on the DRT process. I also would like to thank **Dr Wei Li** and **Dr Shanshan Hu** for their time in instructing me how to choose a proper journal and to be a good paper writer.

I want to thank for the technical supports of **Dr Greg Collins** and **Dr Liang Ma**. My experiment design and equipment set-up involved their professional guidance. **Dr Jerry H. Mason** helped me summarize the table and revise the draft for our review paper. **Dr Zhipeng Zeng** and **Dr Wangying Shi** helped me with testing and data process. **Yi Wang** helped me with the cell testing. **Hanchen Tian** helped me with the data process. I am also greatly thankful to **Bo Guan** for her assistance and support.

Besides, I want to thank committee members, **Dr Terence Musho** and **Dr Kostas Sierros**, for their thoughtful suggestions on this dissertation.

I would also like to thank **Dr Tianliang Zhao** and **Haiyang Li** for their continuous care along the first two-year journey.

I gratefully acknowledge the financial support of U. S. Department of Energy during my research.

Friends outside the lab I wish to thank you for just being there. At this moment I would like to thank my best friends Dr **Yifan Wang**, **Jing Wang** and **Liu Li** for their thoughtful care in my Ph. D life. Most of all, I would like to give my most sincere thanks to my family for their continuous care and love.

TABLE OF CONTENTS

LIST OF FIGURES

LIST OF TABLES

LIST OF SYMBOLS AND NOTATIONS

Greek letters

δ Oxygen non-stoichiometry

η Overpotential, mV

Latin letters

$h^{\cdot}$ Holes

$V_O^{\cdot\cdot}$ vacancies

E Polarization potential, mV

ΔE Polarization potential increase, mV

R_Ω Ohmic resistance, Ω

R_p Polarization resistance, Ω

P Partial pressure, atm

ASR_p Area specific resistance, $\Omega \cdot cm^2$

k_o Surface oxygen exchange coefficient, $m \cdot s^{-1}$

D_O Oxygen diffusion coefficient, $m^2 \cdot s^{-1}$

Abbreviations

SOFCs Solid oxide fuel cells

MICs Metallic interconnects

ORR Oxygen reduction reaction

BoP Balance-of-plant

AFA Alumina-forming austenitic

OCV Open-circuit voltage

LSM Lanthanum strontium manganite

LSF lanthanum strontium ferrite

LSCF lanthanum strontium cobalt ferrite

LNF Lanthanum nickel ferrite

GDC Gadolinium-doped ceria

YSZ Yttria-stabilized zirconia

SASZ Alumina-doped scandia stabilized zirconia

ICP-OES Inductively coupled plasma - optical emission spectrometry

EDS Energy-dispersive X-ray spectroscopy

XRD X-ray powder diffraction

XANES X-ray absorption near edge spectroscopy

XPS X-ray photoelectron spectroscopy

CV Cyclic voltammogram

SIMS Secondary ion mass spectrometry

EPMA Electron probe microanalysis

SEM Scanning electron microscopy

TPB Triple phase boundary

2PB 2-phase boundary

TEC Thermal expansion coefficient

Chapter 1 Literature Review

1.1 Overview of Cr poisoning in SOFCs

The desire to move towards clean, trustworthy, and maintainable energy sources have invigorated great interest in fuel cells. A fuel cell is a high-efficiency energy-conversion device that directly converts chemical energy to electrical energy [1]. Due to the high temperature operation, SOFCs can use hydrocarbon fuels, alkanes, and other renewable fuels which can be electrochemically oxidized at the fuel electrode. Unlike other varieties of fuel cells that require methane reforming to be carried out separately, SOFCs are capable of on-board methane reforming within the cell, which allows for creative thermal design of the system that can recycle the excess heat to obtain superior system efficiencies [2]. A simple schematic of the SOFC basic components is shown in Figure 1.

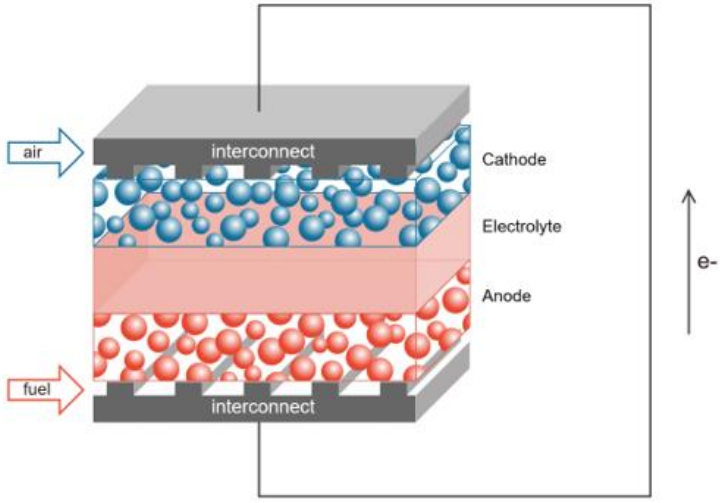

Figure 1. Schematic of SOFC basic units.

Commonly, multiple single cells are assembled together using metallic interconnects (MICs) to form a stack which can meet the voltage and power density requirements of large-scale applications [3]. MICs, which possess high creep strength to support the stack and provide stable performance in dual atmospheres, separate the air and fuel channels of individual cells and provide electrical connection in the SOFC stack. Ceramic and metallic materials are regarded as the two major categories of interconnect materials.

Nowadays, effective measures such as reduction of electrolyte thickness, new electrode and electrolyte material and preparation techniques are advocated by many researchers aiming to reduce the high operating temperature of SOFCs from temperatures above 800°C to the intermediate range of 600-800°C. Higher electronic and thermal conductivity, lower cost and easier fabrication make metallic materials more appealing than ceramic materials as interconnects under intermediate temperature operation [4]. Metallic interconnects include Cr-based oxide dispersed strengthened alloys [5], Fe-Cr-based alloys [3, 5-10] and Ni-Cr-based alloys [11]. A semi-conductive chromia scale will be formed on the surface of the alloy in the presence of oxygen (within SOFC cathodes in particular) which acts as a barrier to reduce the chromium evaporation and diffusion when the alloys are operated at high temperature.

Metallic interconnects with high-temperature oxidation resistance typically contain aluminum, silicon or chromium as a doping element to form alumina, silica or chromia protective scales, respectively. Although alumina or silica scales formed on the surface of the alloy can provide excellent oxidation resistance, they possess much lower electrical conductivities than chromia scales, leading to significantly higher ohmic losses in the cell. One the other hand, porous structures will be formed on chromium containing alloys at the alloy-scale interface after the formation of a chromia scale. Combined with the gradually growing stresses during operation, this can lead to chromium scale cracking and delamination resulting in cell degradation and failure due to loss of electrical connection. At operating temperatures, gaseous Cr species such as chromium oxides, hydroxides and oxyhydroxides will evaporate from the chromia scale layer and then deposit within the cathode, affecting the electrochemical oxygen reduction reaction (ORR). It is generally acknowledged that chromium oxyhydroxide ($CrO_2(OH)_2$) and chromium oxide (CrO_3) are the predominant species in wet air and dry air, respectively, within the temperature range relevant to SOFC operation [12-14]. Thermodynamic calculations by Ebbinghaus [15] clearly indicate the dominance of $CrO_2(OH)_2$ and CrO_3 as shown in Figure 2, which is reproduced using the data presented by Ebbinghaus. Gaseous Cr species can also be generated from balance-of-plant (BoP) components, such as gas pumps, valves, heat exchangers and pipe, and have been shown to cause a rapid degradation of SOFCs stacks [16-19]. In some cases, it is straight forward to add a protective coating to reduce/eliminate chromium volatilization from BoP components. However, some BoP

components such as the valves and elbows of pipes cannot be effectively protected by coatings. In this case, Al_2O_3-forming Austenitic (AFA) stainless steels are promising materials to replace the conventional BoP components used in SOFC stacks since protective Al_2O_3 scale formation can suppress the diffusion and evaporation of chromium [20]. AFA stainless steels also possess great mechanical and corrosion-resistant properties [21, 22].

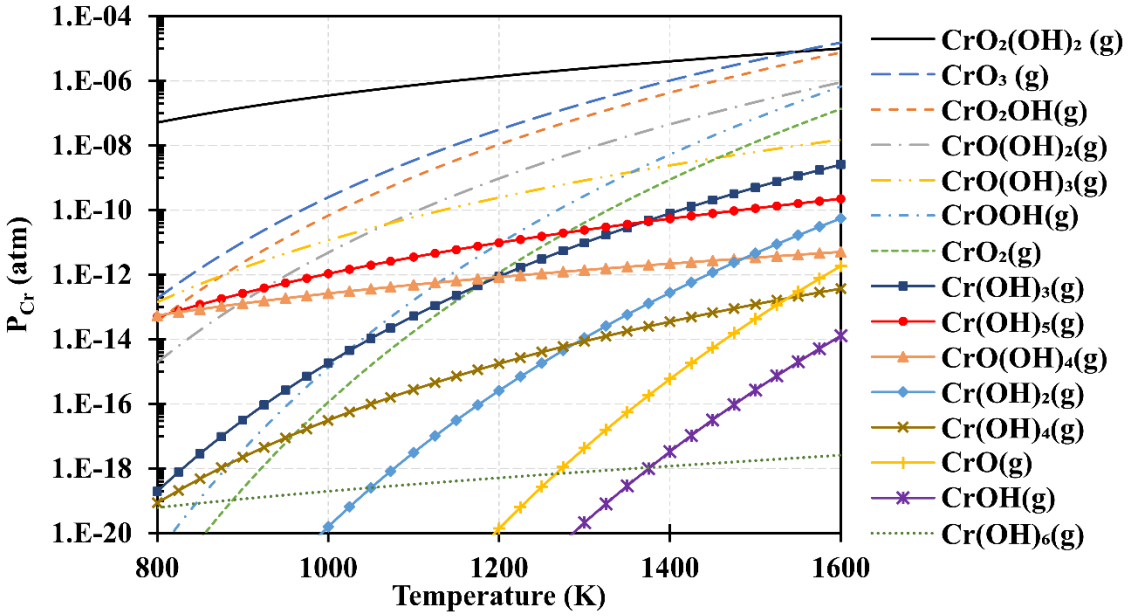

Figure 2. Partial pressures of several gaseous chromium species over a Cr_2O_3(s) source as a function of temperature for 1 atm humidified air, 21% P_{O_2}, 3% P_{H_2O} calculated using thermodynamic data presented by Ebbinghaus [15].

The reaction between gaseous Cr species from the above-mentioned components and SOFC cathodes has been widely studied over the last few decades. However, the underlying process of chromium deposition and poisoning remains abstruse considering many factors involved, such as cell varieties, temperature, O_2 partial pressure, H_2O partial pressure, flow rate of air, contact between interconnect and electrode, current density, electrolyte and various electrode materials. Each of these factors influences the quantity and location of chromium deposition and the observed phase formed at the electrolyte/cathode interface, within the cathode support layer or on the surface of the cathode. Thus, the exact driving force of the deposition and mechanisms of poisoning by gaseous Cr species in cathodes remains unclear [13, 23-25].

1.2 Quantification of chromium species

Relatively low operation temperature, higher conductivity, lower cost and easier fabrication make metallic materials more attractive than ceramic interconnect materials, such as lanthanum chromite perovskite-based ceramic oxides, as interconnect materials for SOFCs. Almost all alloys being used as interconnect materials form chromia scales during oxidation at high temperature [26]. There is therefore a trade-off which occurs such that cells that utilize MIC's will have improved baseline performance over cells with ceramic interconnects, but as is shown by Matsuzaki and Yasuda [27], the presence of a chromium containing MIC will result in significantly worse performance degradation than the presence of a ceramic interconnect material such as Sr-doped $LaCrO_3$. The evaporation reactions of the most prevalent gaseous Cr species from a Cr-oxide scale are listed as below:

$$1.5O_2(g)+Cr_2O_3(s)+2H_2O = 2CrO_2(OH)_2(g) \quad (1)$$

$$O_2(g)+Cr_2O_3(s)+H_2O = 2CrO_2(OH)(g) \quad (2)$$

$$1.5O_2(g)+Cr_2O_3(s)=2CrO_3(g) \quad (3)$$

The gaseous Cr species evaporated from the oxide scales strongly depends on O_2 partial pressure and H_2O partial pressure in the air stream. Hilpert et al. [13] have demonstrated that chromium vapor pressure in the anode side will be much lower than that in the cathode side. Therefore, the deposition of the gaseous Cr species on the SOFC anode can be neglected. In this section, the influencing factors of the chromium oxide species evaporation such as temperature, flow rate and the partial pressures of water and oxygen are discussed. The dominant chromium species and their concentrations are calculated by distinct methods. As will be discussed in later sections, the proximity of the chromium source to the electrode will impact the deposition rate of chromium, such that solid phase transport of chromium should also be considered. A review of experiments studying the gas phase and solid phase transport of chromium is therefore discussed. Additionally, chromium quantification methods for both solid deposits and gas phase species concentrations are presented.

1.2.1 Chromium Oxide Species Evaporation

1.2.1.1 Effects of partial pressure and temperature on the chromium evaporation

Ebbinghaus [15], Graham [28] and Stearns [29] investigated the kinetics of oxidation of materials with Cr_2O_3 scales to analyze the evaporation of fifteen gaseous chromium species several decades ago. From these studies, it is determined that CrO_3(g) is the species which accounts for most of the evaporation of chromium oxide when Cr_2O_3 is heated in dry air (lower water partial pressure). Furthermore, subsequent researchers [12-14, 30, 31] have established that $CrO_2(OH)_2$(g) is the predominant gaseous species existing over solid Cr_2O_3 in a humid oxidizing environment (higher water partial pressure). Thermodynamic data from Ebbinghaus [15] and Opila et al. [31] have been used to predict the steam partial pressure at which the concentrations of $CrO_2(OH)_2$ and CrO_3 will be equivalent as a function of temperature and plotted in Figure 3. Above these curves, $CrO_2(OH)_2$ will become dominant while CrO_3 will be dominant below. As can be gleaned from this figure, $CrO_2(OH)_2$ will be the primary phase of Cr gas in the typical operation of intermediate temperature SOFCs (600-800 °C) even for relatively dry conditions (≥0.1% H_2O).

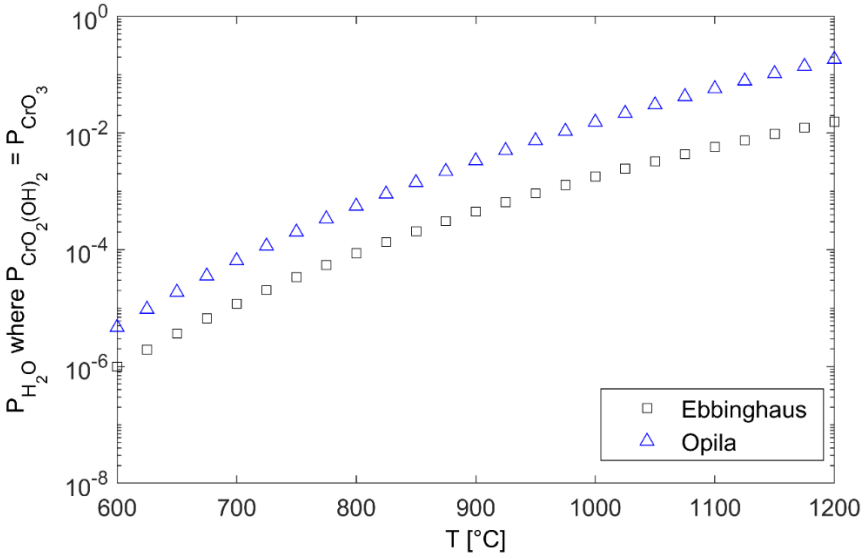

Figure 3. Partial pressure of steam (in atm) at which the concentrations of CrO_3(g) and $CrO_2(OH)_2$(g) are predicted to be equivalent according to thermodynamic data from Ebbinghaus [15] and Opila [31].

From Eq. (1) it is known that the partial pressure of $CrO_2(OH)_2$ increases linearly with steam partial pressure ($P_{CrO_2(OH)_2} \propto P_{H_2O}$). Therefore, thermodynamic calculations have verified that moisture in air could significantly aggravate the Cr deposition in SOFC cathodes. Experimentally, Chen et al. [32] found that the

increase in degradation rate with increasing humidity is attributed to the increased evaporation rate of chromium oxyhydroxides from the Fe-Cr alloy interconnect. Wang et al. [33] also investigated the roles of humidity and cathodic current in chromium poisoning on the LSM cathode. Anode-supported cells are operated at 800 °C under different atmospheric conditions (10% humidified air and dry air) and current densities (open circuit and 0.75 A/cm^2) with Crofer22APU interconnects. Results from this study are summarized in Figure 4. The maximum power density of the cell tested with an applied current density in dry air decreases by 31% (from 1.07 W/cm^2 to 0.74 W/cm^2), whereas the maximum power density of the cell tested under open-circuit voltage (OCV) with dry air remained nearly unchanged (1.02 W/cm^2). There is a more severe degradation when the cells are tested in humidified air where the power density decreases by 12% and 35% for no current and 0.75 A/cm^2, respectively. Therefore, this study finds that humidity and applied current density both promote Cr deposition and that the applied current density will further exacerbate Cr deposition on LSM.

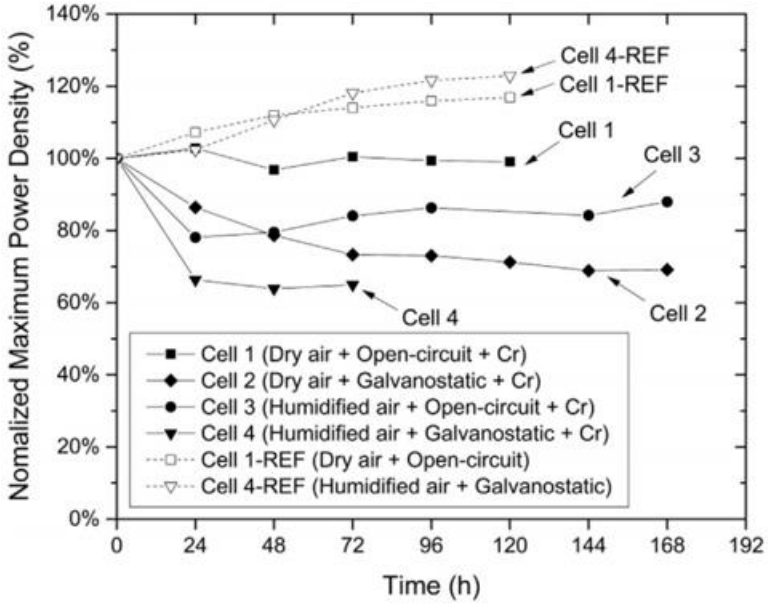

Figure 4. Variation of maximum power densities measured at 800 °C as a function of time (Values are normalized). Reprinted with permission from [33], Copyright [34], Elsevier.

The O_2 partial pressure has also been shown to contribute to the evaporation of chromium gaseous species $CrO_3(g)$, $CrO_2(g)$, and CrO(g), as pointed out by Yokokawa et. al [14]. Chromium gas species concentrations as a function of oxygen partial pressure calculated using data from Ebbinghaus [15] are shown in Figure 5.

The results show that the partial pressures of CrO_3(g), CrO_2(g), and CrO (g) over Cr_2O_3 exhibit different dependencies on oxygen potential. CrO_3(g) increases with increasing oxygen concentration to a greater extent than CrO_2(g) while CrO(g) concentration decreases. The thermodynamic calculations also suggest that gaseous species $CrO_2(OH)_2$(g) and CrO_3(g) are the most abundant Cr species in the equilibrium vapor, with the dominant species depending on the temperature and humidity. It should be noted that the predicted $CrO_2(OH)_2$(g) partial pressure will differ when calculated by the thermodynamics using different databases [13, 15, 31](also see Figure 3), which demonstrates that the evaluated $CrO_2(OH)_2$(g) data is uncertain. However, the CrO_3(g) partial pressures data estimated from different databases generally agree.

Besides water partial pressure and O_2 partial pressure, the operating temperature also influences the partial pressure of the chromium species. Hilpert [13] specifically studied the temperature dependence of the evaporation of Cr_2O_3(s) in relatively moist air [$p(O_2) = 2.13 \times 10^4$ Pa, $p(H_2O) = 2 \times 10^3$ Pa]. As can be gleaned from Figure 2 and Figure 3, $CrO_2(OH)_2$(g) is the most abundant vapor species for these conditions while the partial pressure of CrO_3(g) exhibits larger temperature dependence compared to the partial pressure of $CrO_2(OH)_2$(g). Several studies [31, 35, 36] have also shown that $CrO_2(OH)_2$(g) is the predominant Cr species when Cr-containing materials are exposed to O_2 and H_2O atmosphere for an extensive range of temperatures.

In summary, the partial pressure of these chromium species increased with increasing partial pressure of water and oxygen based on Eq. (1), (2) and (3). In terms of the temperature, the reaction rates of above three equations increases with increasing temperature contributing to the increased partial pressure of these chromium species. Because of the different temperature and partial pressure dependencies, the ratio between the equilibrium concentrations of each species will change depending on the conditions, but for general application conditions the dominant species will be $CrO_2(OH)_2$ and CrO_3 in humid and dry environments, respectively.

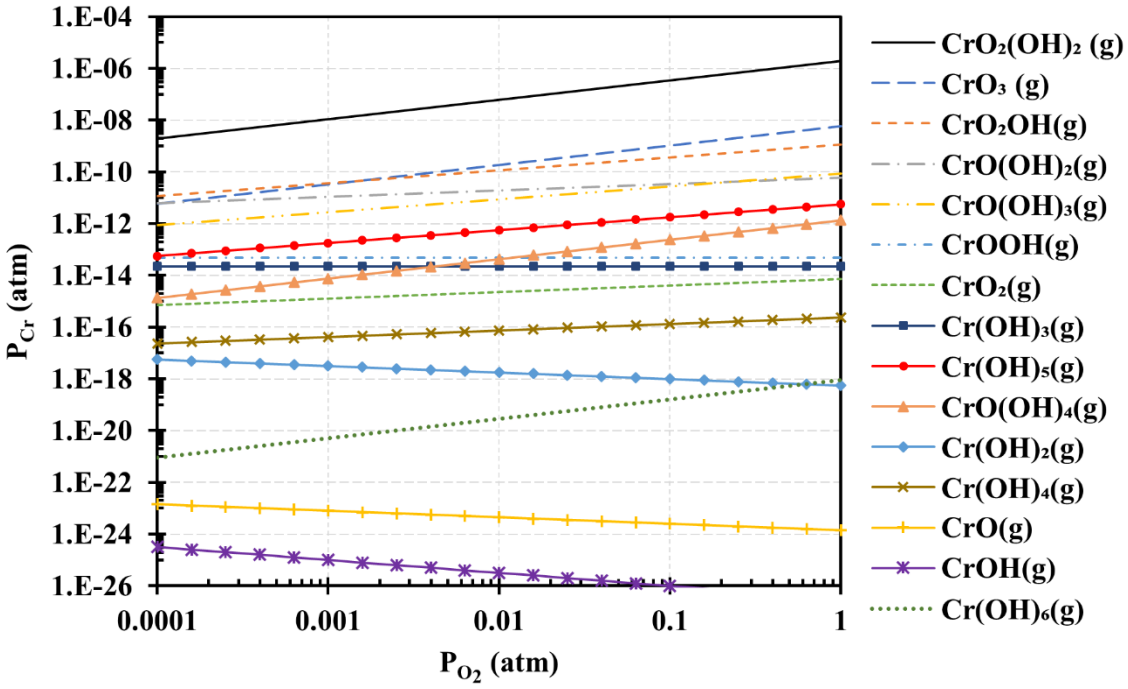

Figure 5. Partial pressures of different chromium species over Cr_2O_3(s) at 800°C, 3% H_2O as a function of P_{O_2} [15].

1.2.1.2 Effects of flow rate on chromium evaporation

Flow rate is another crucial factor as the vapor transport of gaseous Cr species plays a role in the Cr deposition within the cathode. Researchers [12, 28, 35] have studied the chromium transport rate at different flow rates using both Ducralloy ($Cr_5FeY_2O_3$) and Cr_2O_3 samples. Figure 6 shows the chromium transport rate versus flow rate using Cr_2O_3 as the chromium source material [12]. Three regions (diffusion region, equilibrium region and non-equilibrium region) are observed. In the diffusion region, chromium vapor is oversaturated in the carrier gas because of the low flow rate and mass transport of diffusion. The equilibrium region is where chromium evaporation rate varies linearly with the flow rate which indicates that the carrier gas is saturated with chromium vapor. An appropriate flow rate is determined experimentally as the flow rate at which the vapor is in thermal equilibrium with the carrier gas such that the chromium species is at the equilibrium partial pressure. The non-equilibrium region occurs at higher flow rates where the rate of diffusion of the vaporized species is too slow relative to the carrier gas flow rate to achieve a complete saturation in the reaction chamber. It is recommended that researchers consider the effect that their chosen flow rate will have on the chromium concentration in their experimental set up, as low flow rates will lead to

higher chromium species concentrations in the gas (equilibrium region) while high flow rates might result in a lower concentration but a higher amount of total chromium exposure over time.

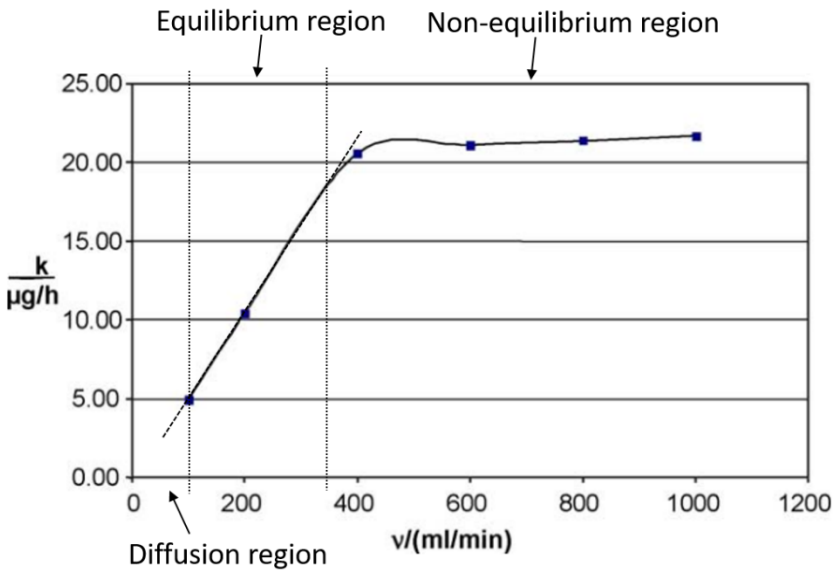

Figure 6. Chromium evaporation rate of Cr_2O_3(s) at 950 °C in humid air with different flow rates. Reprinted with permission from [12], Copyright [37], Elsevier.

1.2.2 Chromium vapor pressure quantification

Ambrose [38] claimed that the equilibrium vapor pressure of volatile chromium species could be determined experimentally if the equilibrium constants of reactions (1)-(3) are known. Vapor pressure of three major chromium containing species formed under different humidity levels and temperatures can be calculated based on reactions (1)-(3). Assuming thermal equilibrium between the solid phase and the gas phase, and assuming the activity of Cr_2O_3 to be 1 for pure chromium oxide (the activity of other chromium-containing oxides will be ≤1) the equilibrium partial pressure of each species is represented by Equations (4)-(6):

$$P_{\mathrm{CrO_2(OH)_2}} = P_{\mathrm{H_2O}} \cdot P_{\mathrm{O_2}}^{3/4} \cdot K_{eq,\mathrm{CrO_2(OH)_2}} \quad (4)$$

$$P_{\mathrm{CrO_2(OH)}} = P_{\mathrm{H_2O}}^{1/2} \cdot P_{\mathrm{O_2}}^{1/2} \cdot K_{eq,\mathrm{CrO_2(OH)}} \quad (5)$$

$$P_{\mathrm{CrO_3}} = P_{\mathrm{O_2}}^{3/4} \cdot K_{eq,\mathrm{CrO_3}} \quad (6)$$

The total partial pressure of the Cr-containing gaseous species is the sum of all the species above (P_{CrO_3}+ $P_{CrO_2(OH)}$+$P_{CrO_2(OH)_2}$), assuming all other Cr species have negligible concentrations. However, Gindorf [35]

put forward another way to calculate the partial pressure of gaseous Cr species. The partial pressure is calculated according to the ideal gas law:

$$P(\mathrm{Cr}) = \frac{RTk(\mathrm{Cr})}{vM(\mathrm{Cr})} \tag{7}$$

where R is the gas constant, T is the temperature, $k(\mathrm{Cr})$ is the resulting mass transport rate of the condensed chromium, v is the flow rate and $M(\mathrm{Cr})$ is the atomic mass of chromium. Herein, $P(\mathrm{Cr})$ only represents the partial pressure of $CrO_2(OH)_2$(g) and/or CrO_3(g). Gindorf [12] determined by thermodynamic calculations that $CrO_2(OH)$(g) will be negligible in comparison to $CrO_2(OH)_2$(g) or CrO_3(g), consistent with the calculations presented in this study. In consideration of $P_{\mathrm{CrO_2(OH)}} << P_{\mathrm{CrO_3}}$ and $P_{\mathrm{CrO_2(OH)_2}}$, the total partial pressure of gaseous chromium species is simply:

$$P_{\mathrm{Cr},total} = P_{\mathrm{CrO_3}} + P_{\mathrm{CrO_2(OH)_2}} \tag{8}$$

It is known that the partial pressure of CrO_3(g) is independent of $P_{\mathrm{H_2O}}$ (Equation (6)), while the partial pressure of $CrO_2(OH)_2$(g) does depend on $P_{\mathrm{H_2O}}$. For a constant oxygen partial pressure and temperature, Equation (4) can be reduced to $P_{\mathrm{CrO_2(OH)_2}} = b \cdot P_{\mathrm{H_2O}}$ where $b = a_{\mathrm{Cr_2O_3}}^{1/2} \cdot P_{\mathrm{O_2}}^{3/4} \cdot K_{eq,\mathrm{CrO_2(OH)_2}}$. Replacing $P_{\mathrm{CrO_2(OH)_2}}$ by $(b \cdot P_{\mathrm{H_2O}})$ in Equation (8) yields:

$$P_{\mathrm{Cr},total} = P_{\mathrm{CrO_3}} + b \cdot P_{H_2O} \tag{9}$$

However, these calculations assume that the total quantity of air entering the reactor achieves the equilibrium value (saturation) of $P_{CrO_2(OH)_2}$. Considering that the Cr species is transferred quite sluggishly from the Cr-containing materials into the passing air, this approach is not accurate for high gas flow rates when the Cr concentrations will be much less than the equilibrium value [30].

To quantify concentrations of gaseous chromium species experimentally, the transpiration method has been used extensively [5, 31, 39]. Konysheva et al. [5] adopted this method to assess the chromium evaporation rate from Cr5Fe1Y2O5 and Crofer22 APU ferritic steels. The electrochemical performance of the cells operating with Crofer22 APU is shown to be more stable than the cells with Cr5Fe1Y2O5, which is in accordance with the lower Cr evaporation rate from Crofer22 APU compared to Cr5Fe1Y2O5. Froitzheim et al. [40, 41] coated the inner wall of silica glass denuder tubes with Na_2CO_3 to absorb the vaporized Cr species.

Although the transpiration method allows for control of the temperature, flow rate, H_2O and O_2 partial pressure to precisely measure the Cr evaporation rate, the set-up of the device, long-term operation and the post-measurement of Cr species are intricate and time-consuming. Therefore, the transpiration method cannot be used to directly measure the chromium evaporation from metallic interconnects in real time during SOFC operation. It is feasible to estimate the average amount of volatilized chromium over the duration of an experiment by combining the total mass of the chromium collected by a getter downstream of the cell, as is implemented in experiments by Hardy et al [42].

Table 1**.** Common chromium containing interconnect materials and their chromium weight percentages.

Material Name	**Weight % Cr**
Crofer22APU	23%
Ducrolloy (Cr5Fe1Y2O3)	94%
Inconel 600	16%
Stainless Steel	25%
RA446	23-27%
Ni-Mo-Cr	12.24%
SUS430 Nisshin Steel Co. Ltd.	16.03%
ZMG232 Hitachi Metals Co. Ltd.	22%
17-4 PH SS	15.21%
E-Brite	26%
430SS	17%
SUS420 Nippon Steel Corp., Japan	16-18%
Crofer22H	20-24%
RA600	14-17%
FeCM	16.65%
ITM/ITM-14	26%

1.2.3 Solid phase chromium transport and quantification

Above only the gas phase transport of Cr species is discussed, considering the Cr-containing gaseous species as the source for the chromium transfer from the alloy to the cathode and the electrolyte. The driving force for the chromium transport increases if the temperature is increased or if the partial pressures of oxygen and water are increased. However, chromium is also considered to be transported via solid state surface diffusion in addition to vapor transport [43]. In general, it is assumed that the vapor transport and the surface diffusion reactions are dominant in proximity to the channels and the ribs of the interconnect, respectively. There is a sharp distinction between the vapor transport and surface diffusion mechanisms pertaining to the degree of chromium deposition from metallic interconnects and BoP components [13, 44, 45].

Nevertheless, the dominant transport path for the chromium species has not been confirmed. Tucker et al. [26] studied chromium deposition on different SOFC cathodes (including LSM and LSCF) at 700-1000 °C. It is concluded that the surface diffusion mechanism predominates in Cr deposition at open circuit conditions at any temperature. Jiang et al. [44] reported significant difference in the amounts of Cr deposition on the LSCF cathode under the rib and channel which indicates that vapor transport is much quicker than surface diffusion. Lau et al. [46] found that Cr deposition by gas phase transport is substantial on lanthanum nickel ferrite (LNF), while no Cr deposits occurs under the rib area with no discernible reaction at the rib/LNF interface. Presently, the diffusion rate of solid chromium species and the nature of this transport mechanism is not well understood and requires further investigation to understand how this transport might be influenced by temperature, cathode materials and polarization.

The relationship between the quantities of Cr species being deposited and the cathode performance degradation is still ambiguous, and in fact may not be directly correlated [47-49]. However, this relationship needs to be elucidated to formulate a coherent Cr poisoning mechanism which accurately describes the negative effects on SOFC operation as well as the morphology and quantity of chromium deposits produced under various conditions.

Jiang et al. [50] investigated the deposition behavior of Cr species on an LSM electrode/ yttria-stabilized

zirconia (YSZ) electrolyte half-cell in the presence of different alloys under 200 mA cm^{-2} current density in air at 900°C. The three alloys tested are RA600, RA446 and Crofer22APU. After operating for 20 h, the polarization potential increase (ΔE) is reported as 1170 mV for RA600, 400 mV for RA446 and 126 mV for Crofer22 APU, which is in accordance with the decreased relative amount of the observed Cr species deposition on YSZ (RA600 < RA446 < Crofer22 APU). The qualitative relation between ΔE and Cr deposition demonstrates that Cr evaporation from metallic interconnects and BoP components could be estimated by this kind of fast and easy electrochemical polarization method in the LSM/ YSZ system. Chen et al. [51] put forward another method to compare the Cr concentration deposited between different samples. The ratio of $La_{L\alpha}$ to $La_{L\beta}$ indicated by energy-dispersive X-ray spectroscopy (EDS) is used to compare the Cr concentration on the LSCF surface as the K_α peak of Cr and Lβ peak of La overlap with each other. The lower this ratio, the higher the Cr concentration on LSCF surface. However, the precise values of Cr concentration deposited in the LSM and LSCF systems are not reported by Jiang et al.

Schuler et al. [52, 53] also observe superimposed peaks in EDS spectra of the LSM system. Several ratios are used ($L_{\beta1}/L_{\alpha1}$, $L_{\beta2.15}/L_{\alpha1}$, $L_{\beta2.15}/L_{\beta}1$ and $K_{\beta1.3}/K_{\alpha1}$) to quantify the Cr concentration by EDS (Figure 7). The Cr concentration in the LSM system is also quantified by inductively coupled plasma - optical emission spectrometry (ICP-OES) after dissolving the cathode in nitric acid. By comparing the EDS spectra method with the ICP-OES measurements, it is found that the $L_{\beta2.15}/L_{\alpha1}$ ratio is the most reliable for determining chromium concentrations. The similar result obtained from ICP-OES and EDS quantification demonstrates that $L_{\beta2.15}/L_{\alpha1}$ ratio could be applied to precisely quantify Cr concentrations in the LSM system. From this observation, an empirical equation for Cr quantification is formulated:

$$Cr\% = 16.24 \frac{La_{L\beta2.15}}{La_{L\alpha1}} - 4 \quad (10)$$

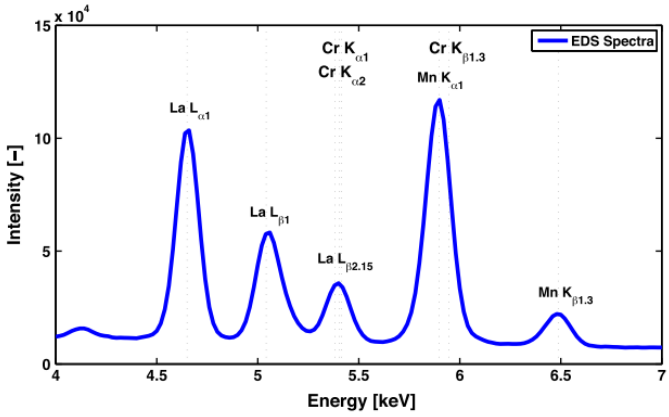

Figure 7. Overlapped Cr peaks with La, Mn and O in EDS spectra. Reprinted with permission from [52], Copyright [52], Elsevier.

Other methods have also been used to quantify the chromium concentration at the cathode/electrolyte interface and cathodes. For example, Horita et al. [54, 55] utilized secondary ion mass spectrometry (SIMS) to assess the Cr concentration distribution in LSM and LSF cathode and Liu et al. [56] applied high energy X-ray microbeam to accurately measure the Cr concentration distribution in the degraded cell.

In summary, Cr concentrations can be measured by several methods. It is possible to estimate gradients in Cr concentration using microscopy techniques. However, it is recommended that these methods be accompanied by physical measures of total quantities of Cr, as is done by Horita et al., to properly calibrate the measurement.

1.3 Approaches to Alleviate Cr-poisoning

It is known that Cr gaseous species evaporated from the chromia containing oxide layer formed on metallic interconnects at high temperature will cause serious degradation to SOFC cathodes. To minimize the effects of Cr several techniques have been studied. Development of novel cathode materials and modification of the cathode surface have been shown to enhance the Cr tolerance of SOFCs [7, 52, 57, 58]. For metallic interconnect and BoP components, it is possible to adjust the composition of their respective materials and/or apply protective coatings on these components to limit the amount of chromium in the air flow [59-66]. Instead of developing new alloys, applying effective coatings on the surface of interconnects and components might be more cost-effective as the coatings can prevent Cr vaporization without needing to manufacture these components from all new materials. However, coatings cannot always be easily applied to BoP

components. Thus, it is necessary to develop a new alloy to replace certain existing BoP components materials. In addition, Cr getters have been devised to be placed at the inlet of the fuel cell air stream to significantly reduce the partial pressures of gaseous Cr species before they reach the cathode region as an alternative to reducing the amount of Cr vaporized upstream.

1.3.1 Alternative Cathode Materials

Novel cathode materials have been designed which demonstrate extraordinary tolerance toward Cr poisoning and comparatively stable electrochemical performance compared to the traditional cathodes, such as LSM and LSCF which contain nucleation elements such as Mn and Sr. In this section some novel electrode materials are highlighted which are free from both Sr and Mn and tolerant to Cr poisoning while also having relatively good stability and performance.

$La(Ni,Fe)O_3$ has been developed as one of the most promising cathode materials due to its high electric conductivity (580 S/cm at 800 °C) , matched thermal expansion coefficient (TEC) (11×10^{-6} K^{-1}) with YSZ and a high tolerance towards Cr poisoning [67]. LNF hardly reacts with Cr_2O_3 powder when heated for 1000 h at 800 °C [68], whereas Cr replacing Ni and Fe in the perovskite phase is observed by Stodolny [69]. Lau et al. [46] concluded that Cr deposits are observed on LNF, but without noticeable direct reaction between Cr containing interconnect and the LNF surface. While Cr is shown to degrade LNF cells, it is verified that the electrochemical performance and the Cr tolerance of cells with LNF cathodes are superior to LSM and LSCF cathodes [7, 52, 57, 58]. A cell using an LNF cathode made by Orui [70] exhibited the optimal power density of 1.56 W cm^{-2} at 1073 K. The effect of current load on the long-term operation of LNF cathodes in the presence of Cr is investigated by several researchers [17, 57, 71-75]. When low current load ($\leq$1 A cm^{-2}) is applied, the voltage decreases linearly [71] attributed to the Cr-incorporation in the surface of the LNF grains [17]. However, the degradation rate is relatively slow compared to LSCF and LSM [58]. The degradation rate of the cell with the LNF cathode is 0.5%/1000 h and 0.86%/1000 h for 7000 h under an applied current density of 0.28 A cm^{-2} and 5200 h under a constant current density of 0.4 A cm^{-2}, respectively. Chiba et al. [75] show it is possible to enhance the LNF performance by adding an active layer between the LNF and electrolyte and the minimal reaction between LNF and Cr_2O_3 at 600°C reported by Stodolny et al. [69]

indicate LNF may be promising for intermediate temperature application.

Jiang et al. [76] propose that substituting Sr with Ba could drastically decrease the Cr deposition. Cells with LBCF cathodes show stable electrochemical performance and no change in microstructures compared to those with LSCF cathodes. Large deposited particles of $SrCrO_4$ phase are observed on LSCF, while there are no visible Cr deposits on LBCF. Chen et al. [77] employed a method of infiltrating LSCF with BaO nanoparticles which made LSCF a superior Cr-tolerant material compared to un-infiltrated LSCF. This improvement is attributed to the formation of $BaSrO_4$ reducing SrO segregation.

$LnBaCo_2O_{5+\delta}$ series double perovskites are promising novel cathodes due to their superior performance [78]. However, Sr and Ba doped in these cathodes could induce the deposition of vaporized Cr species. Nevertheless, Li et al. [79] report the Cr deposition and poisoning on the $La_2NiO_{4+\delta}$ (LN)-coated PBSCF cathodes compared to untreated PBSCF. They found that coating with LN not only improves the cell performance, but also blocks the reaction between Cr gaseous species and the cathode. Similarly, Chen et al. [80] infiltrated a hybrid catalyst coating consisting of $PrNi_{0.5}Mn_{0.5}O_3$ (PNM) and exsolved PrO_x nano-particles to greatly reduce the Cr poisoning of LSCF cathodes. Zhao et al [81] found that the chromium tolerance of LSCF electrodes may be improved by impregnating the cathode with GDC nanoparticles. Simultaneously, the electrocatalytic activity of the cathode is improved significantly. It is found that the GDC, which does not react readily with Cr, acts as a barrier between the Cr gas and the LSCF while facilitating oxygen reduction.

Depending on the application, it might be more economically feasible to infiltrate Cr-tolerant materials into previously developed cells to improve their degradation rate rather than expending resources on the development of new electrodes, interconnects or BoP components. However, the long-term stability and catalytic activity of the cells needs to be maintained and the process to apply infiltration needs to be economical for the infiltrated cells to be commercially viable.

1.3.2 Coatings and alternative BoP components (AFAs)

Efforts have been made to optimize the compositions of metallic interconnects to suppress the spinel formation on the alloy surface while maintaining performance and stability. However, due to the high costs and complex processes involved in inventing a new alloy, it may be more prudent to apply an effective coating on the metallic interconnects to decrease the evaporation of gaseous Cr species.

A Fe-Cr-Mo-Mn alloy interconnect has been developed by Xiong et al. [82] to reduce Cr vaporization and mitigate poisoning of LSM cathodes. Newly added minor elements result in different microstructural properties and change the composition of oxides formed on the interconnect, negating Cr evaporation. Half cells with YSZ electrolytes and LSM cathodes are operated under an applied current density of 200 mA cm^{-2} at 850 °C for 20 h with the Fe-Cr-Mo-Mn alloy and commercial SUS430 ferritic stainless-steel interconnects. R_p decreases by 2.19 Ω cm^2 (36.7%) and overpotential increases by 0.58V for the cell contacted with SUS430, while the R_p decreases by 4.08 Ω cm^2 (70.8%) and the overpotential also decreases by 0.27V for the cell contacted by the new alloy. The cell tested with SUS430 experiences a significant increase in Ohmic resistance, attributed to the formation of a low conductivity Cr oxide layer on the interconnect/cathode interface, while the cell with the new alloy has a stable ohmic resistance. It is found that the deposition ring of solid Cr species on the YSZ surface is significantly narrower for the F-Cr-Mo-Mn alloy with the interface between YSZ/LSM being covered with small Cr oxide particles while the cell with the SUS430 interconnect develops large spinel crystals at this interface. The superior Cr-resistant property of Fe-Cr-Mo-Mn alloy is attributed to the Mo-rich oxide formed on the alloy which can reduce both the formation of Cr-Mn spinel and the evaporation of Cr volatile species. In stack level application, Haart et al. [47] apply alternative MICs to replace Crofer 22APU and succeed in reducing the degradation rate of the cells, including a reduction in Cr poisoning. Chen et al. [83] apply a novel Ni-Mo-Cr alloy to replace the commercially available RA446 alloy, aiming to alleviate Cr poisoning of the MIC. The results demonstrate that the overpotential of the cell decreases in the presence of Ni-Mo-Cr alloy, whereas the overpotential of the cell with RA446 alloy increases. This decrease in overpotential is attributed to the formation of a $NiMn_2O_4$ layer on the surface of the alloy, which reduces Cr volatilization.

Numerous coatings have been developed to prevent the evaporation of Cr gaseous species. Wang and Sun [59, 60] test a $CuMn_{1.8}O_4$ spinel coating on Crofer 22 APU and Crofer 22 H alloys for mitigating the Cr poisoning on the anode-supported cells compared to untreated alloys and alloys coated with commercial $CuMn_2O_4$ coating. After operation under an applied current density of 500 mA cm^{-2} at 800 °C for 48 h, the Rp increases by 1.1%, decreases by 16.2% and decreases by 29.9% for the cells in contact with the untreated alloy, the alloy with $CuMn_2O_4$ coating and the alloy with $CuMn_{1.8}O_4$ coating, respectively. Moreover, the cell potential decreases by 30% over 144 h, increases by 3% over 240 h and increases by 18% over 240 h of operation for the samples with no coating, the $CuMn_2O_4$ coating and the $CuMn_{1.8}O_4$ coating, respectively. The excellent Cr-suppressing performance of the $CuMn_{1.8}O_4$ coating is ascribed to the reaction between Cr_2O_3 and $CuMn_{1.8}O_4$ that results in the formation of Cr-doped copper manganese spinel $(Cu,Mn,Cr)_{3-x}O_4$ which acts as a Cr getter to reduce the Cr vaporization. However, if the solubility limit of Cr in $(Cu,Mn,Cr)_{3-x}O_4$ is reached over time, Cr_2O_3 will further react to form an outer $MnCr_2O_4$ layer. Another positive result is that the interfacial ASR between the LSF cathode and coated Crofer22 APU is about 3 times smaller than that of the uncoated [65]. Zhao et al. [66] achieved an ASR of 49.25 mΩ cm^2 after 15 weeks of exposure with a $NiFe_2$ alloy coating. Stanislowski et al. [84] also found that Cr evaporation can be reduced by 99% when Co, Ni and Cu metallic coatings are applied. Grolig et al. [85] applied reactive element (La and Ce) coatings coupled with a Co layer on stainless steel to effectively reduce the Cr evaporation by 90% compared to untreated alloys. A Cu-containing perovskite material (LCC10) is utilized [48, 49, 86] between the cathode and the MIC to reduce the ohmic resistance and the Cr evaporation rate. Fujita et al. [87] used electron beam physical vapor deposition (EBPVD) and spin-coating techniques to deposit a lanthanum strontium cobalt oxide coating on the commercial SUS430 alloy, finding that the coating can effectively suppress the growth of the chromium oxide and reduce the Cr deposition on the cell. However, the introduction of Cu containing coatings resulted in Cu containing spinels depositing in the cathode in addition to Cr containing spinels [48].

While coatings have been shown to effectively reduce Cr vaporization, BoP components cannot be fully protected by coatings. Therefore, it is necessary to develop a new alloy to replace iron-chromium alloys used for components such as heat exchangers, turbines and converters which will release Cr gaseous species under

high-temperature operation. Unlike interconnect materials, BoP components are not restricted by their electrical conductivity or their thermal expansion properties. With this in mind, a new Al_2O_3-forming austenitic (AFA) stainless steel with low cost, high Cr-resistance and high-creep strength is developed by Yamamoto and Brady [20, 88-91]. It is shown that on the new material, an alumina-based protective layer forms under high temperature that is invulnerable to water vapor effects and suppresses the diffusion of chromium and manganese preventing the generation of spinels on the alloy surface. Work is still being done to optimize the compositions of the AFA alloys for the application of long-term high-temperature operation [61-64].

1.3.3 Cr getters

In recent years, Cr getters have been used to reduce chromium poisoning by directly capturing gaseous chromium species from the air flow upstream of SOFC's. Singh and his co-workers applied Cr getters in LSM [92] and LSCF [93] systems showing that getters have stable performance and high efficiency of Cr species capture. Moreover, electrochemical methods [94] and modelling [95, 96] demonstrate the feasibility of Cr getter application in the SOFCs.

An example of a stable Cr getter is $Sr_9Ni_7O_{21}$ (SNO) synthesized by pyrolysis of nitrate solutions is tested by Liang et al. under 3% H_2O at 850 °C for 500h in the LSM system [92]. By comparing the evaporated Cr amounts to the ICP measurements, it is found that a high efficiency of 98.38% Cr reduction could be achieved. Chou et al. [93] also synthesize $Sr_9Ni_7O_{21}$ and $Sr_4Ni_3O_9$ using the method of solid-state reactions in addition to pyrolysis of nitrate solutions and examine it under a constant current density of 0.375 A/cm^2 at 800 °C for 1000h in humidified air (4.75% H_2O). The resulting degradation rate of the cell tested without a Cr getter is about 56%/kh, while the cell tested with a Cr getter exhibits a degradation rate of only 12.1 %/kh. Aphale et al. [94] also investigate the electrochemical performance of LSM in the absence and presence of Cr getters. It is shown that the cell with a Cr getter exhibits stable performance, however, the cell without a Cr getter degrades rapidly. Uddin et al. [96] apply LSCF+SNO as an in-cell getter layer to reduce the amounts of Cr deposited in the cathode. The cell with the applied layer demonstrates performance in the presence of Cr gas similar to the cell that is not exposed to Cr. Meanwhile, a cell without a getter layer degrades severely

within the first few hours of operation. However, it is postulated that for long term operation the getter layer will become saturated with Cr deposits eventually allowing Cr gas to reach the cathode. Computational modelling by Uddin et al. [95] demonstrates that the support structure and coating porosity of SNO getters can be optimized to effectively capture Cr for 40000-50000 h of operation, which is the target lifetime for commercial SOFC applications. Therefore, Sr-Ni oxides may be a promising candidate for Cr capture.

1.4 High temperature oxidation of alloys

1.4.1 High temperature alloys

1.4.1.1 Austenitic stainless steels

Austenitic stainless steels contain a maximum of 0.15% carbon, a minimum of 16% chromium and sufficient nickel and/or manganese to maintain a face center cubic (FCC) structure at all temperatures from the cryogenic region to the melting point of the alloy. Great resistance to chloride pitting and crevice corrosion of austenitic stainless steels could be enhanced by high molybdenum content (> 6%) and nitrogen additions. Moreover, for the example of 306L, the 'L' stands for the low carbon used to provide extra corrosion resistance after welding and to avoid carbide precipitation. In general, austenitic stainless steels exhibit better corrosion resistance than both ferritic and martensitic stainless steels. Austenitic stainless steels cannot be hardened by heat treatment; however, they could be cold worked to improve hardness, strength and stress resistance. Austenitic stainless steels have good formability and weldability, as well as excellent toughness, particularly at low, or cryogenic, temperatures. They are not very strong materials; however, they have great ductility with about 50 % elongations in tensile tests. They are also possess great oxidation resistance because of the protective surface film, but the usual grades have low strengths at high temperatures. Austenitic stainless steels are less resistant to cyclic oxidation than are ferritic grades because their greater thermal expansion coefficient tends to cause the protective oxide coating to spall. Austenitic stainless steels are often described as non-magnetic but may become slightly magnetic when machined or worked.

1.4.1.2 Ferritic stainless steels

Ferritic stainless steels consist of 11% to 27% chromium, iron with small amounts of ferrite stabilizers, such as niobium and titanium with a body center cubic (BCC) structure. They also contain very little carbon and are non-heat treatable; like austenitic stainless steels, ferritic stainless steels exhibit superior corrosion resistance to martensitic stainless steels and possess good resistance to oxidation. However, their mechanical properties are normally poorer than austenitic stainless steels. Unlike austenitic stainless steels, ferritic stainless steels exhibit ferromagnetic behavior up to a temperature known as the Curie point (650 °C - 750 °C), beyond which materials lose their permanent magnetic properties. They also have a lower thermal expansion coefficient and higher thermal conductivity than austenitic stainless steels. The toughness is limited for thicker dimensions, ferritic stainless steels are readily welded in thin sections, and they suffer grain growth with consequential loss of properties when welded in thicker sections.

1.4.1.3 Martensitic stainless steels

Martensitic stainless steels consist of carbon (0.2-1.0%), chromium (10.5-18%) and iron. Unlike austenitic and ferritic stainless steels, martensitic stainless steels may be hardened by heat treatment to provide a range of mechanical properties. Both their corrosion resistance and toughness are moderate, like ferritic stainless steels, martensitic stainless steels are ferromagnetic, subject to an impact transition at low temperatures but possess poor formability. Their thermal expansion and other thermal properties are similar to ferritic stainless steels.

1.4.1.4 Duplex stainless steel

Duplex stainless steels have a microstructure consisting of austenite and ferrite; they are characterized by high strength, good toughness and very good corrosion resistance in general. They are also ferromagnetic and subject to an impact transition at low temperatures. Their thermal expansion lies between that of austenitic and ferritic stainless steels, while other thermal properties are similar to plain carbon steels. Formability is reasonable, but higher forces than those used for austenitic stainless steels are required.

1.4.1.5 Superalloy

Superalloys are metallic materials for elevated temperature service, usually based on group VIIA elements of

the periodic table, which are proven to have great capabilities to maintain mechanical strength and creep resistance as well as structural and surface stability from room temperature to 0.8 Tm (melting point) of the alloy. Superalloys are generally for most demanding high temperature applications such as steam power plants, petroleum refineries, gas turbines (land, marine and air), rocket engines and nuclear power plants, just to mention a few from the broad spectrum of high-temperature applications where the resistance to deformation and stability are prime requirements. Other high temperature properties include corrosion and oxidation resistance, high creep rupture strength, low thermal fatigue and low coefficient of thermal expansion are also required.

There are three main groups of superalloys: nickel base, cobalt base and iron base. Ni-base alloys are the most widely used for the hottest parts in high-temperature applications and they have the most complex, subtle and sophisticated metallurgy. Ni base superalloys usually contain at least 12 to 13 basic alloying elements and 10 more trace elements such as manganese, silicon, phosphorus, sulfur, oxygen and nitrogen which should be carefully controlled to minimize their deleterious effects.

1.4.2 Effects of the alloying elements

Alloying elements are often added to modify the properties and performance of the steel. It is the synergistic effect of all the alloying elements and, to some extent, the impurities that determine the property profile of a certain steel grade. The effects of some important alloying elements on the materials properties are discussed. It should also be noted that the effect of the alloying elements differs in some respects between the hardenable and the non-hardenable stainless steels.

Chromium is by far the most important alloying element in stainless steel. A minimum of 10.5% chromium is required for the formation of a protective layer of chromium oxide on the steel surface. The corrosion and oxidation resistance of the stainless-steel increases with increasing chromium content. Chromium promotes a ferritic structure and therefore is described as a ferrite stabilizer.

Nickel improves general corrosion resistance and promotes the austenitic structure (it is considered as an austenite stabilizer). Stainless steels with nickel (8-9%) have a fully austenitic structure, further increase in the nickel content improves both corrosion resistance (especially in acid environments) and also increases

ductility and toughness (better workability). Nickel is also used to form the intermetallic compounds that are used to increase the strength in precipitation hardening steels.

Molybdenum substantially increases resistance to both local (pitting, crevice corrosion, etc) and general corrosion. Molybdenum and tungsten promote the ferrite structure, when used in austenitic alloys, must be balanced with austenite stabilizers in order to maintain the austenitic structure. In martensitic steels it will increase the hardness at higher tempering temperatures due to its effect on the carbide precipitation.

Nitrogen is a very strong austenite former; it also substantially increases the mechanical strength and the resistance to localized corrosion. In ferritic stainless steels nitrogen will strongly reduce toughness and corrosion resistance. In the martensitic and martensitic-austenitic steels nitrogen increases both hardness and strength but reduces the toughness.

Carbon is also a strong austenite former; it enhances strength (especially, in hardenable martensitic stainless steels), but may reduce the corrosion resistance by the formation of chromium carbides. Where it is not desirable or, indeed, not possible to control carbon at a low level, titanium or niobium may be used to stabilize stainless steel against intergranular corrosion. As titanium (niobium and zirconium) have greater affinity for carbon than chromium, titanium (niobium and zirconium) carbides are formed in preference to chromium carbide and thus localized depletion of chromium is prevented. These elements are ferrite stabilizers.

Sulfur is added to improve the machinability of stainless steels. Therefore, sulfur will substantially reduce corrosion resistance, ductility and fabrication properties, such as weldability and formability.

Hafnium, Zirconium, Yttrium and similar rare earth metals are added in small amounts to stainless steels or high temperature alloys to improve the oxidation and corrosion resistance and adhesion of the oxide film at high temperatures.

Manganese is generally considered as an austenite stabilizer and used in stainless steels to improve hot ductility. However, at high temperatures manganese will stabilize ferrite. Manganese increases the solubility of nitrogen and is used to obtain high nitrogen contents in austenitic steels.

Silicon improves resistance to oxidation and is also used in special stainless steels exposed to highly

concentrated sulfuric and nitric acid. Silicon is a ferrite stabilizer.

Aluminum improves oxidation resistance, if added in substantial amounts. It is used in certain heat resistant alloys for this purpose. In precipitation hardening steels aluminum is used to form the intermetallic compounds that increase the strength in the aged condition.

1.4.3 oxidation of alloys

The characteristic of the oxidation reaction is that the reaction is heterogeneous and does not proceed exclusively in the interior of one phase. Heterogeneous reactions occur between two immiscible phases and usually result in the formation of a new phase. Such reaction can occur between the oxidants in the gas phase (or liquid phase) and a solid phase (metal or alloys) with formation of normally oxide phase. At low temperatures, the process of oxide phase formation is slow but at high temperatures such oxidation reaction is accelerated. The oxidation process is generally governed by solid-state diffusional transport of atoms or ions and electrons through the oxide phase (scale), when a continuous oxide scale is assumed. High temperature oxidation resistance is often required for alloys service at high temperatures. The knowledge of oxidation theory is a must when designing or/and selecting alloys for high temperature applications.

1.4.3.1 Oxidation Mechanism and Kinetics

The oxidation phenomenon is generally governed by both the principle of thermodynamics and solid-state diffusion. For most metallic elements, a general reaction between the metal (M) and oxygen (O) in the gas phase can be written as

$$\frac{x}{y}\mathrm{M}+\frac{1}{2}\mathrm{O}_2=\frac{1}{y}\mathrm{M}_x\mathrm{O}_y \tag{11}$$

The Gibb's free energy (ΔG) associated with such a reaction is generally negative for a corrosion or oxidation product to form. In practice, it is easier to compare the ΔG^o (standard Gibb's free energy of formation) of typical oxides using a Richardson/Ellingham diagram as shown in Figure 8. The values of ΔG^o are expressed as kJ mol^{-1}, so the relative stabilities of various oxides may be compared directly at different temperatures. It is clear from this diagram that elements like aluminum, silicon and chromium that are near the bottom for unit activity of the metal, the oxides of these metals are more stable than the oxides

of the elements above. The large affinity for oxygen is one of the criteria of choosing desired alloying elements for oxide scale formation.

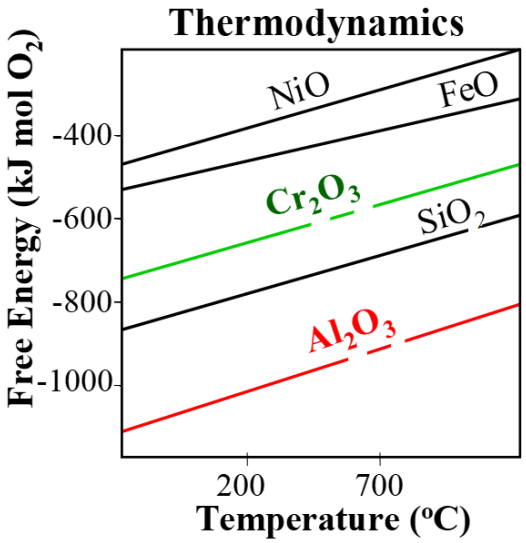

Figure 8 Gibb's free energy of typical oxides in Richardson/Ellingham Diagram [97].

Another criterion of choosing desired alloying element is the kinetics of the oxide scale formation need to be relatively slow. After an initial oxide layer is formed, further oxidation of the metal is achieved by solid-state diffusional transport of ions and electrons through the oxide. The driving force for metal cation and/or oxygen anion diffusion through the oxide (scale) is the activity gradient (or chemical potential) created across the scale as demonstrated in Figure 9 if several assumptions are made as Wagner did in the calculation [98].

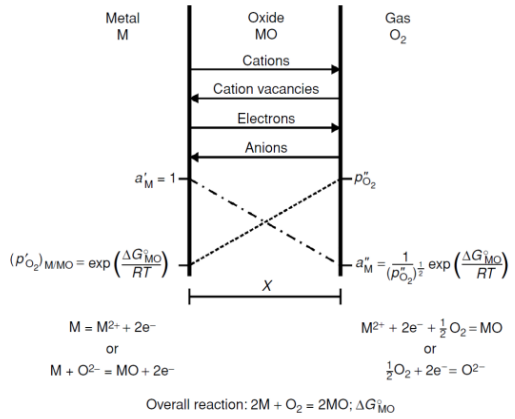

Figure 9 Schematic diagram of species transport and equilibrium reactions

Assuming thermodynamic equilibrium is established at each interface: at the metal-oxide interface, the

activity of the metal at the metal-oxide interface is equal to that in the alloy, and the apparent oxygen partial pressure will be the dissociation pressure for that oxide; similarly at the gas-oxide interface, activity of the metal can be calculated where the oxygen partial pressure is that in the atmosphere.

In theory, two types of ionic transport can co-exist: inward diffusion of the oxygen ions and the other is the outward transport by the cation of the metal species. However, in practice, it is possible to ignore the migration of the slower-moving ionic species as the mobilities of the cation and anion species usually differ by several orders of magnitude.

Wagner quantified growth rate as a function of scale thickness and time. As the scale thickens, the diffusion distance increases and ultimately reduces the reactant flux establishing an ever-decreasing scale growth rate.

$$x^2 = 2k't \tag{12}$$

Where x is scale thickness, the square of which is proportional to time t, and the proportionality constant is *k'*, which is termed as the parabolic rate constant. Experimentally a similar equation was adopted as continuously monitor oxidation by mass change is easier to achieve.

$$\left(\frac{m}{A}\right)^2 = k''t \tag{13}$$

Where A is the area over which reaction occurs; *k''* is also referred to as the practical tarnishing constant or 'scaling constant' and has units of $g^2\ cm^{-4}\ s^{-1}$.

A comparison of parabolic rate constants for selected oxide scales as a function of reciprocal temperature is presented in **Figure 10**.

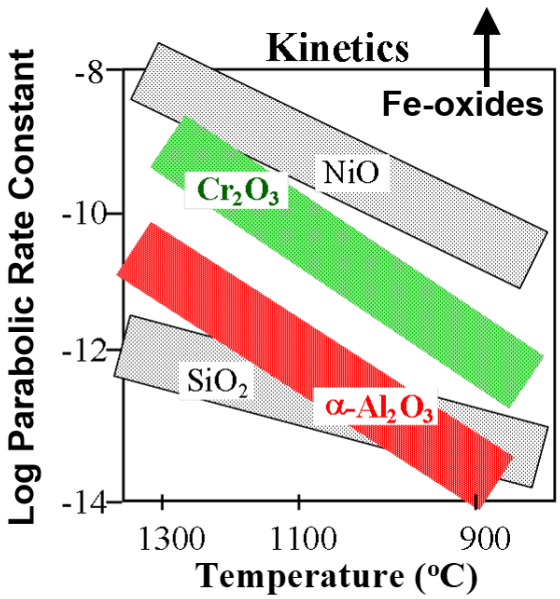

Figure 10 Comparisons of parabolic rate constants for selected oxide scales.

1.4.3.2 Selective Oxidation

The process in which a solute oxidizes preferentially to the parent element and forms a continuous layer on the surface is referred to as selective oxidation. As discussed above, the ability for an alloy to form a protective oxide is both a thermodynamic and a kinetic issue. From thermodynamic point of view, the desired oxide scales need to have large oxygen affinity compared with other elements in the alloy; from kinetic point of view, the desired oxide should also have fairly slow growth rate. In practice, in Ni, Fe, or Co base alloy systems, the desired Cr_2O_3 or Al_2O_3 scale has much lower growth rate compared with the parent metal oxide. During the initial stage of oxidation, all of the elements in the alloy will oxidize and the initial oxide layer formed on the surface will be composed of elements in proportions as they are present in the alloy.

Once this transient oxide forms a continuous layer on the alloy, a drop of oxygen activity at the oxide metal interface will only allow the thermodynamically more stable oxide to continue to form. The capability of the alloy to maintain this oxide depends on the amount of this element in reserve and its ability to diffuse to the scale for further reaction. The concentration in the alloy to achieve this can be represented by

$$N_B^{Critical} = \frac{V_m}{32v}\left(\frac{\pi k_p}{D_B}\right)^{1/2} \quad (14)$$

Where $N_B^{Critical}$ is the concentration of the oxide forming element in the alloy, D_B is diffusivity of element B in the alloy, kp is the parabolic rate constant, Vm is the is the specific volume of the metal and v is the ratio of oxygen to B in the oxide. The selective oxidation of elements which form a slowly growing, protective layer is the basis for the oxidation protection of all alloys and coatings used at high temperature. These contain a sufficiently high concentration of a solute (e.g., Cr, Al, or Si) to produce an external layer of a stable oxide scale.

1.4.3.3 Effects of Water Vapor

Water vapor is present in many gases of industrial importance. It is well known that most technical steels oxidize faster in water vapor or in air or combustion gases containing water vapor than in dry oxygen [71]. Water vapor can interact with metals or alloys in many ways. It can participate in surface reactions, thereby modifying the scale–gas interface; it can also change the microstructure, morphology, properties and growth rate of the scale formed. The surface reactions induced by water vapor are often overwhelmed by changes in the scale microstructure, morphology, and diffusion or transport properties. In principle, there are mainly three ways water vapor can incorporate in the mass transfer processes within the scale: (1) gas transport, which is within cracks, voids or cavities in the scale; (2) molecular transport, which is long grain boundaries that are affected by water vapor; (3) ionic transport, which is possible achieved by dissolving hydrogen into oxide and affecting defects concentrations.

Chapter 2 Research Objectives

- Choose AFA alloys with lower Cr evaporation rates and better oxidation resistance to replace the existing BoP components applied at different temperatures.
- Cr evaporation rates and oxidation behaviors of AFA alloys in comparison with benchmark alloys were studied.
- Verify the formed continuous alumina layer on AFA alloys and characterize its morphology after different oxidation durations
- Demonstrate the long-term stability of AFAs in air with 10% H_2O after 10,000 h long-term cyclic oxidation.
- Investigate the long-term stability of anode-supported cells coupled with AFAs and benchmark alloys.
- Possible Si contamination and Cr deposited on alumina tubes were discussed.

Chapter 3 Experimental Methods

3.1 Materials and sample preparation

The 800-900 °C range of SOFC BOP operation temperatures straddles the transition between typical use of heat-resistant stainless steels and more costly Ni-based alloys. Several different grades of alloys were therefore investigated, including chromia-forming Fe-based 310S stainless steel (lower end of the target temperature range), and chromia-forming Ni-based alloy 625 (higher end of the target temperature range) as reference materials; and three AFA type alloys: internal designation OC5 (3Al-1Nb) [62], OC4 (3.5Al-2.5Nb) [99], and OC11 (4Al-2.5Nb + Hf, Y) [100]. These AFA alloys represent a range of key alloying additions Al, Cr, Nb, Hf, and Y (**Table 2)**. The OC4 has a similar composition to OC5 but higher Al (3.5 vs 3 wt.%) and Nb (2.5 vs 1 wt.%) and is the same nominal AFA alloy composition as was studied in references 22 and 24. The OC11 further increases the Al (4 wt.%), increases the Cr (14 to 15 wt. %), and adds small amounts of Y and Hf. These elements can significantly influence the alloy manufacturability (lower Nb, and no Y preferred), cost (lower Nb and no Hf/Y preferred), creep resistance (lower Nb, Al, and Cr preferred), and oxidation resistance (higher Nb, Cr, Al, and Hf/Y preferred). All AFA alloys [20, 62, 91, 97, 99-101] represent a compromise between alumina formation capability, creep strength, and cost. They exhibit an upper-temperature oxidation limit depending on composition and exposure environment, with a transition from protective alumina formation to internal attack of Al and rapid Fe-rich oxide nodule formation with increasing exposure temperatures. This transition temperature varies from ~750-800 °C to ~950-1000 °C range in 20 to 25Ni-based AFA alloys, depending on alloy Al, C, Cr, Nb, Ni, Ti, and V levels, as well as reactive element microalloying additions.

The 310S (Outokumpu, Nyby Sweden) and 625 (ATI Flat Rolled Products, Brackenridge, PA USA) were procured as commercial sheet. The OC4 and OC5 were made as 180 kg heats by vacuum induction melting (VIM)/vacuum arc remelt (VAR) processing by Carpenter Technology Corporation (Philadelphia, PA USA). The OC11 was made as a 15 kg VIM heat, also by Carpenter Technology Corporation. The AFA alloys were

studied as hot worked and ~1200°C solutionized 12 mm thick plates per reference [62]. Test samples were electro-discharge machine (EDM) cut for oxidation and Cr evaporation tests.

Table 2. Analyzed compositions of AFAs and benchmark commercial Cr_2O_3-forming alloys in weight percent (wt. %) as determined by inductively coupled plasma and combustion techniques.

Grade (Internal designation)	Fe	Ni	Cr	Al	Nb	Mn	Si	Mo	W	C	B	other
OC5	Bal.	25.03	14.01	3.03	1.02	2.00	0.15	2.00	1.00	0.11	0.009	0.51Cu
OC4	Bal.	25.00	14.02	3.52	2.54	1.99	0.16	2.01	0.99	0.11	0.009	0.51Cu
OC11	Bal.	25.10	14.91	4.08	2.54	1.98	0.15	1.98	-	0.10	0.01	0.47Cu 0.18Hf0.03Y
OC11LZ	Bal.	24.94	15.08	3.96	2.46	1.94	0.14	1.97	-	0.11	0.004	0.5Cu 0.09Zr0.02Y
OC11LZA	Bal.	24.52	14.98	4.09	2.44	1.89	0.20	2.01	-	0.11	0.009	0.5Cu 0.1Zr
310S*	Bal.	19.16	25.55	-	-	0.84	0.57	0.20	-	0.05	-	0.20Cu
625*	4.60	Bal.	22.06	0.18	3.38	0.36	0.24	8.22	-	0.04	-	0.21Ti

*Compositions based on manufacturer alloy batch certification

3.2 Cr evaporation rates measurements

For the Cr evaporation rate measurements, all the alloy samples were cut into a rectangular shape. Before oxidation testing, they were wet-polished with silicon carbide (SiC) abrasive paper up to 800 grit, rinsed with acetone, isopropanol, and deionized water. The final dimension of each sample was approximated to 25 mm × 20 mm × 1 mm with an exposed surface area approximately to 11 cm^2.

The Cr vaporization measurements used the transpiration method based on the principle that the vapor over the heated sample will be carried away by constant gas flow and collected in a condenser. The oxidation exposure experiments for the Cr release experiments were carried out in a tube furnace as shown in Figure 11. The gas control system consists of three parts, i.e., flow meter, MH-series humidifier, and PID temperature controller. The Cr species carried by the air gas flow through the tube furnace are collected in the solution of

DI water with a cooling system (Hydrofarm, Model AACH10). The humidity of the air was adjusted by a bubble humidifier, which was controlled by the gas flow meter, PID temperature controller, and MH-series humidifier and was finally fixed at 10% in the quartz tube. The gas flow rate was set at 0.2 L min^{-1} to carry away the gaseous Cr species and then further condensed and collected in the filtering flask. The temperature range of interest is 800-900 °C, which encompasses the transition range between "lower" and "higher" temperature commercial SOFC fuel cell BOP operation targets. Flowing air and 10% H_2O was selected for study to represent the most aggressive oxidation conditions likely to be encountered in SOFC BOP. The cleaned samples were heated to the desired temperatures and hold for 500 hours, during which Cr release is expected to be the highest as the oxide scale is established and enters steady-state growth for the critical temperature range of 800 to 900 °C. To increase the surface area exposed and thus obtain enough Cr-containing vapor, two samples per alloy type handing in an alumina boat were vertically put into the same quartz tube for the Cr vaporization measurements. To ensure the accuracy of the Cr evaporation rate, concentrated HNO_3 was applied to dissolve the residue Cr species from the reactor wall and all the solution was collected for further characterization. The collected Cr-containing solutions were quantitatively analyzed by inductively coupled plasma mass spectrometry (ICP-MS). The average Cr evaporation rate was calculated from the concentration of Cr based on the ICP results, the surface area of the sample, and the duration of the oxidation process.

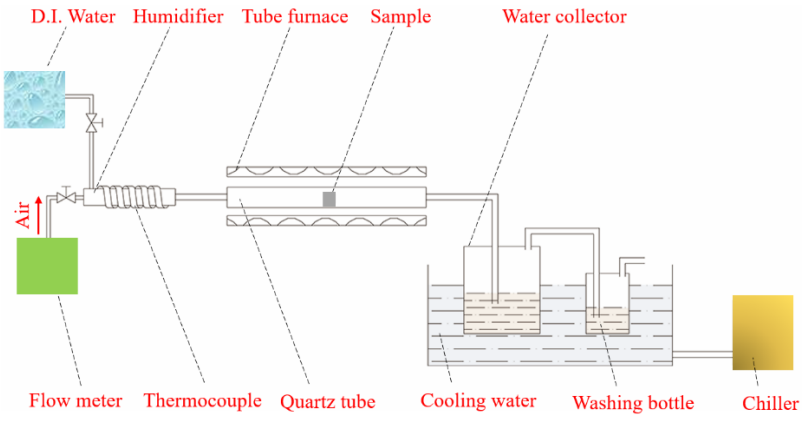

Figure 11 Schematic diagram of the experimental setup for the oxidation test.

3.3 Long-term oxidation kinetics

The long-term cyclic oxidation behavior of the alloys was evaluated at 800, 900, and 1000 °C in the air with 10% H_2O for times up to 10,000 hours using 20 mm × 10 mm × 1 mm samples prepared to a 600-grit surface finish. These exposures were conducted in horizontal alumina tubes, with samples held in alumina boats. Distilled water was added to a flowing air stream at ~500 to 850 cc/min by atomization above its condensation temperature, yielding gas velocities in the ~0.5 to 2 cm/s range. At 800 °C, the samples were taken out from the furnace after cooling to room temperature every 100 h, whereas the 900 and 1000 °C runs were conducted in 500 h cycles. Mass changes were measured with a scale accurate to ± 0.04 mg (~0.01 mg/cm^2). Further details of the test procedures are available in references [102] and [103].

3.4 Post-Exposure Sample Characterization

The Cr evaporation test samples and the AFAs after cell test were characterized by X-ray diffraction (XRD, PANalytical X'Pert Pro X-ray Diffractometer at 45 kV and 40 mA using Cu Kα radiation), and scanning electron microscopy (SEM, Hitachi S-4700). Selected samples were further analyzed by x-ray photoelectron spectroscopy (XPS) and cross-section scanning transmission electron microscopy (STEM). The XPS analysis (Thermo Scientific Model K-Alpha) used a monochromated, micro-focusing, Al Kα X-ray source (1486.6 eV) with a ~400 μm X-ray spot size for maximum signal and to obtain an average surface composition over the largest possible area. Depth profiling analyses were conducted with a EX06 argon ion gun rastered over a 2 mm x 4 mm area with a sputter rate of ~0.2nm/s. Focused ion beam (FIB) milling, performed with a Hitachi NB5000 FIB/SEM instrument, was used to lift-out oxide-alloy regions for STEM analysis. The STEM analysis was primarily conducted using a FEI Talos F200X, equipped with a symmetric A-TWIN objective lens and a SuperX energy dispersive spectrometer system. Moreover, the surface and cross-sectional morphology of anode-supported cells were also characterized by SEM.

3.5 Cell test

In this study anode-supported cells (ASC) were used to study the degradation processes by Cr poisoning. The cells consist of a 300 μm thickness NiO/8YSZ anode substrate and an 10-20 μm thickness 8YSZ electrolyte. Subsequently, a double-layered GDC (10 μm thickness barrier layer)/60-70 μm thickness LSCF cathode was

applied by screen-printing and sintering. The active area of the working cathode was 0.45 cm^2. The cells were tested in a single-cell test bench and characterized by current-voltage (C-V) and EIS measurements.

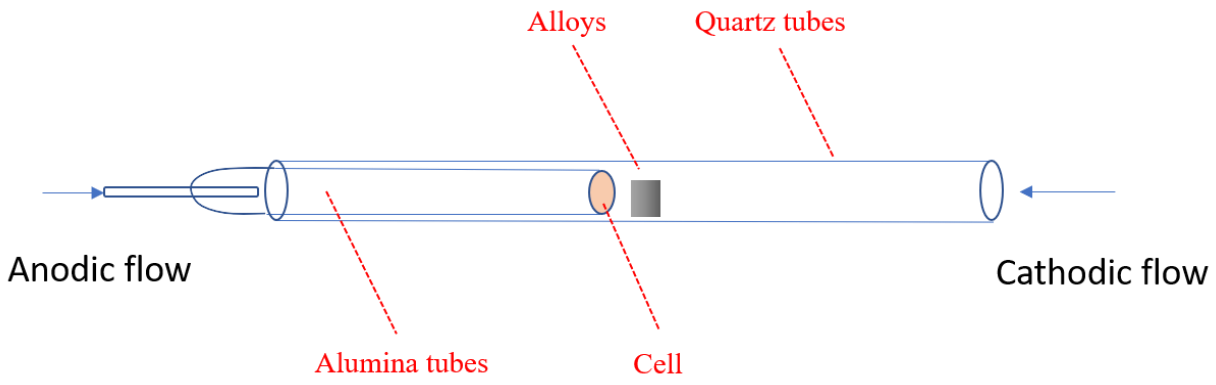

Figure 12 Schematic of the Cr poisoning test of ASC cells with different alloys

Figure 12 displays the single cell test setup. Silver paste and Pt mesh was applied to the anode and cathode as current collector, respectively. Silver wire was used as lead wire in the anode atmosphere; however, gold wire was used as lead wire in the cathode atmosphere to prevent the reaction between silver wire and gaseous Cr species. At the cathode, four different alloys were place 10 mm away from the cathode. Different alloys were applied in this study to investigate the degradation of ASC performance by Cr poisoning via gaseous Cr species. The chemical composition of these AFA alloys and commercial alloys is shown in **Table 2**.

The cells were operated under ambient pressure with air at the cathode side and H_2O/H_2 mixtures at the anode side. The total anodic and cathodic gas flow rates were maintained at a constant value of 200 ml min^{-1} during all experiments. The cells were tested at an operating temperature of 800 °C. The cell performance was evaluated by a galvanostatic test. Impedance was collected over the frequency range from 100 kHz to 0.1 Hz with an AC perturbation of 10 mV at open-circuit voltage condition (OCV). The galvanostatic test is carried out with a constant current density of 0.5 A/cm^2 for 500 h. The galvanostatic test is interrupted to do the EIS measurements at several specific dates. The EIS is typically analyzed by CNLS fitting using an equivalent circuit model [27]. However, it is sometimes difficult to determine an exact model with optimal initial parameters. Thus, the DRT analysis is applied to analyze the electrochemical data which suggests a number of resistance-capacitance (RC) elements and appropriate values of resistance (R) and time constant (t) for the polarization resistance. Details for the DRT analysis can be found in our previous research [104].

Chapter 4 Short-term Chromium Evaporation and Oxidation behavior of AFAs

From an alloy selection perspective for SOFC BOP components, the alumina-forming FeCrAl Aluchrom type alloys exhibit very promising oxidation resistance and Cr evaporation reduction, but they do not have the creep strength needed for 800-1000°C SOFC BOP applications. Alumina-forming Ni-based alloys such as alloy 214 exhibit promising oxidation resistance, reduced Cr evaporation rates and excellent high-temperature creep resistance; however, they are quite costly, typically ~5 times (and higher) the cost of heat-resistant stainless steels. Alumina-forming austenitic (AFA) stainless steels are a new family of high-temperature alloys developed by Oak Ridge National Laboratory (ORNL), which attempt to bridge the performance gap between stainless steels and chromia- or alumina- forming Ni-base alloys [20, 62, 91, 97, 99-101]. The AFA alloys offer good creep resistance, comparable to the best stainless-steel alloys, form protective alumina scales, and are Fe-based for lower cost [20, 62]. All AFA alloys also contain Cr to aid the establishment of protective alumina via the third element effect [20, 21, 62, 91, 105, 106]. Therefore, they do not terminate the Cr evaporation but can reduce it. At present, only two studies [107, 108] that we are aware of have examined the Cr evaporation behavior of AFA stainless steels with regards to SOFC BOP applications, both of which studied the same Fe-25Ni-14Cr-2.5Nb based AFA alloy grade.

In this chapter, we have explored the Cr evaporation rates of three different AFA alloys representing a range of key alloying additions and oxidation behaviors at 800 to 900 °C in air with 10% H_2O, relative to benchmark chromia-forming 310 stainless steel and Ni-based alloy 625. In this chapter, we used a cycle of 500 h exposure and correlation of how alloy composition influenced the chemistry, structure, and Cr evaporation from the oxide scale were studied. To provide additional insights for SOFC BOP alloy selection, long-term oxidation kinetics of select alloys were also studied from 800 to 1000 **°C** for up to 10,000 h in air with 10% H_2O. The results help provide the basis for developing and optimizing AFA alloys for SOFC BOP components.

4.1 Cr evaporation rates

The Cr evaporation rates resulting from 500 h exposures at 800 °C to 900 °C in air with 10% H_2O are summarized in **Figure 13**. The Cr evaporation rates from the AFA alloys OC4, OC5, and OC11 were generally over an order of magnitude lower than the chromia-forming alloys 310S and 625, which exhibited roughly comparable Cr evaporation rates. For example, at 800 and 850 °C, the Cr evaporation rate of OC4 was 35 times and 30 times lower than 310S, respectively, although only 10 times lower at 900 °C. In contrast, the Cr evaporation rate of OC11 was 11 to 13 times lower than 310S from 800 to 900 °C. The Cr evaporation rates increased with increasing temperatures for all alloys, with only 2 times range increases for 310S and OC11 between 800 and 900 °C. An acceleration in Cr evaporation rates was observed between 800 and 850°C for OC5, and between 850 and 900°C for OC4, likely related to reaching their upper temperature use limit to form a protective alumina scale. Overall, OC4 exhibited the lowest Cr evaporation rates at 800 and 850°C, and OC11 at 900 °C.

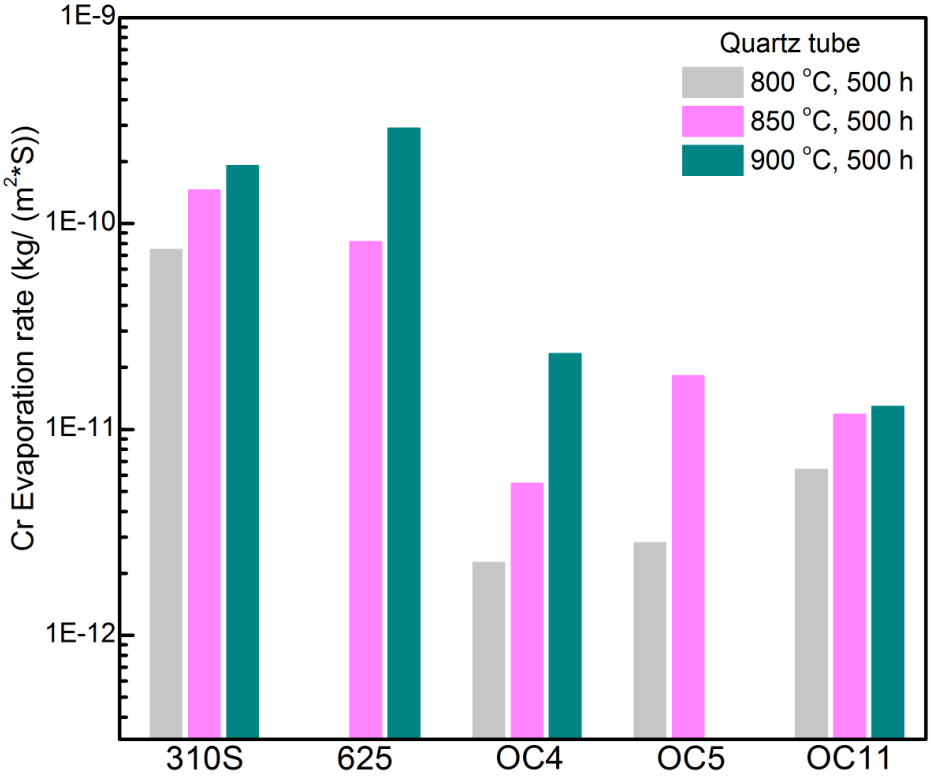

Figure 13. Cr evaporation rates of various alloys tested in quartz tubes at 800 °C to 900 °C for 500 h in air with 10% H_2O.

4.2 Microstructure and composition of oxide scales

The phases, surface morphology, and compositions of the oxide scales formed on the alloys after the Cr evaporation measurement exposures of 500 h at 850 °C in air with 10% H_2O (and select alloys at 900 °C) were characterized by XRD, SEM, XPS, and cross-section STEM (Figures 14-22).

4.2.1 Phase determination

Figure 14 shows the XRD patterns of various alloys after the Cr evaporation measurement at 850 °C and 900 °C for 500 h in air with 10% H_2O. For 310S and 625 alloys at 850 °C (**Figure 14a**), the major phases of the oxide scale were Cr_2O_3 and Cr-Mn-rich spinel. In addition, several possible trace metastable γ-Al_2O_3 peaks were also detected in the 625. The α-Al_2O_3 phase was detected in all the AFA alloys (**Figures 14b and d**). Cr-Mn-rich spinel phase and Cr_2O_3 were also detected, particularly for OC4.

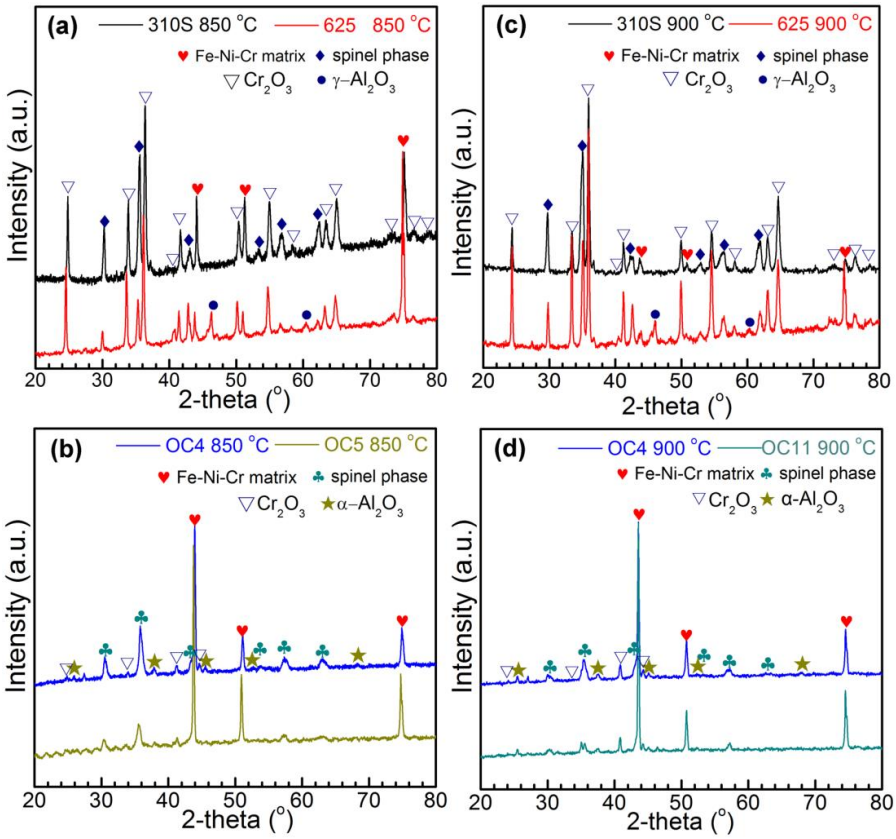

Figure 14. XRD patterns of alloys after Cr evaporation tests for 500 h at 850 and 900 °C in air with 10% H_2O. 310S and 625 alloys at (a) 850 °C and (c) 900 °C, (b) OC4 and OC5 at 850 °C, (d) OC4 and OC11 at 900 °C.

4.2.2 Surface morphology after oxidation

Figure 15 shows SEM images for the surface morphology of the alloys after 500 h exposure at 850 °C in air with 10% H_2O. For 310S, the surface of oxide scale was not uniform and consisted of locations with coarser, faceted oxide grains (**Figure 15a**) and 'cauliflower'-shaped oxide clusters (**Figure 15b**). Analysis by EDS indicated that the cluster areas were rich in Si, Cr, and Mn while the faceted oxide grain areas were Cr and Mn rich, consistent with spinel. In contrast, the oxidized surface formed on the 625 was more uniform. The AFA alloys all showed relatively uniform, fine-grained surface oxide structure, with occasional underlying regions of a smoother oxide evident underneath the fine-grained particles (**Figure 15d-f**). The OC4 surface was rich in Al, Cr, and Mn, consistent with the XRD data, although Si was also unexpectedly detected. Moreover, for OC5 and OC11, EDS analysis showed predominant peaks of Al, Cr, Mn and Si. In addition, appreciable oxide spallation was not observed for any of the alloys after the 500 h exposures, and regions indicative of spallation were not generally observed on the SEM surface imaging.

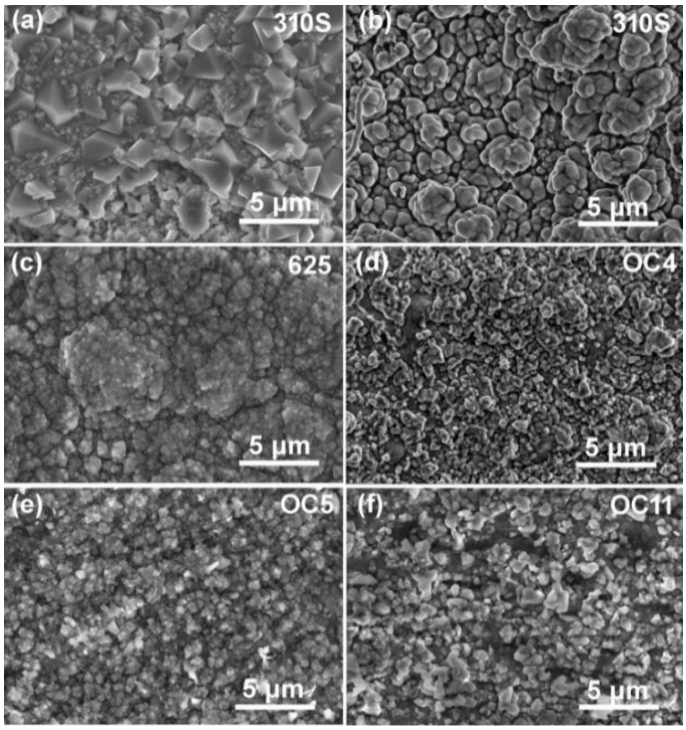

Figure 15. Surface SEM images of (a, b) 310S, (c) 625, (d) OC4, (e) OC5, and (f) OC11 alloys after oxidation at 850 °C in 10% H_2O for 500 h.

4.2.3 Composition analysis of oxide scales

To further investigate the oxide chemistry, sputter depth profiling by XPS was pursued. An overview plot of all elemental sputter depth concentration profiles for the alloys after the Cr evaporation measurement exposures at 850 and 900 °C in air with 10% H_2O are shown in **Figure 16**, with key individual element profiles shown in **Figure 17**. The XPS data was obtained over a roughly 400 mm diameter region of the surface. For the chromia-forming 625, the surface oxide formed at 850 °C was rich in Cr and Mn, with decreasing levels of Mn and increasing levels of Cr with depth, consistent with a Cr-Mn spinel overlying a chromia-based scale (**Figures 16b and 17a and b**). In contrast, although Cr and Mn were present in the oxide on the chromia-forming 310S, the surface was unexpectedly dominated by Si (**Figures 16a and 17 a, b, and d**). This level of Si at the surface, approaching 35 at.%, is not typical of the oxide scales formed on 310S, where some SiO_2 formation at the alloy-scale interface, but not the outer surface, could be expected [102, 109]. There was also no evidence of extensive oxide spallation in the 310S, which otherwise may have exposed SiO_2 formed at the alloy-oxide interface to the surface (appreciable SiO_2 was also not detected in the XRD data for 310S, **Figure 14**). Rather, it is hypothesized to result from deposition of volatile Si-rich species from the quartz tube (to be discussed later). At the surface of the oxidized alloy 625, 3 at.% Si was present but rapidly decreased to well less than 1 at.% Si with increasing sputter depth. It is interesting to note that this surface Si does not appear to slow the evaporation of Cr from the 310S, as the evaporation rate was comparable to that of the 625, which showed little Si at the surface (**Figure 13**).

All the AFA alloys (both at 850 °C and 900 °C) yielded Al-based oxide surfaces (**Figure 16c-g**), consistent with their significantly lower Cr evaporation rates (**Figure 13**). At 850°C, OC4 had considerably lower levels of Al in the surface oxide than OC5 and OC11 due to higher levels of an Al-Mn-Fe-Cr rich outer layer at 850 °C (**Figures 17f, g, and h**) At 850 °C, there was 3 at.% Cr at the surface of the OC4, compared to 2 at.% for OC11, and well less than 1 at.% for OC5. For the OC4 and OC11, the Cr levels increased with increasing sputter depth in the oxide, whereas the OC5 remained below 1 at.% Cr (**Figure 17f**). At 900 °C, the OC4 and OC11 showed more exclusive Al-rich oxide formation, with lesser amounts of Cr, Mn, and Fe at the scale surface.

Unexpected Si at the surface of the oxides was again observed for the AFA alloys (**Figure 17i**), reaching levels of 4 to 7 at.%. Given that the AFA alloys contained only 0.15 wt.% range Si (**Table 2**), and Si incorporation in this manner at the outer surface is not typical of AFA alloy oxidation, it is again hypothesized that the Si resulted from deposition of volatile Si-rich species from the quartz tube.

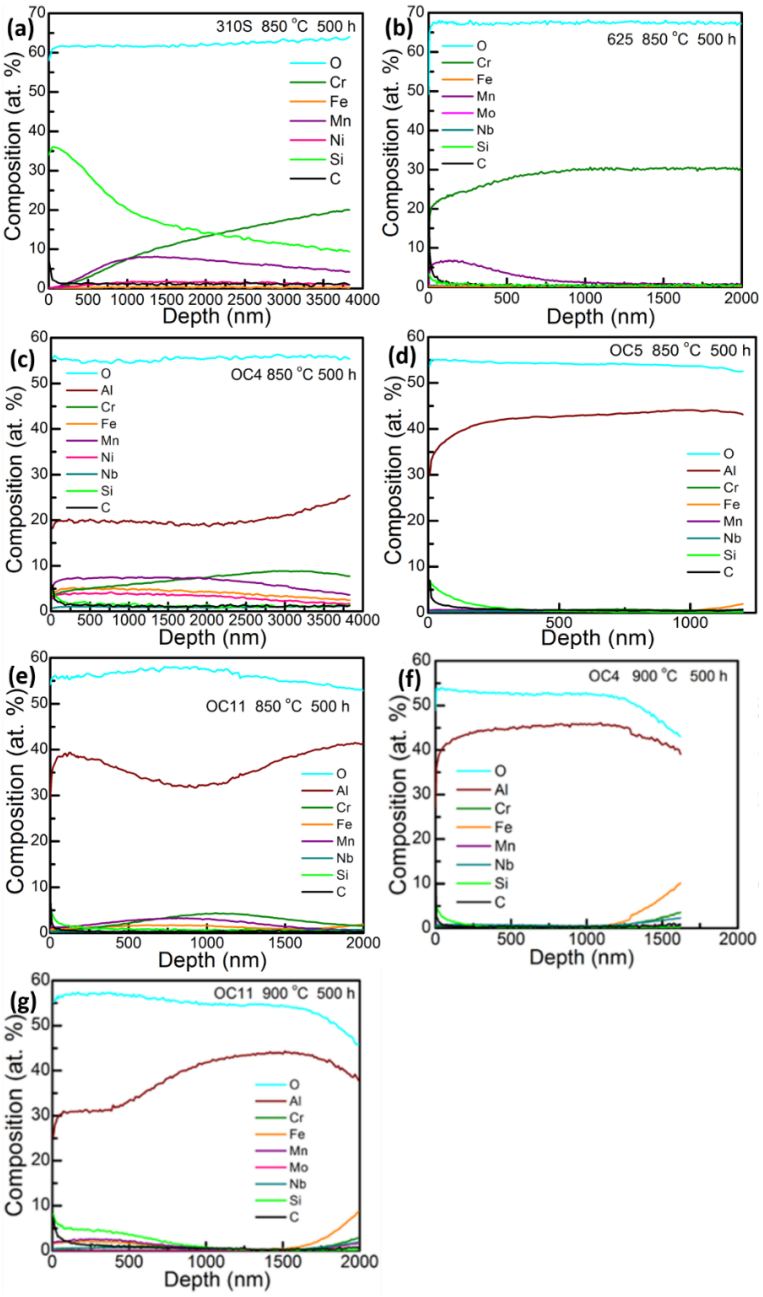

Figure 16. Sputter depth concentration profiles (at.%) of the alloys after 500 h exposure at 850 °C (a-e) and 900 °C (f, g) in air with 10% H_2O. The sputtering depth was estimated based on a 100 nm thick SiO_2 standard, with a sputter rate of approximately 0.2 nm/s. However, the actual sputtering rates for the oxidized surfaces could vary from this value by up to 2 to 3 times.

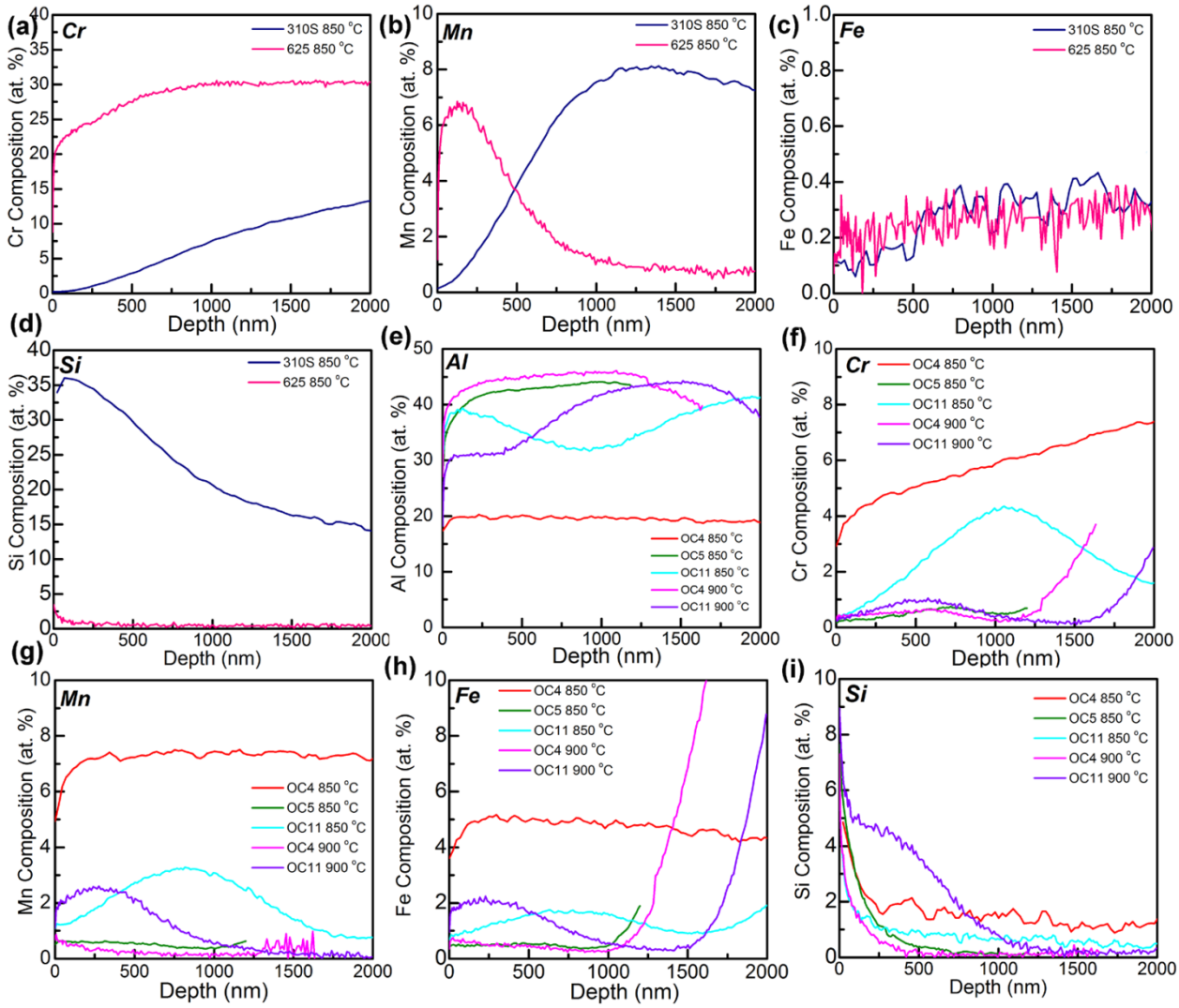

Figure 17. Elemental concentration-depth profiles of (a-d) chromia-forming alloys after oxidation at 850 °C, and (e-i) AFA alloys after oxidation at 850 °C and 900 °C. The sputtering depth was estimated based on a 100 nm thick SiO_2 standard, with a sputter rate of approximately 0.2 nm/s. However, the actual sputtering rates for the oxidized surfaces could vary from this value by up to 2 to 3 times.

4.2.4 Cross-sectional analysis by STEM/EDX mapping

Figure 18 compares the cross-section morphology and chemistry of oxide scales formed on 310S, 625, and OC4 after oxidation at 850 °C for 500 h in air with 10% H_2O as determined by STEM imaging and EDS mapping. Consistent with the XRD and XPS data (**Figures 14, 16, and 17**), 310S formed a complex oxide scale structure rich in Cr, Mn, and Si (**Figure 18a**). At the scale-alloy interface regions, local semi-continuous areas of Si-rich oxide consistent with SiO_2 were observed. Such local formation of SiO_2 at the scale-alloy

interface is frequently reported for oxidation of Fe-based Cr_2O_3-forming alloys such as 310S due to the greater thermodynamic stability of SiO_2 versus Cr_2O_3 [109]. For the 310S with 0.57 wt.% Si (**Table 2**), the Si present throughout the external Cr_2O_3 and spinel oxide structure is again unexpected and hypothesized to result from interactions with the quartz tube in the water vapor environment. The oxide scale formed on 625 (**Figure 18b**) consisted primarily of a Cr-rich oxide region consistent with Cr_2O_3, with a thin surface transient oxide layer rich in Cr, Mn, and Fe consistent with spinel, as expected based on the XRD and XPS data (**Figures 14, 16, and 17**). Minor, local enrichment of Al at the scale-alloy interface and in the alloy beneath the scale was also observed, ascribed to the γ-Al_2O_3 detected in XRD (**Figure 14**) and likely associated with a minor degree of internal oxidation. The AFA alloy OC4 (**Figure 18c**) formed a multi-layered oxide scale, with an outer Al-Cr-Mn-Fe-Ni-rich oxide layer, an intermediate layer rich in Cr, consistent with Cr_2O_3 and an inner Al-rich region consistent with Al_2O_3. This structure is in agreement with past studies of AFA alloy oxidation [100], although the degree of transient oxidation was fairly extensive in this sample, as was observed in the XPS data (**Figures 16 and 17**).

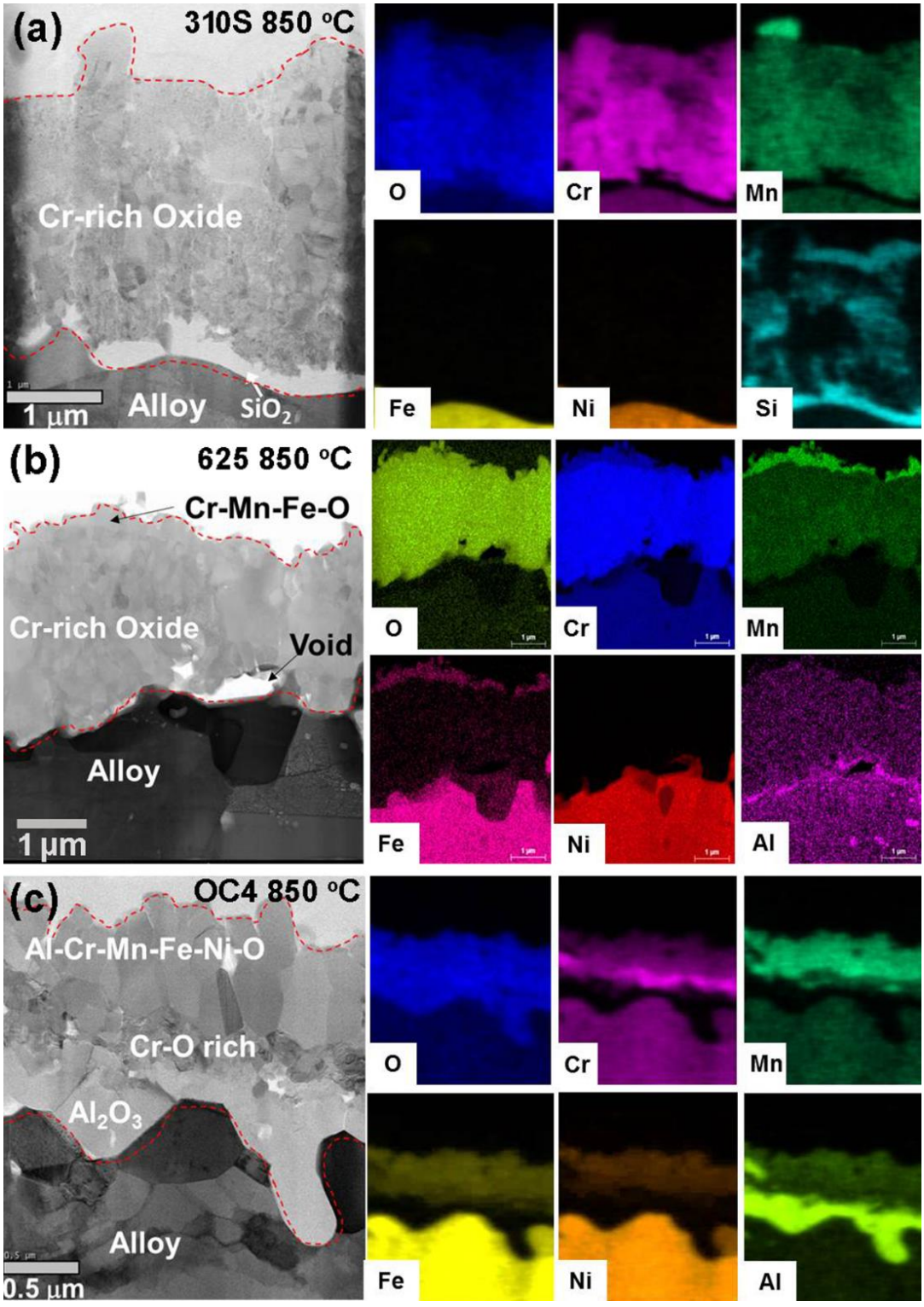

Figure 18. Cross-section STEM images of (a) 310S, (b) 625, and (c) OC4 after oxidation at 850 °C in 10% H_2O for 500 h with the corresponding EDX elemental mapping.

Cross-section STEM image and EDS mapping images of OC5 and OC11 after oxidation at 850 °C in air with 10% H_2O are shown in **Figure 19** and **20**, respectively. The OC5 and OC11 formed a similar scale structure to

the OC4, with a complex outer transient oxide and an inner Al_2O_3 layer. At the location imaged for the OC5, a Cr-rich oxide region at the interface between the outer transient and inner Al_2O_3 layers was also evident. Although not seen in the cross-section image, the XPS data also indicated an intermediate Cr rich layer in the oxide formed on OC11 (**Figure 17**). A local region with surface Si was also evident in the STEM cross-section images of OC5 at 850 °C.

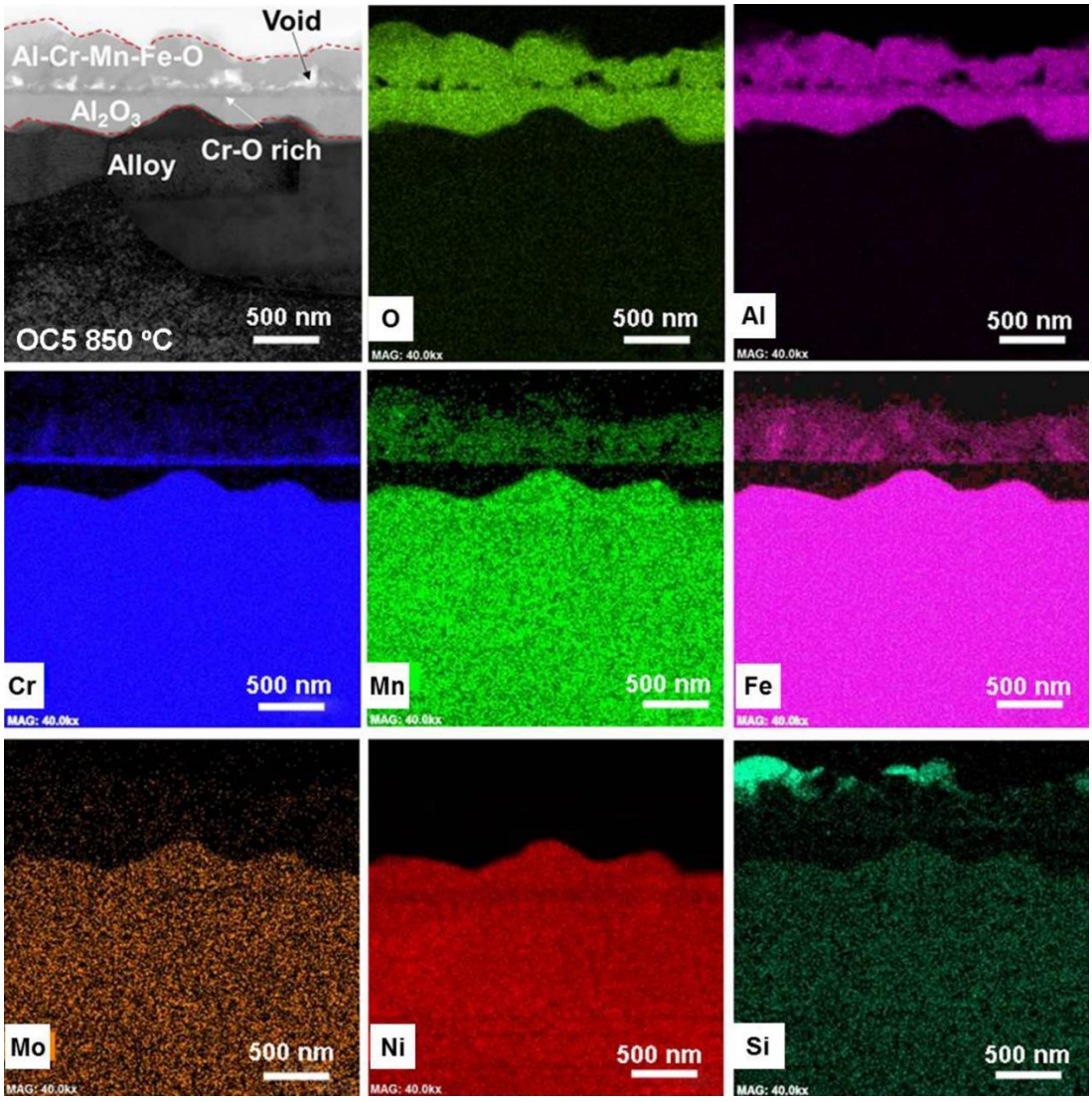

Figure 19. STEM cross-sectional images of OC5 after oxidation at 850 °C for 500 h with corresponding EDX mapping.

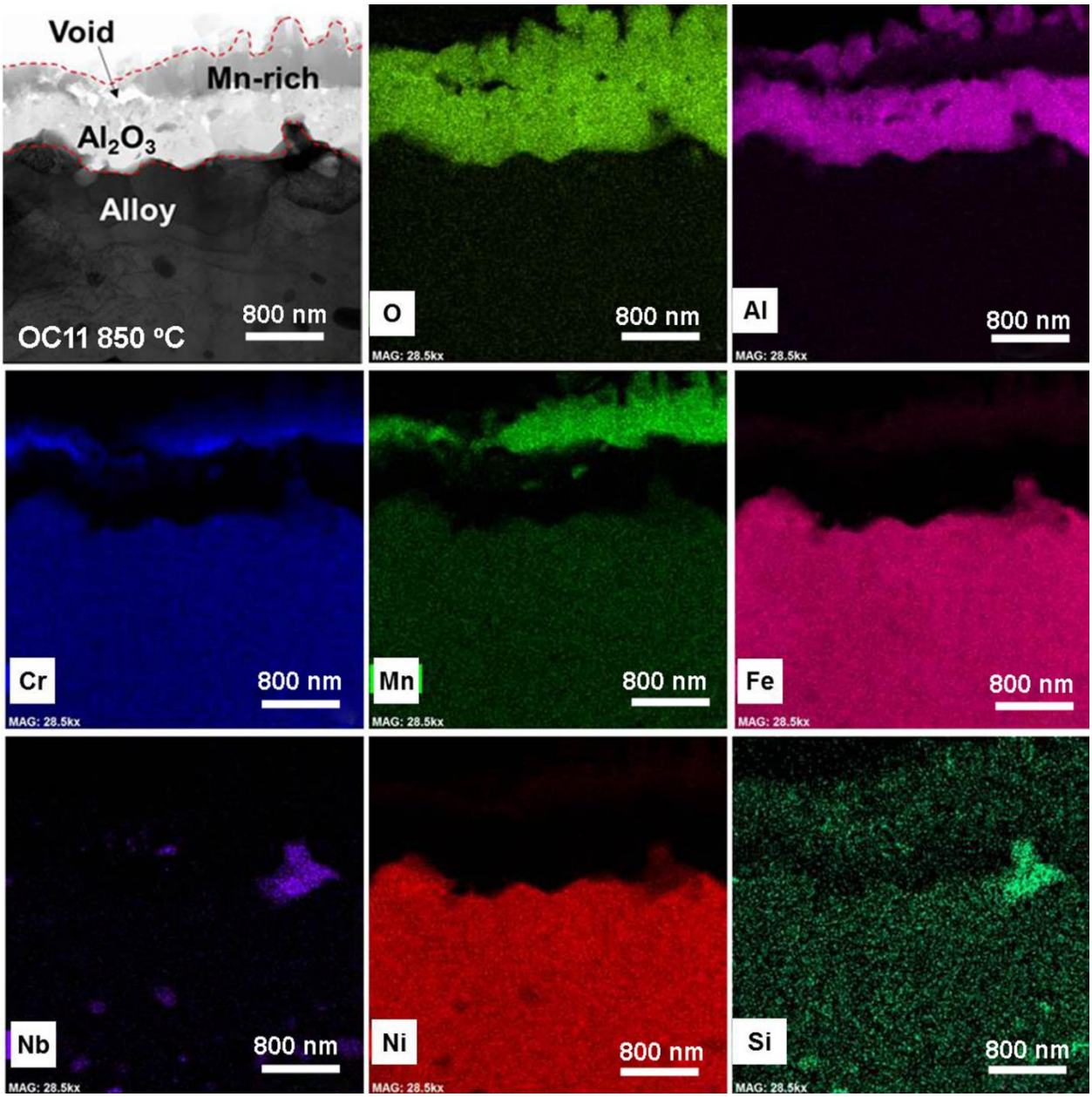

Figure 20. STEM cross-sectional images of OC11 after oxidation at 850 °C for 500 h with corresponding EDX mapping.

4.3 Long-term cyclic oxidation measurements

Long-term cyclic oxidation data of the alloys at 800, 900, and 1000 °C in air with 10% H_2O are shown in **Figures 21a-c**. Data at 800 °C is shown for comparative reasons, with some of this data previously published and/or from different alloys batches (similar alloy chemistries for OC4 and OC5) to that studied in the present work. At 800 °C, 310HCNB (a higher C, Nb added variation compared to 310S) exhibited relatively rapid mass gain followed by a transition to mass loss after ~1000 hours oxidation, indicative of typically observed accelerated oxidation of Cr_2O_3 forming alloys in high-temperature water vapor containing environments [110]. In contrast, the AFA alloys OC4, OC5, and OC11 show low mass gains consistent with protective alumina scale formation, with data obtained out to 8000 to 10,000 h for the OC4 and OC5. The mass gains were slightly higher for OC4 than OC5 and OC11, consistent with more transient oxidation by OC4 as seen in the XPS and STEM EDS data (**Figures 16-20**).

When the oxidation temperature increasing to 900 °C (**Figure 21b**) in air with 10% H_2O, extensive spallation can be observed for the Cr_2O_3-forming 310S and 625 alloys after ~4000 to 7000 h of exposure, indicating they may not exhibit sufficient oxidation resistance to meet the desired 40,000 h + lifetime for SOFC BOP applications at these temperatures, in addition to issues related to Cr species volatilization and poisoning. A transition to mass loss and scale spallation was also observed for OC4 and OC5 after 1000 to 4000 h of exposure, indicating 900 °C is a too high operation temperature for these AFA alloys in air with 10% H_2O. This loss of protective alumina forming capability in AFA alloys with increasing temperature has been previously observed and is related to the composition compromises needed to balance alloy cost and mechanical properties with oxidation resistance [20, 62, 91, 97, 99-101]. In contrast, the OC11 alloy which used higher levels of Al and Cr, as well as Hf and Y, exhibited low positive mass gains consistent with protective alumina scale formation out to 10,000 h at 900 °C in air with 10% H_2O. Even at 1000 °C (**Figure 21c**), the OC11 alloy maintained excellent oxidation resistance without significant mass loss during the 10,000 h of exposure, showing great potential for the 40,000+ h lifetime desired for SOFC BOP in the 900 °C temperature range of interest.

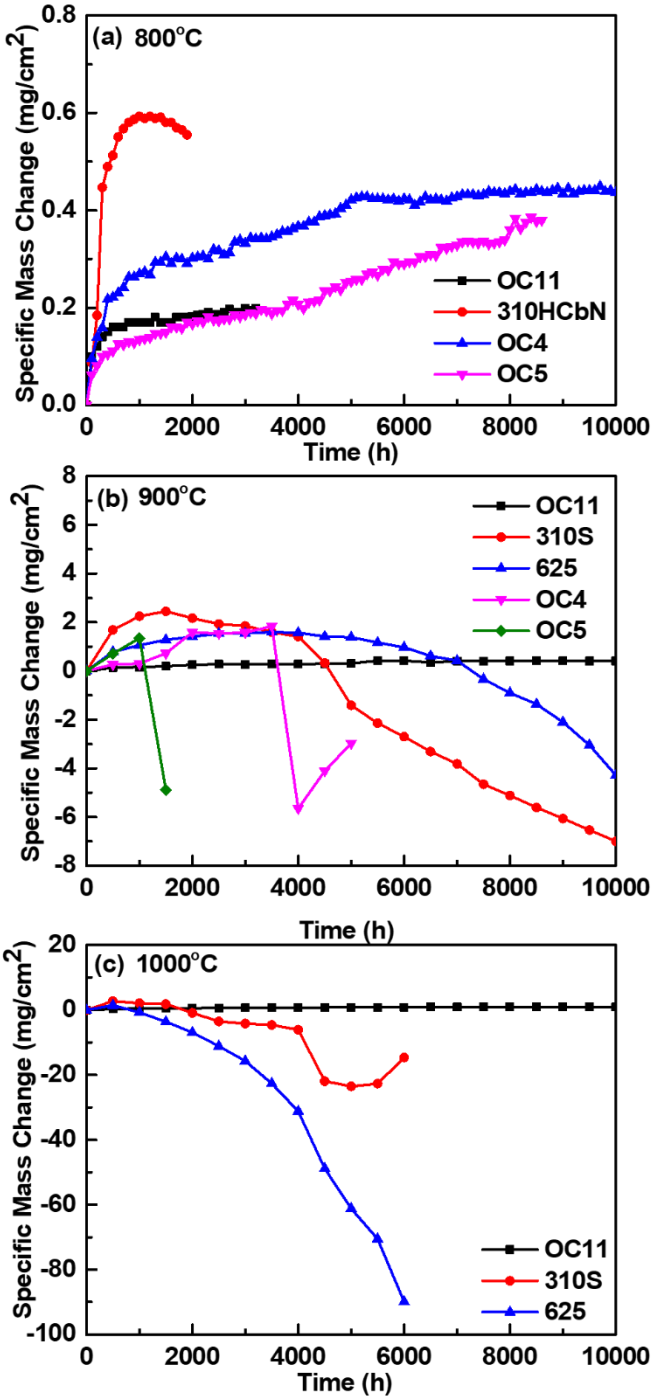

Figure 21. Specific mass changes at (a) 800 °C, (b) 900 °C and (c) 1000 °C in air with 10% H_2O. In the 800 °C data, the 310HCNB data and OC5 data is from reference [62], and the OC4 and OC5 samples are from different, although similar chemistry, alloy batches than shown in Table 2.

4.4 Implications of Findings

Based on the results above, it is demonstrated that the AFA alloys exhibit much more stable oxidation behavior and ~5 to 35 times lower Cr evaporation rates than 310S and 625 alloys by forming an inner dense and protective α-Al_2O_3 layer. Comparison with literature data is shown in **Table 3**. The Cr evaporation rates of oxidizing samples (including Cr_2O_3, Al_2O_3 formers and mixed formers) with tube materials, flow rates, and levels of H_2O are summarized.

Most Cr evaporation rates of Cr_2O_3 formers are reported to be in the magnitudes of 10^{-10} to 10^{-9} kg/(m^2·s) at 850-900 °C in 3 to 12% H_2O (**Table 3**); although the Cr evaporation rates of Sanergy HT and Crofer 22H alloys were reported to be in the magnitudes of 10^{-7} kg/(m^2·s) based on conversions from [111]. This higher Cr evaporation rate is likely due to the very high flow rate of 6 L/min used in those studies. The Cr evaporation rate for 310S in the present work was 1.45 ×10^{-10} kg/(m^2·s) at 850 °C in air with 10% H_2O, which is ½ to 1 order of magnitude lower than that reported in [22, 23]. As shown in **Figure 17**, significant Si contamination was observed on the 310S sample in the present work, which could account for the lower Cr evaporation values. However, the Cr evaporation rates for alloy 625 in the present work were comparable/moderately lower than that for 310S despite very little Si contamination evident, which suggests that the Si contamination did not significantly contribute to the lower Cr evaporation rates measured. Rather, the differences between the present work and Cr evaporation rates reported for Cr_2O_3 formers in [21-23] are more likely the result of minor to moderate differences in alloy and test conditions, exposure, and measurement protocols, including impacts on transient oxidation processes prior to a protective inner Cr_2O_3 or Al_2O_3 scale being established. This supposition is consistent with the Cr evaporation rates of alumina-forming OC4, OC5, and OC11 in the present work falling about ½ to 1 order of magnitude lower than OC4 in [107] and AFA25 in [108] from 800-900 °C. Therefore, although the absolute levels of Cr evaporation measurement levels differed between the present work and the literature reported data (**Table 3**), the relative differences between Cr_2O_3 and Al_2O_3 formers were roughly comparable. The Cr evaporation rates of the AFA alloys in

the present work were also of the same magnitude as that reported for Aluchrom YHf in [39]. These Cr evaporation values were also, one-magnitude higher than four pre-oxidized alumina-forming alloys in [112]. This observation highlights the importance of the transient oxidation period and could be attributed the establishment of continuous alumina layer prior to the Cr evaporation tests from the pre-oxidation, with the greatest Cr release occurring during the initial transient stage of oxidation as the protective Al_2O_3 layer is established.

According to the XPS and STEM EDS mapping composition analysis of the oxide scale in the present work, unexpected Si contamination was detected in the sample surfaces. With the exception of the 310S sample, the levels of surface Si were relatively low, 4 - 7 at.% Si range. The differences between 310S with nearly 35 at.% Si detected at the surface, 625 and AFA alloys are speculated to be related to differences in the transient oxide chemistry and/or extent of oxidation, and the manner they interact with the furnace test tube. A mechanistic understanding of this phenomena is the subject of future study. The source of the Si-contamination likely resulted from the quartz tubes, however, Si species volatilization in the air with 10% H_2O mixture studied are likely low enough to not show a significant impact on the Cr evaporation during the short 500 h exposures. It is not clear if the Si contamination was unique to the present work with regards to the experimental apparatus or test conditions, or if it may have occurred to some extent in previous studies by others utilizing quartz tubes. The present results do show the importance of extensive oxide scale characterization after Cr evaporation tests to assess possible interactions with apparatus materials.

An attempt was made to repeat the experiments using an alumina tube to measure the Cr evaporation rates of 625 and OC11 at 900 °C. As shown in **Table 4**, the results obtained in the quartz tube are repeatable. However, the Cr evaporation rates tested in alumina tubes are unexpectedly lower than those tested in quartz tubes (it should be similar or higher if there was no Si contamination layer to possibly impede the Cr vapor diffusion outwards). A possible reason for the reduced Cr release output is that the Cr species either interact more with alumina than quartz or can be deposited or adsorbed on the relatively porous alumina tubes compared to the quartz tubes. In addition, the lower Cr evaporation rates could also be partly attributed to the lower flow rates used in alumina tubes than the quartz tubes in the present work (due to tube geometry

considerations) based on flow rate studies of Gindorf [12, 113]. Denser and more thermally stable tube materials or inner surface coatings in high temperature water vapor environments such as zirconia-based, for example, should be explored for future long-term measurements to minimize the interaction between oxidizing sample surfaces, Cr vapor release, and tube materials. In this way, the more efficient collection solution and highly efficient cooling system will be needed to ensure the accuracy of Cr-evaporation rates.

Table 3 Comparison of the Cr evaporation rates for different alloys.

	Alloy	Cr-rate ($kg/(m^2 \cdot s)$)	Tube materials	Flow rates (L/min)	H_2O (%)	T (°C)	References
Cr_2O_3-formers	**310S**	7.45×10^{-11}	quartz	0.2	10%	800	This study
		1.45×10^{-10}		0.6		850	
		1.91×10^{-10}				900	
		5.65×10^{-10}		0.3	3%	850	[39]
		1.03×10^{-9}				950	
		1.11×10^{-9}			12%	850	
		4.55×10^{-9}				950	
	441	6.67×10^{-10}			3%	850	[107]
	MCO coated 441	5.33×10^{-12}					
	625	0.82×10^{-10}	quartz	0.6	10%	850	
		2.89×10^{-10}				900	
		0.49×10^{-10}	alumina	0.2		900	
	Sanergy HT	8.33×10^{-7}	quartz	6	3%	850	[111]
	Crofer 22H	6.66×10^{-7}					
	Preoxidized Ducrolloy	1.2×10^{-9}	quartz	1.5	1.86%	900	[112]
	Chromia	3.2×10^{-9}	quartz	0.3	3%	850	[39]
mixed chromia-alumina former	**Preoxidized Nicrofer 6025 HT**	7.5×10^{-10}	quartz	1.5	1.86%	900	[112]
	602CA	$\sim5\times10^{-10}$	quartz	0.3	3%	850	[108]
	Nicrofer 6025 HT	8.4×10^{-11}	quartz	0.3	3%	850	[39]

		4.4×10^{-10}				950	
Al_2O_3-formers	**OC4**	1.23×10^{-11}	quartz	0.3	3%	800	[107]
		2.58×10^{-11}				850	
		7.12×10^{-11}				900	
	OC4	2.25×10^{-12}	quartz	0.2	10%	800	This study
		5.45×10^{-12}		0.6		850	
		2.33×10^{-11}				900	
	OC5	2.80×10^{-12}	quartz	0.2	10%	800	
		1.82×10^{-11}		0.6		850	
	OC11	6.37×10^{-12}	quartz	0.2	10%	800	
		1.18×10^{-11}		0.6		850	
		1.29×10^{-11}				900	
		0.4×10^{-11}	alumina	0.2		900	
	H214	$\sim1.8\times10^{-10}$	quartz	0.3	3%	850	[108]
	Preoxidized Aluchrom YHf	0.95×10^{-12}	quartz	1.5	1.86%	900	[112]
	Preoxidized PM 2000	0.8×10^{-12}				900	
	Preoxidized Kanthal AF	1.05×10^{-12}				900	
	Preoxidized Aluchrom YB	1.3×10^{-12}				900	
	Aluchrom YHf	$\sim7.5\times10^{-12}$	quartz	0.3	3%	850	[39]
		$\sim9.0\times10^{-12}$			3%	950	
		$\sim1.1\times10^{-11}$			12%	850	
		$\sim1.15\times10^{-11}$			12%	950	
	AFA25	$\sim8\times10^{-11}$	quartz	0.3	3%	850	[108]

FeCrAl-coated Ducrolloy	4.58×10^{-12}	quartz	1.8	2%	950	[113]

Table 4. Comparison of Cr-evaporation rates at 900 ºC for 500 h in quartz (600 mL/min) and alumina (200 mL/min) tubes.

Cr-evaporation rate ($kg/(m^2*S)$)	**900 ºC quartz**	**900 ºC quartz-Repeat**	**900 ºC alumina**
625	2.89×10^{-10}	2.69×10^{-10}	4.93×10^{-11}
OC11	0.91×10^{-11}	1.29×10^{-11}	4.0×10^{-12}

From an alloy design perspective, the oxidation resistance and mechanical properties vary depending on the alloying additions, typically in opposite directions [89, 114]. For all the AFA alloys in the present work, the dense and continuous α-Al_2O_3 inner layer and outer Al-rich transient oxide layer can be formed, although often with Cr-rich regions at the interface between them and/or in the transient surface oxide. Due to this protective Al_2O_3, oxidation rates and Cr evaporation rates of AFA alloys were superior to that of Cr_2O_3 forming benchmark alloys 310S and 625. There were no indications in the data for significant differences in Cr evaporation rates between the AFA alloys (**Figure 13**); however, there were significant differences in their long-term oxidation resistance with regards to their upper temperature limits for protective alumina formation (**Figure 21**). This suggests that AFA alloy optimization for SOFC BOP in the 800-900 °C range should focus on compositions capable of alumina formation to higher temperature, rather than attempting direct alloy design efforts to reduce Cr evaporation rates by manipulation of AFA oxide scale chemistry.

In this study, the compositions of OC5 and OC4 varied primarily in Nb content (1 wt.% and 2.5 wt.%, and Al content (3 vs 3.5 wt.%), respectively. They showed similar oxidation behavior and Cr evaporation rates at 800 °C in air with 10% H_2O, albeit with slightly higher oxidation rates by OC4 due to enhanced transient oxidation, which may have slightly reduced Cr evaporation rate (**Figures 13 and 21**). These differences are not considered to be significant. Either alloy is a good candidate for SOFC BOP use up to 800 °C range but cannot be used much beyond this temperature in air with 10% H_2O. To push past 800 °C and into the 900 °C range of operation, OC11 type AFA alloys are needed.

The addition of Cr aids the establishment of protective alumina and the additives of rare earth elements (Y and Hf) can enhance the oxidation performance at high temperatures [84, 112, 115]. Based on this knowledge, OC11 was manufactured by further increasing the Cr (15 wt. %), Al (4 wt. %) contents, along with the additive of Y and Hf. This resulted in an alloy capable of long-term use approaching 1000 °C, which is of strong interest for SOFC BOP components. As a result, the Cr-evaporation rate of OC11 just slightly increased when temperature increasing from 800 °C to at 900 °C compared with OC4, which experienced a great relative increase due to the beginning of the loss of protective alumina forming ability at 900 °C (**Figures 13 and 21**).

Future direction will investigate OC11 alloy types with variations to lower cost and improve manufacturability, e.g., Zr for Hf, drop Y, decreased Nb levels, etc. Work will also focus on measurement of Cr evaporation rates for longer term exposures. Previous work by Stanislowski et al [112] also suggested that higher rates of Cr evaporation occurred during the initial establishment of the Al_2O_3 scales and were reduced during long-term steady state oxidation for alumina-forming alloys.

4.5 Summary

In this chapter, Cr evaporation rates of AFA alloys are compared to benchmark Cr_2O_3 forming alloys at 800-900 °C in air with 10% H_2O and the protective mechanism of AFA alloys have been discussed. The main conclusions of this study are listed as follows:

(1) Cr evaporation rates of AFA alloys were ~5 to 35 times lower than Cr_2O_3 forming 310S and 625 benchmarks under 800-900 °C operation.

(2) The studied AFA alloys with different composition ranges exhibited similar Cr evaporation rates, but significantly different upper temperature oxidation limits for protective alumina scale formation. This finding indicates that design of AFA alloys for SOFC BOP components should be focused on long-term oxidation resistance at the targeted operation temperatures rather than attempting to modify the AFA alloys to achieve oxide scale structures to further reduce Cr release.

(3) Surface Si contamination on all samples was observed after 500 h operation at 800-900 °C in air with 10% H_2O with the use of a quartz furnace tube. Although it did not appear to significantly impact Cr release behavior for 500 h exposure, potential interactions need to be considered and assessed after long-term exposure. The use of an alumina furnace tube unexpectedly resulted in low Cr evaporation rates at 900 °C in air with 10% H_2O compared with quartz tubes. One reason was speculated to be the result of chemical interactions of volatile Cr species with the alumina, or a more porous inner surface of the alumina furnace tube vs a quartz furnace tube, and another reason was attributed to the lower flow rates.

Chapter 5 Alumina-Forming Austenitic Stainless Steel for High Stable and Chromium-Evaporation Minimized Balance of Plant Components in Solid Oxide Fuel Cells

A solid oxide fuel cell (SOFC) is high-efficient energy conversion device that produces electricity directly from versatile fuels [1, 16, 116, 117]. Metallic interconnects (MICs) and balance-of-plant (BoP) components are used to assemble multiple single cells to meet the requirements of a stack [13, 118, 119]. Generally, a protective scale based on an inner continuous chromia layer, often with outer Fe-Cr-Mn or Ni-Cr based spinel and/or related transient oxidation phases(s), are formed on the surface of Fe-based and/or more costly Ni-based Cr_2O_3-forming alloys as BoP components at high temperatures (temperature range of interest in 700-1000C depending on SOFC stack design) [39, 120-123]. However, as the operation of SOFC stack continues, the formed Cr-rich scales will react with water vapor produced in the SOFC operating environment to generate gaseous Cr species , primarily oxyhydroxides, which can contaminate the SOFC stack as well as lead to the more rapid deterioration of the protective oxide scales [31, 110, 112, 123-127]. Chen et al. [128] investigated the oxidation behavior of Fe-20Cr-25Ni-Nb-based Cr_2O_3-forming alloys with a small amount of water vapor under 1000 °C, cracking and spallation of the protective chromia layer were observed after only 4 h of operation. Moreover, the oxide spallation was also observed for an Fe-16Cr alloy after 500 h test at 850 °C in a simulated SOFC cathode atmosphere, which could severely degrade the electrical performance when it served as a metallic interconnect in SOFC stack [129]. Alloying with Mn to favor formation of $MnCr_2O_4$ on the surface of Cr_2O_3-forming alloys to reduce Cr evaporation has also been pursued, although the Mn also increases oxidation rate and tendency for spallation [120]. Therefore, researchers had devoted to devising coatings [40, 127, 130, 131] to protect the alloys from Cr evaporation during long-term operations, although the extra cost from the coatings can be prohibitive.

While coatings have been demonstrated to reduce the oxidation rates and Cr evaporation rates of chromia-forming alloys [65, 84, 132, 133] complex shaped components , such as the tubing, heat exchanger and valves in the BoP components in SOFCs are quite challenging to be appropriately coated. Therefore, it is of interest to develop a new alloy to replace Fe-based chromia-forming alloy in SOFC BOP operation with water vapor at high temperatures. It is known that the parabolic oxidation rate of alumina is up to one to two orders of magnitude lower than chromia's, and is far more stable in water vapor encountered in SOFC operation conditions as well as a range of energy conversion, combustion, and process system environments [105, 134-136]. In regards, researchers had been working in the past decades to create Fe-based alumina-forming alloys for high-temperature conditions [102, 137, 138]. Among many candidates, a new AFA stainless steel with low cost, high oxidation resistance and high-creep strength stood out [20, 91, 97, 139-141]. It is shown that a continuous protective alumina layer was formed on these AFA alloys in air and water vapor environments, thus suppressing the more rapid oxidation of Fe, Ni, Cr, and Mn alloy components. Investigations are still in progress to optimize the compositions of the AFA alloys for the application of long-term, high-temperature operation, with multiple grades needed to balance the upper temperature limit of the AFA alloys ability to form aluimina with mechanical properties and cost [91, 97, 140].

To date, multiple studies have been focused on the short-term oxidation behavior and Cr evaporation rates of Fe- and Ni- based chromia- and alumina- forming alloys, including AFA alloys [39, 107, 123, 142-144]. It is generally recognized that the formation of alumina scale could greatly reduce the oxidation rate, Cr evaporation rate and remain intact in the short-term operation. However, there are no studies concerning the long-term operation of AFA alloys in water vapor under high-temperature environments relevant to SOFC BoP components that also monitor Cr evaporation aspects. Such data is needed as SOFCs are intended for many tens of thousands of hours operation, including continuous isothermal operation as well as periodic shutdowns (heating/cooling cycles can exacerbate oxide scale adherence and spallation). Thus, this paper is devoted to investigating the long-term oxidation and Cr evaporation behavior of two candidate AFA alloys in an atmosphere with 10% water vapor at 800 °C in comparison with 310S. The oxidation and Cr evaporation behaviors are characterized by transpiration methods, weight change measurements and oxide scales

examination. Moreover, the protection mechanism of AFA alloys has been comprehensively discussed in this chapter.

5.1 Cr evaporation rates

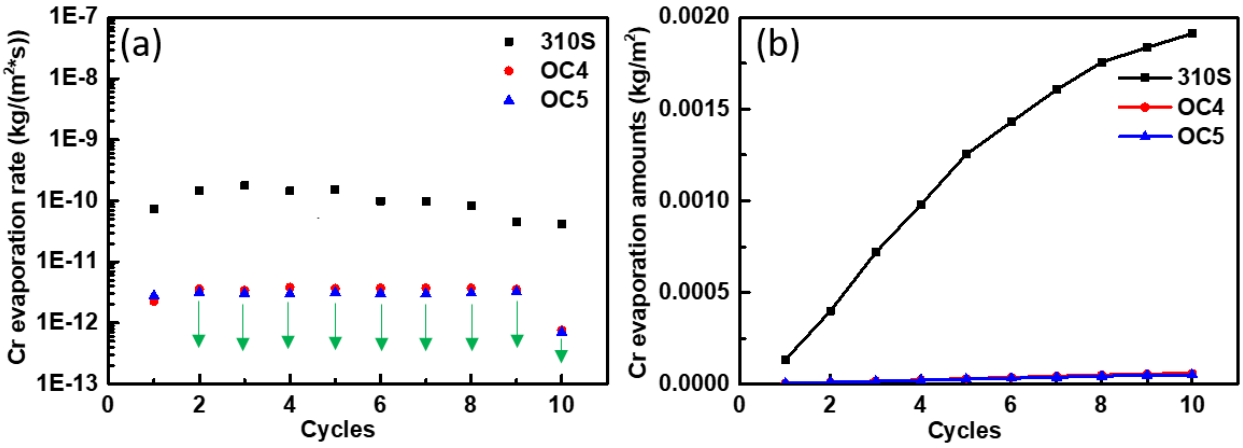

Figure 22 (a) Chromium evaporation rates and (b) accumulated evaporated Cr amounts of each cycle for 310S and AFA alloys in 10% H_2O at 800 °C. (Green arrows denote the Cr concentration at this cycle is below the detection limit)

It is worth noting that the Cr concentration of collected solutions from OC4 and OC5 are just barely detectable at the first cycle and Cr concentrations after the first cycle are below the detection limit of ICP-MS transpiration test conditions used (**Figure 22a**). A sudden decrease of the calculated Cr evaporation rate from 9th to 10th cycle is attributed to the change of detection limit from 0.009mg/L to 0.002mg/L resulting from re-calibration of the ICP-MS unit near the end of the 10 cycles (5000 h) of exposure studied. The Cr evaporation rates for the AFA alloys were assumed to be the detection limit for cycles 2-10 for a conservative, worst-case estimate to compare with Cr evaporation rate of the 310S. These maximum Cr evaporation amounts values are taken to intuitively demonstrate the Cr evaporation rates difference between 310S and AFA alloys, with the Cr evaporation rates resulting from 5000 h exposures (10 cycles) at 800 °C in air with 10% H_2O are summarized in **Figure 22a**. The Cr evaporation rates of the AFA alloys are generally over an order of magnitude lower than the chromia-forming alloys310S at 800 °C in air with 10 vol% H_2O , which exhibits roughly comparable Cr evaporation rates of OC4 and OC5. For example, at 800 °C, the Cr evaporation rate of OC4 and OC5 is at least 20~35 times lower than 310S. The large Cr evaporation rates difference between 310S and the two AFA alloys is attributed to the formation of a protective alumina scale on the AFA alloys. To clearly demonstrate the difference between AFA alloys and 310S, the accumulated Cr amounts of all alloys per cycle were plotted in **Figure 22b**, again conservatively using the detection limit as the level of Cr

released for the AFA alloys in cycles 2-10. A 35 times higher amount of evaporated Cr of 310S than AFA alloys could be observed after 5000 h operation at 800 °C. The detailed Cr evaporation rates after each cycle are listed in **Table 5**.

Table 5 500 hours (10 cycle) Cr release measurements in air + 10% H_2O to date (Unit: kg/(m^2·s)).

Cycle		1st	2nd	3rd	4th	5th	6th	7th	8th	9th	10th
Detection limit		9E10^{-6}Kg/L	9E10^{-6}Kg/L	9E10^{-6}Kg/L	9E10^{-6}Kg/L	9E10^{-6}Kg/L	9E10^{-6}Kg/L	9E10^{-6}Kg/L	9E10^{-6}Kg/L	9E10^{-6}Kg/L	2E10^{-6}Kg/L
800 °C	310S	7.45 ×10^{-11}	1.48 ×10^{-10}	1.77 ×10^{-10}	1.45 ×10^{-10}	1.52 ×10^{-10}	9.85 ×10^{-11}	9.79 ×10^{-11}	8.28 ×10^{-11}	4.5 ×10^{-11}	4.18 ×10^{-11}
	OC4	2.25 ×10^{-12}	<3.61 ×10^{-12}	<3.44 ×10^{-12}	<3.83 ×10^{-12}	<3.67 ×10^{-12}	<3.73 ×10^{-12}	<3.73 ×10^{-12}	<3.73 ×10^{-12}	<3.56 ×10^{-12}	<7.66 ×10^{-13}
	OC5	2.8 ×10^{-12}	<3.17 ×10^{-12}	<3.04 ×10^{-12}	<2.98 ×10^{-12}	<3.15 ×10^{-12}	<3.05 ×10^{-12}	<3.00 ×10^{-12}	<3.09 ×10^{-12}	<3.23 ×10^{-12}	<7.02 ×10^{-13}

5.2 Oxidation kinetics

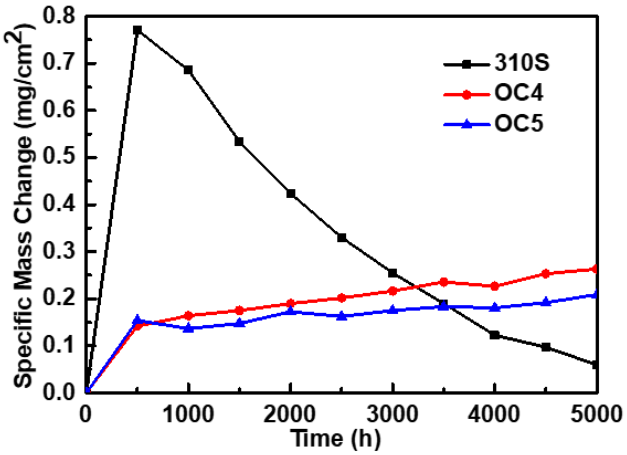

Figure 23 Weight change as a function of time for 310S and AFAs in air with 10% water vapor at 800°C.

Specific mass changes of 310S and AFA alloys as a function of exposure time in air with 10% water vapor at 800 °C are shown in **Figure 23**. For 310S, the specific mass reaches a maximum after one cycle (500h) and then slowly decreases with time, whereas for the AFA alloys, they exhibit greater oxidation resistance than 310S, with slow, positive mass gains consistent with alumina scale formation. The mass loss for 310S is likely a combination of Cr evaporation and a modest degree of oxides spallation. Trace amounts of spallation oxides were observed after 5000 h test. The trend of AFA specific mass change is small increases, though there is a very slight fluctuation (gain and loss), which suggests a very minor amount of spallation may have occurred, given the low levels of Cr evaporation observed (**Figure 22**) during the oxidation process, even though no evident oxides spallation had been observed. Moreover, results show that the weight gain of AFA alloys reaches 0.15 mg/cm^2 at 800 °C after the first cycle which can be attributed to formation of a transient oxide and the establishment of the continuous alumina layer. The weight gain of the OC4 and OC5 in the subsequent 9 cycles test is less than 0.10 mg/cm^2 which substantiates the stability of the oxide scales during the long-term operation. Under this condition, the oxidation resistance of OC4 and OC5 was effectively the same based on the specific mass change data.

5.3 Oxide scales characterization

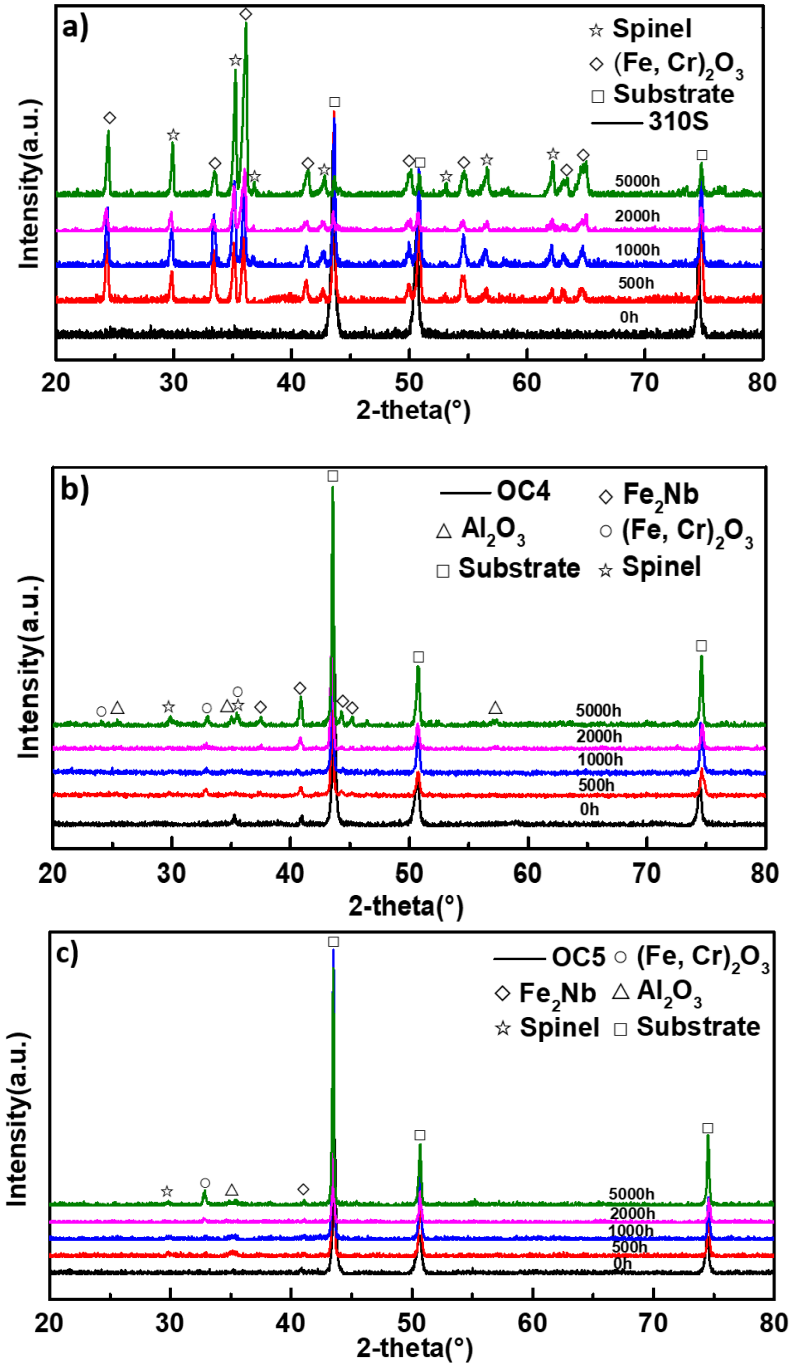

Figure 24. XRD patterns of the a) 310S, (b) OC4, and c) OC5 samples after oxidation in 10% water vapor for different durations (0, 500, 1000, 2000, 5000h).

Figure 24 shows XRD patterns of 310S and AFA alloys after oxidation in 10% water vapor for different durations. The results reveal that spinel and Cr_2O_3 are two major phases formed during oxidation for 310S.

One can notice in Figure 4a that the main difference of XRD patterns of 310S for different durations is the peak height ratio of spinel to chromia getting larger which indicate 310S shifts to form more spinel. Nevertheless, the main peaks for AFA alloys during the whole oxidation process are the substrate austenite (major peaks) and Fe_2Nb Laves phases (minor peaks)which suggests that the oxide scales formed on the AFA alloys are relatively thin [20] In addition, some minor peaks related to primary coarse NbC observed on the matrix without test were observed, which could be attributed to the leftover from initial casting and solutionizing. Substrate austenite peak can be observed as the main peak couple with some small peaks of chromia, alumina and spinel. For OC4 and OC5 tested at 800°C, the peak intensity of spinel for the OC4 is higher than OC5 which is in accordance with the weight gain curve. It is clearly seen that AFA alloys exhibit significantly greater oxidation resistance than the chromia-forming 310S in 10% water vapor environments. **Figure 25a** shows the surface morphology of 310S after testing for different periods in 10% water vapor at 800 °C. After oxidized for one cycle, plate-like oxides and some diamond-like oxides covered the entire surface (**Figure 25-a1**). According to the corresponding XRD pattern, these two phases can be identified as Cr_2O_3 and $(Cr, Mn)_3O_4$, respectively. It can be seen that there is some brighter phase deposited on the plate-like oxides which was examined to be Si-rich, presumably SiO_2 by EDS (**Figure S1b**) which can be attributed to the volatilization deposits from quartz furnace tubes (discussed in detail in reference [144]). Spinel grains with different sizes can be observed at higher magnification (**Figure 25-a5**) which was also observed by Ge *et al.* and Behnamian *et al.* [39, 145] who studied the high-temperature oxidation behavior of 310S in water-containing atmosphere at 500 °C and 950 °C, respectively. After two cycles (1000h) exposure, the size of Cr_2O_3 plates (3 ~ 10 μm diameter with 0.3 μm thickness) and $(Cr, Mn)_3O_4$ diamonds (0.3 to 1 μm) almost remains the same. In addition, deposition of SiO_2 on the Cr_2O_3 plates can also be observed (**Figure 25-a2**). However, there are some wave patterns obviously seen on the Cr_2O_3 plates which could be assigned to the reaction between Cr_2O_3 and water vapor (**Figure 25-a6**). The size of the oxides stayed almost the same after four cycles (2000h) of oxidation test (**Figure 25-a3**). However, the blunt edges of these oxides indicated the further reaction of Cr_2O_3 with water (**Figure 25-a7**). Even though the deposited SiO_2 was not observed on the Cr_2O_3 at this surface location, the EDS still showed there were SiO_2 deposits across the surface. After the

entire oxidation process, some Cr_2O_3 particles even broken which verified the severe reaction between Cr_2O_3 and water (**Figure 25-a8**). Moreover, the size of $(Cr, Mn)_3O_4$ particles significantly increased after the entire oxidation process and the SiO_2 deposits were identified by EDS.

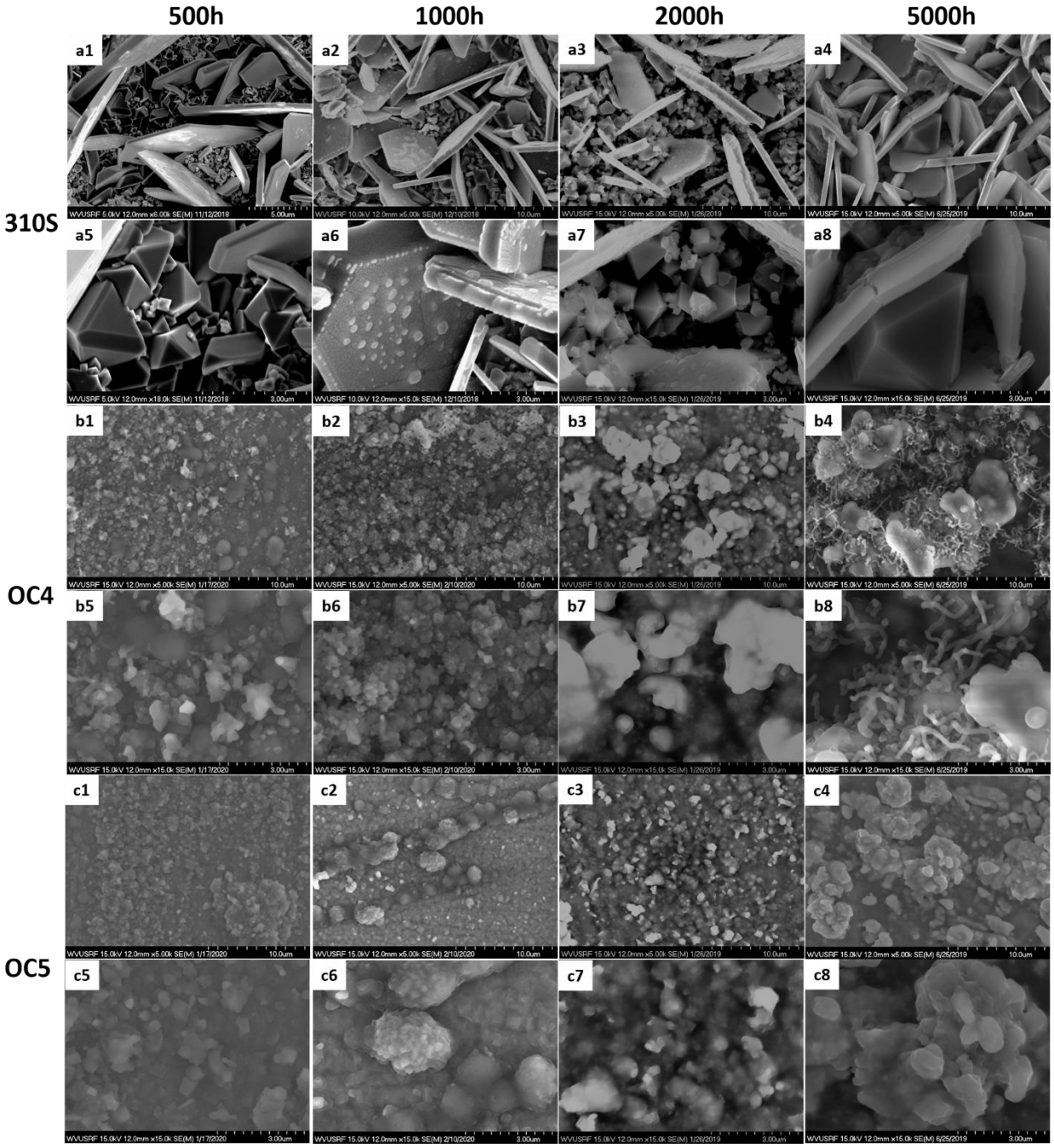

Figure 25 SEM surface morphologies of (a) 310S, (b) OC4 and (c) OC5 after test in 10% water vapor at 800 °C for: (a1, a5, b1, b5, c1 and c5) 500 h, (a2, a6, b2, b6, c2 and c6) 1000 h, (a3, a7, b3, b7, c3 and c7) 2000 h, (a4, a8, b4, b8, c4 and c8) 5000 h.

Surface morphologies of OC4 after testing for different durations in 10% water vapor at 800 °C are shown in

Figure 25b. For the OC4 sample, numerous nodular oxide grains are formed and cover the entire surface after one cycle of oxidation (**Figure 25-b1**). With the increase of exposure time, the size of these particles increases from 0.3-3 μm (500 h and 1000h oxidation) to 1-5μm (2000 h oxidation) which can be assigned to Fe-Cr-Mn-Al-Nb rich transient oxides. After 5000h oxidation, some whiskers can be easily observed on the surface which is also SiO_2 deposition from quartz tube (**Figure 25-b4**) as evidenced in **Figure S1d**. Moreover, Fe-Cr-Mn-Al-Nb-rich oxides continue to grow with the exposure process (**Figure 25-b8**).

Figure 25c demonstrates SEM surface morphologies of OC5 sample after testing for different durations in 10% water vapor at 800 °C. The morphology is similar to that of OC4. In addition, there are no whiskers after the whole oxidation process for OC5. However, there are some SiO_2 deposits on the alloy surface indicated by EDS (**Figure S1f**). Plenty of nodular oxide grains are formed after 500 h oxidation (**Figure 25-c1**). With the increase of exposure duration, the size of these particles increases during the whole oxidation process. In addition, there is more and more conglomerate of these oxides with the exposure which also can be attributed to the Fe-Cr-Mn-Al-Nb-rich transient oxides (**Figure 25-c8**).

5.4 Oxide scale growth

The cross-sectional SEM and light microscopy images of 310S and AFA alloys after tested for 5000 h are shown in **Figure S2**. The scale thickness of 310S varies extensively over the sample (**Figure S2-a1**), on the order of 5 to 40 microns thick, and SiO_2 are indicated by the red arrows in **Figure S2-a2**. However, the thickness of AFA alloys is much more uniform, on the order of one micron range (**Figure S2-b1 and c1**), except for occasional 5 μm size range nodules location where the primary NbC was oxidized and then undercut by Al_2O_3, indicated by red arrows in **Figure S2-b2 and c2**. The cross-sectional morphology and EDS line scanning profiles of a thinner scale location for 310S and a typical location for the AFA alloys at 800 °C after testing for 500, 1000, 2000, and 5000 h are shown in **Figures 26-28**. After 500 h test, the oxide scale on 310S displays a (Cr, Mn)-rich oxide layer, which coincides with the results of XRD and SEM analysis (**Figures 24 and 25**). In addition, SiO_2 oxides formed at/near the oxide/alloy interface are evident (dark particles marked by red arrows in **Figure 26a**). This scale structure is maintained in the longer exposure times, although with increasing levels of Mn in the outer scale regions in the overall Cr-rich scales.

For the first 500 h, the thickness of the oxide scales formed on OC4 and OC5 is in a range of 0.5-1 μm, respectively (**Figure 27a and 28a**). The scales formed on these AFA alloys were Al-rich, with minor amounts of Cr, Fe, and Mn. Qualitatively, the EDS data suggested that the Cr, Fe, Mn are present more so in the outer scale regions than the inner scale, although the scales are too thin for a conclusive observation in the SEM/EDS data (further analysis of scale chemistry is presented in section 5.5 STEM/EDS data). The thickness of the oxide scale formed on AFA alloys only slowly increases from 500 to 5000 h (**Figures 27 and 28 c, e, g**) which is consistent with the specific mass change data (**Figure 23**) and the protectiveness of alumina-based scales in this environment. The formation of Al-rich oxides at the oxide/alloy interface distinguishes the oxidation performance of AFA alloys from the Cr- rich oxide scale formed on 310S, thus decreasing the Cr evaporation rates.

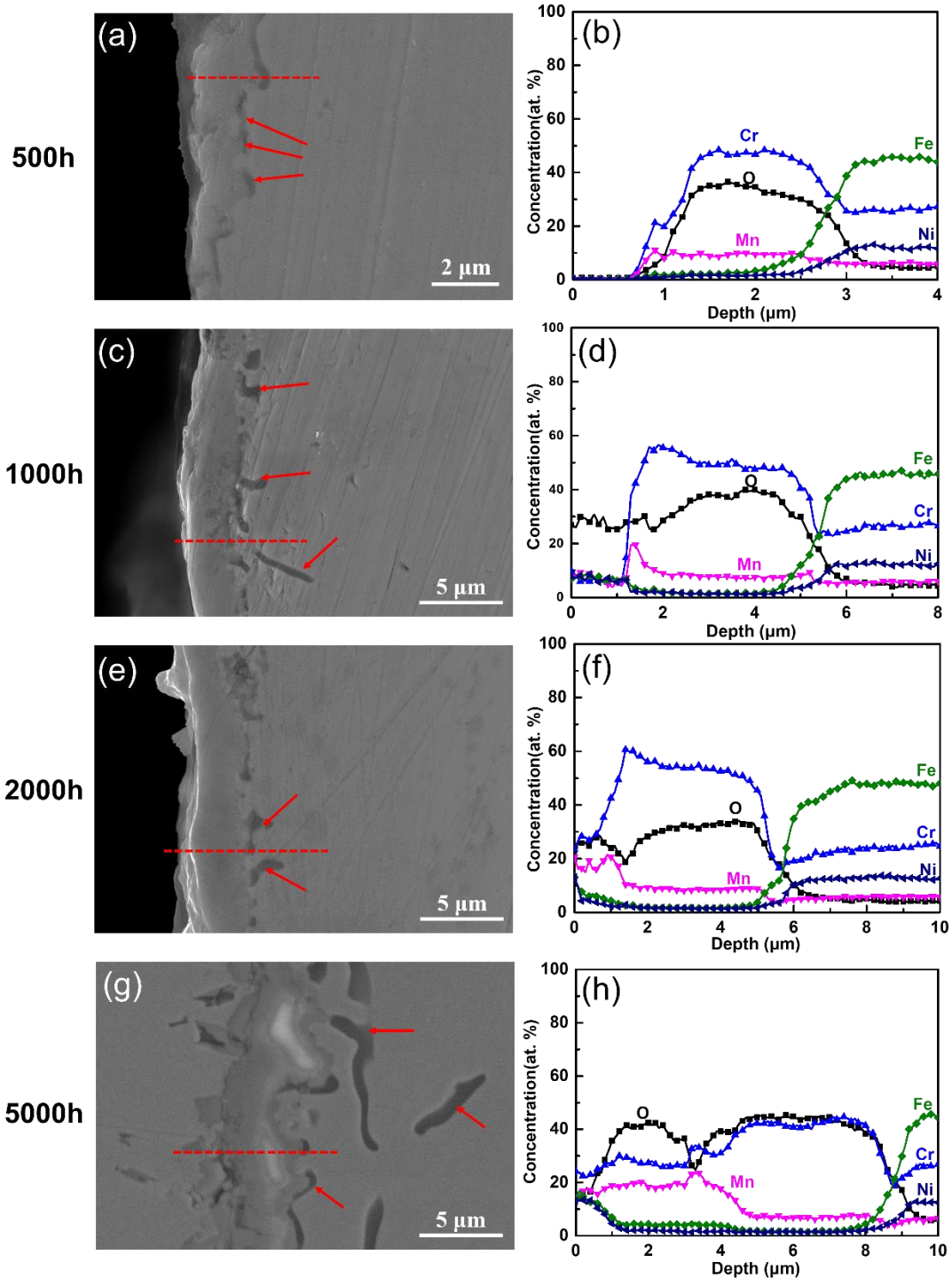

Figure 26 Cross-section profiles of oxide scales formed on 310S after tested in 10% water vapor at 800 °C for: (a, b) 500 h, (c, d) 1000 h, (e, f) 2000 h, and (g, h) 5000 h.

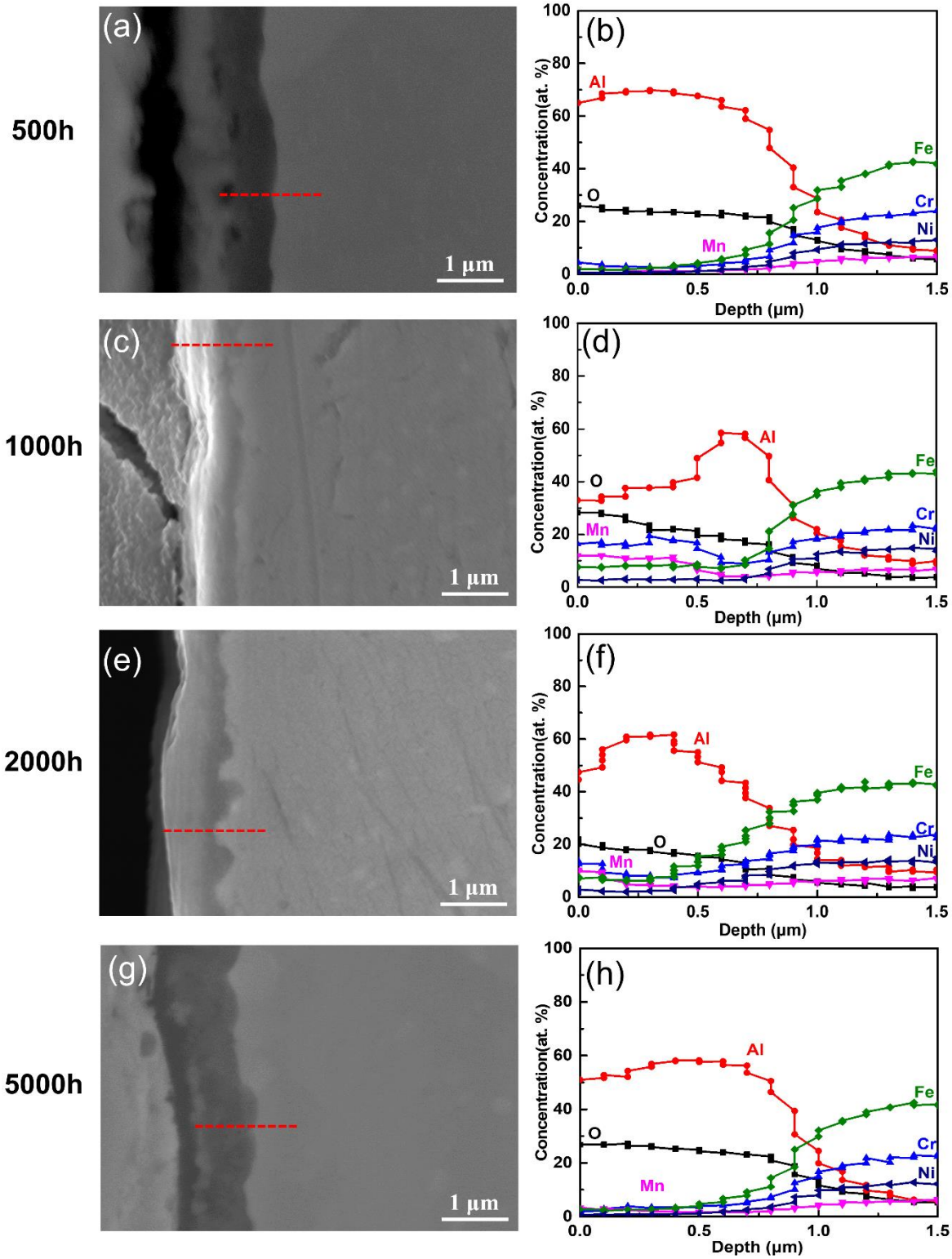

Figure 27 Cross-section profiles of oxide scales formed on OC4 after tested in 10% water vapor at 800 °C for: (a, b) 500 h, (c, d) 1000 h, (e, f) 2000 h, and (g, h) 5000 h.

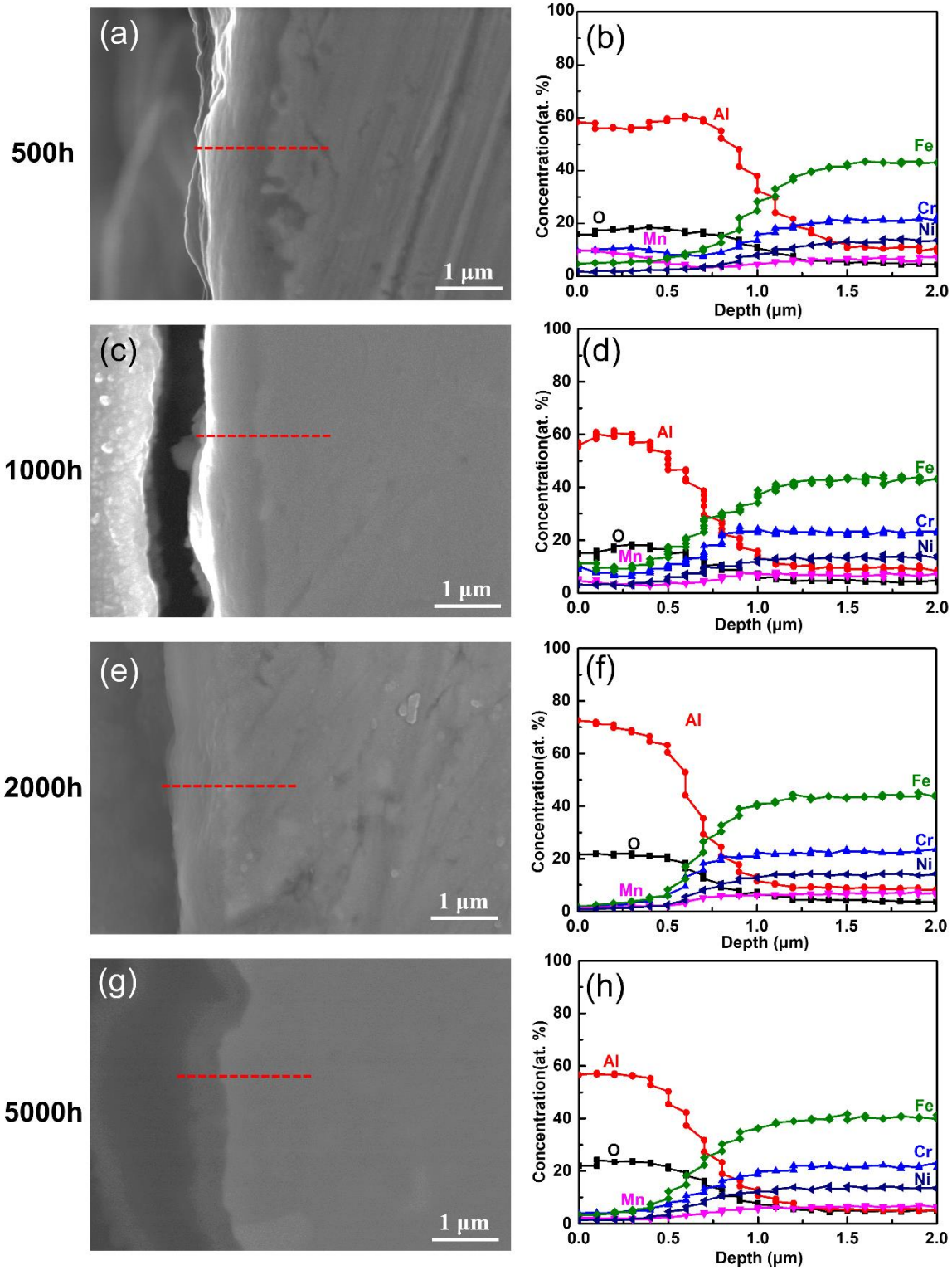

Figure 28 Cross-section profiles of oxide scales formed on OC5 after tested in 10% water vapor at 800 °C for: (a, b) 500 h, (c, d) 1000 h, (e, f) 2000 h, and (g, h) 5000 h.

5.5 STEM/EDS mapping

To show the morphology and chemistry of oxide scales formed on 310S and AFA alloys in detail, **Figure 29** compares the STEM/EDS mapping profiles of 310S, OC4 and OC5 after tested in air with 10% H_2O at 800 °C for 5000 h. For 310S, the region examined exhibited an outer chromia layer and an inner semi-continuous silica layer which is consistent with the XRD and SEM/EDS line scanning data (**Figures 22 and 26h**). An Ni/Fe metal particle was entrapped/interdispersed in the inner scale region. Little Mn was detected, which suggests that the location examined is from the inner regions of a thicker scale location, where the Mn was likely primarily present in the outer scale regions as shown in **Figure 26f**. Chromia-forming stainless steels such as 310S also contain appreciable quantities of Si, typically 0.5 to 1.5 wt.% Si. The present 310S batch contained 0.57 wt.% Si (**Table 2**). Silica formation at the scale-alloy interface regions in such alloys has been widely reported due to the greater thermodynamic stability of SiO_2 versus Cr_2O_3, and further can slow oxidation rate under some conditions [109, 110, 144]. This inner SiO_2 is in contrast to the SiO_2 deposits observed by SEM/EDS at some 310S surface locations at the outer scale/gas interface resulted from quartz tube volatilization.

The oxide scale location examined for OC4 after 5000 h operation (**Figuire 29b**) consisted of an outer silica layer, attributed to volatilization deposits from the quartz furnace tube [43], and an inner continuous alumina layer. Within the alumina, a thin Cr-rich oxide line likely leftover from the transient oxidation processes was observed. The OC5 formed a similar Al-rich scale structure to the OC4 (**Figuire 29c**). Discrete silica deposits were observed on the outer scale, along with some Mn-rich oxide. Within the alumina scale, some local, discrete spots of Cr-rich oxide were found. There is little Cr-rich oxide in the Al-rich oxide scales formed on OC4 and OC5 after 5000 h at 800 °C in air with 10% H_2O, which verifies its stability and capability of preventing significant Cr diffusion to the oxide surface which would otherwise evaporate and poison the SOFC cathodes.

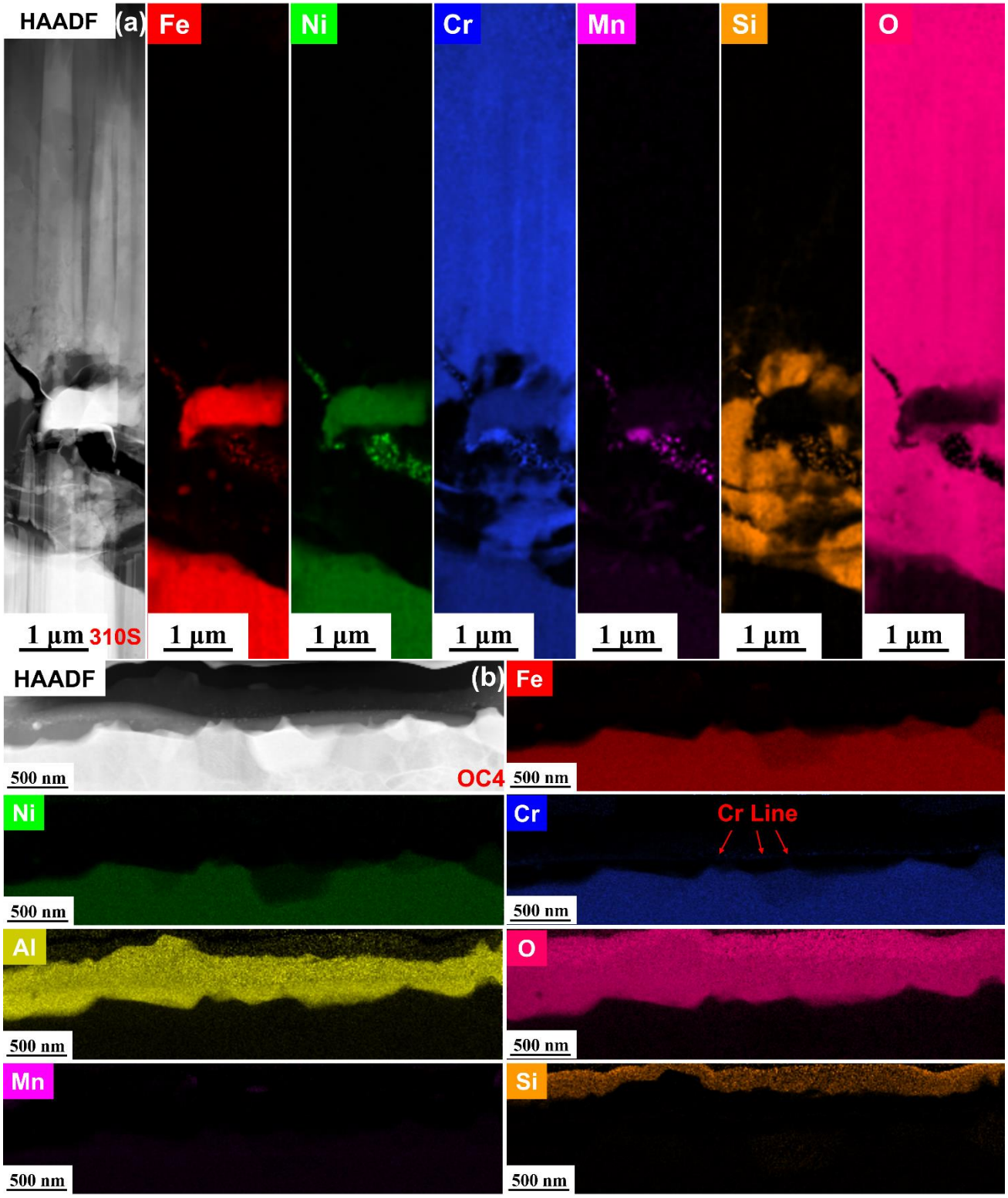
HAADF
(a)
Fe
Ni
Cr
Mn
Si
O
1 µm
310S
1 µm
1 µm
1 µm
1 µm
1 µm
1 µm
HAADF
(b)
Fe
500 nm
OC4
500 nm
Ni
500 nm
Cr
Cr Line
500 nm
Al
500 nm
O
500 nm
Mn
500 nm
Si
500 nm

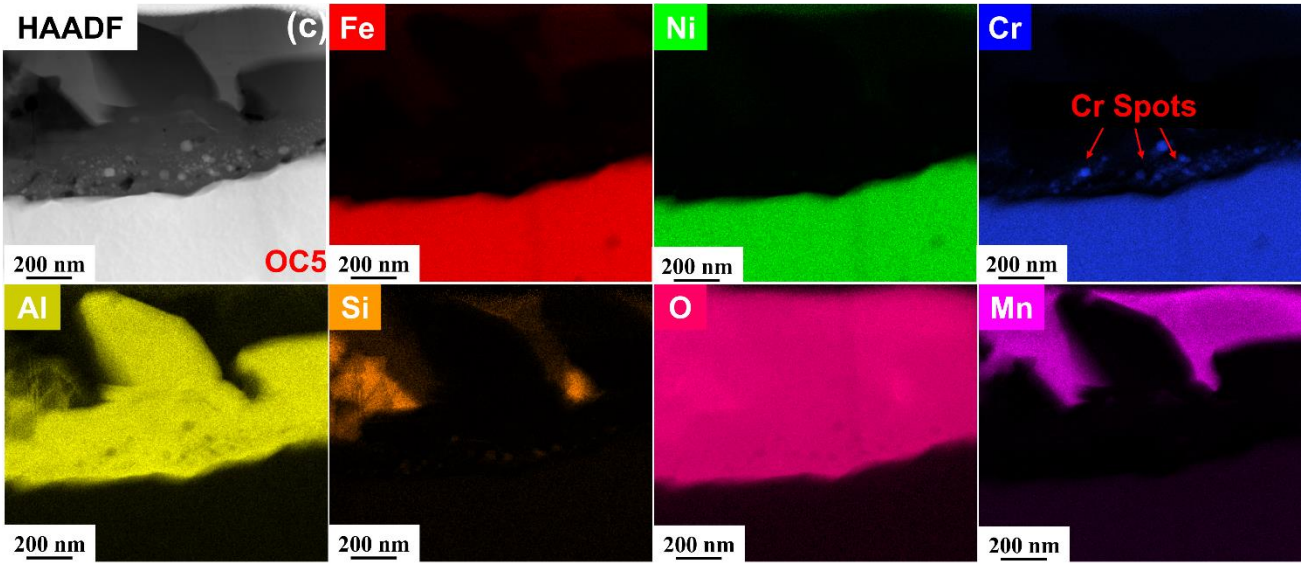

Figure 29 STEM/EDS mapping of (a) 310S, (b) OC4 and (c) OC5 after tested in 10% water vapor at 800 °C for 5000 h.

5.6 Discussion

Figures 22 and 23 demonstrate the average Cr evaporation rates and specific mass change of 310S and AFA alloys as a function of exposure durations (10 cycles) in air + 10% water vapor at 800 °C. The average Cr evaporation rates of 310S after each cycle are over a magnitude higher than AFA alloys. Moreover, the Cr evaporation rates of AFA alloys of the first cycle are only just at the detection limit of (2 to 4) x 10^{-12} kg/(m^2*s)., while the Cr evaporation rates of 310S maintain around 10^{-10} kg/(m^2*s). The AFA alloys exhibited slow, positive specific mass gains cycle-by-cycle with the increasing of exposure durations for AFA alloys, consistent with parabolic-like kinetics and protective alumina scale formation. In contrast, the specific mass of 310S peaks at the first 500h cycle then decreases with the increasing exposure durations. For 310S, the specific mass loss of 310S after 500h (one cycle) through the remaining cycles to 5000 h can be attributed to the Cr oxy-hydroxide volatilization and a modest degree of oxide spallation. The average evaporated Cr quantities curve (**Figure 22b and Table 5**) shows a modest decrease in Cr evaporation kinetic of 310S from cycles 5 ($1.5x10^{-10}$ kg/(m^2*s) to 10 ($4.18x10^{-11}$ kg/(m^2*s), suggesting a sub-linear to slightly parabolic accumulated Cr evaporation behavior over the course of the 10 cycles. It is hypothesized that this minor decrease in Cr evaporation in 310S may be due to increasing Cr-Mn rich spinel in the outer surface scale with

continued oxidation exposure time (**Figure 22**), although further study will be needed to better confirm this supposition.

For the AFA alloys, slow, parabolic-like oxidation kinetic and a barely detectable Cr evaporation rate only in the first 500 h cycle, with average Cr evaporation rates below the detection limit in the subsequent test cycles are observed (**Figures 22 and 23**). The barely detectable Cr release at the first 500 cycle for the AFA alloys is attributed to the initial formation and full establishment of the protective alumina scale, with Cr present only in minor amounts in the outer transient oxide layer (**Figures 27-29**). As demonstrated in reference 18, Cr release from an Aluchrome YHf FeCrAl type alloy oxidizing in humid air at 800-1000 °C was highest on initial exposure, but decreased significantly (1 to 2 orders of magnitude range) over the first 300-500 h of exposure (800 °C) as the protective alumina scale was fully established. A similar sequence of behavior is believed to occur in the present AFA alloys. It was unfortunately not possible to establish the long-term kinetic of Cr release in the AFA alloys under the condition studied, as the levels of Cr release for cycles 2-10 were below the detection limit of the experimental setup used.

That said, this continuous, protective alumina layer formed on the AFA alloys is sturdy, compact and essentially free of voids or cracks and was successful in reducing Cr evaporation over 5000 h of total testing in air with 10% H_2O at 800C. The evaporated Cr quantities of AFA alloys are about 35 times lower than 310S after the 5000 h test, assuming a worst case scenario of the levels of Cr release for the AFA being at the detection limit for each test cycle (**Figure 22b**). Therefore, the AFA alloys offer good promise in long-term exposure in SOFCs stacks operation conditions. The negligible oxidation and Cr evaporation behavior differences between OC4 and OC5 indicate that for 800 °C SOFC BoP components use, it is possible to go with OC5 with lower Al and Nb alloy, which is less costly and more readily processed than OC4 with higher Al and Nb. Finally, it is worth noting that the Si deposition contamination observed on the oxidized alloy surface from the quartz tubes during the test does not appear to influence the significant differences of evaporated Cr quantities between 310S and AFA alloys. (As discussed in reference [144], the use of alumina tubes result in interaction with the gaseous Cr species, reducing the measured flux of Cr release, with quartz tubes favored for measurement of Cr release despite the Si issue). In particular, 310S still exhibited extensive

Cr evaporation throughout the 5000 h test in the quartz tube which strongly suggests that the Si contamination did not significantly retard the process of Cr evaporation (**Figure 22**). Further, the oxidation kinetics for 310S, OC4, and OC5 in the present work using quartz tube at 800 °C in air with 10% H_2O were quite similar to those observed in an alumina tube with no occurrence of surface Si contamination [43, 48].

5.7 Summary

The Cr evaporation and oxidation behavior of alumina-forming austenitic (AFA) stainless steel and 310S in Air + 10 vol% H_2O at 800 °C is comprehensively studied with application to SOFC BoP components. The main conclusions of this study are:

(1) At 800 °C in air with 10% H_2O, oxides scale formed on the 310S alloy consisted of an outmost (Cr, Mn)$_3O_4$ spinel rich region and an inner Cr_2O_3- rich region, overlying a semicontinuous silica at the scale/alloy interface. The extent of spinel formation at the surface increased with increasing oxidation duration. The scale/alloy interface silica results from the 0.57 wt.% Si in the alloy. The scale thickness on the 310S was heterogenous, ranging from approximately 5 to 40 microns after 5000 h test, typical of the accelerated oxidation observed on chromia-forming alloys in the presence of water vapor. In contrast, the AFA alloys exhibit Al-rich scales on the order of a micron thick after 5000 h test, with minor amounts of Fe, Cr, Mn, and Nb also observed in the near surface regions.

(2) The 310S releases at least 35 times more gaseous Cr species than AFA alloys after 5000 h test at 800 °C in air with 10% H_2O, with the levels of Cr from the AFA alloys below the detection limit after the first 500 h test cycle. These findings indicate that the AFA alloys exhibit great potential for long-term application as SOFC BoP components. The similarity in oxidation behavior and Cr release observed for the two AFA formulations studied also suggest that it is possible to use OC5 with lower Al and Nb under this condition, which is less costly and more readily processed than OC4 with higher Al and Nb.

(3) Silica was also observed at the surface of the oxidized 310S, OC4, and OC5 test samples, and is attributed to volatilization from the quartz tube. However, this surface silica contamination did not appear to significantly impact the Cr evaporation rates and oxidation behavior of the alloys, as the 310S still exhibited order of magnitude higher Cr release than the AFA alloys on each cycle test, and the oxidation behavior was comparable to previous testing conducted with an alumina tube where no silica contamination was observed.

Chapter 6 Long-term Oxidation and Chromium Evaporation Behavior of Al_2O_3-Forming Austenitic Stainless Steel

Great efforts have been made to improve the efficiency of gas turbine engine which can vastly decrease the operational costs and gross emissions[146]. Nonetheless, increasing efficiency means to increase operating temperature which usually desires better alternative materials to achieve the long-term operation. A large number of high temperature alloys had been tested in the past decades due to the increasing fuel costs[147, 148].

In the beginning, type 347 stainless steel is the standard material that applied in recuperators or heat exchangers to improve the efficiency of gas turbines up to 600 °C [149, 150]. However, it has been reported that type 347 stainless steel suffered from accelerated oxidation attack in the water vapor environments resulted from the combustion process above 600 °C [151, 152]. Therefore, numerous researchers are devoting to devise an alternative for type 347 stainless steel in the past ten years. For recuperators operating above 600°C, these alternatives including Ni-based alloy 625, alloy 709 and alloy 120 have been tested to show better oxidation resistance than type 347 stainless steel due to the higher Cr and Ni contents[124, 153-156]. Higher operating temperature and efficiency were achieved on the recuperator in the 4.6MW Mercury 50 gas turbine with the application of alloy 625[153]. However, taking the initial cost into consideration, Ni-base alloys are quite expensive for large-scale application. Therefore, some work has focused on Fe-base alloys, such as alloy 709 and alloy 120 which possess higher oxidation resistance and longer lifetime in water vapor environment[124, 154, 157].

Generally, these alloys rely on the formation of chromia layer for protection which still could be undermined in the water vapor environment during the long-term high temperature operation due to evaporation of gaseous chromium species resulted from the chemical reaction between chromia layer and water vapor[28-30, 110, 125, 158, 159]. It is worth noting that the slower growth rate of alumina layer than chromia and its

immune property to water vapor makes it the candidate material in the water vapor environment has been reported in several research[39, 123, 143, 144]. In our previous review, a continuous alumina layer formed on alumina-forming austenitic (AFA) stainless steel could greatly prevent the outward chromium diffusion, thus showing much lower Cr evaporation rates than chromia-forming alloys[127]. Long-term stability of continuous alumina layer formed on AFA alloys at 800 °C had been reported. However, a transition from continuous alumina layer to internal attack of Al had been observed when they were operating at higher temperatures [61, 89, 91, 101, 144]. Therefore, reactive elements such as Y, Hf and Zr are added as the alloying additions to increase the upper-temperature limit and the adherence of the alumina layer formed on AFA alloys [160-167].

In this chapter, AFA alloys aimed at the application in higher temperature recuperators which could form a protective alumina layer that are more stable in the presence of water vapor than chromia-forming alloys are studied. Cr evaporation and oxidation behaviors of two AFA alloys with different reactive elements additions are evaluated compared to alloy 625 at 900 °C in 10% H_2O + air environment. The objective is to achieve a better understanding of the oxidation mechanisms in water vapor containing atmospheres and to study the effect of alloy composition on their Cr evaporation and oxidation behavior. These results should also guide the designed composition of the alloys for long-term operation in other water vapor containing environments.

6.1 Cr evaporation rates

The Cr concentration rates of 625, OC11 and OC11LZ tested after each cycle at 900 °C in air with 10% H_2O in quartz tubes were summarized in **Figure 30a**. The collected solutions from OC11 after the first cycle and OC11LZ at fifth, sixth and tenth cycle are below the detection limit of ICP test. Then maximum values were taken to clearly show the Cr evaporation rates difference between commercial alloys and AFA alloys, the accumulated Cr amounts after different durations were summarized **Figure 30b**. It can be seen that Cr evaporation rates of the AFA alloys are typically over an order of magnitude lower than 625 after each cycle test, which verifies the protective effects on preventing Cr diffusion of AFA alloys. In detail, the Cr evaporation rates of OC11 tested after each cycle were in the magnitude of 10^{-11} kg/m^{2}s with only first cycle

higher than 10^{-11} and all the other nine cycle lower than 10^{-11} which may give a hint that formed continuous alumina layer during the first cycle could decrease the evaporated Cr species in the consequent test. The Cr evaporation rates of OC11LZ tested after each cycle were also mainly in the magnitude of 10^{-11}. However, compared to stable evaporation rates of OC11, it is worth noting that oscillations after the first cycle have been observed on OC11LZ which may imply that the alumina layer formed on OC11LZ is not stable during the whole operation. However, the Cr evaporation rates of 625 tested after each cycle were in the magnitude of 10^{-10} and 10^{-9} kg/m^{2}s which exhibits a typically high Cr evaporation rates of chromia-forming alloys. In addition, the difference between accumulated Cr amounts became larger and larger with increasing testing cycles. A 22- and 12-times higher amounts of evaporated Cr of 625 than OC11 and OC11LZ was observed after first cycle, respectively. However, a 56- and 28-times higher Cr amounts of 625 than OC11 and OC11LZ was observed after the entire long-term operation, respectively.

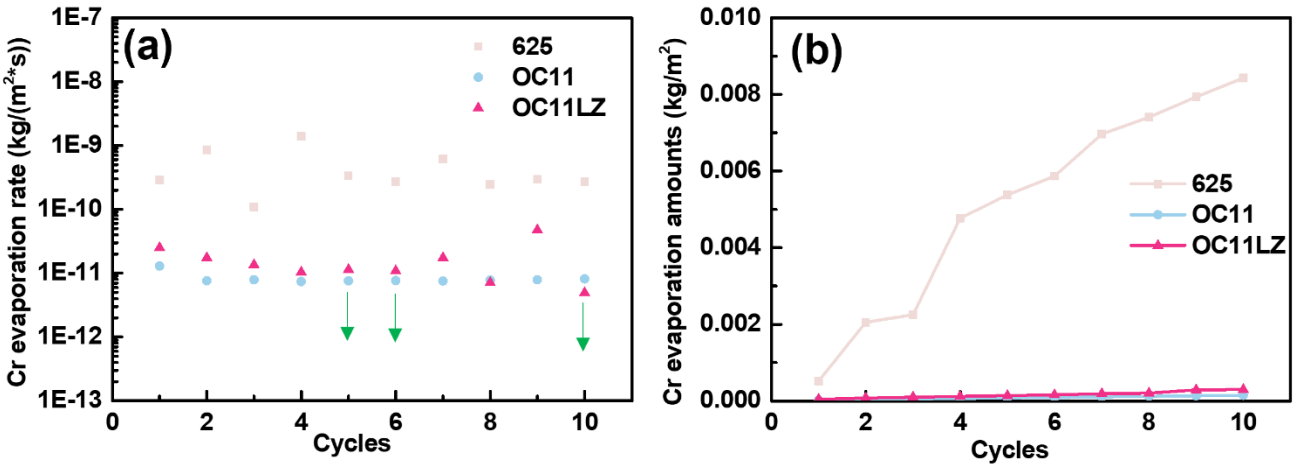

Figure 30 Cr evaporation rates and accumulated Cr amounts of each cycle for various alloys tested at 900 °C in air with 10% H_2O for 5000 h.

6.2 Long-term oxidation kinetics

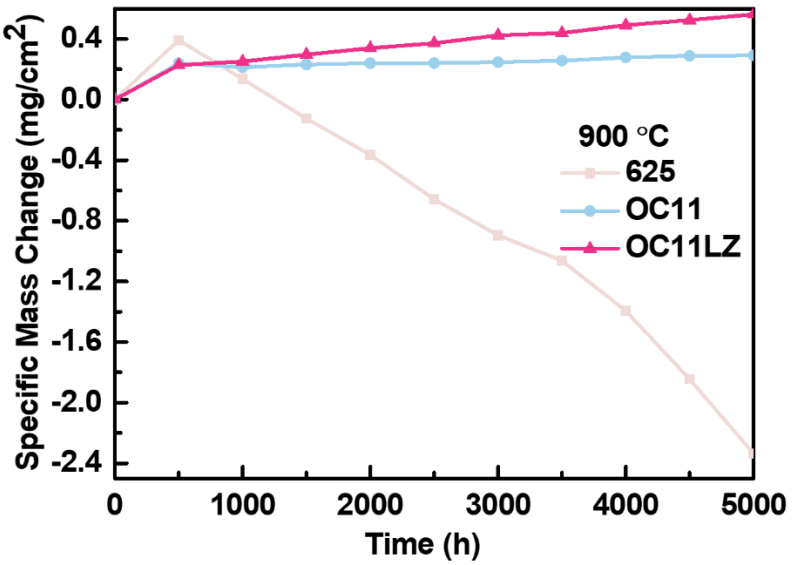

Figure 31 weight gain profiles for various alloys tested at 900 °C in air with 10% H_2O.

Figure 31 shows how the weight gain profiles of 625 and AFA alloys changes with the exposure time in air with 10% water vapor at 900 °C. For AFA alloys, the weight gain increased quickly in the first cycle (0.20 mg/cm^2) and then slowed down. This could be explained by the transient oxidation of Fe-Cr-Mn-Al-rich oxides and the formation of a continuous alumina layer after the first cycle. However, the continuous alumina layer formed on the alloy surface can work as a barrier for the outward diffusion of cations, so the weight gain after the first cycle slowed down. In contrast, the weight gain of 625 reaches a maximum after first cycle because of the formation of oxide layers. These oxide layers are porous and can react with H_2O which will cause the spallation of the oxide layers. When a certain thickness of the oxide layers is achieved, the outmost layer of the oxide will crack, which causes the upcoming weight loss during the remaining operation. It is worth noting that the weight gain of the OC11 and OC11LZ in the subsequent 9 cycles test is 0.10 mg/cm^2 and 0.30 mg/cm^2, respectively. This results also substantiates the stable oxide scales formed on OC11, however, the oxide scale formed on the OC11LZ during the long-term operation is not stable and robust which may provide an alternative path for the outward diffusion of cations and inward diffusion of oxygen that causes the higher weight gain.

6.3 Phase characterization

Figure 32 presents the XRD profiles of 625 and AFA alloys after tested at 900 °C in air with 10% H_2O in quartz tubes for various periods. For 625, spinel and Cr_2O_3 are the two major phases that formed during the long-term operation at 900 °C. After first cycle (500 h) test, the substrate peak of 625 was much lower than 0 h which demonstrates the thick oxides formed on 625. It is worth noting that the main difference of XRD patterns of 625 for different durations is the peak intensity of the spinel and Cr_2O_3 which can be attributed to the evaporation of the chromium species. However, substrate and Fe_2Nb Laves phases are the main peaks for AFA alloys during the whole oxidation process which demonstrates that the oxide scales formed on the AFAs could be much thinner [20]. Moreover, some small peaks of chromia, alumina and spinel also could be observed. For OC11 and OC11LZ tested at 900°C, the peak intensity of alumina for the OC11LZ is higher than OC11 which is in accordance with the weight gain results. It is clearly seen that the alumina layer formed on AFA alloys exhibit significantly greater oxidation resistance than 625 in 10% water vapor environments which make it desirable material for the application in recuperators.

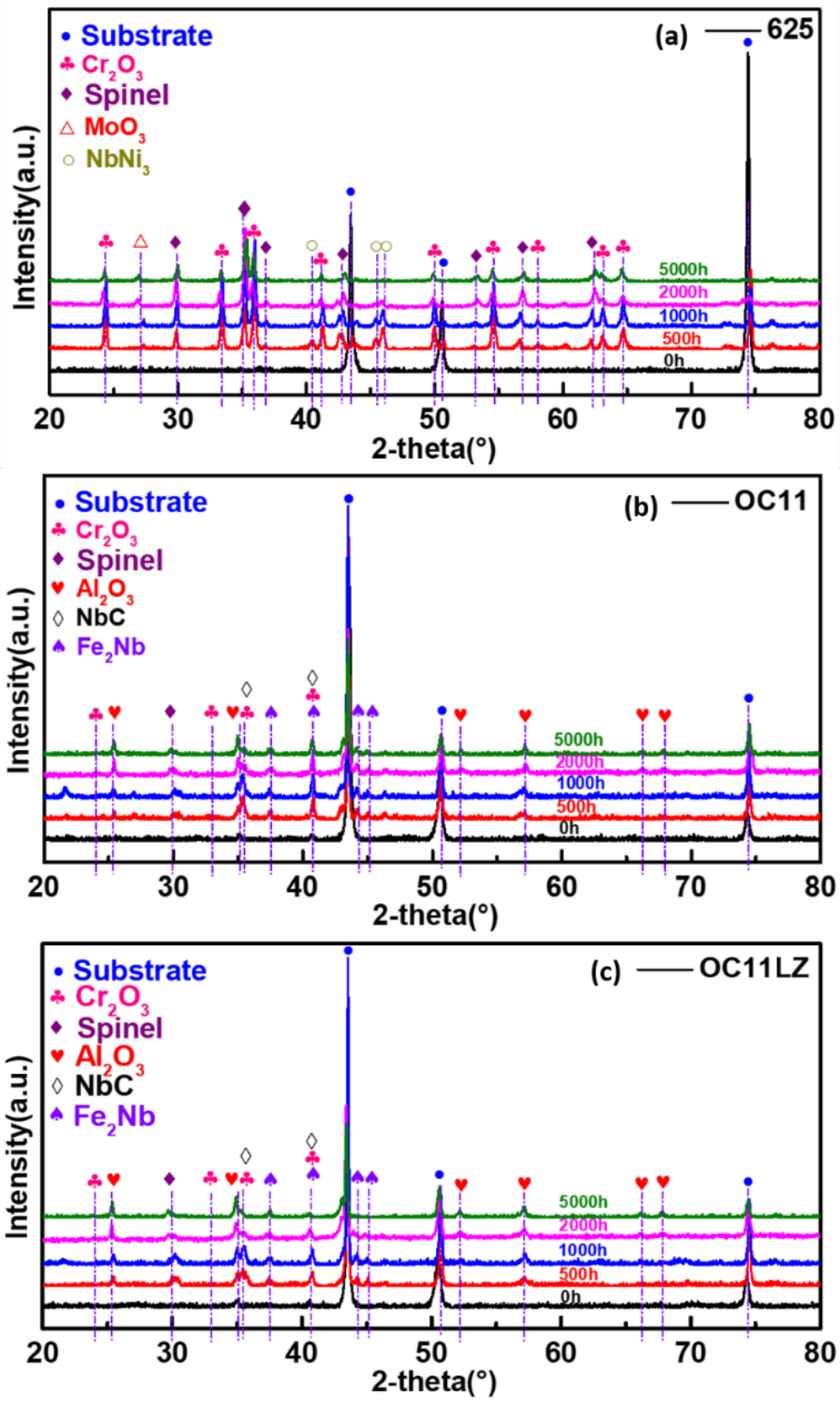

Figure 32 XRD profiles for different alloys after tested at 900 °C in air with 10% H_2O for different periods (0, 500, 1000, 2000, 5000h).

6.4 Surface morphologies

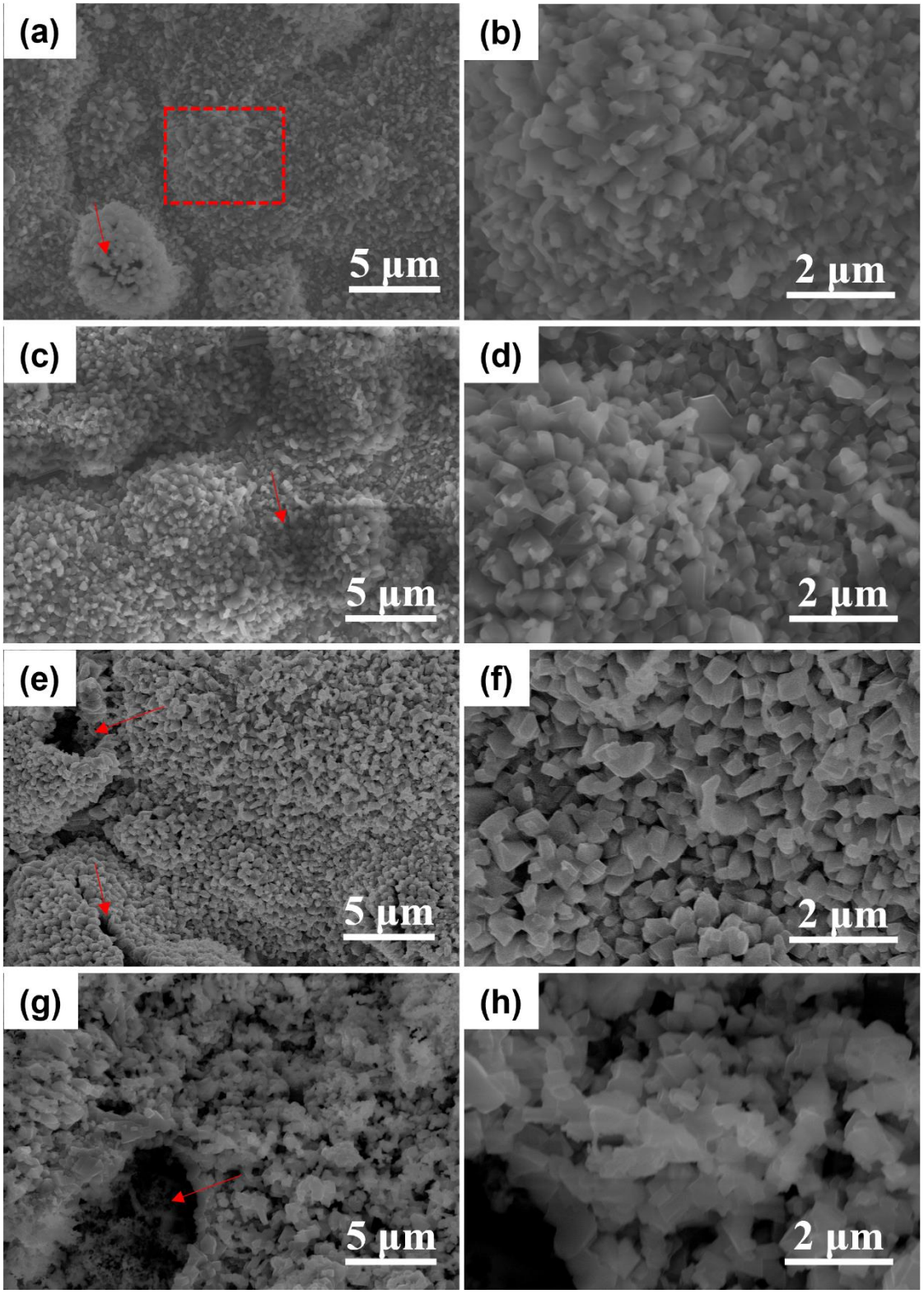

Figure 33 SEM images of the 625 surfaces after tested at 900 °C in air with 10% H_2O for (a, b) 500h, (c, d) 1000h, (e, f) 2000h and (g, h) 5000h.

Figure 33 illustrates the surface morphologies of 625 after testing for different lengths of time in air with 10% H_2O at 900 °C. As shown in **Figure 33a**, after first cycle test, the surface is quite rough and not uniform, covered by diamond-like oxides. The region indicated by the red square in **Figure 33a** a is shown as a magnified image in **Figure 33b**, there were a large number of diamond-like oxide particles with different sizes distributing on the alloy surface. EDS analysis of the surface shows these oxides uniformly formed could be assigned to the Cr-Mn spinel with size of 0.1-0.3 μm. It is worth noting that minor spallation takes place after only one cycle test indicated by red arrow (**Figure 33a**) that can provide an extra path for the water vapor ingression which can react with chromia layer to release the gaseous Cr species. **Figure 33c** shows the surface morphology of 625 after two cycles (1000h) exposure. The size of Cr-Mn spinel (0.1 to 0.3 μm) almost remains the same. However, minor cracks can be observed on the surface. It is clear that the oxides formed on the surface are loose (**Figure 33d**). **Figure 33e** shows the surface morphology of 625 after four cycles (2000h) exposure. More cracks are observed on the surface which may promote the further Cr evaporation and spallation. In addition, the majority of Cr-Mn spinel particles have a size larger than 0.3μm (**Figure 33f**). **Figure 33g** shows the surface morphology of 625 after ten cycles (5000h) exposure, the morphology greatly changes, it can be easily observed that there are two different kinds of morphologies, spallation area and the area with diamond oxides (**Figure 33g**). For the spallation area, the oxides are mainly Cr-Mn-Ni oxides. However, for the area with diamond oxides in size from 0.3 to 1 μm, severe spallation can be observed. Moreover, the spallation area has a larger proportion after the entire operation. Therefore, the external water vapor can easily enter the oxides layer through this spallation area and result in more severe Cr evaporation.

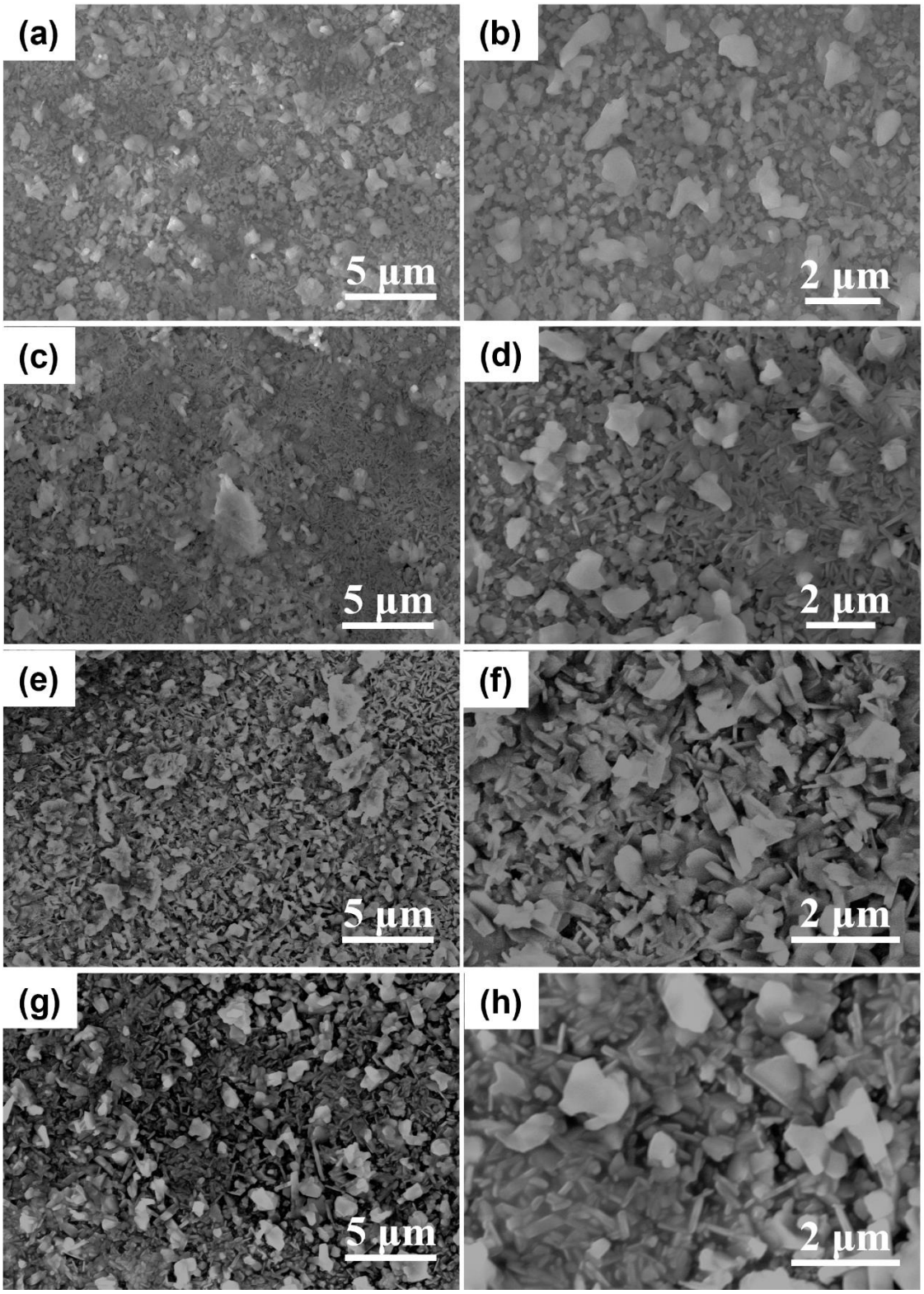

Figure 34 SEM images of the OC11 surfaces after tested at 900 °C in air with 10% H_2O for (a, b) 500h, (c, d) 1000h, (e, f) 2000h and (g, h) 5000h.

Figure 34 shows the surface morphologies of OC11 after testing for different lengths of time in air with 10% H_2O at 900 °C. As shown in **Figure 34a**, after first cycle of test, the alloy surface is covered with all kinds of oxides with different shapes. A large number of nodular oxides could be seen. EDS analysis demonstrated that the composition of these oxides was mainly consisted of Fe, Cr, Mn, Al, Nb and Ni. **Figure 34c** shows the surface morphology of OC11 after two cycles (1000h) exposure. There are mainly two types of oxides formed on the surface: bar-shaped oxides (length × width: 0.1 μm × 0.5 μm) and oxide nodules (0.3 to 1 μm). Based on EDS analysis, Cr-Mn-rich oxides and alumina are the mainly oxides for numerous oxide nodules and bar-shaped oxides, respectively. The formation of bar-shaped oxides indicates the formation of continuous alumina layer which can provide protective effect to reducing the Cr evaporation rate in the second cycle test (**Figure 30a**). **Figures 34e and 34g** show the surface morphology of OC11 after two cycles (1000h) and four cycles (2000h) exposure, respectively. The amounts and the size of the bar-shaped oxides does not change much for longer exposure time, which verifies the stability of alumina. However, the size of numerous oxide nodules increased with the operation time.

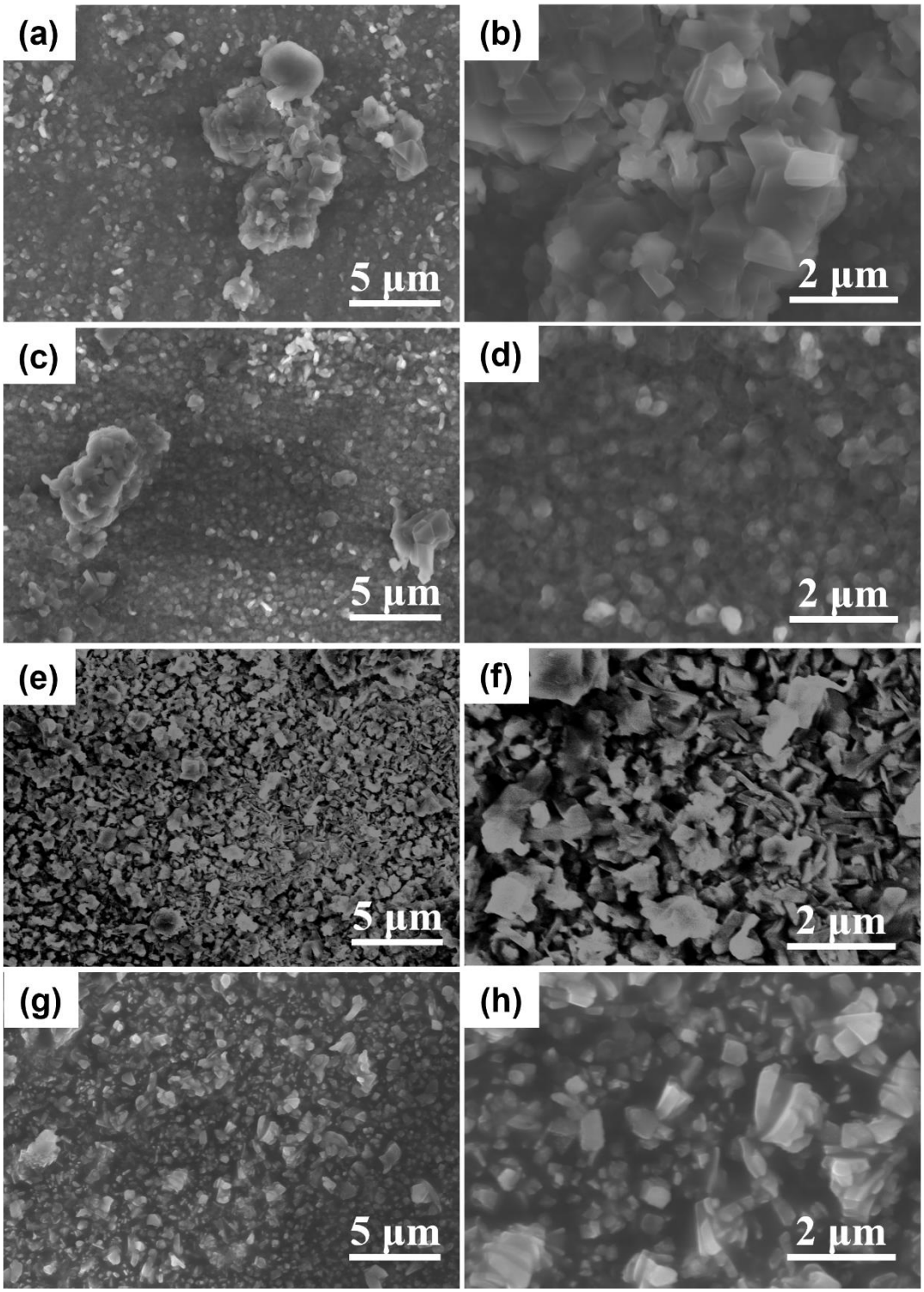

Figure 35 SEM images of the OC11LZ surfaces after tested at 900 °C in air with 10% H_2O for (a, b) 500h, (c, d) 1000h, (e, f) 2000h and (g, h) 5000h.

Figure 35 shows the surface morphologies of OC11LZ after testing for different lengths of time in air with 10% H_2O at 900 °C. As shown in **Figure 35a**, after first cycle of test, the morphology of OC11LZ is different from

that of OC11. There are much more oxides formed on the surface than OC11 which is in accordance with the weight gain curve. Diamond-like oxides with the size of 0.3 to 1 μm are the main oxides formed on the surface coupled with some bigger Nb-rich oxides with the size of about 3 μm. **Figure 35c** shows the surface morphology of OC11 after two cycles (1000h) exposure, the surface morphology almost has no change except that more diamond-like oxides were formed on the surface. It can be deduced that the continuous alumina layer is not completely formed after two cycles of exposure. **Figure 35e** shows the surface morphology of OC11 after four cycles (2000h) exposure, the oxide scale on the surface has a great change compared to 500 and 1000 h. The surface is covered by numerous oxide nodules coupled with some emerged bar-shaped oxides and diamond like oxides (**Figure 35f**). Moreover, this is the time point when the Cr evaporation rate could not be detected that can be ascribed to the formation of continuous alumina layer which is in accordance with the Cr evaporation rates results (**Figure 30a**). **Figure 35g** shows the surface morphology of OC11 after ten cycles (5000 h) exposure, the size of these oxides remains almost the same as 2000 h. However, the size of diamond like oxides increases with the operation time (**Figure 35h**).

6.5 Oxide scales composition

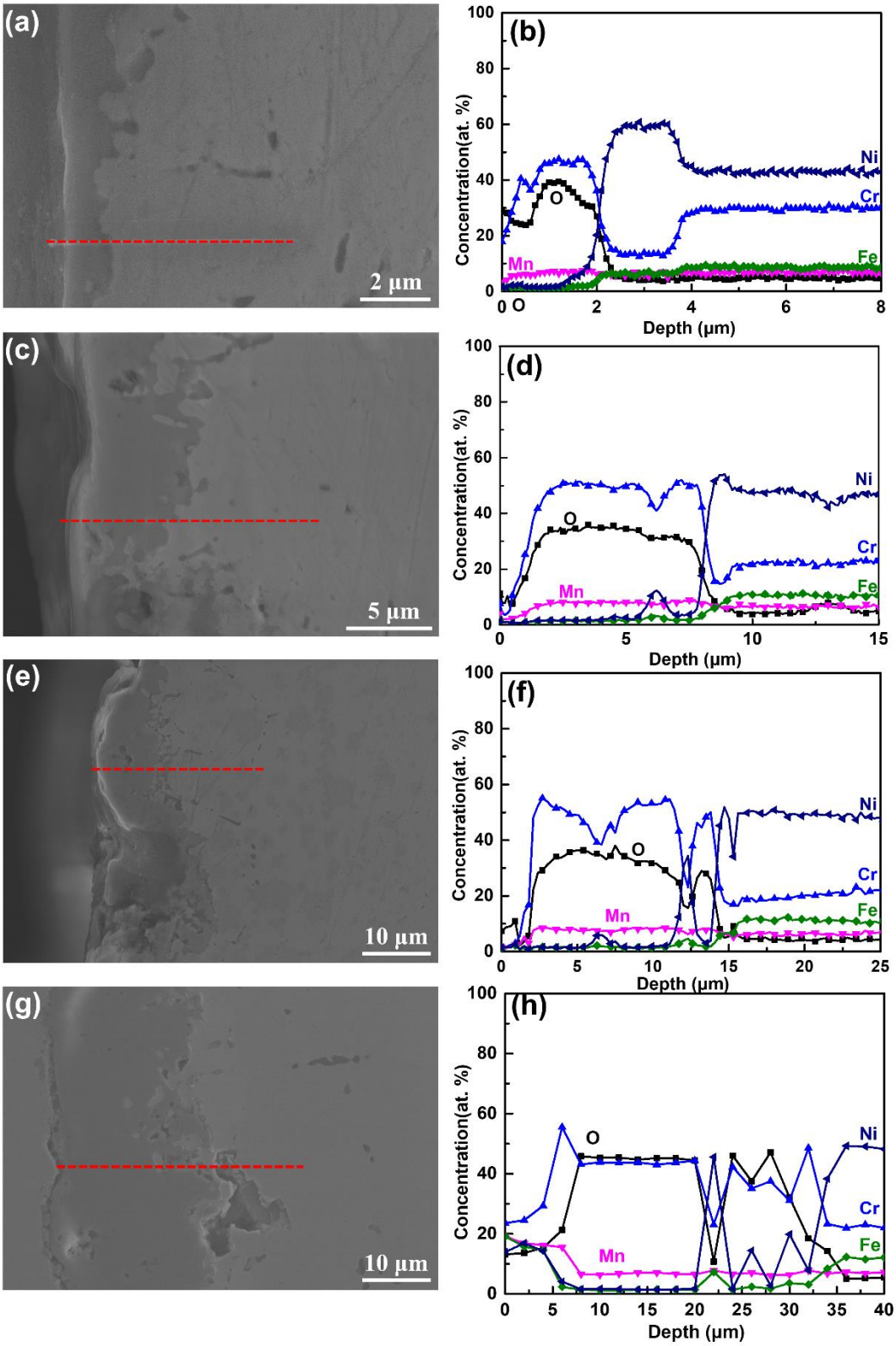

Figure 36 SEM micrographs and EDS line scan results for typical cross-sections of 625 after tested at 900 °C in air with 10% H_2O for (a, b) 500h, (c, d) 1000h, (e, f) 2000h and (g, h) 5000h.

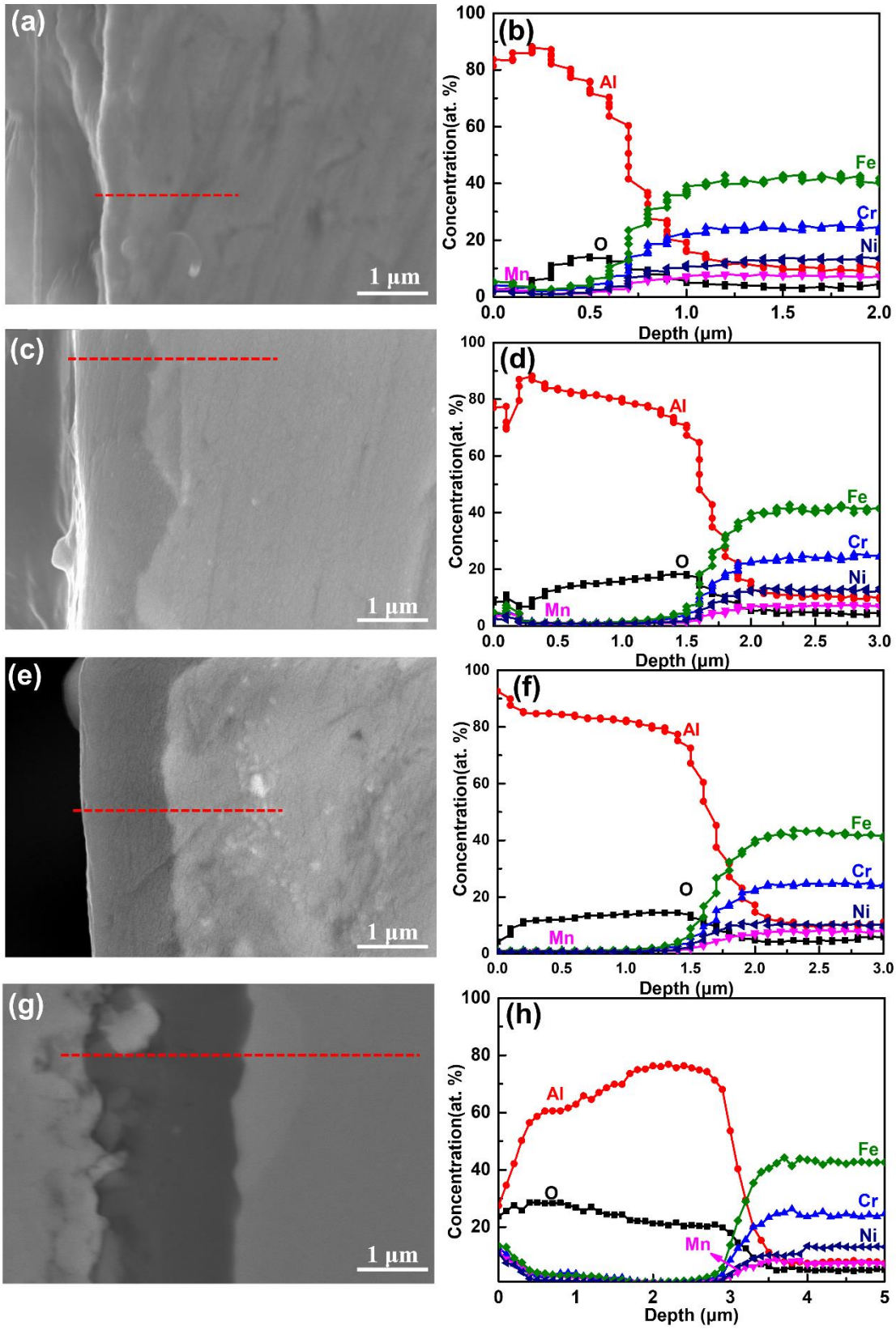

Figure 37 SEM micrographs and EDS line scan results for typical cross-sections of OC11 after tested at 900 °C in air with 10% H_2O for (a, b) 500h, (c, d) 1000h, (e, f) 2000h and (g, h) 5000h.

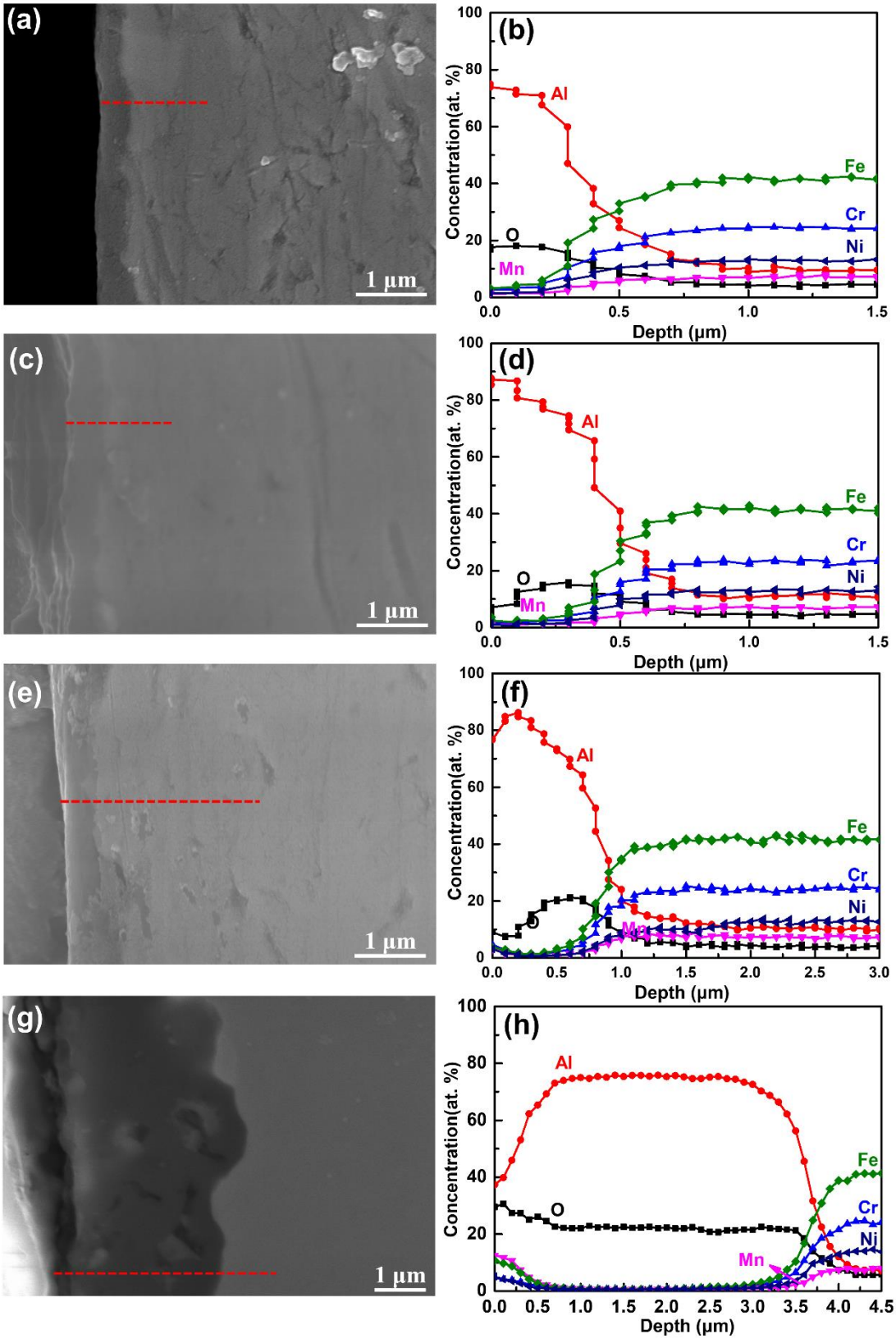

Figure 38 SEM micrographs and EDS line scan results for typical cross-sections of OC11LZ after tested at 900 °C in air with 10% H_2O for (a, b) 500h, (c, d) 1000h, (e, f) 2000h and (g, h) 5000h.

Figure 36-38 demonstrate the cross-sectional morphology and the corresponding EDS line scanning profiles of 625 and AFA alloys at 900 °C after test for different durations. It is worth noting that reactive elements such as Zr and Hf are added to increase the oxide scale adherence and the high-temperature limit of AFA alloys [100]. After test for the first 500 h, the thickness of the oxide scales formed on two AFA alloy is about 0.5 μm (**Figure 37a and 38a**), while the thickness of 625 is about 2 μm (**Figure 36a**). In addition, the oxide scales formed on 625 display an outer (Cr, Mn)-rich oxide layer, which coincides with the results of XRD (**Figure 32a**). And a 2 μm deep Cr depletion region beneath the oxide scales could be observed. There are no cracks or voids formation on 625 and AFA alloys after 500 h test. In contrast to the three different oxide layers formed on AFA alloys at 850 °C in our previous research, only an inner alumina layer with a thimble of outer Fe-Cr-Mn-Al rich oxide layer could be observed. The disappearance of intermediate chromia layer could be ascribed to the accelerated reaction between chromia layer and water vapor at higher temperature. With continuing the test to 1000 h, the thickness of the oxide scale formed on 625 increases to 5-8 μm, and it is observed that some voids are starting to form in the oxide scales (**Figure 36c**). In the case of AFAs, there are no pores. The continuous alumina layer formed on AFA alloys greatly decreases the Cr evaporation rates (**Figure 32b**), which is about 2 orders of magnitude lower than 625. Moreover, the thickness of the oxide scale formed on OC11 increases to 0.8-1 μm, while the thickness of OC11LZ almost remains the same. It is also clearly shown from **Figure 36d** that 625 suffers from Cr depletion in the sub-scale regions after 1000 h oxidation which could result in the spallation of oxide scales. After 2000 h testing, the formation of voids and holes in the oxide scales contributes to the spallation of the oxide scale on certain surface sites (**Figure 36e**), thus, resulting in formation of an uneven oxides layer with thickness of 5-15 μm for 625. In contrast, no cracks have been observed for the AFAs and the thickness of OC11 increases to 1.2 μm, while the thickness of OC11LZ remains the same. The sturdy and compact continuous alumina layer formation on AFA alloys lead to decreased Cr evaporation rates (**Figure 37b**). After 5000 h test, apparently more spallation areas could be observed for 625, and the line scans (**Figure 38g**) demonstrates that the Cr depletion beneath the oxide layer corresponds to the spallation area. In addition, the enrichment of Ni and Fe (**Figure 38h**) can also be observed which corresponds to the XRD profiles (**Figure 30a**). In contrast, OC11 still possesses a more

uniform oxide scale (about 2μm thickness) with no defects observed. This plays an important role on decreasing the Cr evaporation rates during the 5000 h operation (**Figure 37g**). However, discrepancies in AFA alloys begin to show up after 5000 h operation which could be ascribed to the different reactive elements added. A large number of voids in the oxide scales of OC11LZ after 5000 h operation were observed which is corresponding to the Cr evaporation rates results (only fifth, sixth and tenth cycle cannot be detected in (**Figure 28b**).What's more, the formation of these voids provides an alternative transport path for the inward oxygen diffusion and outward chromium diffusion, thus resulting in the turbulent Cr evaporation rates during the 10 cycles and the increase of the oxide scales thickness in the long-term operation.

6.6 STEM/EDS cross-sectional mapping

To further demonstrate the morphology and chemistry of oxide scales formed on 625 and AFA alloys after long-term operation. **Figures 39-41** compares the STEM/EDS mapping profiles of 625, OC11 and OC11LZ after test at 900 °C for 5000 h in air with 10% H_2O. The oxide scale formed on 625 (**Figure 39a**) consisted primarily of an outer thin surface transient oxide layer rich in Cr, and Mn consistent with spinel, an Cr-rich oxide region consistent with Cr_2O_3 and with a spallation region rich in Fe, Cr, Mn, Ni and Si which is in accordance with the XRD and line scanning data (**Figures 32 and 36**). It is worth noting that minor local enrichment of Fe, Ni, Cr, Mn and Si at the spallation region was also observed. In addition, big cracks in the chromia layer could be observed, which will lead to significant spallation of oxide scales after 5000 h operation. In contrast, the oxide scales formed on OC11 after long-term operation mainly consist of an outer Fe-Al-Si-Cr-Mn-rich oxides layer and an inner continuous alumina layer with minor Hf and Y-rich oxides indicated by red arrows (**Figure 40a**). The OC11LZ formed a similar scale structure to the OC11, with a complex outer transient oxide and an inner Al_2O_3 layer with Zr-rich oxides indicated by red arrows (**Figure 41a**). However, a chromia layer and some voids were observed in the continuous alumina layer which verifies its non-stability in the water vapor environment during long-term operation, thus causing the oscillation of Cr evaporation rates during the last several cycles. Moreover, the large number of Si deposits on the AFA alloys is unexpected and deduced to result from interactions with the quartz tube in the water vapor environment.

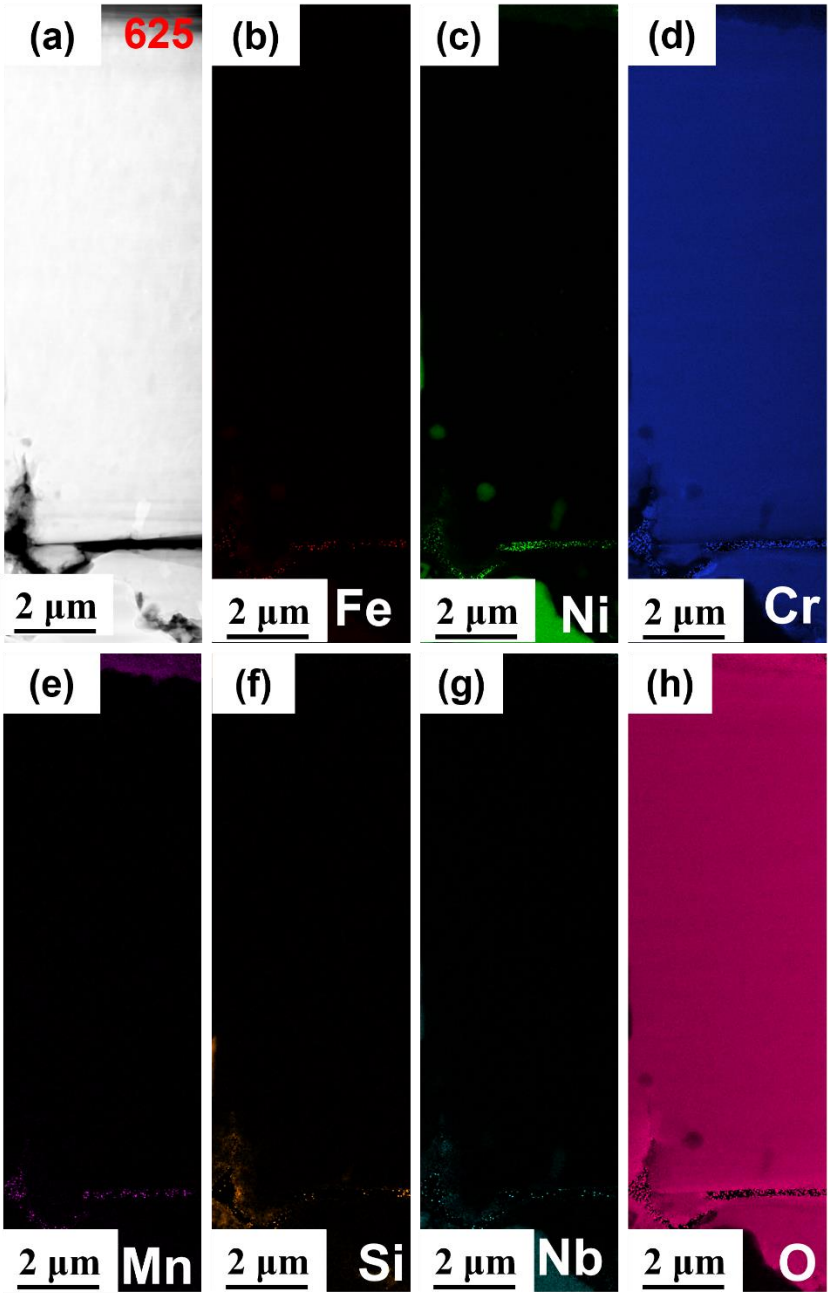

Figure 39 (a) HAADF-STEM image and cross-sectional mapping image of alloy 625 after tested at 900 °C in air with 10% H_2O for 5000 h, (b) Fe, (c) Ni, (d) Cr, (e) Mn, (f) Si, (g) Nb and (h) O.

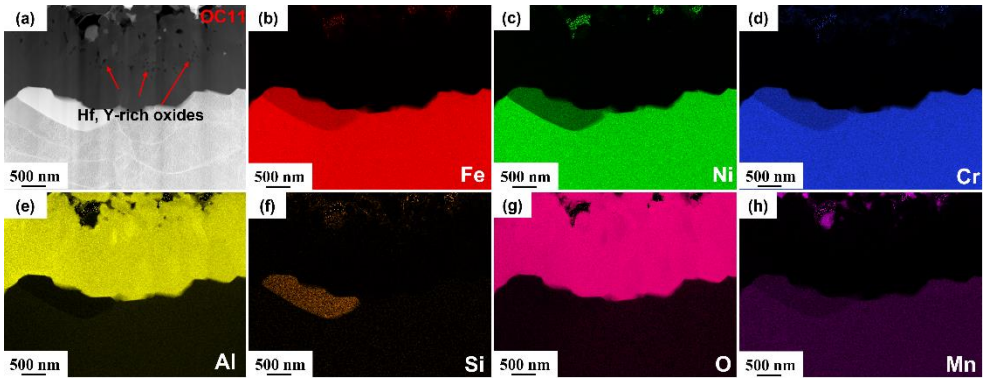

Figure 40 (a) HAADF-STEM image and cross-sectional mapping image of alloy OC11 after tested at 900 °C in air with 10% H_2O for 5000 h, (b) Fe, (c) Ni, (d) Cr, (e) Al, (f) Si, (g) O and (h) Mn.

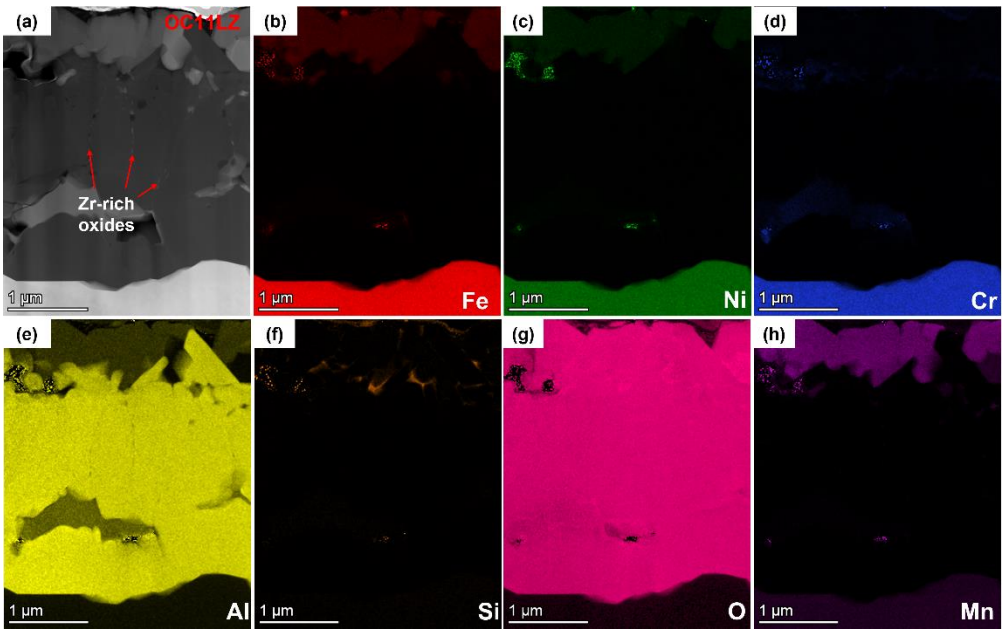

Figure 41 (a) HAADF-STEM image and cross-sectional mapping image of alloy OC11LZ after tested at 900 °C in air with 10% H_2O for 5000 h, (b) Fe, (c) Ni, (d) Cr, (e) Al, (f) Si, (g) O and (h) Mn.

6.7 Relationship between the weight change and Cr evaporation rates

As discussed in our previous study, the chromia-forming alloys exhibited higher oxidation rates and Cr evaporation rates in water vapor environment than AFA alloys, indicating that the characteristics of formed oxide scales are of great importance for the long-term operation of high-temperature alloys. In this study, the Cr evaporation rates of 625 were about 2 orders of magnitude higher than AFA alloys after each cycle test. The environment is thought to considerably affect the oxidation kinetics and the Cr evaporation behaviors of different alloys. Based on **Figure 30**, the accumulated Cr evaporation amounts value after the entire test for 625, OC11 and OC11LZ were 8.43, 0.148 and 0.298 Kg/cm^2, suggesting the 625 tested in water vapor

environments were extremely prone to release Cr gaseous species. Moreover, the weight gain for 625, OC11 and OC11LZ tested after first cycle were 0.392, 0.239 and 0.228 mg/cm^2, suggesting that the oxides growth rate of 625 is greater than AFA alloys. In addition, the mechanical properties of oxide scale were also significantly affected by the water vapor environment. The continue decreasing of weight gain of 625 and the higher weight gain of OC11 than OC11LZ, was possibly related to the evaporation and spallation of oxide scale formed on chromia-forming alloys and the effect of reactive elements on the formed alumina layer of AFA alloys [168]. In addition, the higher Cr evaporation rates and the change of the mechanical properties of 625 are related to the drastic reaction between water vapor and oxide scales compared to AFA alloys.

The XRD test results indicated that the predominant oxides formed on 625 and AFA alloys during the entire test were chromia and alumina, respectively (**Figure 32**). Moreover, some spinel peaks were also observed. The SEM surface morphology and line scanning results indicated that 625 exhibited an outmost spinel layer and an inner chromia layer, which led to the weight gain after the first cycle test. Mn additive to 625 could result in the Cr, Mn-rich spinel layer formed on the surface of the matrix. It was reported that the spinel formed on chromia could greatly decrease the Cr evaporation from chromia layer. However, water vapor can easily reach the chromia layer via the loose formed spinel layer and the spallation area (**Figure 33a**). Thus, both the continuation of Cr evaporation and the more severe spallation after the first cycle contribute to the continuous weight loss of 625 (**Figure 31**). In contrast, an outer Fe-Cr-Ni-Mn-Al-rich layer and an inner continuous alumina layer were observed on AFA alloys after the first cycle test which resulted in the sudden weight gain (**Figure 34b and 35b**). The reason why no clear intermediate chromia layer could be observed is that the intensive reaction between water vapor and chromia layer at 900 °C which results in the detectable Cr evaporation rates after the first cycle for AFA alloys. However, in the following test, the growth rate of oxides scale decreased which could be attributed to the formed continuous alumina layer that suppressed the outward diffusion of cations and the inward diffusion of oxygen. Thus, the Cr evaporation rates in the following cycles could not be detected for OC11. However, there were several cycles of Cr evaporation that could be detected. It could be attributed to the property variation of oxides scale during the long-term operation for OC11LZ.

6.8 Effect of reactive elements on oxides scale growth of AFA alloys

It is proverbial that the alumina layer forms by inward diffusion of oxygen via grain boundaries and outward diffusion of aluminum, therefore the new scale formed will be beneath the earliest formed scale [105, 110, 165]. Under this condition, stress will be gradually concentrated inside the scale which may result in the spallation of alumina layer. In our previous research, AFA alloys without reactive elements additions suffered from spallation in the long-term operation at high temperatures [144]. The additions of reactive elements (REs) in alloys could improve the adherence of alumina and decrease the oxides scale growth by changing the transport in the scale to inward diffusion of oxygen [164, 169, 170]. It was reported that single RE doping can only provide slight advantages in improving the oxidation resistance due to the low solubility in alloy matrix [171, 172]. However, superabundant doping of single RE would contribute to the internal oxidation and further the scale spallation. Therefore, researchers had been devoting to improve the oxidation resistance by applying co-doping RE in alloys which had achieved significant breakthroughs. Pint et al. [173] reported that Y and Hf co-doping resulted a more adhesive scale than Y single doping. According to the weight gain results in **Figure 31** and cross-sectional morphologies results in **Figure 40 and 41**, co-doping of Hf and/or Y in OC11 and Y and/or Zr in OC11LZ could both beneficially increase the oxidation resistance of the oxide scale and prevent the spallation from taking place which resulted in the lower Cr evaporation rates than 625 at higher temperature. Pint proposed a dynamic-segregation theory [174] to elucidate that reactive elements firstly segregated at the metal-scale interface which can greatly improve the adhesion of the oxides scale and halt the void formation at the interface, then these REs can diffuse along the grain boundary to the oxides scale surface which can inhibit the outward diffusion of cations. Several researchers [175-177] reported that the blocking effect of Hf, Y and Zr could effectively prevent the outward diffusion of cations and further decrease the oxidation rate of alumina-forming alloys. To investigate the effect of co-doping reactive elements on alumina layer and further optimize AFA alloys, microstructure of alumina scale after the entire test in water vapor environment was prudently characterized. **Figure 40a and 41a** shows the HAADF image of oxides scale formed on the Hf-Y co-doped OC11 and Y-Zr co-doped OC11LZ after 5000 h test at 900 °C. It is worth noting that, for OC11, Hf and Y oxides particles segregated within the grain boundaries at some regions

which could contribute to the lower oxidation rate than OC11LZ and a thinner oxides scale after the entire test. Moreover, Li et al. [178] also observed the Hf and Y segregation within grain boundary at some regions, they reported that Hf and Y ions could form either Y-Hf composite oxides or ionic clusters which could prevent the outward diffusing of cations due to the synergistic effect of these two REs. In terms of OC11LZ, although the segregation of REs could also be observed indicated by the red square, the oxidation rate was slightly higher than OC11 which could be attributed to the ZrO_2 formation inside the alumina layer which would serve as a facilitating pathway for inward diffusion of oxygen, thus causing the thicker alumina layer with porosity (**Figure 40a and 41a**) [179]. In addition, Wessel et al. [180]also reported that the oxides scale growth rate and the in-scale porosity of Zr-doped FeCrAlY-alloy was higher than FeCrAlY-alloy with no doping. Therefore, preferential oxidation was needed to consume the Zr by internal oxidation during the fabrication process due to the fast incorporation of Zr into alumina layer in operation of gas turbines.

6.9 Summary

The long-term oxidation and chromium evaporation behaviors of AFA alloys were characterized compared to chromia-forming alloy 625. The addition of different reactive elements to an AFA-base composition plays a significant role in the alumina scale formation during long-term oxidation at high temperatures. The main findings of this study were listed as follows based on a combination of surface analysis techniques:

(1) The chromia layer formed on 625 was more vulnerable to water vapor effect than continuous alumina layer formed on AFA alloys. Such difference is contributed to the more drastic reaction between oxides scale of 625 and water vapor, validated by SEM and STEM characterization, which resulted in the much high Cr evaporation rates than AFA alloys.

(2) The Cr evaporation test profiles and weight gain profiles indicated that the OC11 possessed lower oxides scale growth rate and lower Cr evaporation rate than OC11LZ because of the formed alumina layer variation. Based on SEM cross-sectional line-scanning and STEM/EDS mapping, more voids in the thicker oxides scale of OC11LZ were revealed.

(3) The observation of HADDF images verified the segregation of reactive elements. The synergistic effect of Hf and Y prevented the outward diffusion of cations which resulted in the thinner oxides scale, while the fast corporation of Zr to the scale would provide an alternative pathway for the inward diffusion of oxygen, thus causing a thicker oxides scale with defects.

Chapter 7 Genuine Evaluation of the Cr Evaporation Rates of Al_2O_3-forming Austenitic Stainless Steels

Chromia-forming alloys [5, 24, 181, 182] and alumina-forming alloys [39, 112] have been widely used in solid oxide fuel cell (SOFC) stacks. SOFC is an efficient energy-conversion device that directly converts chemical energy to electrical energy without combustion and mechanical processes [80, 127, 183]. Metallic interconnects (MICs), which have high creep-resistance and strength, are applied to assemble numerous single cells to form a SOFC stack that can meet the voltage and power density requirements of large-scale applications [184, 185]. Moreover, BoP components such as pumps, valves, heat exchangers and piping are also of great importance for the long-term operation of the stacks [130]. Generally, Fe-based Cr_2O_3-forming alloys were applied as MICs and BoP components in the stacks because of their matched thermal expansion coefficient with the electrolyte [50, 181, 186]. When the stacks run at high temperatures, a protective scale such as chromia will form on the surface of these MICs and BoP components. However, as the operation continues, the formed chromia scale layer would react with oxygen and water to generate gaseous Cr species such as chromium oxides, hydroxides and oxyhydroxides which will evaporate from the oxide scales and then deposit within the SOFC cathode, thus poisoning the performance of SOFC stacks [187-189]. Even though the addition of trace elements such as Mn made it possible for a Cr-Mn spinel layer formation on the chromia scale layer to reduce the gaseous Cr evaporation [120], the deterioration by Cr poisoning is still severe. Therefore, researchers have devoted themselves to take measures to alleviate the Cr poisoning. One key to decreasing the evaporation of gaseous Cr species is to devise an effective coating on the MICs [84, 127, 132, 190]. While effective coatings have been applied to reduce Cr evaporation on MICs, the BoP components cannot be thoroughly coated. Therefore, it is stringent to develop a new alloy to replace Fe-based alloy for these components such as heat exchangers, turbines and converters to eliminate or minimize release of Cr gaseous species under high-temperature operation. Unlike interconnect materials, BoP components are not restricted by their electrical conductivity or their thermal expansion properties. With this in mind, researchers worked in the past decades to create Fe-based Al_2O_3-forming alloys (AFA) for use under high-temperature

conditions [102, 137, 144], but had not been successful until recent. A new Al_2O_3-forming austenitic stainless steel with low cost, high Cr-resistant and high-creep strength was recently developed by Yamamoto and Brady [20, 101]. It is shown that a continuous protective alumina layer could be formed on these AFA alloys, thus suppressing the diffusion of chromium and manganese ions and furtherly preventing the generation of spinel on the alloy surface. Investigation of these AFAs is still undergoing to optimize the compositions for the application of long-term high-temperature operation [61, 62, 140].

While chromium evaporation from Cr_2O_3 and MICs has been studied widely in the past decades [30, 35, 40, 41, 85, 108, 111, 191-193], research on the BoP components are scarce [39, 107, 108, 194]. All Cr evaporation tests in these papers were conducted in quartz tube. As will be shown below, Si evaporates and deposits on the alloy surface. It will alter the oxidation process of the alloys and bring error to the Cr quantities in the long-term operation of SOFC stacks. In addition, Thomann and Froitzheim [40, 41, 85, 111, 193, 194] applied denuder technique to accurately quantify the evaporated Cr quantities. Taking into consideration of the above-mentioned problems, the present paper was designed to investigate the Cr evaporation of the AFA in an atmosphere with 10% water vapor at 800 °C and 900 °C in comparison with commercial alloys and to figure out a reliable and accurate method to evaluate Cr evaporation. All commercial alloys chosen are chromia-forming alloys, whereas AFA alloys are selected as alloys which are able to form a continuous alumina layer that can ensure the long-term operation as well as reduce the evaporated Cr quantities. Alloy specimens operated with various method were characterized with XRD and SEM after the test to evaluate its feasibility. The characterization of the specimens using optimal method (No Si, Na deposition and/or reaction with tube) were illustrated in this chapter, and the characterization of the problems occurred in other methods were demonstrated in the supplementary materials. Moreover, these various methods and the corresponding problems were compared and discussed in detail.

7.1 Chromium Evaporation from different alloys using different methods

The volatility of chromium compounds is a well-known phenomenon which limits the use of chromia-forming alloys to service temperatures below 1100°C [188]. In the presence of humidity, the dominant species is

chromium oxyhydroxide [127] which is formed according to Equation [1].

$$1.5O_2(g)+Cr_2O_3(s)+2H_2O = 2CrO_2(OH)_2(g) \quad (1)$$

And the absorption reaction between Sodium carbonate and chromium volatile species which is according to Equation [18].

$$CrO_2(OH)_2(g) + Na_2CO_3(s) = Na_2CrO_4(s) + H_2O(g) + CO_2(g) \quad (18)$$

Cr evaporation rates of various alloys after 500 h test using different methods are shown in **Figure 42**. In general, for all the testing methods, it is clearly observed that 310S and 625 exhibits a comparatively higher Cr evaporation rate than OC4 and OC5 under 800 °C and OC11 and OC11LZ under 900 °C, respectively, which can be attributed to the formed thick chromia scale on 310S and 625 [144]. The schematics of the Cr evaporation test are shown in **Figure 43**.

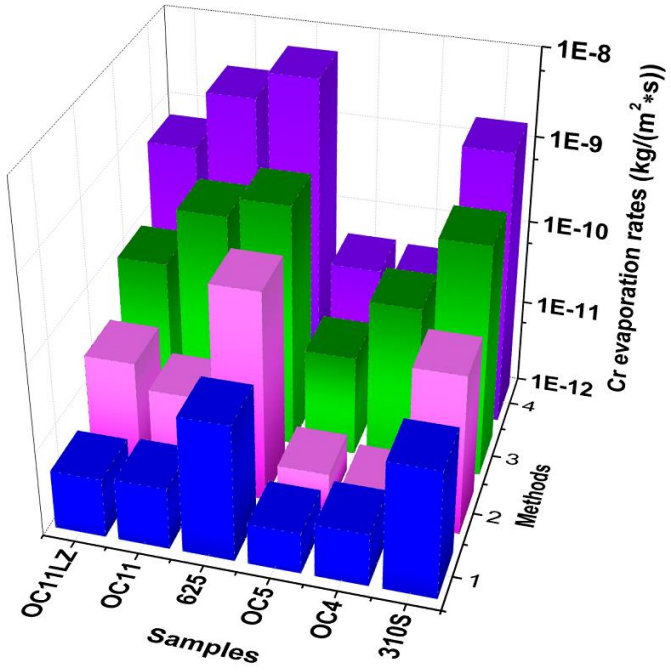

Figure 42 Cr evaporation rates of 310S, OC4 and OC5 800 °C and 625, OC11 and OC11LZ at 900 °C tested in 1) alumina tube, 2) quartz tube, 3) sodium carbonate coated thin alumina tube and 4) sodium carbonate coated alumina tube for 500 h in air with 10% H_2O.

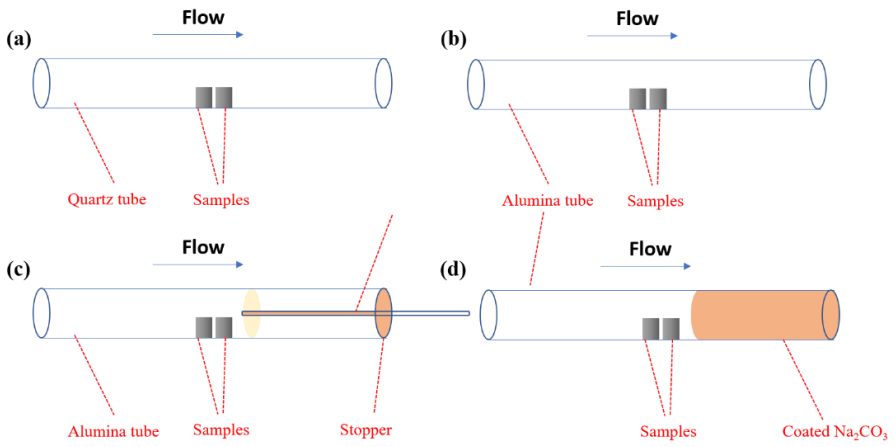

Figure 43 Schematic of the Cr evaporation test of different alloys in a) alumina tube, b) quartz tube, c) sodium carbonate coated thin alumina tube and d) sodium carbonate coated alumina tube.

7.2 Testing in quartz tubes (method 2)

Many researchers [30, 35, 40, 41, 85, 108, 111, 191-193] had evaluated the Cr evaporation rates of chromia-forming alloys and alumina-forming alloys using quartz tubes with different humidity at different temperatures with different flow rate in the last decades. It was unanimous that the Cr evaporation rates of alumina-forming alloys were much lower than that of chromia-forming alloys which can be attributed to the formed continuous alumina layer that could prevent the diffusion of chromium, thus greatly reducing the corresponding Cr evaporation rates. However, some problems could occur in this testing method which we used in our previous paper to check the feasibility to replace chromia-forming alloys with AFA alloys for the application of balance of plant in SOFC industry [144]. One is the Cr deposits on the quartz tubes, and the other one is the Si deposits on the alloy surface. The former problem could be solved by cleaning the quartz tubes after every test [108]. However, in the case of the latter problem which might affect the long-term Cr evaporation rate of alloy even though we figured out that the Si deposits after 500 h test was not enough to severely influence the Cr evaporation rates in comparison with many studies [144]. The Si deposits on the alloy surface at the range of 800-900 °C were characterized by XPS in the previous research. Moreover, the Si deposits on the alloy surface may affect the establishment of oxide scales and the diffusion of chromium which may also lead to the imprecise tested Cr evaporation rates of various alloys in the long-term operation. The long-term operation of 310S, OC4 and OC5 at 800 °C and 625, OC11 and OC11LZ at 900°C for 4500 h

using quartz tubes had been conducted in this paper. The SEM images of alloy surfaces and the corresponding EDS after 4500 h test were demonstrated in **Figure S3 and S4**. It could be clearly observed that there were Si deposits for the all the alloys except 625. The Cr deposits on 625 alloy surfaces after 500 h test had been validated even though there were no Si deposits for the 4500 h sample of which reason had not been figured out. In addition, the Cr evaporation rates of alloys using quartz tubes were about one magnitude lower than that tested with sodium carbonate coated thin alumina tubes, implying that the Si deposits on the surface must have some effects to reduce the Cr evaporation rates. The effect of Si deposits on the Cr evaporation rates and the establishment of oxide scales during the long-term operation will be studied in the future. In a word, there could be plenty of Si deposits on the alloy surface after the long-term test using the quartz tubes which could contribute to the lower Cr evaporation rates.

7.3 Testing in alumina tubes (no coating, method 1)

Up to now, almost all studies were using quartz tubes to investigate the Cr evaporation rates of alloys. Researchers might neglect the effect of Si deposits on the Cr evaporation rates and oxidation process of alloys in the short-term operation. However, there could be a great number of Si deposits on the alloy surface after 4500 h operation (**Figure S3c**). In order to exclude the effect of Si deposits, alumina tubes were used to replace the quartz tubes. The phase determination of oxide scales was characterized by XRD and SEM and the problems occurred in these testing methods were discussed below.

Herein, we applied alumina tubes (**Figure 43b**) to evaluate the Cr evaporation rates of these alloys. It could be seen from **Figure 42** that the Cr evaporation rates tested in were even lower than that of quartz tubes which could be attributed to the chemical interaction between Cr gaseous species and alumina tubes. Many researchers [195-198] had reported the reaction mechanism of alumina/chromia solid solution. The evaporated Cr species could react with alumina tube to form the solid solution on alumina tubes which could be extremely difficult to be fully cleaned. The phase determination of oxide scales tested in alumina tubes was shown in **Figure S5**. These peaks were quite similar as the samples tested in the sodium carbonate coated thin alumina tube and no other secondary phases could be observed. It verifies that the oxidation process would

not be undermined in alumina tubes. In addition, morphologies of samples after the Cr evaporation test in alumina tube were shown in **Figures S6 and S7**. The morphologies were almost the same as that tested in the sodium carbonate coated thin alumina tube, and no spallation could be observed.

7.4 Testing in sodium carbonate coated alumina tubes (method 4)

As there were solid solutions formed resulted from the chemical reaction between gaseous Cr species and alumina tube at the high temperature region which contributed to the lower Cr evaporation rates, we managed to coat the inner wall of alumina tube to alleviate the chemical reaction (**Figure 42d**). The Cr evaporation rates of 310S at 800 °C and 625, OC11 and OC11LZ at 900 °C were much higher than that tested with method 3, however, the Cr evaporation rates of OC4 and OC5 at 800 °C were in the same magnitude as method 3. In order to figure out this abnormal phenomenon, the XRD profiles of these alloys tested with method 4 were shown in **Figure S8**. It could be seen that hematite (Fe_2O_3) and magnetite (Fe_3O_4) were formed on 310S at 800 °C, OC11 and OC11LZ at 900 °C and nickel oxide (NiO) were formed on after the test with method 4 which could contribute to the abnormal higher Cr evaporation rates. EDS analysis of these alloys were shown in **Figure S9** to examine the integrity of the oxide scales. It could be seen that the morphologies of these alloys were totally different compared to that tested with method 3. Sodium pollution on the 310S surface (**Figure S9b**) and the breakaway oxidation of 625, OC11 and OC11LZ at 900 °C could be obviously observed (**Figure S9d, f, h**). The thermal decomposition of sodium carbonate had been studied by many researchers [199-201], the backflow of the sodium species could deposit on the alloy surface and result in the breakaway of these alloys which contributed to the abnormal higher Cr evaporation rates. However, the Cr evaporation rates of OC4 and OC5 were in the same magnitude as method 3 that did not suffer from sodium pollution which was in agreement with the Cr evaporation rates data and XRD profiles.

7.5 Testing in sodium carbonate coated thin alumina tubes (method 3)

7.5.1 Oxide Phase characterization

In order to verify the feasibility of method 3, the surface morphology, cross-sectional morphology and the chemical analysis of oxides scale of each alloy are also evaluated by XRD and SEM. X-ray diffraction (XRD)

profiles from commercial alloys and selected AFA alloys tested under 800 °C and 900 °C in air + 10% H_2O are demonstrated in **Figure 44**. It is clearly observed that 310S and 625 forms an oxide scale predominantly rich in Cr_2O_3, along with the presence of minor peaks related to spinel. Significant differences in the peak intensities of Cr_2O_3 scales appear for OC4 and OC5 alloys at 800 °C and OC11 and OC11LZ under 900 °C, respectively. Relative peak intensity of Cr_2O_3 is smaller compared to the peak of substrate, suggesting a thin scale formation on 310S at 800 °C. However, for the 625 sample, the peak of Cr_2O_3 is even larger than the substrate peak at 900 °C.

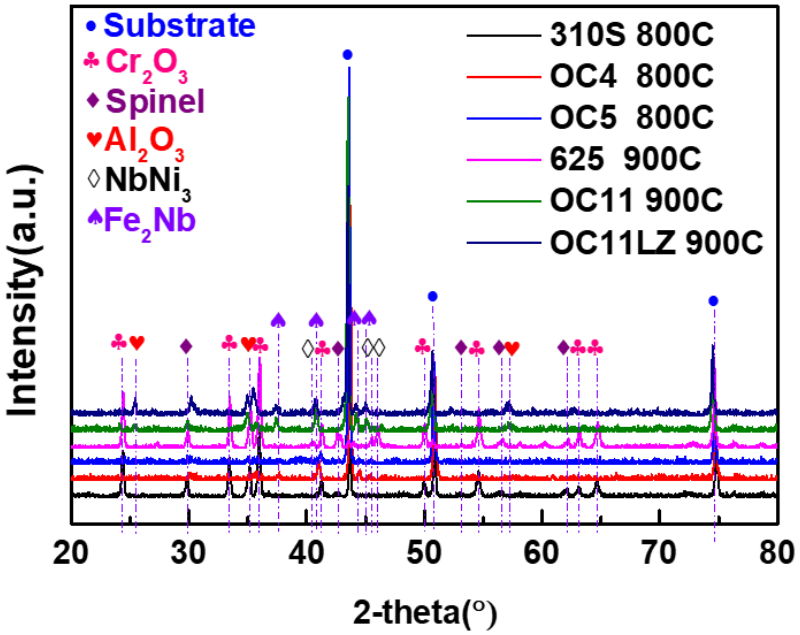

Figure 44. XRD profiles of the oxide scales developed on 310S, OC4 and OC5 at 800 °C and 625, OC11 and OC11LZ after 500 h chromium evaporation test in sodium carbonate coated thin alumina tube.

Oxidation of OC4 and OC5 at 800 °C in humidified air shows similar peaks. As can be seen from the XRD profiles, formation of Cr_2O_3 scale is observed along with large peaks from the substrate, while minor peaks from Cr_2O_3 and spinel are also observed.

The oxidation behavior of OC11 and OC11LZ demonstrates significantly different as compared to commercial alloys and AFA alloys at 800 °C. Oxidation of OC11 and OC11LZ at 900 °C results in the formation of mixed oxide scales. Large intensities from Al_2O_3 and Cr_2O_3 appear on the alloy surface. In addition, spinel peaks with smaller intensities could also be observed.

7.5.2 Oxide Scale Morphology

Figures 45 and 46 show the morphology of tested samples. Details of SEM-EDS analyses of all the specimens are provided in supplementary **Figure S10 and 11**. The microstructure of 310S sample oxidized under 800 °C is shown in **Figure 45a and 45b**. A uniform, porous oxide scale is observed to cover the alloy surface. Elemental analysis (**Figure S10b**) of the surface indicates formation of a mixed oxide scale riched in Cr and Mn at 800 °C which indicates formation of mostly chromia scale and some $(Cr, Mn)_3O_4$ spinel.

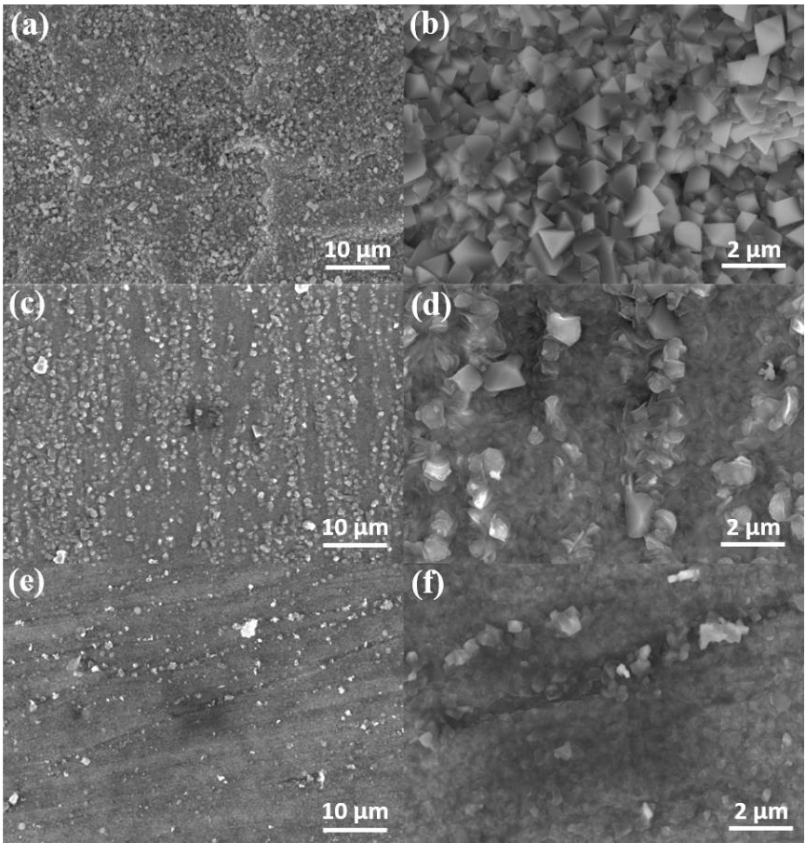

Figure 45. Oxide scale morphologies developed on (a, b) 310S, (c, d) OC4 and (e, f) OC5 tested for 500 h in air + 10% H_2O at 800 °C in sodium carbonate coated thin alumina tube.

Distinct morphologies of the surface scale formed on OC4 samples are shown in **Figure 45c and 45d**. Uniform scale formation with minor overgrown areas could be observed on the OC4 samples surface. Surface elemental analyses using EDS (**Figure S3d**) reveal that the overgrown areas are highly rich in Fe, Cr and Mn. The subscale, however, appears to have a high concentration of Al. The Al-dominant scale appears to be very uniform and dense as compared to the Fe-Cr-Mn-rich microstructure. Whereas there are less overgrown areas

for the OC5 sample whose scale are uniform Fe-Cr-Mn-rich scales which validated in the EDS analysis (**Figure S3f**), in addition, the uniform Al-dominant scale can also be observed (**Figure 45e and 45f**).

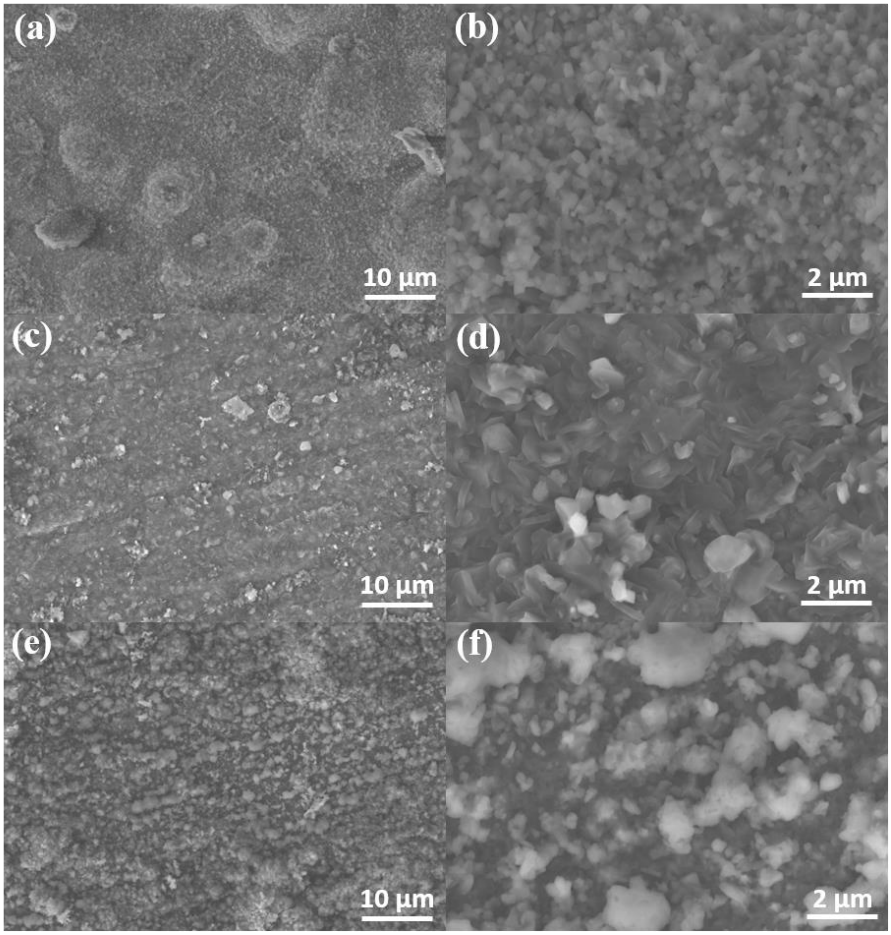

Figure 46. Oxide scale morphologies developed on (a, b) 625, (c, d) OC11 and (e, f) OC11LZ tested for 500 h in air + 10% H_2O at 900 °C in sodium carbonate coated thin alumina tube.

The morphology of 625 sample oxidized at 900 °C is shown in **Figure 46a and 46b**. A uniform oxide scale is observed to cover the alloy surface which is similar as 310S. However, some minor spallation could be observed on the morphology (**Figure 46a**). Elemental analysis of the surface indicates formation of a mixed oxide scale at 900 °C with a top layer that is rich in Cr and Mn and a chromia subscale (**Figure S4b**). Oxidation behavior of OC11 at 900 °C is shown in **Figure 46c and 46d**. OC11has almost the same oxide scales as compared to OC4 under 800 °C. Higher magnification images reveal crystalline overgrown structures and a smooth surface underneath at 900C. Oxide scale analyses indicate the formation of an Al-rich surface as a sublayer with surface oxides rich in Fe, Cr and Mn (**Figure S4d**). Oxidation of OC11LZ under 900 °C (**Figure 46e and 46f**) shows a more overgrown area than OC11. The faceted grains on the surface

could be attributed to the Fe-Cr-Mn-rich oxides and the dense subscale is Al-rich scales which is indicated by EDS analyses (**Figure S4f**).

In summary, using method 1 will result in the Si deposits on the alloy surface which may influence the oxidation process and reduces the Cr evaporation rates of alloys. Method 2 is applied to exclude the effect of Si deposits, however, the alumina/chromia solid solution resulted from chemical interaction between gaseous Cr species and alumina tube also reduces the Cr evaporation rates of alloys. And the Cr deposits using method 1 and 2 are extremely difficult to be cleaned. Thus, method 4 is invented to absorb the evaporated Cr species and alleviate the Si deposits on the alloy surface and the chemical interaction. However, the backflow of the sodium species on the alloy surface results in the breakaway oxidation of the alloys, thus contributing to the abnormal high Cr evaporation rates. Based on these problems, method 3 with thin alumina tube is applied to prevent the backflow of the sodium species which evaluates the Cr evaporation rates more accurate. However, there is also a problem that some solid solution formed in the high temperature region cannot be avoided.

7.5.3 Cross-sectional images

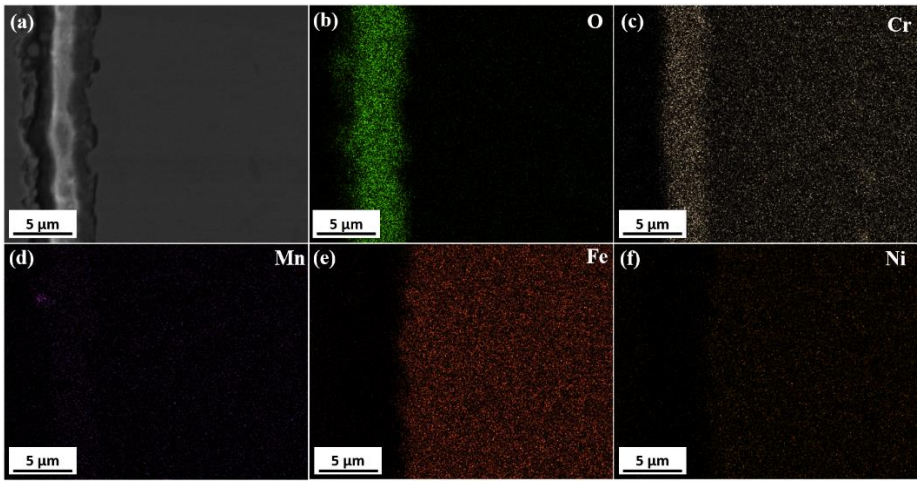

Figure 47. SEM/EDX mapping of the cross-sectional of the 310S tested for 500 h in air + 10% H_2O at 800 °C in sodium carbonate coated thin alumina tube.

In order to analyze the chemical composition across the depth of the oxide scales, a cross section of alloy 310S tested for 500 h in air + 10% H_2O at 800 °C was characterized by SEM/EDS mapping. It can be seen from **Figure 47**. that the outmost oxide layer which is about 2 µm thickness and the inner oxide layer which is about 2 µm thickness are assigned to $(Cr, Mn)_3O_4$ spinel and Cr_2O_3, respectively. This result is consistent with

the XRD results described in **Figure 44**. In addition, plenty of voids can be easily observed at the interface of the oxide scales and the alloy substrate. The highest chromium evaporation rate of alloy 310S among the three tested alloys at 800 °C is assigned to the formation of a chromium-rich scale which can react with oxygen and water to form chromium oxyhydroxide. The alloy addition of manganese in alloy 310S contributed to the formation of the outmost layer of (Cr, $Mn)_3O_4$ spinel, whereas the inner scale was Cr_2O_3. There were researchers reporting that the presence of the protective (Cr, $Mn)_3O_4$ spinel can lower the chromium evaporation by an order of magnitude when compared to pure chromia [63, 120]. However, it can be seen from **Figure 45a, 45b and 47** that the outmost (Cr, $Mn)_3O_4$ spinel layer not covering the entire alloy surface and the loose (Cr, $Mn)_3O_4$ spinel layer resulted in the exposure of Cr_2O_3 to humid air for alloy 310S which accounted for the higher chromium evaporation rate. However, the cross-sectional SEM/EDX mapping images in **Figures 48 and 49** show the chemical analysis of oxide scales formed on OC4 and OC5 tested for 500 h in air + 10% H_2O at 800 °C. It can be seen that the outmost layer is enriched in Fe, Cr, Mn and Al and the inner layer is a continuous alumina layer for OC4 and OC5. Moreover, there are no voids observed at the interface between the oxide scales and the alloy substrate. The continuous alumina layer formed on OC4 and OC5 remains dense and uniform in thickness of which is about 500nm and 400nm, respectively. The continuous alumina layer can prevent the diffusion of chromium and manganese which contributes to lower Cr evaporation rates which is consistent with the comparison of Cr evaporation rates in **Figure 42**.

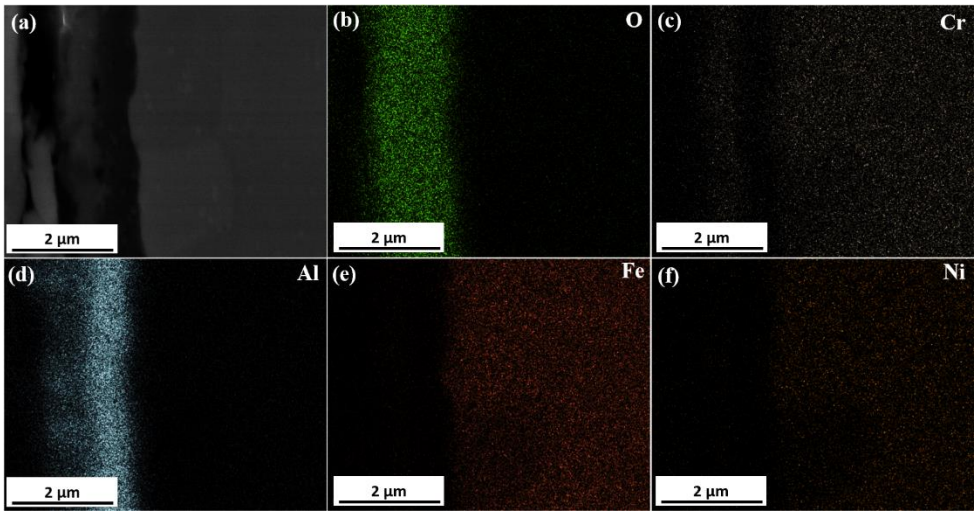

Figure 48. SEM/EDX mapping of the cross-sectional of the OC4 tested for 500 h in air + 10% H_2O at 800 °C in sodium carbonate coated thin alumina tube.

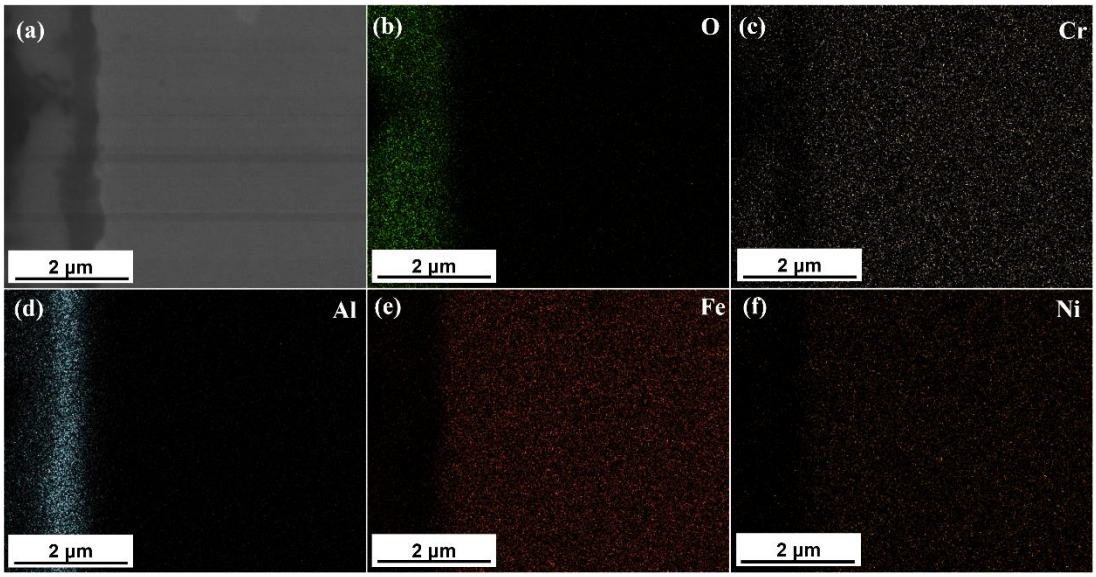

Figure 49. SEM/EDX mapping of the cross-sectional of the OC5 tested for 500 h in air + 10% H_2O at 800 °C in sodium carbonate coated thin alumina tube.

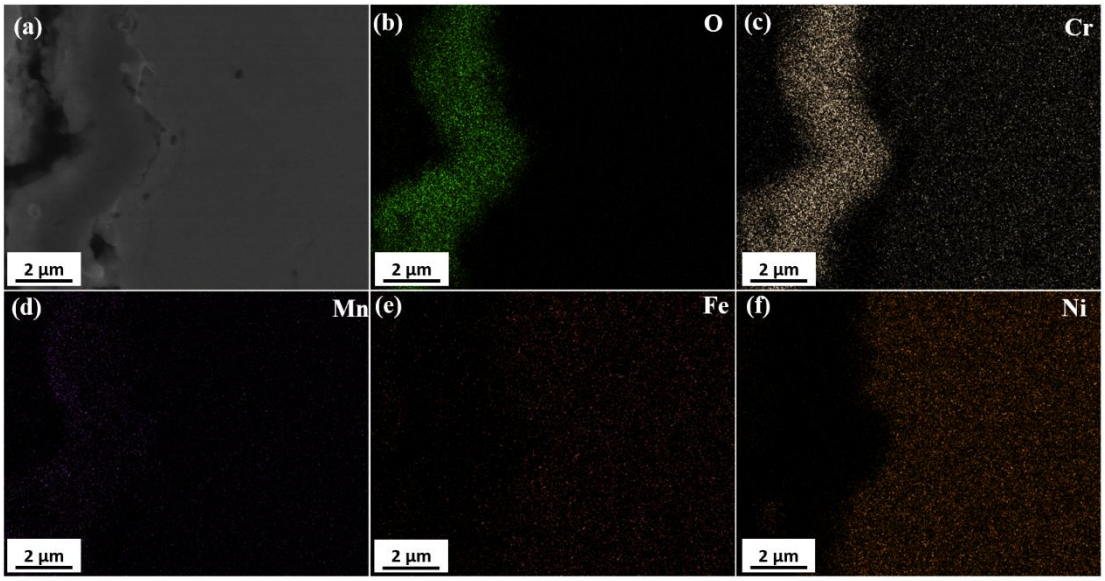

Figure 50. SEM/EDX mapping of the cross-sectional of the 625 tested for 500 h in air + 10% H_2O at 900 °C in sodium carbonate coated thin alumina tube.

The SEM/EDS cross-sectional images of the oxide scales of 625, OC11 and OC11LZ are shown in **Figures 50, 51 and 52**. It can be seen from **Figure 50** that the outmost layer is $(Cr, Mn)_3O_4$ spinel of which thickness is ~500 nm and the inner layer is Cr_2O_3 of which thickness is 2.5 µm. The spallation of the outmost $(Cr, Mn)_3O_4$ spinel layer and the direct exposure of Cr_2O_3 inner layer to humified air reasonably accounted for the high Cr evaporation rate of 625 in these three alloys tested at 900 °C. Whereas for the OC11 and OC11LZ, an outmost layer enriched in Fe, Cr, Mn and Al, an intermediate layer consisted of Cr_2O_3 and an inner continuous

Al_2O_3 layer could be observed from the SEM/EDS mapping analysis (**Figure 51 and 52**). The layers of Cr_2O_3 and Al_2O_3 confirm by XRD (**Figure 44**) are also consistent with the reported nature of the oxide scales developed on a similar steel in steam [19,22]. However, they also reported that vapor environment could contribute to the spallation of the alumina layer which has not been observed in this paper.

The formation of thick Cr_2O_3 layer which can react with oxygen and water to form chromium oxyhydroxide (**Figure 47 and 50**) accounts for the higher chromium evaporation of alloy 310S and 625 that OC4 and OC5 at 800 °C and OC11 and OC11LZ at 900 °C. The formation of a continuous alumina layer on AFA alloys can effectively decrease the diffusion of chromium, thus decreasing the Cr evaporation rates of AFA alloys which makes it potential for the application of BoP components in SOFC industry.

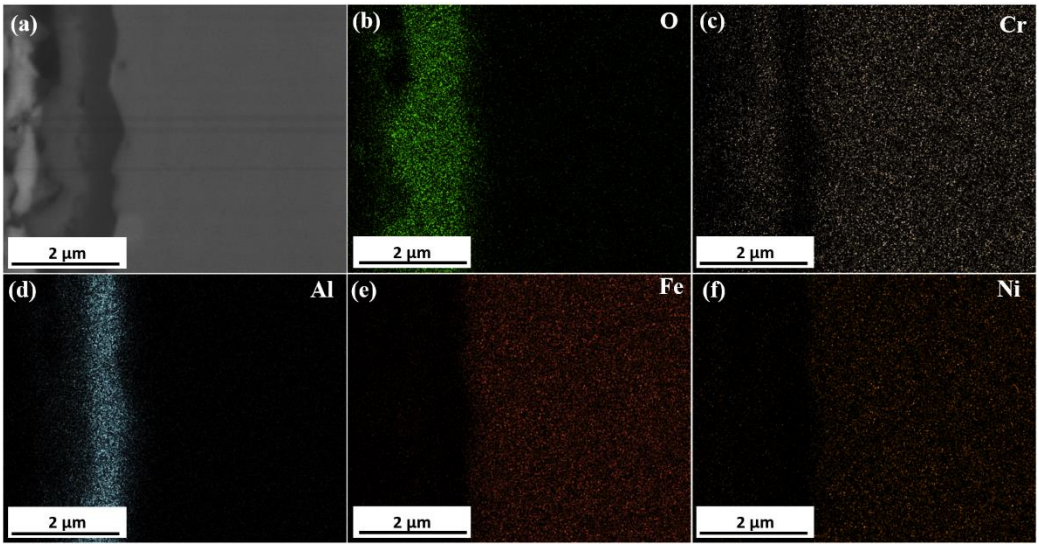

Figure 51. SEM/EDX mapping of the cross-sectional of the OC11 tested for 500 h in air + 10% H_2O at 900 °C in sodium carbonate coated thin alumina tube.

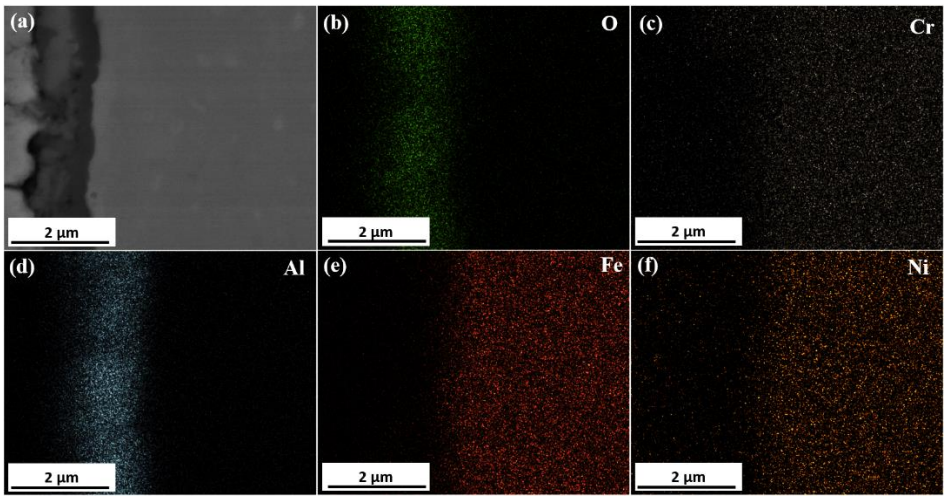

Figure 52. SEM/EDX mapping of the cross-sectional of the OC11LZ tested for 500 h in air + 10% H_2O at 900 °C in sodium carbonate coated thin alumina tube.

7.6. Summary

An optimal method is invented to accurately evaluate the Cr evaporation rates of different alloys which can exclude the effect of Si, Na deposition and the reaction between evaporated Cr gaseous species and used tubes. In this paper, Cr evaporation rates of AFA alloys are compared to benchmark Cr_2O_3 forming alloys at 800-900 °C in air with 10% H_2O for 500 h and the problems of these methods have been discussed. The main conclusions of this study are listed as follows:

(1) Cr evaporation rates of AFA alloys were lower than Cr_2O_3 forming 310S and 625 alloys at 800-900 °C operation with all four methods.

(2) Surface Si contamination on all samples was observed after 500 h operation at 800-900 °C in air with 10% H_2O using quartz furnace (method 1) tube in our previous study. Although it did not appear to significantly impact Cr evaporation behavior for short-term exposure, however, a great number of Si deposits could be observed after 4500 h operation using quartz tube in this paper which could significantly alter the evaporated Cr species quantities.

(3) Surface Na pollution on all samples (method 4) and chemical interaction between gaseous Cr species and alumina tube (method 2) which could result in the lower Cr evaporation rates of alloys were observed after 500 h exposure.

(4) Si contamination, Na pollution and the chemical interaction were solved using the sodium carbonate coated thin alumina tubes (method 3) which could accurately evaluate the Cr evaporation rates of alloys.

Chapter 8 Cr-poisoning of the SOFC Cathode Assembled with AFAs

The rapid development of solid oxide fuel cells (SOFCs) has attracted much attention over the past decades for their lack of pollution, their versability as energy sources and their high fuel to power efficiency [2, 202-204]. In general, metallic interconnects (MICs) and balance of plant (BoP) components are used to assemble multiple single cells as a stack to meet the power density requirements[4, 24, 121]. However, not only do the MICs configuration contribute to the stack deterioration, but the evaporated gaseous chromium (Cr) species from MICs and BoP components gradually degrade the stack performance during the operation [119, 127, 183].

Cr poisoning of SOFC cathodes has been studied for decades [13, 23-25, 144, 183, 205-208], however, the mechanism still remains elusive. An electrochemical mechanism was proposed by Hilpert *et al.* [13]. The Cr poisoning was attributed to the electrochemical reduction of hexavalent Cr species to Cr_2O_3 in competition with O_2 reduction and the active sites were blocked by the Cr_2O_3 resulting in drastic degradation. However, Jiang *et al.* [25, 206, 207] believed that the segregation of manganese ions (Mn^{2+}) and strontium ions (Sr^{2+}) under cathodic polarization or high temperatures could be attributed to the driving forces for Cr deposition in the lanthanum strontium manganite (LSM) and lanthanum strontium cobalt ferrite (LSCF) systems, respectively. Different nuclei formed by different metal ions and gaseous Cr species would facilitate the deposition of Cr_2O_3 thus poisoning the cathodes. Moreover, the loss contribution to LSM and LSCF systems were investigated using electrochemical impedance spectroscopy (EIS) by Zhen and Lee [181, 209], respectively. Zhen [181] attributed the high-frequency arc and low-frequency arc to migration of oxygen ions from triple-phase boundary (TPB) to yttria-stabilized zirconia (YSZ) and dissociative adsorption and diffusion of oxygen on LSM, respectively. The Adler-Lane-Steele model was applied to extract the contributions of the self-diffusion coefficient and surface exchange rate constant to the Cr poisoning on LSCF cathode [209]. However, the overlap in impedances from different processes in actual electrochemical cells caused limited

resolution of EIS spectra and uncertainty in using an equivalent circuit model (ECM) which may resulting in imprecise interpretations. The distribution of relaxation times (DRT) analysis has been developed to overcome these shortcomings [210]. Sumi *et al.* [211, 212] applied DRT analysis to investigate the effects of anode microstructure on the performance and the degradation mechanisms of anode-supported microtubular SOFCs. Ivers-Tiffée *et al.* [213-219] studied the effect of temperature and fuel ratio to identify the performance-limiting processes in the anode-supported SOFCs using DRT and the corresponding modeling was also discussed. Moreover, DRT was also used in half-cell to study the effect of polarization on cell degradation [220]. A 11% decrease of power density of anode supported cell (ASC) coupled with Crofer22APU MIC was observed after operated at a constant current load of 500 mA cm^{-2} for ~280 h by Kornely [221] *et al.* and the details of Cr poisoning from MIC were analyzed by DRT.

Cr poisoning of SOFC cathodes is one of the most intractable problems that needs to be solved. Although several effective coatings have been developed to reduce the Cr evaporation from MICs and balance of plant (BoP) components, the valves and elbows of pipes cannot be effectively protected by coatings [59, 131, 194, 222-224]. In terms of this problem, Al_2O_3-forming austenitic (AFA) stainless steels could be applied to replace the conventional BoP components used in SOFC stacks [89, 225, 226]. Cr poisoning of ASCs from MIC was investigated by Kornely, however the effect of BoP component on the Cr poisoning of ASCs has not been reported. Therefore, in this chapter, we investigated the Cr deposition of anode-supported cell under a constant current density of 0.5 A cm^{-2} at 800 °C with AFA alloys commercial alloys compared with commercial alloys. In addition, the anodic and cathodic processes are deconvoluted by distribution of relaxation times (DRT) method which are comprehensively discussed.

8.1 Galvanostatic test

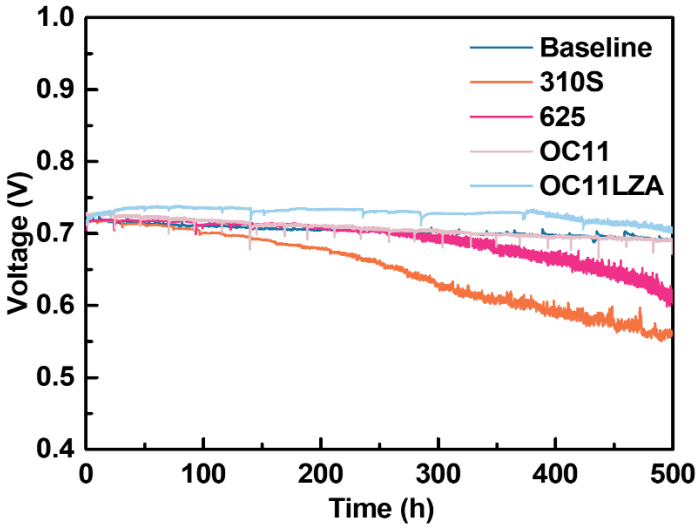

Figure 53. Voltage versus time curves of ASC during the galvanostatic test at 0.5 A/cm^2 and 800 °C w/wo alloys.

Figure 53 shows the time course of cell voltage during the galvanostatic test at 500 mA cm^{-2} of the ASC in the presence of different alloys at the cathode region. During the 500-hour test the cell voltage decreases about 4.4% ($V_{baseline,\ t = 0\ h}$ = 724 mV, $V_{baseline,\ t = 500\ h}$ = 692 mV) in the absence of alloys. However, a considerable decrease of 22.1 % ($V_{310S,\ t = 0\ h}$ = 718 mV, $V_{310S,\ t = 500\ h}$ = 559 mV) and 12.1 % ($V_{625,\ t = 0\ h}$ = 705 mV, $V_{625,\ t = 500\ h}$ = 620 mV) was determined in the presence of 310S and 625 alloys, respectively. Gaseous Cr species evaporated from chromia-forming 310S and 625 are believed to cause the significant deterioration in the performance of the ASC cells. However, a slight decrease of 5.1 % ($V_{OC11,\ t = 0\ h}$ = 727 mV, $V_{OC11,\ t = 500\ h}$ = 690 mV) and 1.5 % ($V_{OC11LZA,\ t = 0\ h}$ = 712 mV, $V_{OC11LZA,\ t = 500\ h}$ = 701 mV) was determined in the presence of OC11 and OC11LZA alloys, respectively. The lower degradation rates of cells tested with alumina-forming alloys are attributed to the continuous alumina layer formed on the alumina-forming alloys which inhibits the outward diffusion of Cr from the alloy matrix.

8.2 Electrochemical analysis

In order to clarify the physical origins of the performance degradation caused by Cr poisoning from different alloys, EIS were measured at open circuit at periodic intervals during the galvanostatic test. It is well known

that the ohmic resistance (Ro: limiting Z' value at the highest frequency) and the polarization resistance (Rp: difference between Ro and the limiting Z' value at the lowest frequency) are influenced by the presence of different alloys. There is only slight difference in R_o for ASC tested w/wo alloys. However, significant differences in R_p and the degradation rate can be assigned to the presence of different alloys as discussed below.

8.2.1 Baseline

Firstly, all EIS data sets have been massaged to eliminate the noise effect, anomalous high frequency behavior and the faulty data points. The inductance was estimated by plotting log(-Z") vs log f at the highest frequencies (10 kHz to 100 kHz) and changing the inductance (L) value until the data points are linear.

Secondly, DRT spectra were calculated in Excel using the method described by Schichlein et al. [210]. This method is based on Fourier transforms and requires that the Z" data be extrapolated to very high and very low frequencies. The extrapolation is again based on the assumed linearity of log(-Z") vs log f at the highest and lowest frequencies in the data sets. Take baseline data sets as an example, the Nyquist plots of the smoothed impedance spectra, the calculated corresponding DRT spectra and the calculated R_o and R_p resistance change were shown in **Figure 54**. Based on the Nyquist plots (**Figure 54a**), the ohmic resistance is almost unchanged during the 500 h test. However, the polarization resistance has a slight increase during the 500 h operation time. The DRT spectra calculated from the EIS spectra are shown in **Figure 54b** in which three main DRT peaks can be observed for the ASCs. We assume that each peak corresponds to a distinct process in the mechanisms of the SOFC. We also recognize that DRT peaks at the frequency limits of the EIS data are still subject to minor artifacts caused by inductance (high frequency) and noise (low frequency) after the massage. It is seen that the quantities and shift of peaks distributed at low frequency (0.1-5 Hz) have no irregularity which can be attributed to gas diffusion. The peak P_1 assigned to mixed solid-state oxygen diffusion and reaction in the cathode and peak P_2 assigned to chemisorption of oxygen on the cathode are generally observed at 100-2000 Hz and 8-20 Hz, respectively [227]. **Table 6** lists the physical origin of DRT peaks for ASCs. It is seen that the quantities and shift of peaks (P_3) distributed at low frequency (0.1-5 Hz) have no irregularity which can be attributed to the remaining noise in the EIS data. Moreover, the peaks P_1 and P_2

slightly change with the prolonged operation time, suggesting that the cathode properties are nearly constant in the absence of alloy. **Figure 54c** shows the variation of calculated R_o and R_p resistances versus time during galvanostatic test. Both R_o and R_p have a slight increase ($R_{o\ baseline,\ t = 0\ h}$ = 0.148 Ω·cm^2, $R_{o\ baseline,\ t = 500\ h}$ = 0.155 Ω·cm^2, $R_{p\ baseline,\ t = 0\ h}$ = 1.048 Ω·cm^2, $R_{p\ baseline,\ t = 500\ h}$ = 1.113 Ω·cm^2). The details of the variation of R_o and R_p during galvanostatic test are summarized in **Table 7**.

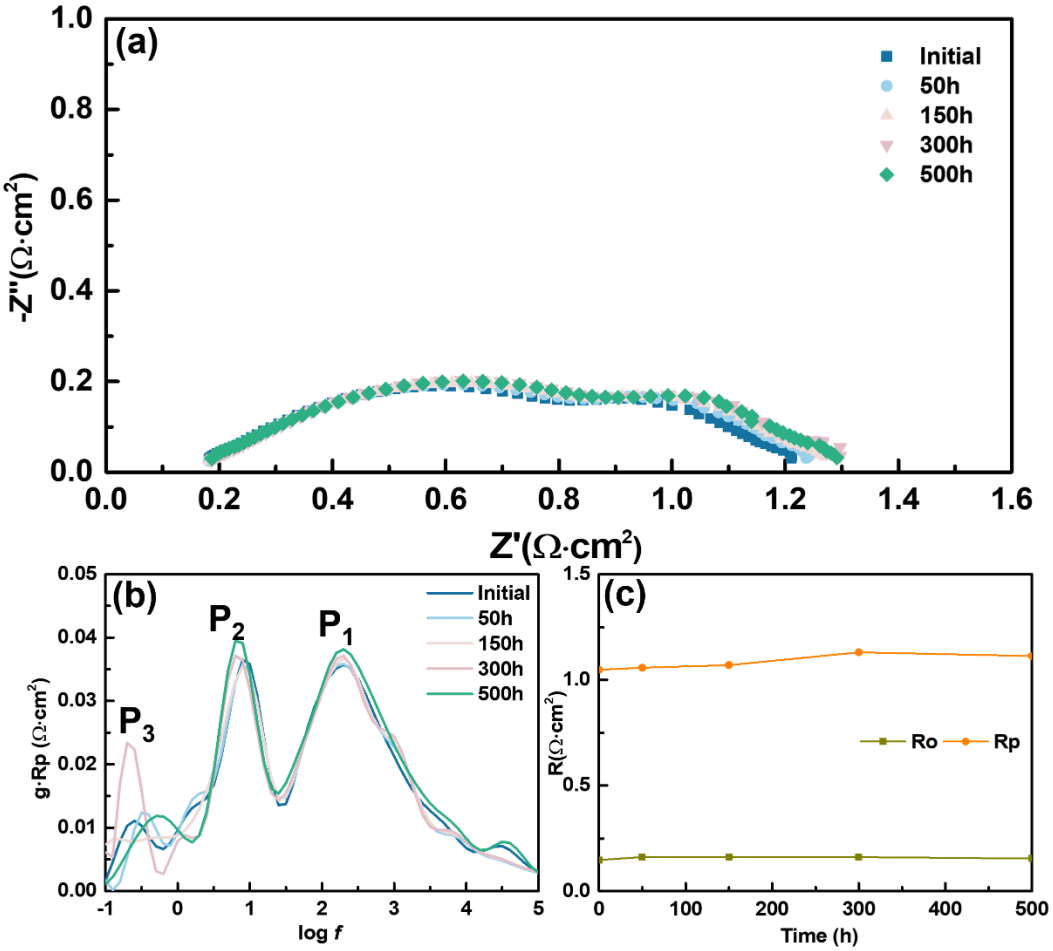

Figure 54 (a) Nyquist plots of the impedance spectra, (b) the corresponding DRT spectra and (c) calculated R_o and R_p resistance variation versus time curves under OCV during the galvanostatic test at 0.5 A/cm^2 under 800 °C for cell tested without alloy.

Table 6 Proposed physical origin of each DRT peak for anode-supported cells coupled with various alloys

Process	Frequency (Hz)	Electrode	Physical origins
P_1	100-2000	cathode	Mixed solid-state Oxygen diffusion and reaction in the cathode
P_2	8-20	cathode	Chemisorption of oxygen on the cathode
P_3	0.1-5	cathode	Gas diffusion losses within the Ni/YSZ anode and LSCF/GDC cathode substrate

Table 7 Calculated R_o and R_p resistance variation versus time for anode-supported cells with and/or without alloys.

	baseline		310S		625		OC11		OC11LZA	
Time(h)	R_o	R_p	R_o	R_p	R_o	R_p	R_o	R_p	R_o	R_p
0	0.148	1.048	0.1969	1.27	0.2181	1.307	0.141	1.048	0.2	1.184
50	0.162	1.058	0.1833	1.234	0.1830	1.337	0.163	1.157	0.205	1.14
150	0.162	1.07	0.1909	1.281	0.1936	1.521	0.165	1.291	0.202	1.171
300	0.162	1.131	0.22	1.289	0.2084	1.594	0.169	1.449	0.205	1.203
500	0.155	1.113	0.2598	1.421	0.2717	1.702	0.175	1.567	0.204	1.217

Thirdly, based on the DRT spectra of baseline above, three distributed elements are used to model the baseline data sets. The distributed elements for the two lower frequency peaks are modeled by a parallel RQ circuit, where R is a resistance and Q is a constant phase element (CPE). The admittance of a CPE is given by:

$$Y = T(j\omega)^P$$

Where T is a magnitude, j is the square root of -1, $\omega = 2\pi f$, and P is an exponent. When P = 1, the CPE is a pure capacitance (T = capacitance in farads). Generally fitted P values are less than 1 and the units of T become complicated. And the shape of DRT peak at 200 Hz characteristic of a Gerischer impedance element which has a steeper slope on the low frequency side than on the high frequency side. The Gerischer impedance is calculated with the following equation:

$$Z = R/((1 + j\omega T)^P)$$

A pure Gerischer impedance has P = 0.5. A modified Gerischer impedance allows P to deviate from 0.5. This impedance can be calculated in ZView software as a Distributed Element type 6 (Havriliak-Negami) in which the U value is fixed to 1.

The proposed equivalent circuit model is shown in **Figure 55**. L_1 is the inductance and R_0 is the series resistance R_o.

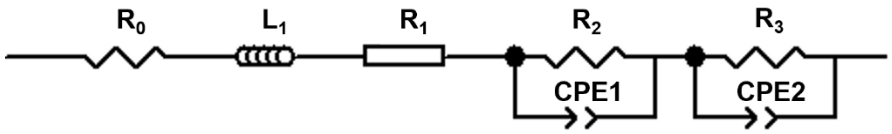

Figure 55 Baseline equivalent circuit model

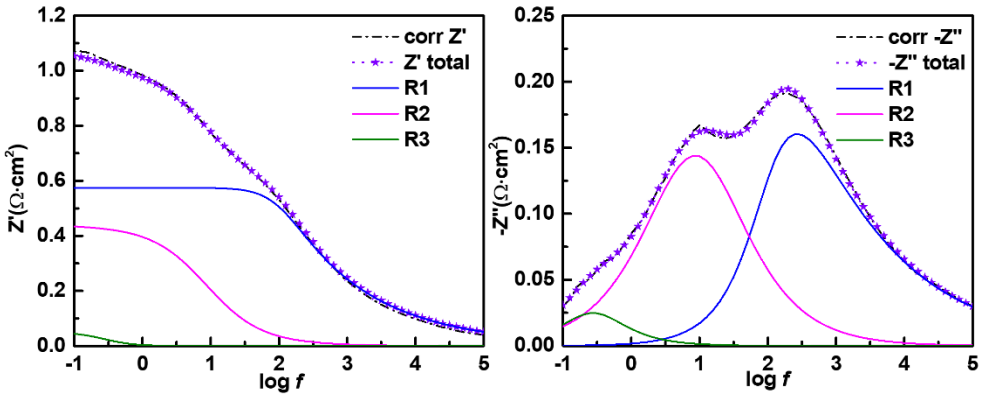

Figure 56 Fitted real parts and imaginary parts verses log f plots of baseline initial data

The impedances of each element are fitted by using a spreadsheet program. Taking baseline initial data as an example, the fitted real parts and imaginary parts verses log f plots are demonstrated in **Figure 56**. As shown in the plots, both the real parts and imaginary parts are fitted well to the corrected data. Similar as the baseline initial data, 310S, 625 and OC11 data sets are fitted in the same way. For OC11LZA data sets, the shape of the high frequency arc in the DRT spectra is more symmetrical, therefore we used another equivalent circuit model to fit the real parts and imaginary parts. The fitted polarization resistance of each element as a function of time curve of baseline data sets is shown in **Figure 57**. Moreover, the whole fitted parameters of baseline data sets are listed in **Table 8**.

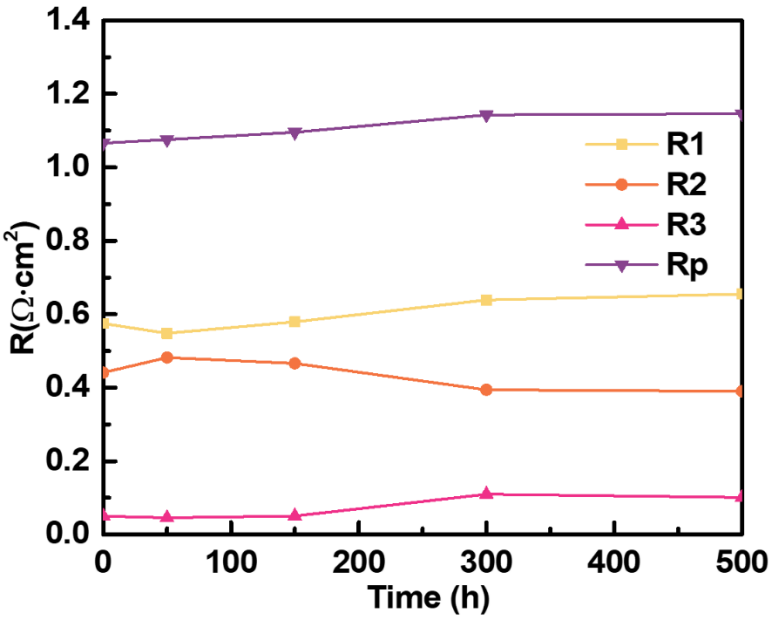

Figure 57 Fitted polarization of each element as a function of time curve of baseline data sets.

Table 8 Fitted parameters of baseline data sets.

	Elements	Units	Time (h)				
			0	50	150	300	500
baseline	L_1	H	1.16E-07	7.00E-09	7.60E-09	9.20E-09	1.20E-07
	R_o	$\Omega \cdot cm^2$	0.141	0.15	0.148	0.146	0.125
	R1	$\Omega \cdot cm^2$	0.575	0.548	0.579	0.639	0.655
	T1		0.00142	0.001285	0.00134	0.00149	0.001525
	P1		0.336	0.358	0.353	0.352	0.325
	R2	$\Omega \cdot cm^2$	0.441	0.482	0.466	0.394	0.39
	T2		0.119	0.122	0.114	0.0961	0.101
	P2		0.737	0.703	0.7325	0.818	0.805
	R3	$\Omega \cdot cm^2$	0.0502	0.0456	0.0505	0.11	0.101
	T3		11.55	12.1	12.2	5.86	5.18
	P3		0.995	0.94	1	0.832	0.73
	R_p	$\Omega \cdot cm^2$	1.066	1.076	1.096	1.143	1.146

Fourthly, as shown in **Figure 57**, the fitted polarization resistance of the three elements only has a slight change after the galvanostatic test which indicates that the cathode processes are almost unaffected in the absence of alloy.

8.2.2 Commercial alloys

Figure 58 shows the Nyquist plots, the corresponding DRT spectra and calculated R_o and R_p resistances variation versus time curves under OCV during the galvanostatic test at 0.5 A/cm^2 under 800 °C for 310S. R_o

exhibits a slight increase ($R_{o\ 310S,\ t = 0\ h}$ = 0.197 Ω·cm^2, $R_{o\ 310S,\ t = 500\ h}$ = 0.260 Ω·cm^2), while R_p exhibits a significant increase ($R_{p\ 310S,\ t = 0\ h}$ = 1.270 Ω·cm^2, $R_{p\ 310S,\ t = 500\ h}$ = 1.421 Ω·cm^2) (**Figure 58c and Table 7**). Three main DRT peaks are calculated for the ASCs tested with 310S (**Figure 58b**). The peak assigned to the mixed solid-state oxygen diffusion and reaction in the cathode (P_1) and the peak assigned to the mixture of cathode diffusion and anode processes (P_2) are observed to increase during the test. As noted in the introduction, the degradation is attributed to the formation of gaseous Cr species from which deposit on the cathode, thus causing the deterioration. Some irregularities are observed at the low frequency region (P_{diff}) which is resulted from the data noise. It can be seen more clearly from **Figure 59** that polarization resistances (R_3) due to gas diffusion is small during the test and their contribution to the entire polarization resistance is much lower than R_{DE1} and R_2. The R_1 that related to the mixed solid-state oxygen diffusion and reaction in the cathode increases by 5.74% ($R_{1\ 310S,\ t = 0\ h}$ = 0.488 Ω·cm^2, $R_{1\ 310S,\ t = 500\ h}$ = 0.516 Ω·cm^2) and R_2 that related to the mixture of cathode diffusion and anode processes increases by 40.58% ($R_{2\ 310S,\ t = 0\ h}$ = 0.621 Ω·cm^2, $R_{2\ 310S,\ t = 500\ h}$ = 0.873 Ω·cm^2). The whole fitted parameters with different durations are listed in **Table 9**. Both intensities of P_1 and P_2 are increased with time which suggests that cathode processes are both influenced by gaseous Cr species from 310S. It is worth noting that P_2 is more influenced by Cr poisoning than P_1.

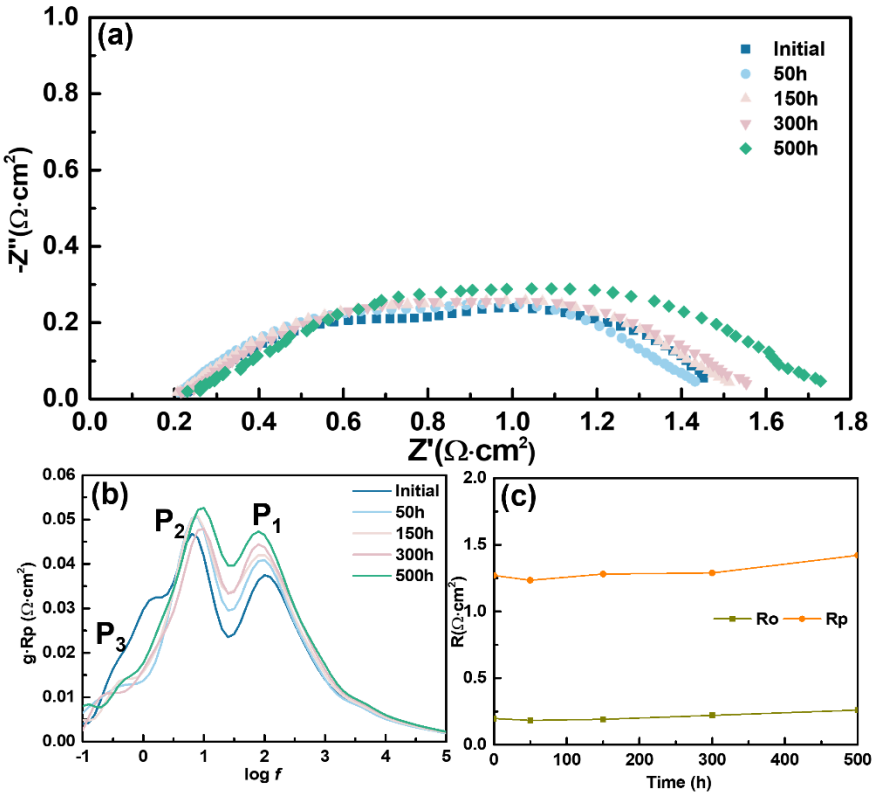

Figure 58 (a) Nyquist plots of the impedance spectra, (b) the corresponding DRT spectra and (c) calculated R_o and R_p resistance variation versus time curves under OCV during the galvanostatic test at 0.5 A/cm^2 under 800 °C for cell tested with 310S.

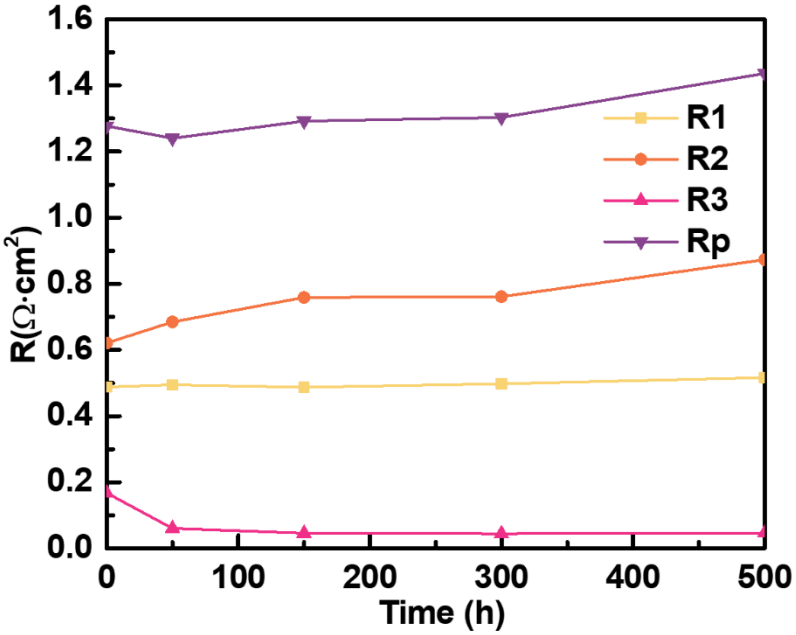

Figure 59 Fitted polarization of each element as a function of time curve of 310S data sets.

Table 9 Fitted parameters of 310S data sets.

	Elements	Units	Time (h)				
			0	50	150	300	500
310S	L_1	H	1.16E-07	7.00E-09	7.60E-09	9.20E-09	1.20E-07
	R_o	$\Omega \cdot cm^2$	0.141	0.15	0.148	0.146	0.125
	R1	$\Omega \cdot cm^2$	0.575	0.548	0.579	0.639	0.655
	T1		0.00142	0.001285	0.00134	0.00149	0.001525
	P1		0.336	0.358	0.353	0.352	0.325
	R2	$\Omega \cdot cm^2$	0.441	0.482	0.466	0.394	0.39
	T2		0.119	0.122	0.114	0.0961	0.101
	P2		0.737	0.703	0.7325	0.818	0.805
	R3	$\Omega \cdot cm^2$	0.0502	0.0456	0.0505	0.11	0.101
	T3		11.55	12.1	12.2	5.86	5.18
	P3		0.995	0.94	1	0.832	0.73
	R_p	$\Omega \cdot cm^2$	1.066	1.076	1.096	1.143	1.146

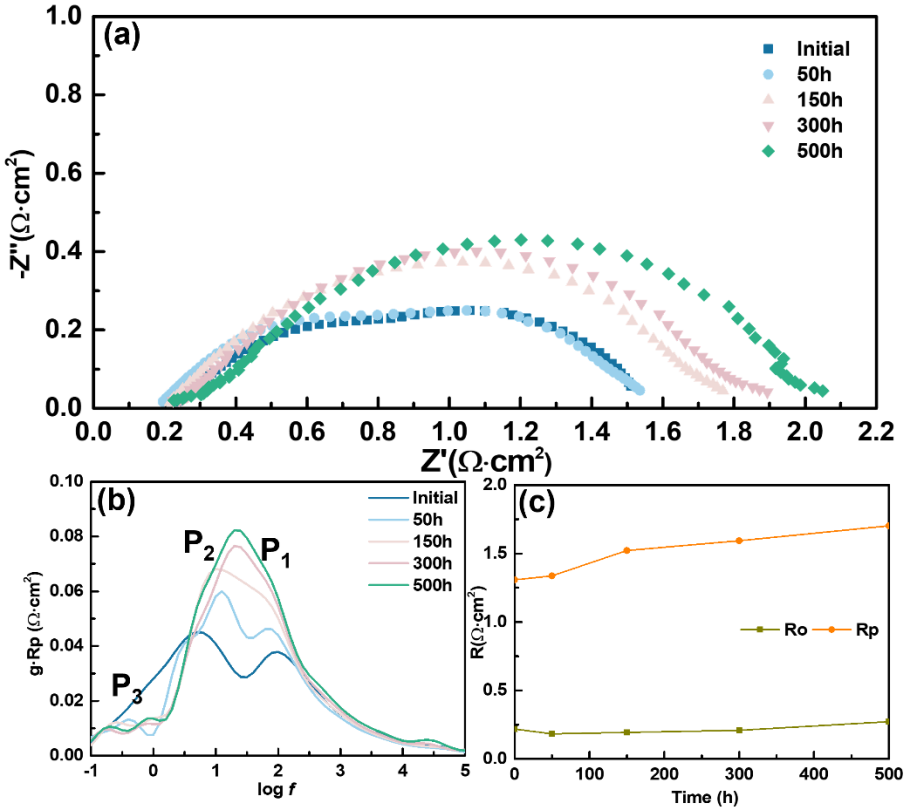

Figure 60 (a) Nyquist plots of the impedance spectra, (b) the corresponding DRT spectra and (c) calculated R_o and R_p resistance variation versus time curves under OCV during the galvanostatic test at 0.5 A/cm^2 under 800 °C for cell tested with 625.

Figure 60 shows the Nyquist plots, the corresponding DRT spectra and calculated R_o and R_p resistances variation versus time curves under OCV during the galvanostatic test at 0.5 A/cm^2 under 800 °C for 625. Similar as 310S, R_o of 625 exhibits a slight increase ($R_{o\ 310S,\ t=0\ h}$ = 0.197 Ω·cm^2, $R_{o\ 310S,\ t=500\ h}$ = 0.260 Ω·cm^2, $R_{o\ 625,\ t=0\ h}$ = 0.218 Ω·cm^2, $R_{o\ 625,\ t=500\ h}$ = 0.272 Ω·cm^2), while R_p exhibits a significant increase ($R_{p\ 310S,\ t=0\ h}$ = 1.270 Ω·cm^2, $R_{p\ 310S,\ t=500\ h}$ = 1.421 Ω·cm^2, $R_{p\ 625,\ t=0\ h}$ = 1.307 Ω·cm^2, $R_{p\ 625,\ t=500\ h}$ = 1.702 Ω·cm^2) (**Figure 60c and Table 7**). Three main DRT peaks are calculated for the ASCs tested with 625 (**Figure 60b**). Peak P_1 and peak P_2 are also observed to increase during the test. It is worth noting that the strong overlap of P_1 and P_2 appears to increase with time, i.e., the peak frequencies converge (**Figure 60b**). The increase in area is consistent with the interpretations that these peaks are associated with the cathode and that the alloy is causing severe degradation of the cathode. Some irregularities are also observed at the low frequency region (P_3) which is resulted from the data noise. Fitted resistance of each process variation versus time curves are shown in **Figure 61**. R_1 increases by 13.30% ($R_{1\ 625,\ t=0\ h}$ = 0.534 Ω·cm^2, $R_{1\ 625,\ t=500\ h}$ = 0.605 Ω·cm^2), and R_2 increases by 44.16% ($R_{2\ 625,\ t=0\ h}$ = 0.711 Ω·cm^2, $R_{2\ 625,\ t=500\ h}$ = 1.025 Ω·cm^2). The whole fitted parameters

with different durations are listed in **Table 10**. Both intensities of P_1 and P_2 are increased with time which suggests that cathode processes are both influenced by gaseous Cr species from 625 and P_2 is more influenced by Cr poisoning than P_1. It is worth noting that the higher degradation rate of 625 than 310S is attributed to the larger R_p increase during the test.

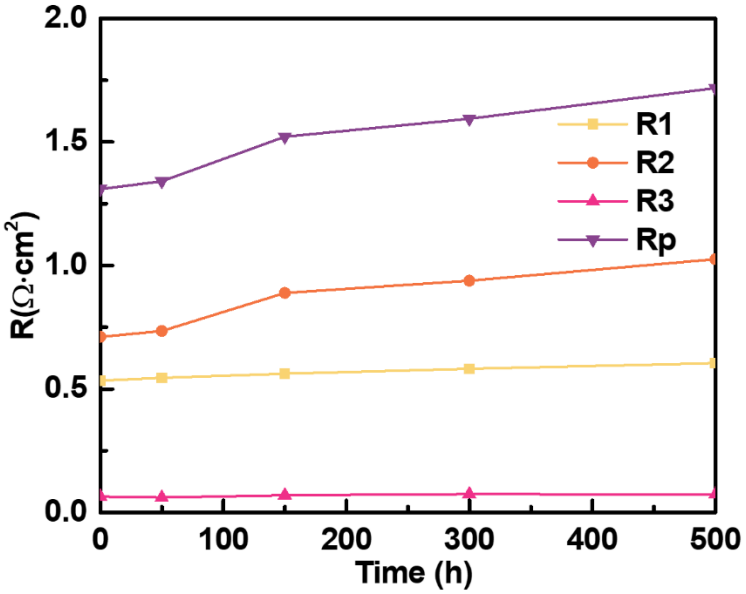

Figure 61 Fitted polarization of each element as a function of time curve of 625 data sets.

Table 10 Fitted parameters of 625 data sets.

	Elements	Units	Time (h)				
			0	50	150	300	500
625	L_1	H	1.16E-07	7.00E-09	7.60E-09	9.20E-09	1.20E-07
	R_o	$\Omega \cdot cm^2$	0.141	0.15	0.148	0.146	0.125
	R1	$\Omega \cdot cm^2$	0.575	0.548	0.579	0.639	0.655
	T1		0.00142	0.001285	0.00134	0.00149	0.001525
	P1		0.336	0.358	0.353	0.352	0.325
	R2	$\Omega \cdot cm^2$	0.441	0.482	0.466	0.394	0.39
	T2		0.119	0.122	0.114	0.0961	0.101
	P2		0.737	0.703	0.7325	0.818	0.805
	R3	$\Omega \cdot cm^2$	0.0502	0.0456	0.0505	0.11	0.101
	T3		11.55	12.1	12.2	5.86	5.18
	P3		0.995	0.94	1	0.832	0.73
	R_p	$\Omega \cdot cm^2$	1.066	1.076	1.096	1.143	1.146

8.2.3 AFA alloys

Figure 62 shows the Nyquist plots, the corresponding DRT spectra and calculated R_o and R_p resistances variation versus time under OCV during the galvanostatic test at 0.5 A/cm^2 under 800 °C for OC11. R_o of OC11 remains nearly constant ($R_{o\ OC11,\ t=0\ h}$ = 0.167 $\Omega \cdot cm^2$, $R_{o\ OC11,\ t=500\ h}$ = 0.176 $\Omega \cdot cm^2$). In addition, the R_p of OC11 only exhibits a slight increase ($R_{p\ OC11,\ t=0\ h}$ = 1.377 $\Omega \cdot cm^2$, $R_{p\ OC11,\ t=500\ h}$ = 1.602 $\Omega \cdot cm^2$) (**Figure 62c and Table 2**). Three peaks can also be observed for AFA alloys in the calculated DRT spectra (**Figure**

62b). Fitted resistance of each process variation versus time curves are shown in **Figure 63,** As before, the peaks P_3 exhibit at most minor changes during the entire galvanostatic test. For ASC tested with OC11, R_1 increases by 2.35% ($R_{1\ OC11,\ t=0\ h} = 0.639\ \Omega{\cdot}cm^2$, $R_{1\ OC11,\ t=500\ h} = 0.654\ \Omega{\cdot}cm^2$) and R_2 increases by 28% ($R_{2\ OC11,\ t=0\ h} = 0.722\ \Omega{\cdot}cm^2$, $R_{1\ OC11,\ t=500\ h} = 0.925\ \Omega{\cdot}cm^2$) which is much lower than 310S and 625, suggesting that cell tested with OC11 is less influenced which is consistence with the galvanostatic test. The whole fitted parameters with different durations are listed in **Table 11**. The lower increase of fitted polarization resistance is attributed to the lower quantities of gaseous Cr species evaporated from the OC11 alloy than that of commercial alloys.

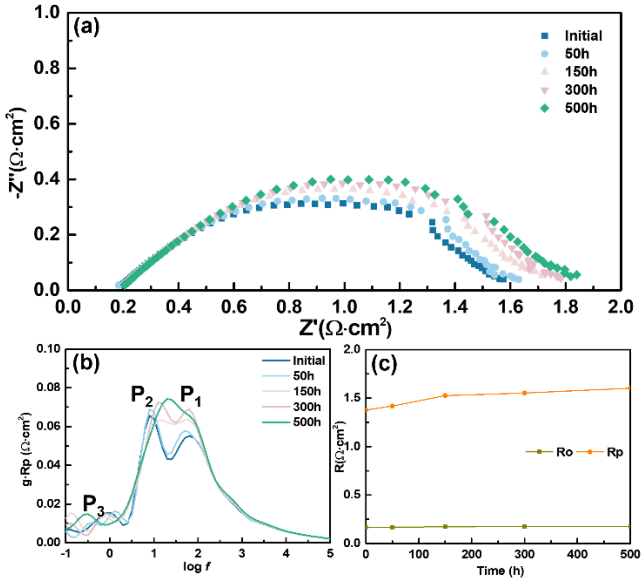

Figure 62 (a) Nyquist plots of the impedance spectra, (b) the corresponding DRT spectra and (c) calculated R_o and R_p resistance variation versus time curves under OCV during the galvanostatic test at 0.5 A/cm^2 under 800 °C for cell tested with OC11.

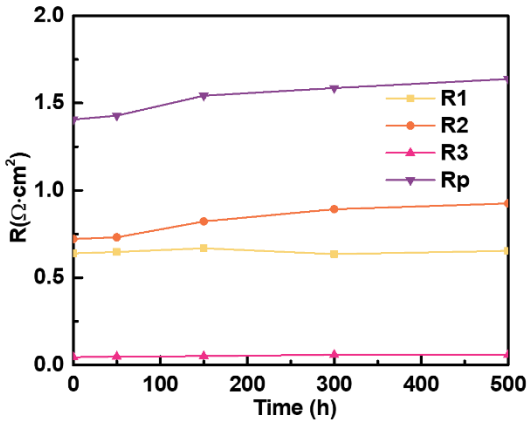

Figure 63 Fitted polarization of each element as a function of time curve of OC11 data sets.

Table 11 Fitted parameters of OC11 data sets.

	Elements	Units	Time (h)				
			0	50	150	300	500
OC11	L_1	H	1.00E-12	1.00E-12	1.00E-12	1.00E-12	1.00E-12
	R_o	$\Omega \cdot cm^2$	0.1663	0.1680	0.1712	0.1734	0.1753
	R1	$\Omega \cdot cm^2$	0.6389	0.6476	0.6687	0.6353	0.6541
	T1		0.003785	0.004232	0.004529	0.006254	0.006311
	P1		0.37	0.38	0.39	0.35	0.35
	R2	$\Omega \cdot cm^2$	0.7223	0.7311	0.8224	0.8922	0.9251
	T2		0.088	0.078	0.075	0.07	0.069
	P2		0.6955	0.6989	0.6599	0.6234	0.6262
	R3	$\Omega \cdot cm^2$	0.045	0.049	0.051	0.059	0.059
	T3		2.745	4.425	4.562	3.253	3.124
	P3		0.75	0.75	0.75	0.53	0.52
	R_p	$\Omega \cdot cm^2$	1.406	1.428	1.542	1.586	1.638

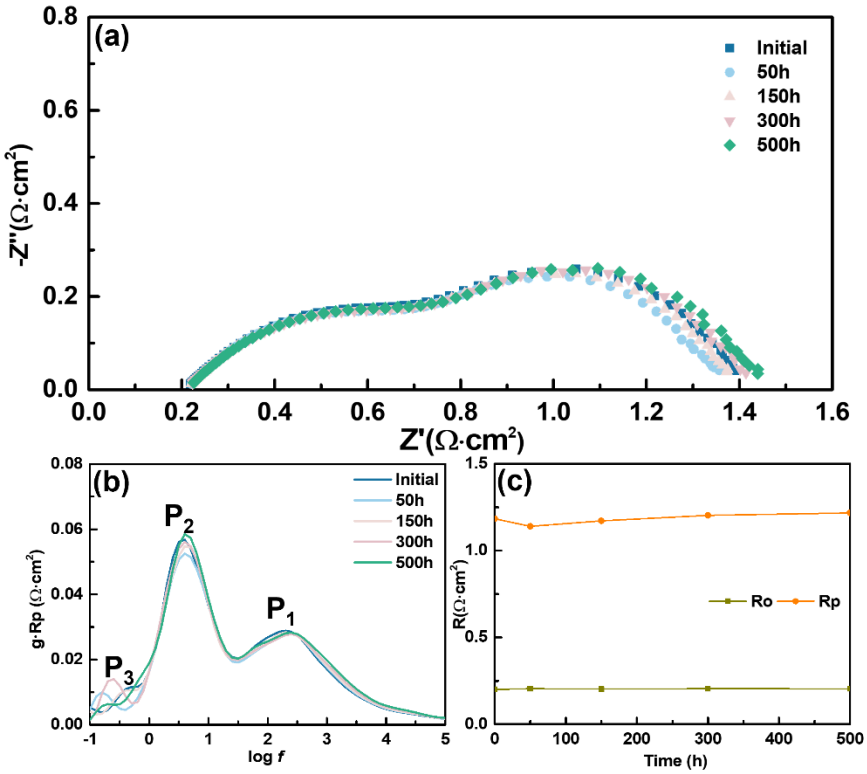

Figure 64 (a) Nyquist plots of the impedance spectra, (b) the corresponding DRT spectra and (c) calculated R_o and R_p resistance variation versus time curves under OCV during the galvanostatic test at 0.5 A/cm^2 under 800 °C for cell tested with OC11LZA.

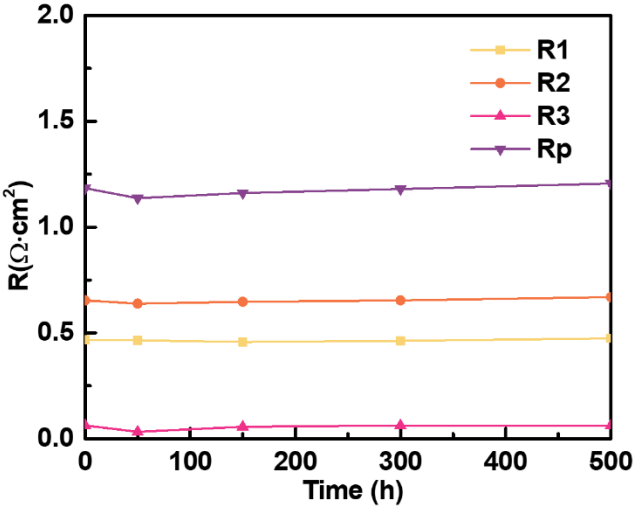

Figure 65 Fitted polarization of each element as a function of time curve of OC11LZA data sets.

Figure 64 shows the Nyquist plots, the corresponding DRT spectra and calculated R_o and R_p resistances variation versus time under OCV during the galvanostatic test at 0.5 A/cm^2 under 800 °C for OC11LZA. R_o of OC11LZA remains nearly constant ($R_{o\ OC11LZA,\ t = 0\ h}$ = 0.200 Ω·cm^2, $R_{o\ OC11LZA,\ t = 500\ h}$ = 0.204 Ω·cm^2). In addition, the R_p of OC11LZA only exhibits a slight increase ($R_{p\ OC11LZA,\ t = 0\ h}$ = 1.184 Ω·cm^2, $R_{p\ OC11LZA,\ t = 500\ h}$

= 1.217 $\Omega \cdot cm^2$) (**Figure 64c and Table 7**). Three peaks are observed for OC11LZA in the calculated DRT spectra (**Figure 64b**). Both the R_1 and R_2 have a slight increase ($R_{2\ OC11LZA,\ t = 0\ h}$ = 0.589 $\Omega \cdot cm^2$, $R_{2\ OC11,\ t = 500\ h}$ = 0.593 $\Omega \cdot cm^2$, $R_{3\ OC11LZA,\ t = 0\ h}$ = 0.589 $\Omega \cdot cm^2$, $R_{3\ OC11LZA,\ t = 500\ h}$ = 0.618 $\Omega \cdot cm^2$), suggesting the evaporated Cr quantities from OC11LZA were quite low. Fitted resistance of each process variation versus time curves are shown in **Figure 65.** The whole fitted parameters with different durations are listed in **Table 12**. The lowest degradation rate of OC11LZA is ascribed to the lowest increase of polarization resistance of each process.

Table 12 Fitted parameters of OC11LZA data sets.

	Elements	Units	Time (h)				
			0	50	150	300	500
OC11LZA	L_1	H	1.00E-12	1.00E-12	1.00E-12	1.00E-12	1.00E-12
	R_o	$\Omega \cdot cm^2$	0.2147	0.2184	0.2163	0.2185	0.2188
	R1	$\Omega \cdot cm^2$	0.4672	0.4651	0.4572	0.4631	0.4741
	T1		0.001855	0.001865	0.001811	0.001755	0.001651
	P1		0.390	0.375	0.370	0.360	0.360
	R2	$\Omega \cdot cm^2$	0.6542	0.6387	0.6471	0.6542	0.6691
	T2		0.106	0.108	0.108	0.101	0.095
	P2		0.7993	0.7893	0.7802	0.7956	0.7945
	R3	$\Omega \cdot cm^2$	0.063	0.033	0.057	0.063	0.0628
	T3		2.745	9.652	3.796	2.123	3.451
	P3		0.8	0.91	0.702	0.651	0.623
	R_p	$\Omega \cdot cm^2$	1.184	1.137	1.161	1.180	1.206

8.3 Cross-sectional mapping of cells tested with alloys

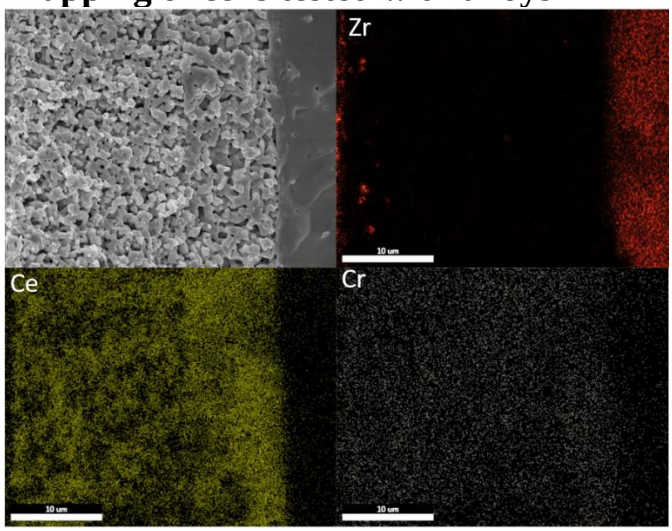

Figure 66 SEM/EDX mapping of the cross-sectional of the anode-supported cell under a constant current density of 0.5 A cm^{-2} at 800 °C with 310S.

In order to analyze the microstructures and Cr distribution at cathode/electrolyte interfaces, cross-sectional images of anode-supported cells tested with 310S, 625, OC11 and OC11LZA under a constant current density of 0.5 A cm^{-2} at 800 °C were characterized by SEM/EDS mapping. In **Figure 66-69**, the LSCF-GDC composite cathode has a porous structure with small grains (1-3 microns) on a barrier GDC layer and a dense YSZ electrolyte. In contrast to the deposition of Cr gaseous species at a LSM cathode/electrolyte interface [54], the deposition of Cr species is distributed over all the cathode region and the interface region for the experiments with the 310S alloy (**Figure 66**) and the 625 alloy (**Figure 67**). However, the signals for chromium in the cathode for OC11 (**Figure 68**) and OC11LZA is much less than the corresponding signals for 310S and 625 (**Figure 69**). These SEM mapping results are consistent with the electrochemical results that discussed before.

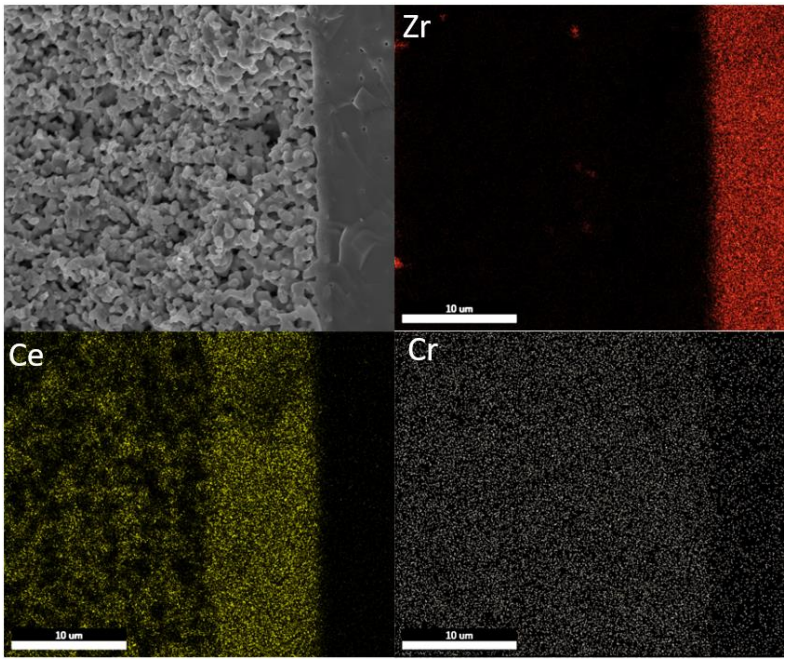

Figure 67 SEM/EDX mapping of the cross-sectional of the anode-supported cell under a constant current density of 0.5 A cm^{-2} at 800 °C with 625.

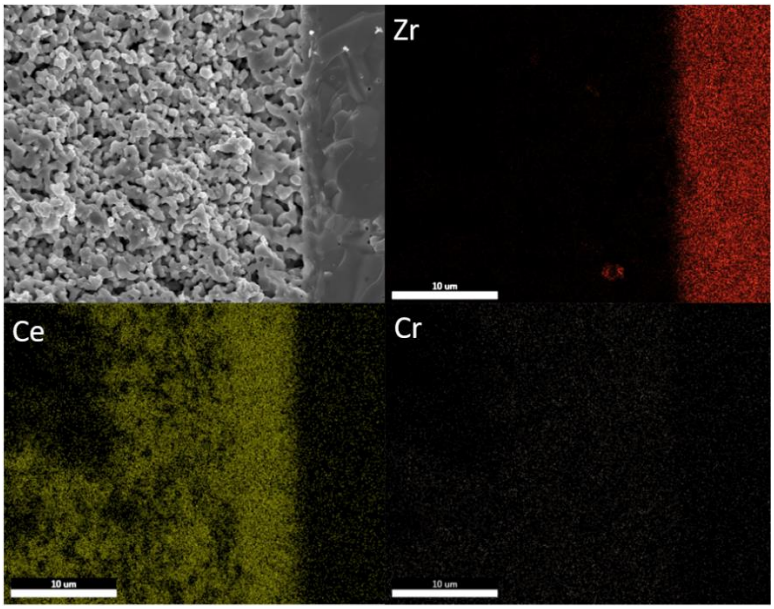

Figure 68 SEM/EDX mapping of the cross-sectional of the anode-supported cell under a constant current density of 0.5 A cm^{-2} at 800 °C with OC11.

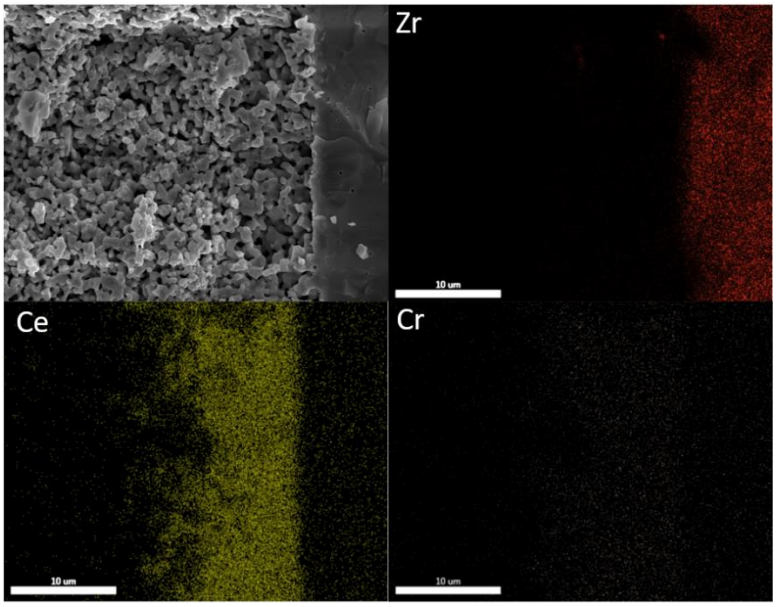

Figure 69 SEM/EDX mapping of the cross-sectional of the anode-supported cell under a constant current density of 0.5 A cm^{-2} at 800 °C with OC11LZA.

8.4 Oxide scales characterization of tested alloys

Based on the results above, the degradation rates of ASC coupled with commercial alloys were much larger and the Cr distribution on the cathode region was more severe than AFA alloys. In order to validate the superior property of AFA alloys over commercial alloys, chemical analysis of the oxides scale formed on various alloys was carried out.

8.4.1 Phase determination

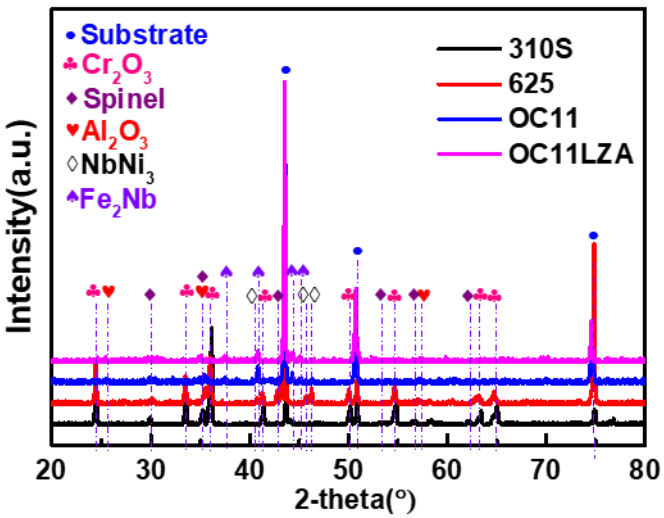

Figure 70 XRD patterns of 310S, 625, OC11 and OC11LZA samples after 500h operation with cell.

Figure 70 shows XRD patterns of 310S, 625, OC11 and OC11LZA alloys after testing with cells for 500 h. The results reveal that $(Mn, Cr)_3O_4$ spinel and Cr_2O_3 are the two major phases formed during cell operation for 310S and 625 sample at 800°C. One can notice that the main difference of XRD patterns of 310S from 625 is the formation of $NbNi_3$. However, the main peaks for OC11 and OC11LZA after the 500 h cell operation are the substrate and Fe_2Nb Laves phases which demonstrates that the oxide scales formed on the AFAs could be thinner than 10 microns. For AFA alloys, substrate peaks can be observed as the main peak couple with some small peaks of alumina. No spinel and Cr_2O_3 peaks could be observed after only 500 h cell operation. It could be deduced that AFA alloys exhibited significantly greater oxidation resistance than the chromia-

forming 310S and 625 in cathode regions environments which indicates of great interest for the BoP application in SOFC industry.

8.4.2 Surface morphology

Figure 71 shows the surface morphology of alloys after 500 h operation with cell. Plate-like oxides and some diamond-like oxides covered the entire surface. According to the corresponding XRD pattern (Figure 10), these two phases can be identified as Cr_2O_3 and $(Cr, Mn)_3O_4$, respectively. Spinel grains with different sizes can be observed at higher magnification (**Figure 71b**). For the 625 tested after 500 h operation (**Figure 71c**), diamond-like oxides with different sizes uniformly covered the whole surface which can be attributed to the $(Cr, Mn)_3O_4$. For the OC11 alloy, numerous oxide nodules are formed and cover the entire surface after the cell operation (**Figure 71e**). Moreover, the size of these particles is about 0.3μm which could be assigned to the Fe-Al-Cr-Mn-rich oxides (**Figure 71f**). The morphology of OC11LZA is similar to that of OC11. However, there are oxides with bigger sizes formed on the surface of OC11LZA than OC11 which could be attributed to the Nb-rich oxides (**Figure 71g**).

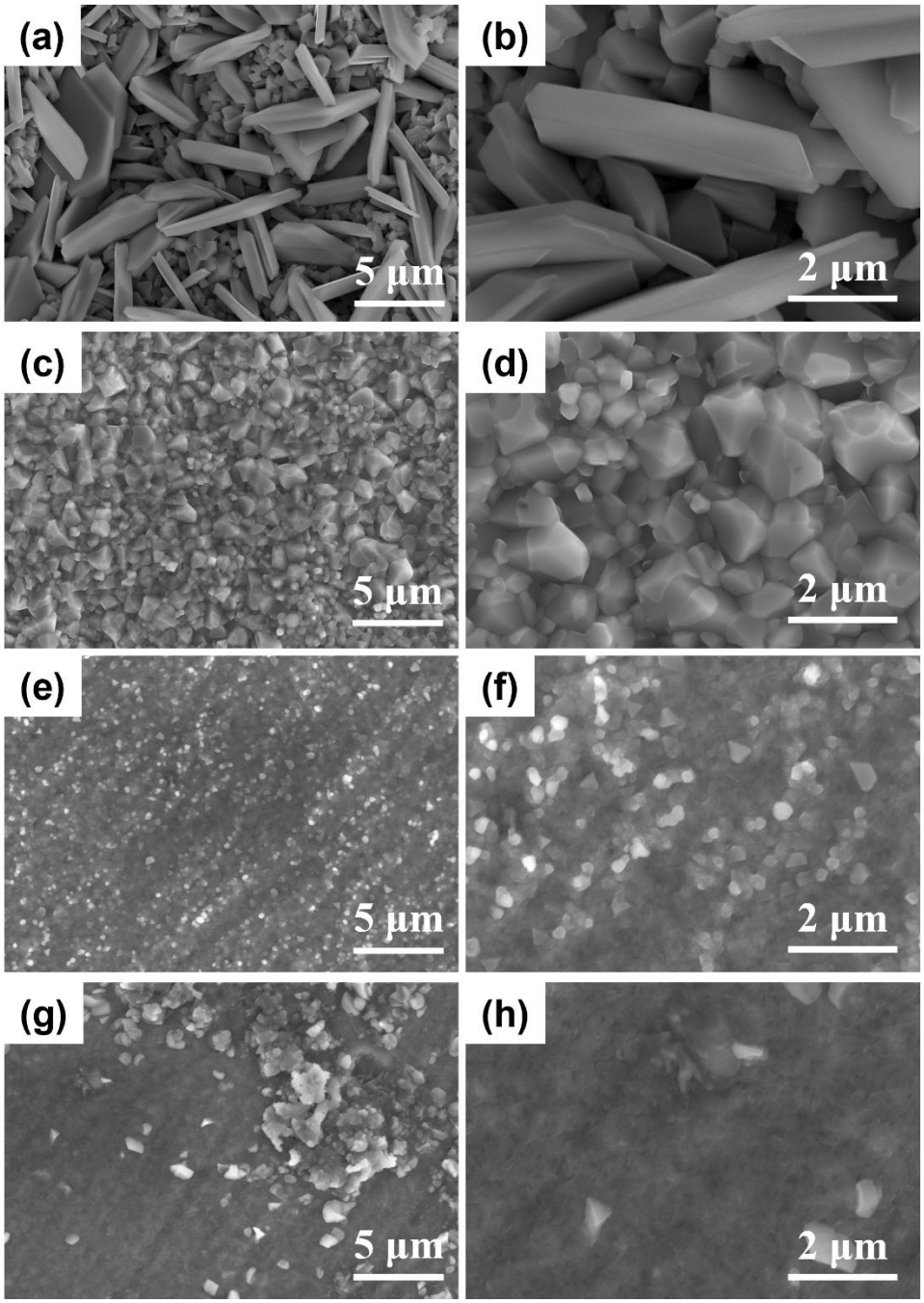

Figure 71 SEM surface morphologies of (a, b) 310S, (c, d) 625, (e, f) OC11 and (g, h) OC11LZA samples after 500 h operation with cell.

8.4.3 Cross-sectional STEM/EDS mapping

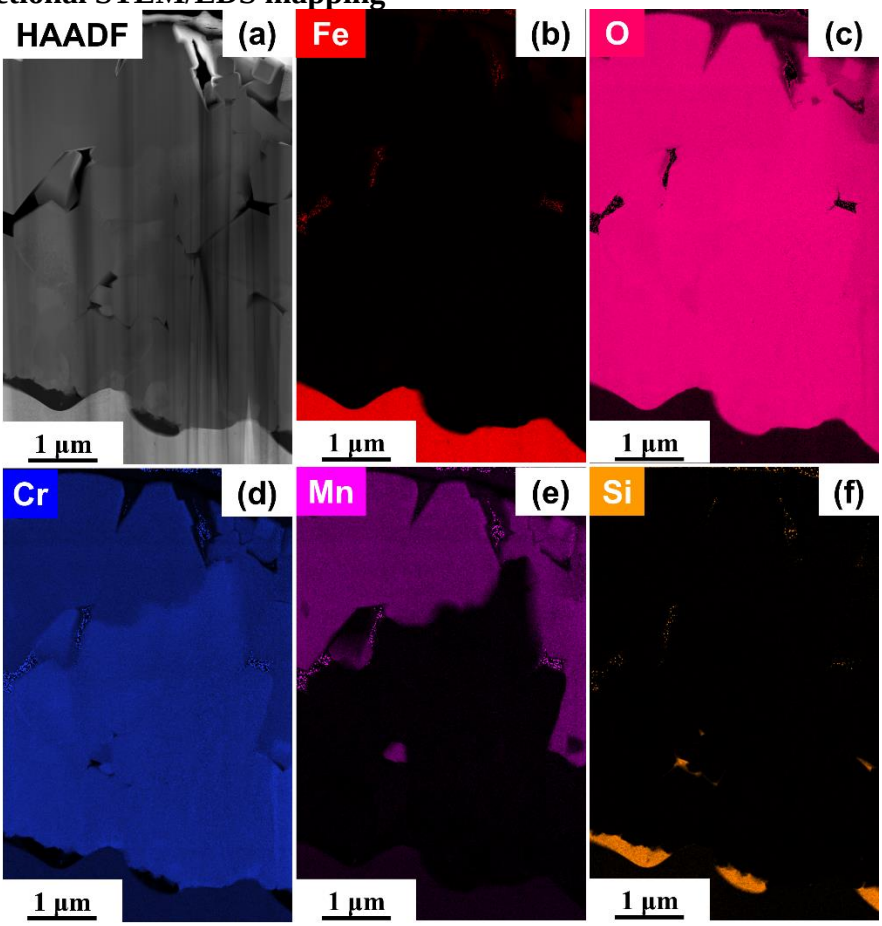

Figure 72 (a) HAADF-STEM image and cross-sectional mapping image of alloy 310S after 500 h operation with cell, (b) Fe, (c) O, (d) Cr, (e) Mn, (f) Si.

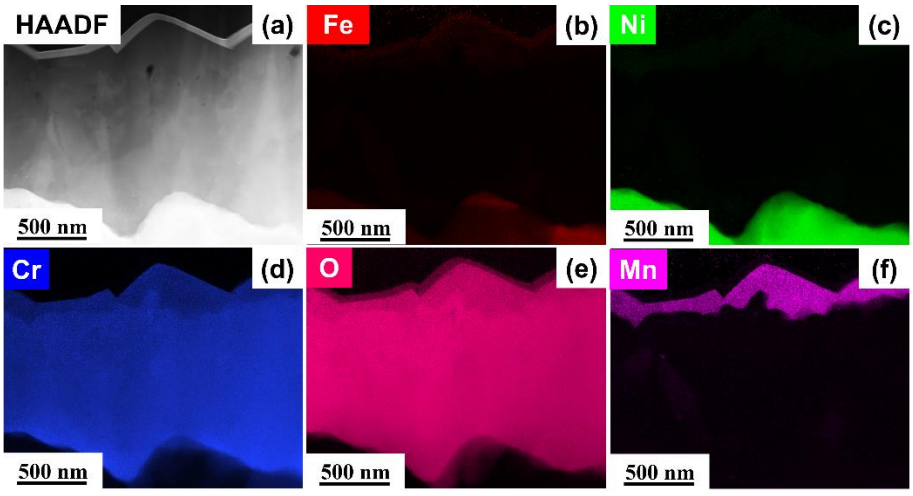

Figure 73 (a) HAADF-STEM image and cross-sectional mapping image of alloy 625 after 500 h operation with cell, (b) Fe, (c) Ni, (d) Cr, (e) O, (f) Mn.

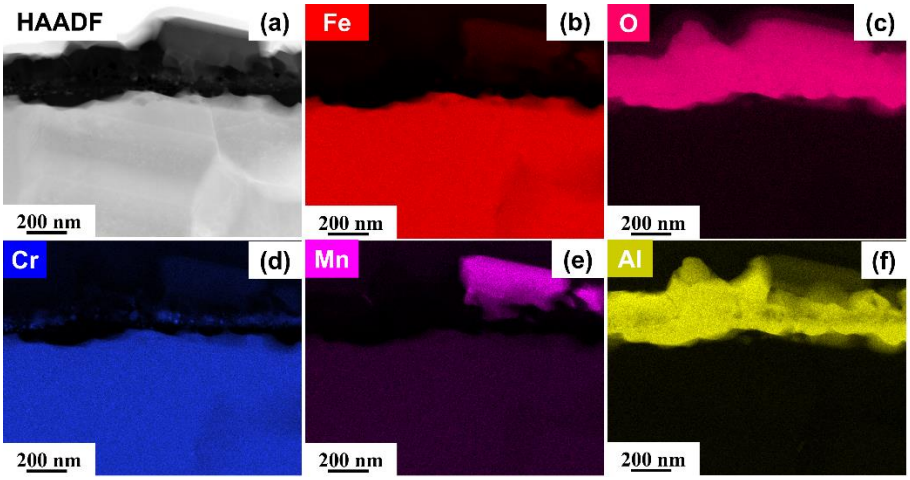

Figure 74 (a) HAADF-STEM image and cross-sectional mapping image of alloy OC11 after 500 h operation with cell, (b) Fe, (c) O, (d) Cr, (e) Mn, (f) Al.

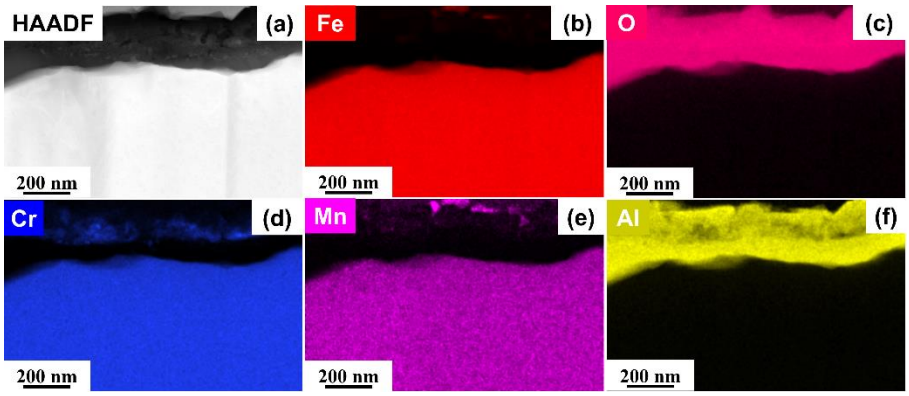

Figure 75 (a) HAADF-STEM image and cross-sectional mapping image of alloy OC11LZA after 500 h operation with cell, (b) Fe, (c) O, (d) Cr, (e) Mn, (f) Al.

Figures 72-75 compares the STEM/EDS cross-sectional morphology and chemistry of oxide scales formed on 310S, 625, OC11 and OC11LZA after tested with anode-supported cells at 800 °C for 500 h. Consistent with the XRD and our previous research (**Figures 70**), 310S formed a complex oxide scale structure with an outer Cr-Mn-rich layer and an inner Cr-rich layer (**Figure 72**). At the scale-alloy interface regions, local semi-continuous areas of Si-rich oxide consistent with SiO_2 were observed. Such local formation of SiO_2 at the scale-alloy interface is frequently reported for oxidation of Fe-based Cr_2O_3-forming alloys such as 310S due to the greater thermodynamic stability of SiO_2 versus Cr_2O_3 [109]. The oxide scale formed on 625 (**Figure 73**) consisted primarily of a Cr-rich oxide region consistent with Cr_2O_3, with a thin surface transient oxide layer rich in Cr, Mn, and

Fe consistent with spinel, as expected based on the XRD data (**Figures 70**). Moreover, small voids could be observed in the chromia layer where Cr evaporation reaction could take place. The AFA alloys (**Figure 74 and 75**) formed a multi-layered oxide scale, with an outer Al-Cr-Mn-Fe-Ni-rich oxide layer, an intermediate layer rich in Cr, consistent with Cr_2O_3 and an inner Al-rich region consistent with Al_2O_3. This structure is in agreement with past studies of AFA alloy oxidation [100], and the formed continuous alumina layer is expected to drastically decrease the evaporated gaseous Cr species from alloys. However, the transient oxides layer and the chromia layer formed on all AFA alloys were fairly extensive, thus making it harder to maintain cell performance during the long-term operation, which needs to be optimized for the future AFA alloys.

8.5 Summary

In this chapter, Cr poisoning of anode supported cells coupled with commercial alloys and AFA alloys was evaluated compared to the cell without alloy using DRT analysis. After the galvanostatic test, the cell voltage decreases about 4.4% in the absence of alloys, a considerable decrease of 22.1 % and 12.1 % was determined in the presence of 310S and 625 alloy, respectively. However, slight decreases of 5.1 % and 1.5 % was determined in the presence of OC11 and OC11LZA alloy, respectively. Three DRT peaks were detected for the anode-supported cells. The increased polarization resistances of mixed solid-state oxygen diffusion and reaction in the cathode (P_1) and chemisorption of oxygen on the cathode (P_2) were the main reason for the performance deterioration. The surface analysis of the AFA alloys suggest that gaseous Cr species were suppressed by the continuous alumina layer formed on AFA alloys. The correlation of the alumina layer and the lower degradation rate of the cells is consistent with inhibition of the formation of gaseous chromium species which are known to poison the LSCF cathodes.

Chapter 9 Conclusion

To alleviate the Cr poisoning and achieve long-term high performance of SOFC stacks, various alumina-forming austenitic (AFA) stainless steels applied at different temperatures are evaluated in this work on the short-term (500 h) and long-term (5000 h) Cr evaporation and oxidation behavior, the accurate method to evaluate the Cr evaporation from alloys and the performance of ASCs coupled with different alloys.

In chapter 4, Cr evaporation rates of AFA alloys are compared to benchmark Cr_2O_3 forming alloys at 800-900 °C in air with 10% H2O and the protective mechanism of AFA alloys have been discussed. Cr evaporation rates of AFA alloys were ~5-35 times lower than Cr_2O_3 forming 310 S and 625 benchmarks under 800-900 °C short-term operation. Surface Si contamination on all samples was observed after 500 h operation at 800-900 °C in air with 10% H_2O with the use of a quartz furnace tube. Although it did not appear to significantly impact Cr release behavior for 500 h exposure, potential interactions need to be considered and assessed after long-term exposure.

Thus, in chapter 5 and 6, long-term Cr evaporation and oxidation rates of 310S, OC4 and OC5 at 800 °C and 625, OC11 and OC11LZ at 900 °C were studied. 310S releases 35 times more gaseous Cr species than AFA alloys at 800 °C, while 625 exhibits a 28-and 56-times higher evaporated Cr amounts than OC11 and OC11LZ, respectively. Extensive gaseous Cr species evaporate from 310S and 625, while the AFA alloys exhibits higher oxidation resistance and lower evaporation rates during the long-term test (5000 h). The inner continuous alumina layer formed on the AFA alloy significantly reduces the outward diffusion of Cr, Mn, Fe, etc through the oxides scale which can immensely alleviate the long-term evaporation of gaseous Cr species. For OC11 and OC11LZ tested at 900 °C, the synergistic effect of Hf and Y in OC11 prevented the outward diffusion of cations which resulted in the thinner oxides scale, while the fast corporation of Zr to the scale would provide an alternative pathway for the inward diffusion of oxygen, thus causing a thicker oxides scale with defects of OC11LZ.

In chapter 7, In order to exclude the effect of Si, Na deposition and the reaction between evaporated Cr gaseous species and used tubes, an optimal method was pursued to accurately evaluate the Cr evaporation

rates of different alloys. Cr evaporation rates of AFA alloys were lower than Cr_2O_3 forming 310S and 625 alloys at 800-900 °C operation with all four methods. Si contamination, Na pollution and the chemical interaction were solved using the sodium carbonate coated thin alumina tubes (method 3) which could accurately evaluate the Cr evaporation rates of alloys.

In chapter 8, based on the great performance of AFAs after long-term operation, Cr poisoning of anode supported cells coupled with commercial alloys and AFA alloys was evaluated compared to the cell without alloy using DRT analysis. After the galvanostatic test, the cell voltage decreases about 4.4% in the absence of alloys, a considerable decrease of 22.1 % and 12.1 % was determined in the presence of 310S and 625 alloy, respectively. However, slight decreases of 5.1 % and 1.5 % was determined in the presence of OC11 and OC11LZA alloy, respectively. Up to three DRT peaks were detected for the anode-supported cells. The increased polarization resistances of mixed solid-state oxygen diffusion and reaction in the cathode (P_1) and chemisorption of oxygen on the cathode (P_2) were the main reason for the performance deterioration. The surface analysis of the AFA alloys suggest that gaseous Cr species were suppressed by the continuous alumina layer formed on AFA alloys. The correlation of the alumina layer and the lower degradation rate of the cells is consistent with inhibition of the formation of gaseous chromium species which are known to poison the LSCF cathodes.

Supplementary materials

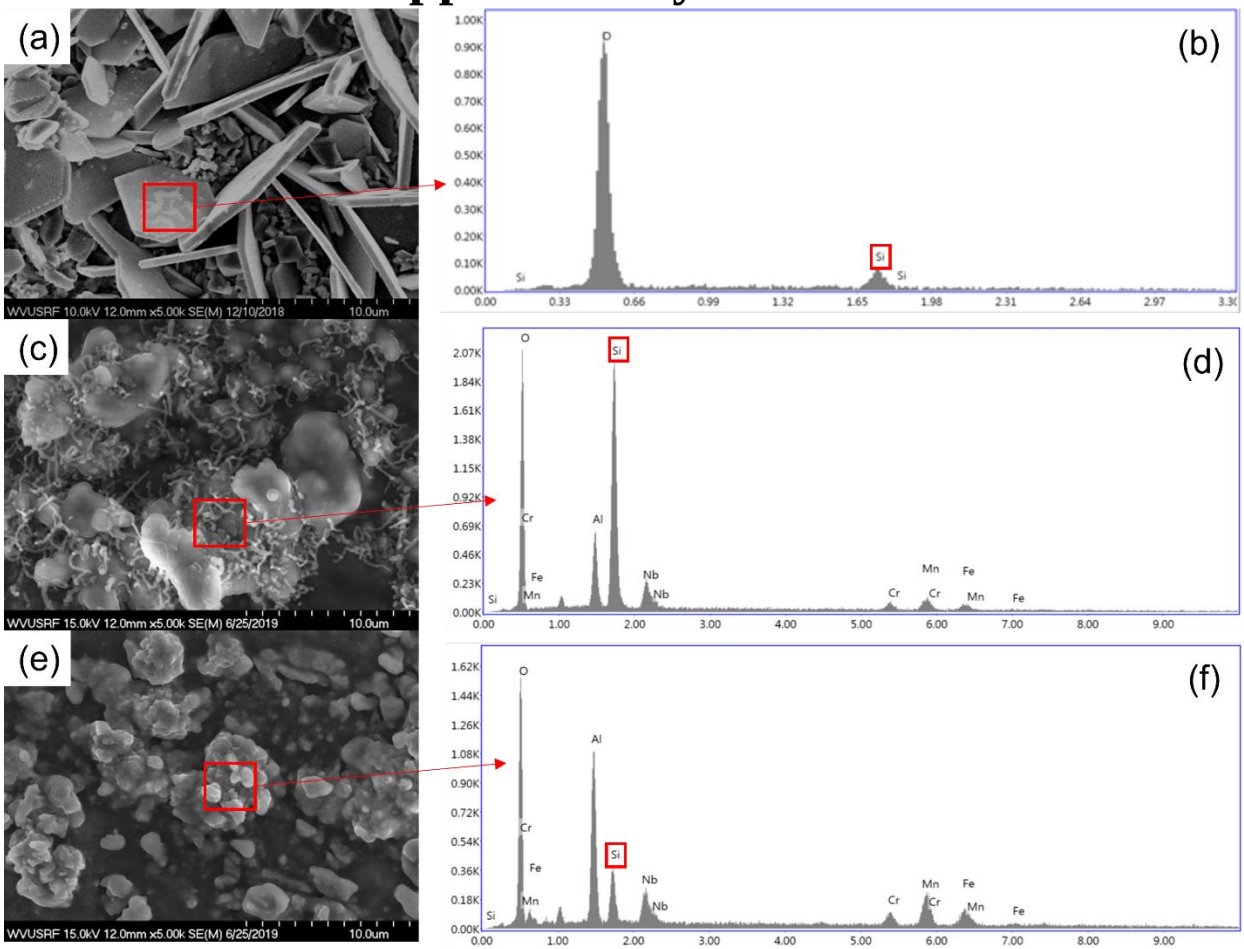

Figure S1. SEM surface images of (a) 310S after 1000 h oxidation, (b) OC4 after 5000h oxidation and (c) OC5 after 5000h oxidation and corresponding EDS analysis of b) 310S, d) OC4 and f) OC5.

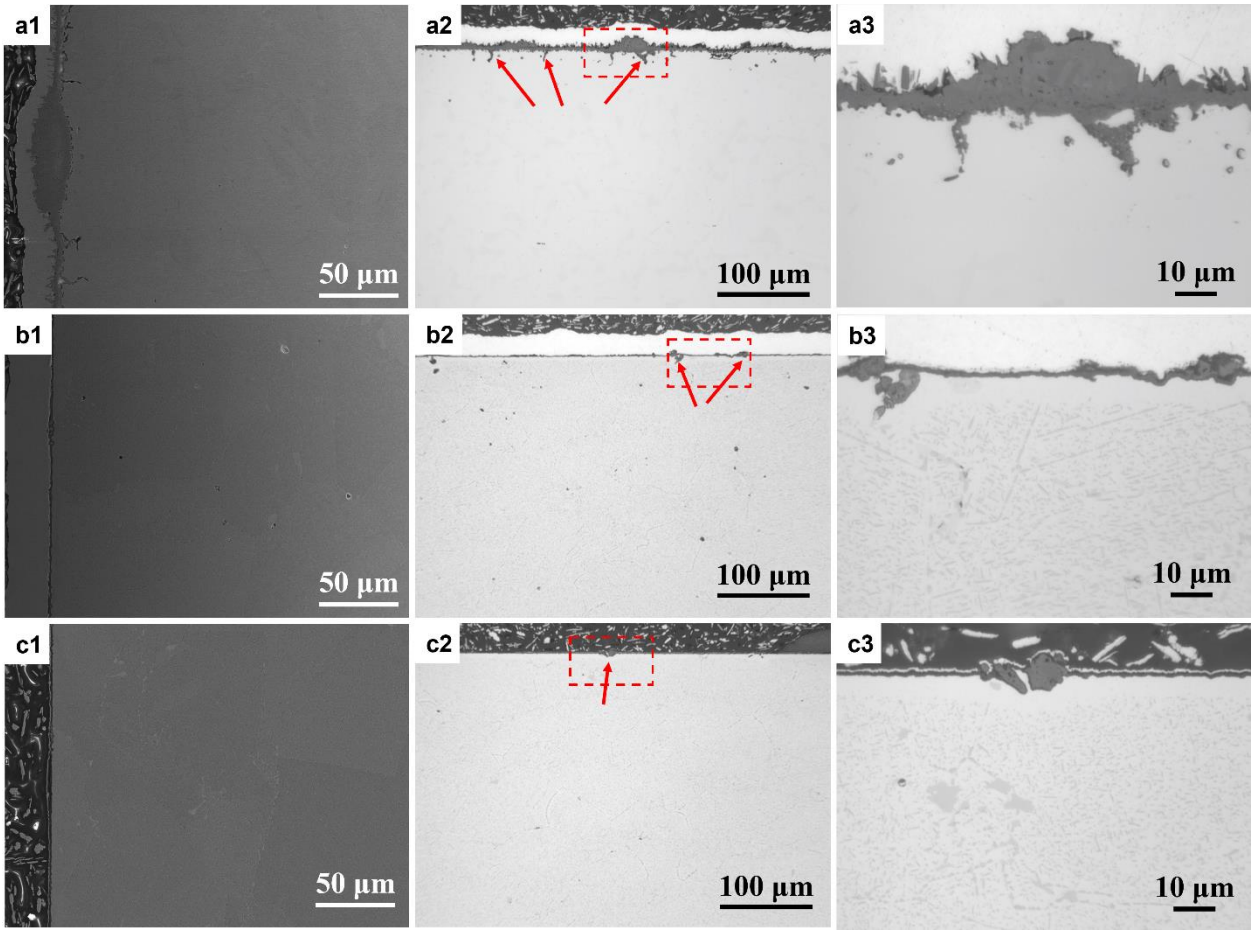

Figure S2 Cross-sectional SEM and light microscopy images of 310S and AFA alloys after tested for 5000 h.

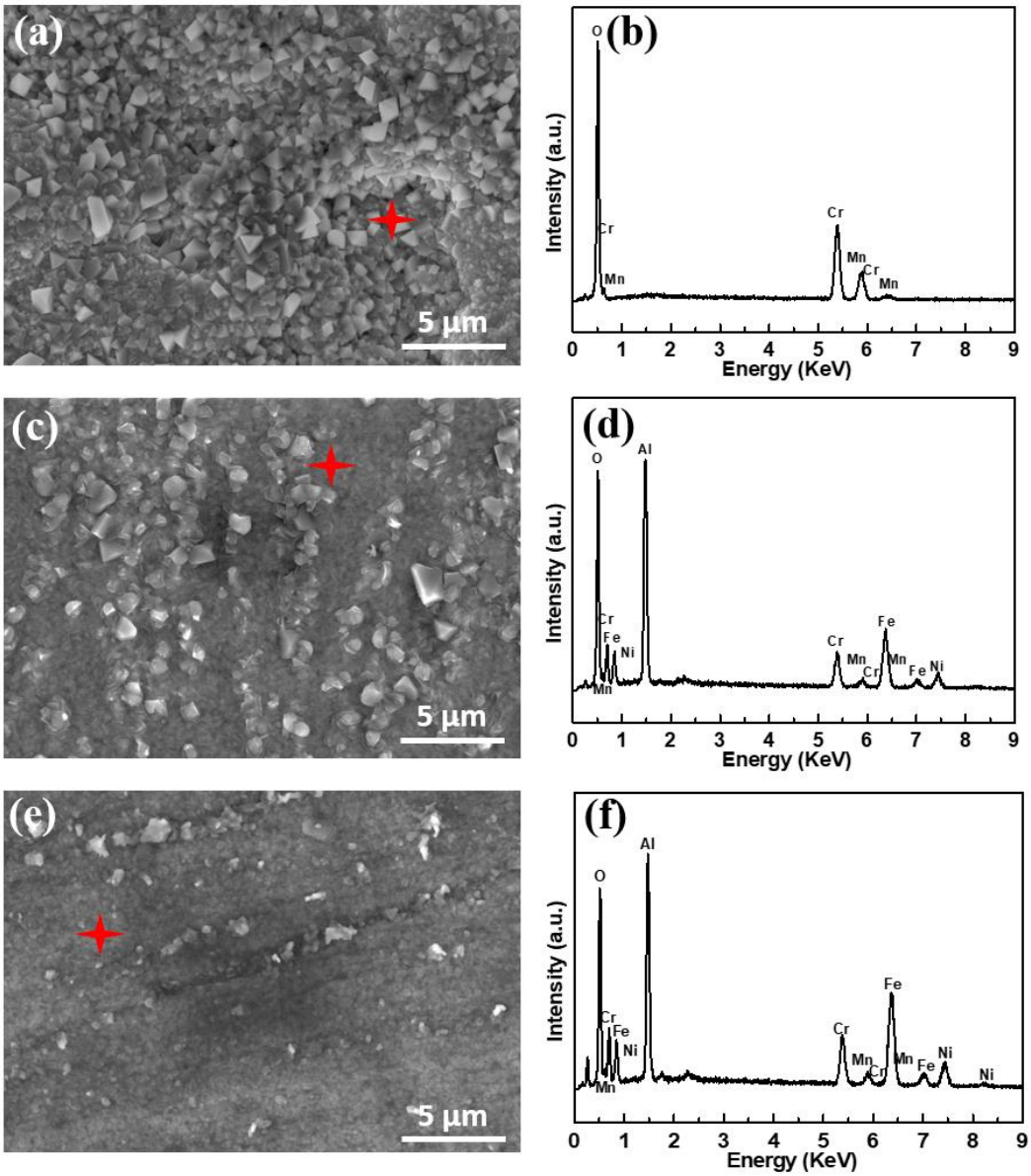

Figure S3 SEM surface images of a) 310S, b) OC4 and c) OC5 and corresponding EDS analysis of b) 310S, d) OC4 and f) OC5 after 500 h chromium evaporation test at 800 °C in Na_2CO_3 coated thin alumina tube.

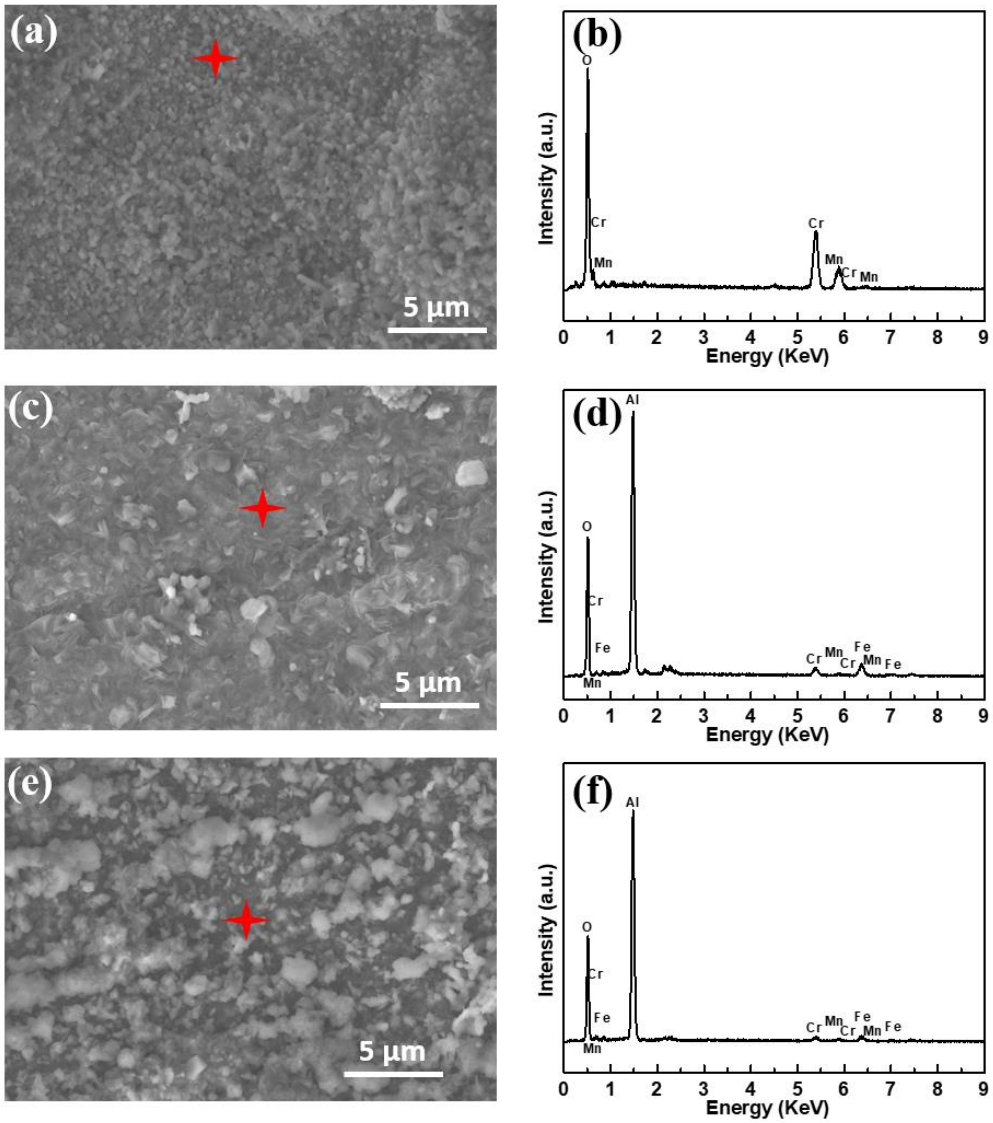

Figure S4 SEM surface images of a) 625, b) OC11 and c) OC11LZ and corresponding EDS analysis of b) 625, d) OC11 and f) OC11LZ after 500 h chromium evaporation test at 900 °C in Na_2CO_3 coated thin alumina tube.

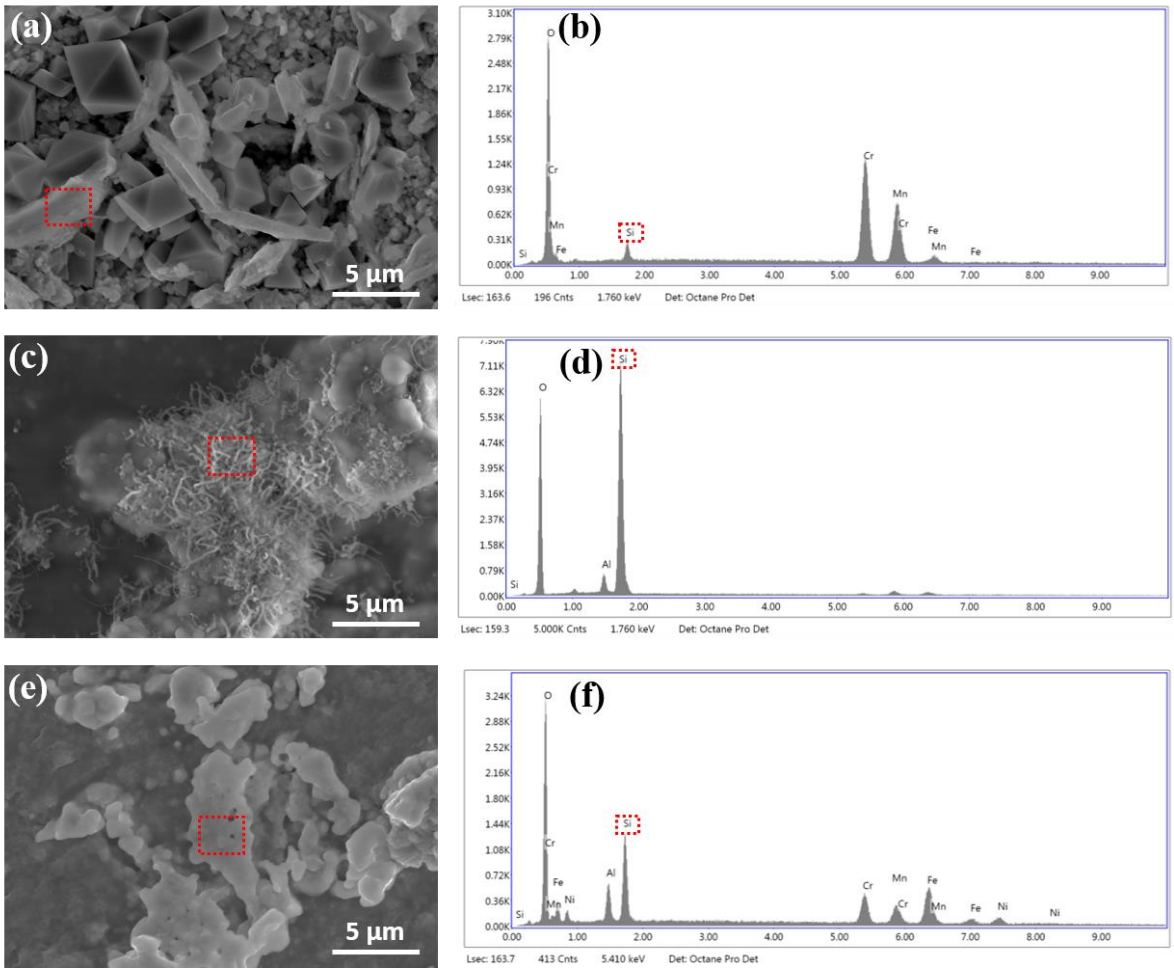

Figure S5 SEM surface images of (a) 310S, (b) OC4 and (c) OC5 after 4500 h test in quartz tube and corresponding EDS analysis of (b) 310S, (d) OC4 and (f) OC5.

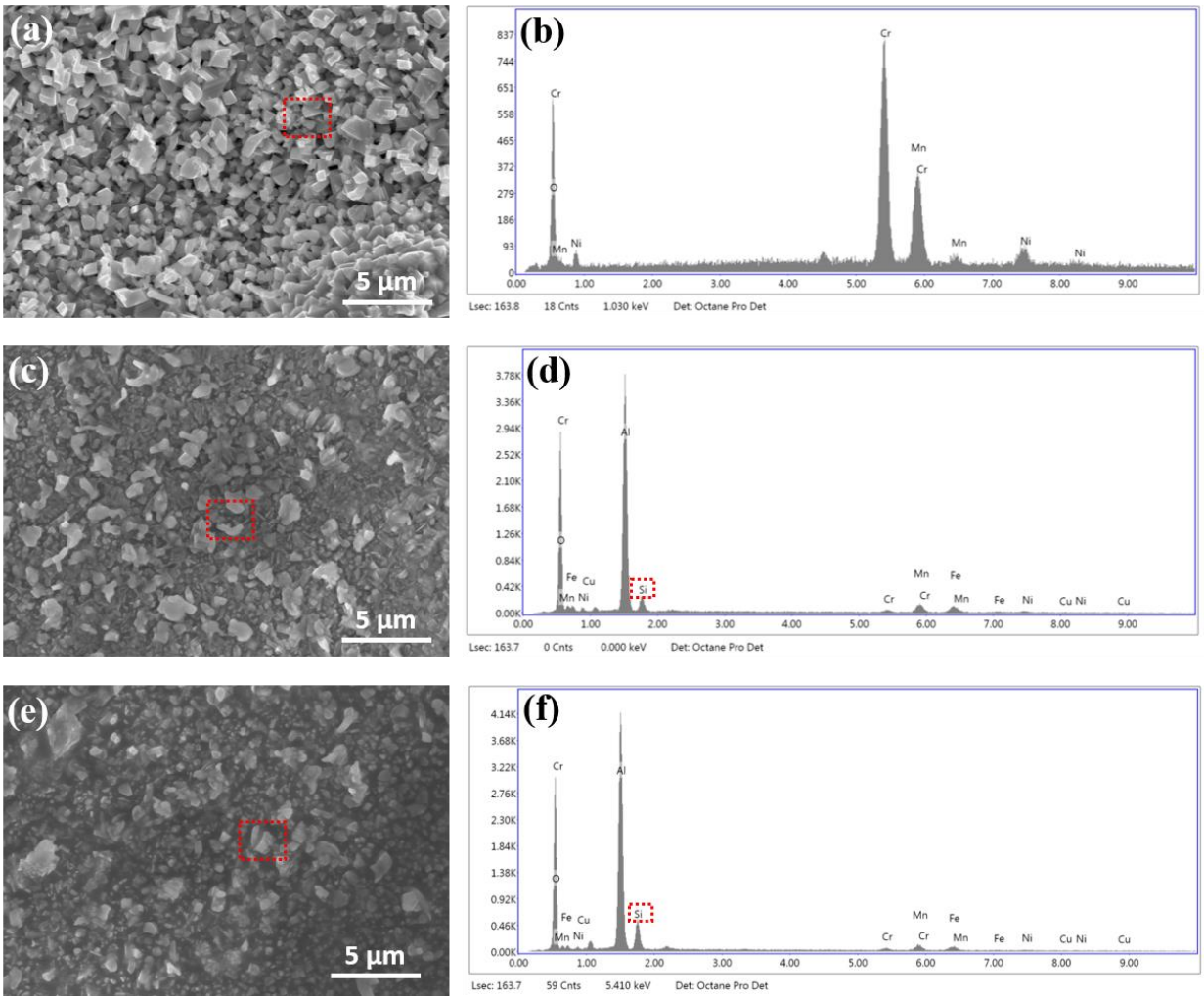

Figure S6 SEM surface images of (a) 625, (b) OC11 and (c) OC11LZ after 4500 h test in quartz tube and corresponding EDS analysis of (b) 625, (d) OC11 and (f) OC11LZ.

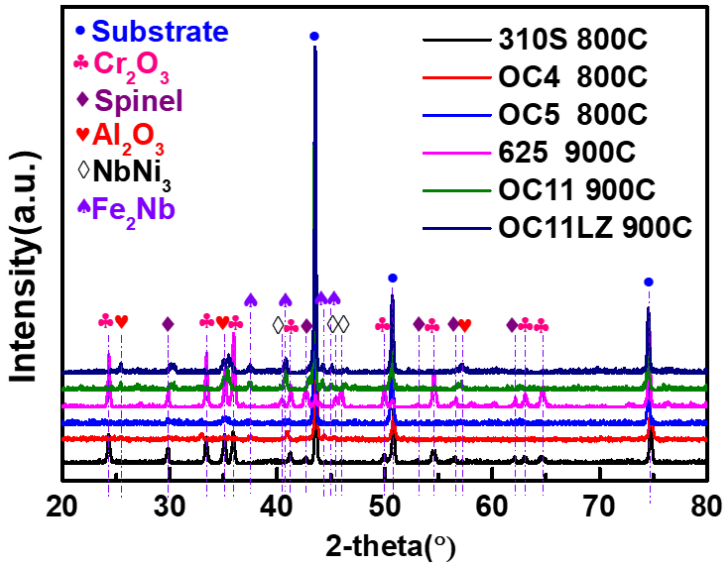

Figure S7 XRD profiles of the oxide scales developed on 310S, OC4 and OC5 at 800 °C and 625, OC11 and OC11LZ after 500 h chromium evaporation test in alumina tube.

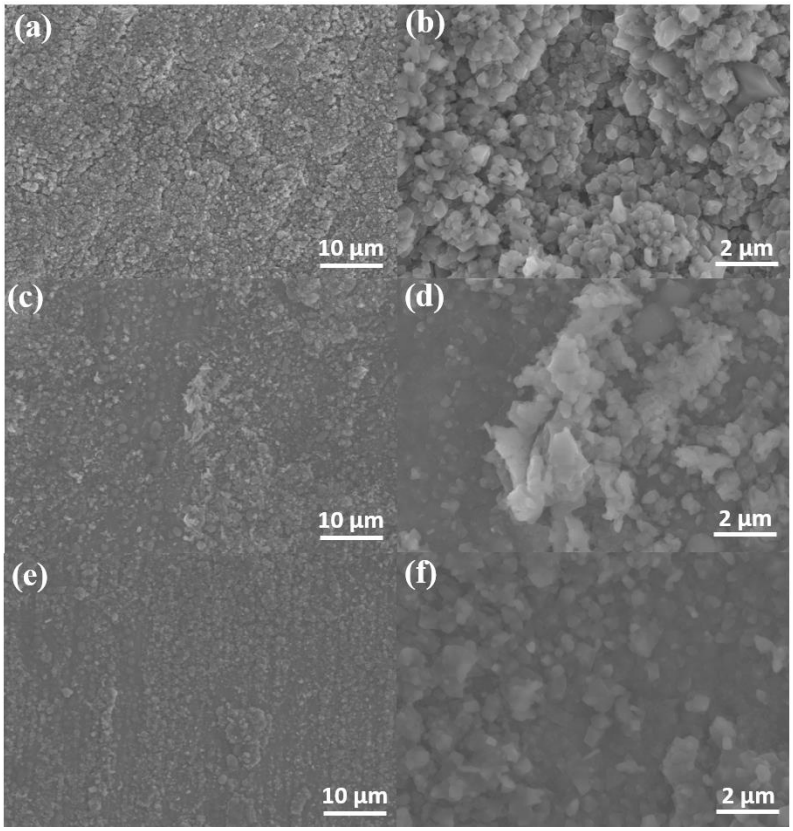

Figure S8 Oxide scale morphologies developed on (a, b) 310S, (c, d) OC4 and (e, f) OC5 tested for 500 h in air + 10% H_2O at 800 °C in alumina tube.

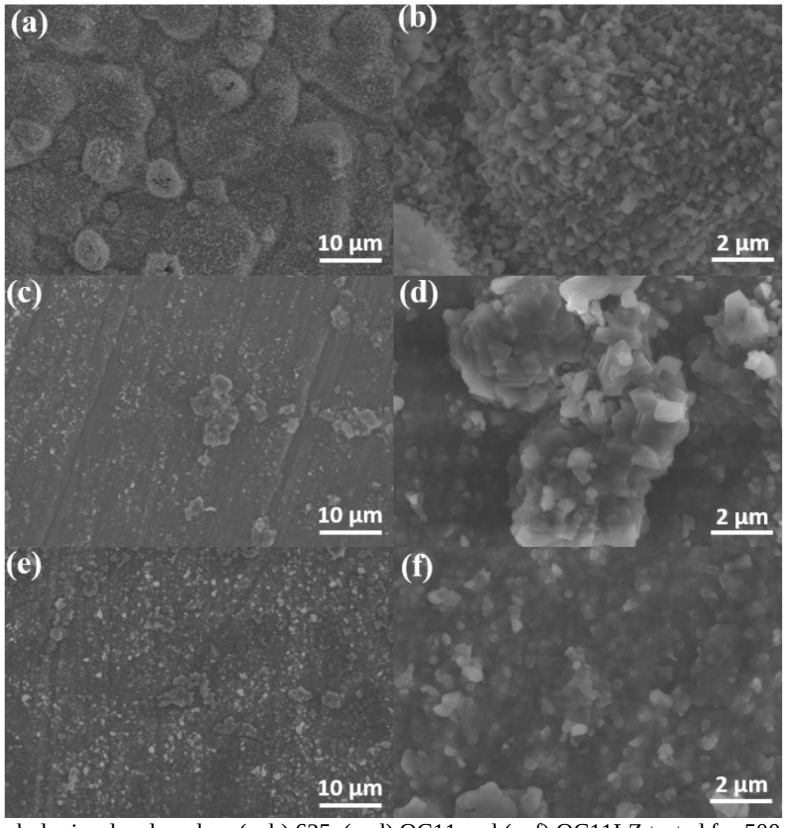

Figure S9 Oxide scale morphologies developed on (a, b) 625, (c, d) OC11 and (e, f) OC11LZ tested for 500 h in air + 10% H_2O at 900 °C in alumina tube.

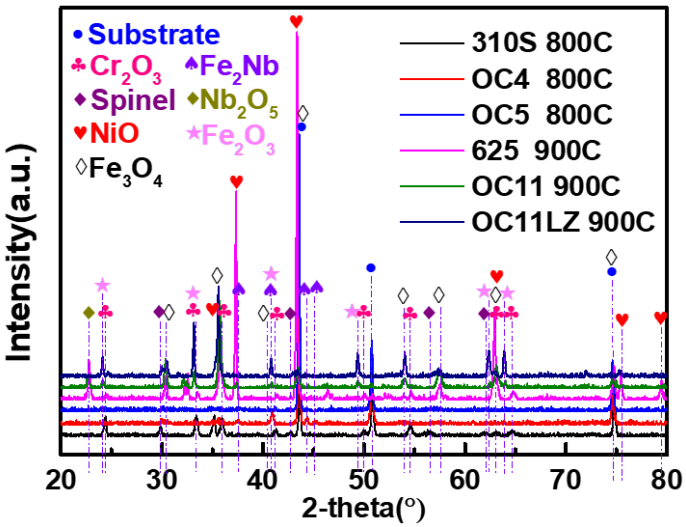

Figure S10 XRD profiles of the oxide scales developed on 310S, OC4 and OC5 at 800 °C and 625, OC11 and OC11LZ after 500 h chromium evaporation test in sodium carbonate coated alumina tube.

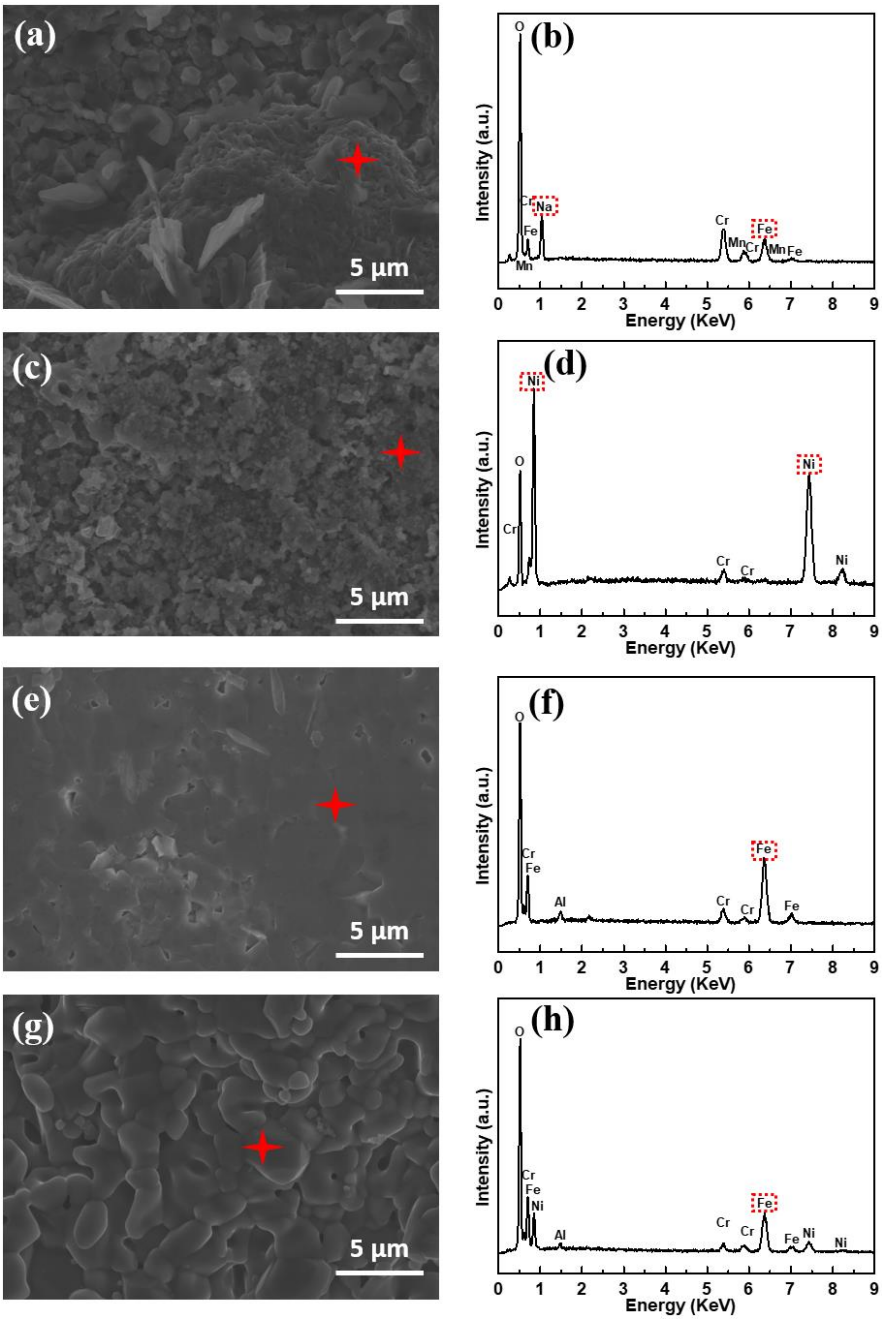

Figure S11 SEM surface images of a) 310S, c) 625, e) OC11 and g) OC11LZ and corresponding EDS analysis of b) 310S, d) 625, f) OC11 and h) OC11LZ after 500 h chromium evaporation test at 800 °C in Na_2CO_3 coated alumina tube.

References

[1] M. Liu, M.E. Lynch, K. Blinn, F.M. Alamgir, Y. Choi, Materials Today, 14 (2011) 534-546.
[2] N. Mahato, A. Banerjee, A. Gupta, S. Omar, K. Balani, Prog Mater Sci, 72 (2015) 141-337.
[3] J. Malzbender, P. Batfalsky, R. Vaßen, V. Shemet, F. Tietz, J Power Sources, 201 (2012) 196-203.
[4] J.W. Fergus, Mater Sci Eng A, 397 (2005) 271-283.
[5] E. Konysheva, H. Penkalla, E. Wessel, J. Mertens, U. Seeling, L. Singheiser, K. Hilpert, J Electrochem Soc, 153 (2006) A765.
[6] J.A. Schuler, Z. Wuillemin, A. Hessler-Wyser, C. Comminges, N.Y. Steiner, J. Van herle, J Power Sources, 211 (2012) 177-183.
[7] Y.D. Zhen, A.I.Y. Tok, S.P. Jiang, F.Y.C. Boey, J Power Sources, 170 (2007) 61-66.
[8] M.R. Ardigò, A. Perron, L. Combemale, O. Heintz, G. Caboche, S. Chevalier, J Power Sources, 196 (2011) 2037-2045.
[9] T. Zhao, Z. Liu, C. Du, C. Dai, X. Li, B. Zhang, Mater Sci Eng A 708 (2017) 181-192.
[10] T. Zhao, Z. Liu, C. Du, M. Sun, X. Li, Int J Fatigue, 110 (2018) 105-114.
[11] J. Andreas Schuler, H. Lübbe, A. Hessler-Wyser, J. Van herle, J Power Sources, 213 (2012) 223-228.
[12] C. Gindorf, L. Singheiser, K. Hilpert, J Phys Chem Solids, 66 (2005) 384-387.
[13] K. Hilpert, D. Das, M. Miller, D.H. Peck, R. Weiss, Journal of the Electrochemical Society, 143 (1996) 3642-3647.
[14] H. Yokokawa, T. Horita, N. Sakai, K. Yamaji, M. Brito, Y. Xiong, H. Kishimoto, Solid State Ion, 177 (2006) 3193-3198.
[15] B.B. Ebbinghaus, Combust Flame, 93 (1993) 119-137.
[16] B.C. Steele, A. Heinzel, Nature, 414 (2001) 345-352.
[17] M.K. Stodolny, B.A. Boukamp, D.H.A. Blank, F.P.F. van Berkel, J Power Sources, 209 (2012) 120-129.
[18] Y.L. Huang, A.M. Hussain, C. Pellegrinelli, C. Xiong, E.D. Wachsman, ACS applied materials & interfaces, 9 (2017) 16660-16668.
[19] N. Ni, S.J. Cooper, R. Williams, N. Kemen, D.W. McComb, S.J. Skinner, ACS applied materials & interfaces, 8 (2016) 17360-17370.
[20] Y. Yamamoto, M.P. Brady, Z.P. Lu, P.J. Maziasz, C.T. Liu, B.A. Pint, K.L. More, H.M. Meyer, E.A. Payzant, Science, 316 (2007) 433-436.
[21] X. Guo, K. Chen, W. Gao, Z. Shen, L. Zhang, Corros Sci, 138 (2018) 297-306.
[22] J.C. Gomez-Vidal, A.G. Fernandez, R. Tirawat, C. Turchi, W. Huddleston, Sol Energy Mater Sol Cells, 166 (2017) 234-245.
[23] S. Taniguchi, M. Kadowaki, H. Kawamura, T. Yasuo, Y. Akiyama, Y. Miyake, T. Saitoh, J Power Sources, 55 (1995) 73-79.
[24] S. Badwal, R. Deller, K. Foger, Y. Ramprakash, J. Zhang, Solid State Ion, 99 (1997) 297-310.
[25] S.P. Jiang, J.P. Zhang, L. Apateanu, K. Foger, J Electrochem Soc, 147 (2000) 4013.
[26] M.C. Tucker, H. Kurokawa, C.P. Jacobson, L.C. De Jonghe, S.J. Visco, J Power Sources, 160 (2006) 130-138.
[27] Y. Matsuzaki, Solid State Ion, 132 (2000) 271-278.
[28] H.C. Graham, H.H. Davis, J Am Ceram Soc, 54 (1971) 89-93.
[29] C.A. Stearns, F.J. Kohl, G.C. Fryburg, J Electrochem Soc, 121 (1974) 945.
[30] D.J. Young, B.A. Pint, Oxid Met, 66 (2006) 137-153.
[31] E.J. Opila, D.L. Myers, N.S. Jacobson, I.M. Nielsen, D.F. Johnson, J.K. Olminsky, M.D. Allendorf, J Phys Chem A, 111 (2007) 1971-1980.
[32] X. Chen, Y. Zhen, J. Li, S.P. Jiang, Int J Hydrogen Energy, 35 (2010) 2477-2485.
[33] R. Wang, M. Würth, U.B. Pal, S. Gopalan, S.N. Basu, J Power Sources, 360 (2017) 87-97.
[34] A.M. Abdalla, S. Hossain, A.T. Azad, P.M.I. Petra, F. Begum, S.G. Eriksson, A.K. Azad, Renewable and Sustainable Energy Reviews, 82 (2018) 353-368.
[35] C. Gindorf, L. Singheiser, K. Hilpert, Steel Res, 72 (2001) 528-533.

[36] Y.W. Kim, G.R. Belton, Metall Trans, 5 (1974) 1811-1816.
[37] M. Amra, S.R. Alavi Zaree, R. Dehmolaei, Metals and Materials International, 27 (2019) 931-945.
[38] D. Ambrose, (1968) 607-656.
[39] L. Ge, A. Verma, R. Goettler, D. Lovett, R.K.S. Raman, P. Singh, Metallurgical and Materials Transactions A, 44 (2013) 193-206.
[40] J. Froitzheim, S. Canovic, M. Nikumaa, R. Sachitanand, L.G. Johansson, J.E. Svensson, J Power Sources, 220 (2012) 217-227.
[41] J. Froitzheim, H. Ravash, E. Larsson, L.G. Johansson, J.E. Svensson, J Electrochem Soc, 157 (2010) B1295.
[42] J.S. Hardy, C.A. Coyle, J.J. Neeway, J.W. Stevenson, ECS Transactions, 78 (2017) 943-953.
[43] J. Fergus, Int J Hydrogen Energy, 32 (2007) 3664-3671.
[44] S.P. Jiang, J.P. Zhang, X.G. Zheng, J Eur Ceram Soc, 22 (2002) 361-373.
[45] S.P. Jiang, S. Zhang, Y.D. Zhen, J Mater Res, 20 (2005) 747-758.
[46] G.Y. Lau, M.C. Tucker, C.P. Jacobson, S.J. Visco, S.H. Gleixner, L.C. DeJonghe, J Power Sources, 195 (2010) 7540-7547.
[47] L.G.J. de Haart, J. Mougin, O. Posdziech, J. Kiviaho, N.H. Menzler, Fuel Cells, 9 (2009) 794-804.
[48] A. Neumann, N.H. Menzler, I. Vinke, H. Lippert, ECS Trans, (2009) 2889-2898.
[49] N.H. Menzler, I. Vinke, H. Lippert, ECS Trans, 25 (2009) 2899-2908.
[50] S.P. Jiang, Y.D. Zhen, S. Zhang, A.I.Y. Tok, P. Wu, J Electrochem Soc, 153 (2006) A2120.
[51] X. Chen, L. Zhang, S.P. Jiang, J Electrochem Soc, 155 (2008) B1093.
[52] J. Andreas Schuler, P. Tanasini, A. Hessler-Wyser, J.V. herle, Scr Mater, 63 (2010) 895-898.
[53] J.A. Schuler, P. Tanasini, A. Hessler-Wyser, C. Comninellis, J. Van herle, Electrochem commun, 12 (2010) 1682-1685.
[54] T. Horita, Y. Xiong, M. Yoshinaga, H. Kishimoto, K. Yamaji, M.E. Brito, H. Yokokawa, Electrochem Solid-State Lett, 12 (2009) B146.
[55] T. Horita, D.-H. Cho, F. Wang, T. Shimonosono, H. Kishimoto, K. Yamaji, M.E. Brito, H. Yokokawa, Solid State Ion, 225 (2012) 151-156.
[56] R.R. Liu, S.H. Kim, S. Taniguchi, T. Oshima, Y. Shiratori, K. Ito, K. Sasaki, J Power Sources, 196 (2011) 7090-7096.
[57] T. Komatsu, H. Arai, R. Chiba, K. Nozawa, M. Arakawa, K. Sato, Electrochem Solid-State Lett, 9 (2006) A9.
[58] T. Komatsu, R. Chiba, H. Arai, K. Sato, J Power Sources, 176 (2008) 132-137.
[59] Z. Sun, R. Wang, A.Y. Nikiforov, S. Gopalan, U.B. Pal, S.N. Basu, J Power Sources, 378 (2018) 125-133.
[60] R. Wang, Z. Sun, U.B. Pal, S. Gopalan, S.N. Basu, J Power Sources, 376 (2018) 100-110.
[61] M.P. Brady, K. Banta, J. Mizia, N. Lorenz, D.N. Leonard, Y. Yamamoto, M. DeFoort, J.R. Keiser, Energy Sustain Dev, 37 (2017) 20-32.
[62] M.P. Brady, J. Magee, Y. Yamamoto, D. Helmick, L. Wang, Mater Sci Eng A 590 (2014) 101-115.
[63] X. Xu, X. Zhang, X. Sun, Z.P. Lu, Oxid Met, 78 (2012) 349-362.
[64] X. Xu, X. Zhang, G. Chen, Z. Lu, Mater Lett, 65 (2011) 3285-3288.
[65] Z. Yang, G. Xia, J.W. Stevenson, Electrochem Solid-State Lett, 8 (2005) A168.
[66] Q. Zhao, S. Geng, G. Chen, F. Wang, J Alloys Compd, 769 (2018) 120-129.
[67] R. Chiba, Solid State Ion, 124 (1999) 281-288.
[68] T. Komatsu, H. Arai, R. Chiba, K. Nozawa, M. Arakawa, K. Sato, J Electrochem Soc, 154 (2007) B379.
[69] M.K. Stodolny, B.A. Boukamp, D.H.A. Blank, F.P.F. van Berkel, J Electrochem Soc, 158 (2011) B112.
[70] H. Orui, K. Watanabe, R. Chiba, M. Arakawa, J Electrochem Soc, 151 (2004) A1412.
[71] T. Komatsu, Y. Yoshida, K. Watanabe, R. Chiba, H. Taguchi, H. Orui, H. Arai, J Power Sources, 195 (2010) 5601-5605.
[72] T. Komatsu, K. Watanabe, M. Arakawa, H. Arai, J Power Sources, 193 (2009) 585-588.
[73] M. Yokoo, Y. Tabata, Y. Yoshida, H. Orui, K. Hayashi, Y. Nozaki, K. Nozawa, H. Arai, J Power Sources, 184 (2008) 84-89.

[74] Y. Yoshida, T. Komatsu, R. Chiba, M. Yokoo, K. Hayashi, H. Orui, H. Arai, ECS Trans, 25 (2009) 421-428.
[75] R. Chiba, H. Orui, T. Komatsu, Y. Tabata, K. Nozawa, M. Arakawa, K. Sato, H. Arai, J Electrochem Soc, 155 (2008) B575.
[76] Y. Zhen, S.P. Jiang, J Power Sources, 180 (2008) 695-703.
[77] K. Chen, N. Ai, K.M. O'Donnell, S.P. Jiang, Physical chemistry chemical physics : PCCP, 17 (2015) 4870-4874.
[78] L. Zhu, B. Wei, Z. Wang, K. Chen, H. Zhang, Y. Zhang, X. Huang, Z. Lu, ChemSusChem, 9 (2016) 2443-2450.
[79] J. Li, J. Li, D. Yan, J. Pu, B. Chi, L. Jian, Electrochim Acta, 270 (2018) 294-301.
[80] Y. Chen, S. Yoo, X. Li, D. Ding, K. Pei, D. Chen, Y. Ding, B. Zhao, R. Murphy, B. deGlee, J. Liu, M. Liu, Nano Energy, 47 (2018) 474-480.
[81] L. Zhao, S. Amarasinghe, S.P. Jiang, Electrochemistry Communications, 37 (2013) 84-87.
[82] C. Xiong, W. Li, J. Xiao, N. Duan, J. Pu, B. Chi, L. Jian, Int J Hydrogen Energy, 40 (2015) 13957-13963.
[83] X. Chen, B. Hua, J. Pu, J. Li, L. Zhang, S.P. Jiang, Int J Hydrogen Energy, 34 (2009) 5737-5748.
[84] M. Stanislowski, J. Froitzheim, L. Niewolak, W.J. Quadakkers, K. Hilpert, T. Markus, L. Singheiser, J Power Sources, 164 (2007) 578-589.
[85] J.G. Grolig, J. Froitzheim, J.E. Svensson, J Power Sources, 248 (2014) 1007-1013.
[86] D. Roehrens, A. Neumann, A. Beez, I.C. Vinke, L.G.J. de Haart, N.H. Menzler, Ceram Int, 42 (2016) 9467-9474.
[87] K. Fujita, T. Hashimoto, K. Ogasawara, H. Kameda, Y. Matsuzaki, T. Sakurai, J Power Sources, 131 (2004) 270-277.
[88] H. Bei, Y. Yamamoto, M.P. Brady, M.L. Santella, Mater Sci Eng A, 527 (2010) 2079-2086.
[89] Y. Yamamoto, M.L. Santella, M.P. Brady, H. Bei, P.J. Maziasz, Metall Mater Trans A, 40 (2009) 1868-1880.
[90] Y. Yamamoto, G. Muralidharan, M.P. Brady, Scr Mater, 69 (2013) 816-819.
[91] M.P. Brady, Y. Yamamoto, M.L. Santella, L.R. Walker, Oxid Met, 72 (2009) 311-333.
[92] C. Liang, B. Hu, A. Aphale, M. Venkataraman, M.K. Mahapatra, P. Singh, ECS Trans, 75 (2017) 57-64.
[93] Y.-S. Chou, J.P. Choi, J.W. Stevenson, C. Liang, B. Hu, W. Rodriguez, A.N. Aphale, P. Singh, ECS Trans, 78 (2017) 1047-1054.
[94] A. Aphale, J. Hong, B. Hu, P. Singh, J Vis Exp, (2019).
[95] M.A. Uddin, C.J. Banas, C. Liang, U. Pasaogullari, K.P. Recknagle, B.J. Koeppel, J.W. Stevenson, P. Singh, ECS Trans, 78 (2017) 1063-1072.
[96] M.A. Uddin, A. Aphale, B. Hu, S.J. Heo, U. Pasaogullari, P. Singh, J Electrochem Soc, 164 (2017) F1342-F1347.
[97] M.P. Brady, Y. Yamamoto, M.L. Santella, P.J. Maziasz, B.A. Pint, C.T. Liu, Z.P. Lu, H. Bei, Jom, 60 (2008) 12-18.
[98] C. Wagner, Zeitschrift für Physikalische Chemie, 21B (1933) 25-41.
[99] Y. Yamamoto, M.P. Brady, M.L. Santella, H. Bei, P.J. Maziasz, B.A. Pint, Metallurgical and Materials Transactions A, 42 (2011) 922-931.
[100] M.P. Brady, K.A. Unocic, M.J. Lance, M.L. Santella, Y. Yamamoto, L.R. Walker, Oxidation of Metals, 75 (2011) 337-357.
[101] M.P. Brady, Y. Yamamoto, M.L. Santella, B.A. Pint, Scripta Materialia, 57 (2007) 1117-1120.
[102] B.A. Pint, R. Peraldi, P.J. Maziasz, Materials Science Forum, 461-464 (2004) 815-822.
[103]
[104] H. Tian, W. Li, L. Ma, T. Yang, B. Guan, W. Shi, T.L. Kalapos, X. Liu, ACS applied materials & interfaces, 12 (2020) 49574-49585.
[105] F.H. Stott, G.C. Wood, J. Stringer, Oxidation of Metals, 44 (1995) 113-145.
[106] X. Xu, X. Zhang, X. Sun, Z.P. Lu, Corrosion Science, 65 (2012) 317-321.
[107] L. Ge, in, University of Connecticut - Storrs, University of Connecticut - Storrs, 2014.
[108] A.N. Aphale, B. Hu, M. Reisert, A. Pandey, P. Singh, Jom, 71 (2019) 116-123.
[109] H.E. Evans, D.A. Hilton, R.A. Holm, S.J. Webster, Oxidation of Metals, 19 (1983) 1-18.

[110] S.R.J. Saunders, M. Monteiro, F. Rizzo, Progress in Materials Science, 53 (2008) 775-837.
[111] H. Falk-Windisch, J.E. Svensson, J. Froitzheim, Journal of Power Sources, 287 (2015) 25-35.
[112] M. Stanislowski, E. Wessel, T. Markus, L. Singheiser, W. Quadakkers, Solid State Ionics, 179 (2008) 2406-2415.
[113] C. Gindorf, L. Singheiser, K. Hilpert, Steel Research, 72 (2001) 528-533.
[114] Y. Shida, H. Anada, Materials Transactions, JIM, 35 (1994) 623-631.
[115] B.A. Pint, Journal of the American Ceramic Society, 86 (2003) 686-695.
[116] M.M. Whiston, I.M.L. Azevedo, S. Litster, C. Samaras, K.S. Whitefoot, J.F. Whitacre, Joule, 3 (2019) 2060-2065.
[117] L. Ma, Y. Wang, W. Li, B. Guan, H. Qi, H. Tian, L. Zhou, H.A. De Santiago, X. Liu, Journal of Power Sources, 488 (2021) 229458.
[118] H. Yokokawa, H. Tu, B. Iwanschitz, A. Mai, Journal of Power Sources, 182 (2008) 400-412.
[119] S.P. Jiang, X. Chen, Int J Hydrogen Energy, 39 (2014) 505-531.
[120] G.R. Holcomb, D.E. Alman, Journal of Materials Engineering and Performance, 15 (2006) 394-398.
[121] K. Gerdes, C. Johnson, Journal of Fuel Cell Science and Technology, 6 (2009) 011018.
[122] J.A. Schuler, C. Gehrig, Z. Wuillemin, A.J. Schuler, J. Wochele, C. Ludwig, A. Hessler-Wyser, J. Van herle, Journal of Power Sources, 196 (2011) 7225-7231.
[123] A.N. Aphale, B. Hu, M. Reisert, A. Pandey, P. Singh, Jom, 71 (2018) 116-123.
[124] B.A. Pint, Oxidation of Metals, 95 (2021) 335-357.
[125] I.G. Wright, R.B. Dooley, International Materials Reviews, 55 (2010) 129-167.
[126] M.P. Brady, G. Muralidharan, D.N. Leonard, J.A. Haynes, R.G. Weldon, R.D. England, Oxidation of Metals, 82 (2014) 359-381.
[127] L. Zhou, J.H. Mason, W. Li, X. Liu, Renewable and Sustainable Energy Reviews, 134 (2020) 110320.
[128] H. Chen, H. Wang, Q. Sun, C. Long, T. Wei, S.H. Kim, J. Chen, C. Kim, C. Jang, Corrosion Science, 145 (2018) 90-99.
[129] P. Jian, L. Jian, H. Bing, G. Xie, Journal of Power Sources, 158 (2006) 354-360.
[130] R.L. Winter, P. Singh, M.K. King, M.K. Mahapatra, U. Sampathkumaran, Advances in Materials Science and Engineering, 2018 (2018) 1-17.
[131] N.S. Waluyo, S.-S. Park, R.-H. Song, S.-B. Lee, T.-H. Lim, J.-E. Hong, K.H. Ryu, W. Bin Im, J.-W. Lee, Ceramics International, 44 (2018) 11576-11581.
[132] P. Gannon, V. Gorokhovsky, M. Deibert, R. Smith, A. Kayani, P. White, S. Sofie, Z. Yang, D. McCready, S. Visco, International Journal of Hydrogen Energy, 32 (2007) 3672-3681.
[133] H. Kurokawa, C. Jacobson, L. Dejonghe, S. Visco, Solid State Ionics, 178 (2007) 287-296.
[134] E.J. Opila, Materials Science Forum, 461-464 (2004) 765-774.
[135] E.J. Opila, N.S. Jacobson, D.L. Myers, E.H. Copland, Jom, 58 (2006) 22-28.
[136] F.H. Stott, G.C. Wood, Materials Science and Engineering, 87 (1987) 267-274.
[137] D.V.V. Satyanarayana, G. Malakondaiah, D.S. Sarma, Materials Science and Engineering: A, 323 (2002) 119-128.
[138] P.J. Maziasz, Jom, 70 (2017) 66-75.
[139] Y. Yamamoto, M.P. Brady, Z.P. Lu, C.T. Liu, M. Takeyama, P.J. Maziasz, B.A. Pint, Metallurgical and Materials Transactions A, 38 (2007) 2737-2746.
[140] Y. Yamamoto, M. Takeyama, Z.P. Lu, C.T. Liu, N.D. Evans, P.J. Maziasz, M.P. Brady, Intermetallics, 16 (2008) 453-462.
[141] M.P. Brady, Y. Yamamoto, D.N. Leonard, H.M. Meyer, S. Momono, S. Fukada, T. Uehara, A. Ashary, L. Zhou, X. Liu, ECS Meeting Abstracts, MA2021-01 (2021) 794-794.
[142] J. Sunarso, S. Baumann, J.M. Serra, W.A. Meulenberg, S. Liu, Y.S. Lin, J.C. Diniz da Costa, Journal of Membrane Science, 320 (2008) 13-41.
[143] K. Zhang, A. El-Kharouf, J.-E. Hong, R. Steinberger-Wilckens, Corrosion Science, 169 (2020) 108612.
[144] L. Zhou, Z. Zeng, M.P. Brady, D.N. Leonard, H.M. Meyer, Y. Yamamoto, W. Li, G. Collins, X. Liu, International Journal of Hydrogen Energy, 46 (2021) 21619-21633.
[145] Y. Behnamian, A. Mostafaei, A. Kohandehghan, B.S. Amirkhiz, J. Li, R. Zahiri, E. Aghaie, W. Zheng, D. Guzonas, M. Chmielus, W. Chen, J.L. Luo, The Journal of Supercritical Fluids, 120 (2017) 161-172.

[146] Z. Bahman, M. Patrick, Chapter 4 - Small modular reactors and a modern power conversion approach, Elsevier, 2021.
[147] M.G.Coombs, L.W.Norman, Progress in Astronautics and Rocketry, 16 (1966) 419-481.
[148] P.J. Maziasz, R.W. Swindeman, J.P. Shingledecker, K.L. More, B.A. Pint, E. Lara-Curzio, N.D. Evans, in: Parsons 2003, Engineering Issues in Turbine Machinery, Power Plant and Renewables, Maney, London, 2003, pp. 1057-1073.
[149] B.A. Pint, J.P. Shingledecker, M.P. Brady, P.J. Maziasz, (2007) 995-1002.
[150] B.A. Pint, M.P. Brady, Y. Yamamoto, M.L. Santella, P.J. Maziasz, W.J. Matthews, Journal of Engineering for Gas Turbines and Power, 133 (2011).
[151] B.A. Pint, Journal of Engineering for Gas Turbines and Power, 128 (2006) 370-376.
[152] W.J. Matthews, K.L. More, L.R. Walker, (2007) 821-828.
[153] I. Stambler, Gas Turbine World (Feb.-Mar.), (2004) 12-16.
[154] W.J. Matthews, K.L. More, L.R. Walker, Journal of Engineering for Gas Turbines and Power, 132 (2010).
[155] B.A. Pint, S. Dryepondt, M.P. Brady, Y. Yamamoto, (2013).
[156] R. Peraldi, B.A. Pint, Oxidation of Metals, 61 (2004) 463-483.
[157] M. Spiegel, P. Schraven, (2017) 375-390.
[158] B. Jönsson, A. Westerlund, Oxidation of Metals, 88 (2017) 315-326.
[159] W.J. Quadakkers, P.J. Ennis, J. Zurek, M. Michalik, Materials at High Temperatures, 22 (2014) 47-60.
[160] A. Strawbridge, P.Y. Hou, Materials at High Temperatures, 12 (2016) 177-181.
[161] G.H. Meier, M.J. Stiger, J.R. Blachere, F.S. Pettit, C. Sarioglu, R. Janakiraman, E. Schumann, A. Ashary, Materials and Corrosion, 51 (2000) 358-372.
[162] A.M. Huntz, Materials Science and Engineering, 87 (1987) 251-260.
[163] J. Smialek, Jom, 52 (2000) 22-25.
[164] D. Delaunay, A.M. Huntz, Journal of Materials Science, 17 (1982) 2027-2036.
[165] A.M. Huntz, (1989) 81-109.
[166] J. Jedlinski, (1989) 131-151.
[167] W.J. Quadakkers, H. Holzbrecher, K.G. Briefs, H. Beske, (1989) 155-173.
[168] B.A. Pint, (2005) 927-934.
[169] C.S. Giggins, B.H. Kear, F.S. Pettit, J.K. Tien, Metallurgical and Materials Transactions B, 5 (1974) 1685-1688.
[170] F.A. Golightly, F.H. Stott, G.C. Wood, Oxidation of Metals, 10 (1976) 163-187.
[171] B.A. Pint, K.B. Alexander, Journal of The Electrochemical Society, 145 (1998) 1819-1829.
[172] B.A. Pint, K.L. More, I.G. Wright, Materials at High Temperatures, 20 (2014) 375-386.
[173] K.A. Unocic, B.A. Pint, Surface and Coatings Technology, 237 (2013) 8-15.
[174] B.A. Pint, Oxidation of Metals, 45 (1996) 1-37.
[175] A.B. Anderson, S.P. Mehandru, J.L. Smialek, Journal of The Electrochemical Society, 132 (1985) 1695-1701.
[176] A.S. Khanna, C. Wasserfuhr, W.J. Quadakkers, H. Nickel, Materials Science and Engineering: A, 120-121 (1989) 185-191.
[177] A. Kumar, M. Nasrallah, D.L. Douglass, Oxidation of Metals, 8 (1974) 227-263.
[178] S. Li, M.M. Xu, C.Y. Zhang, Y.S. Niu, Z.B. Bao, S.L. Zhu, F.H. Wang, Corrosion Science, 178 (2021) 109093.
[179] D. Naumenko, B.A. Pint, W.J. Quadakkers, Oxidation of Metals, 86 (2016) 1-43.
[180] E. Wessel, V. Kochubey, D. Naumenko, L. Niewolak, L. Singheiser, W. Quadakkers, Scripta Materialia, 51 (2004) 987-992.
[181] Y.D. Zhen, J. Li, S.P. Jiang, J Power Sources, 162 (2006) 1043-1052.
[182] M. Stanislowski, E. Wessel, K. Hilpert, T. Markus, L. Singheiser, Journal of The Electrochemical Society, 154 (2007) A295.
[183] Z. Yang, M. Guo, N. Wang, C. Ma, J. Wang, M. Han, Int J Hydrogen Energy, 42 (2017) 24948-24959.
[184] J.R. Mawdsley, J. David Carter, A. Jeremy Kropf, B. Yildiz, V.A. Maroni, International Journal of Hydrogen Energy, 34 (2009) 4198-4207.

[185] W.B. Guan, L. Jin, X. Ma, W.G. Wang, Fuel Cells, 12 (2012) 1085-1094.
[186] S. Geng, J. Zhu, M.P. Brady, H.U. Anderson, X.-D. Zhou, Z. Yang, Journal of Power Sources, 172 (2007) 775-781.
[187] E.A. Gulbransen, K.F. Andrew, Journal of The Electrochemical Society, 104 (1957) 334.
[188] K.P. Lillerud, P. Kofstad, Journal of The Electrochemical Society, 127 (1980) 2397-2410.
[189] I. Panas, J.-E. Svensson, H. Asteman, T.J.R. Johnson, L.-G. Johansson, Chemical Physics Letters, 383 (2004) 549-554.
[190] Z. Sun, S. Gopalan, U.B. Pal, S.N. Basu, (2019) 265-272.
[191] R. Trebbels, T. Markus, L. Singheiser, Journal of Fuel Cell Science and Technology, 7 (2010) 011013.
[192] M. Casteel, D. Lewis, P. Willson, M. Alinger, International Journal of Hydrogen Energy, 37 (2012) 6818-6829.
[193] R. Sachitanand, M. Sattari, J.-E. Svensson, J. Froitzheim, International Journal of Hydrogen Energy, 38 (2013) 15328-15334.
[194] O. Thomann, M.H. Pihlatie, J.A. Schuler, O. Himanen, J. Kiviaho, (2011) 2609-2616.
[195] E.N. Bunting, Bureau of Standards Journal of Research, 6 (1931) 947.
[196] A. Muan, S. Somiya, Journal of the American Ceramic Society, 42 (1959) 603-613.
[197] F. Bondioli, A.M. Ferrari, C. Leonelli, T. Manfredini, L. Linati, P. Mustarelli, Journal of the American Ceramic Society, 83 (2004) 2036-2040.
[198] S.S. Kim, T.H. Sanders, Journal of the American Ceramic Society, 84 (2004) 1881-1884.
[199] K. Motzfeldt, The Journal of Physical Chemistry, 59 (1955) 139-147.
[200] J.-W. Kim, H.-G. Lee, Metallurgical and Materials Transactions B, 32 (2001) 17-24.
[201] D. Sergeev, E. Yazhenskikh, D. Kobertz, M. Müller, Calphad, 65 (2019) 42-49.
[202] H. Tu, U. Stimming, Journal of Power Sources, 127 (2004) 284-293.
[203] N. Minh, J. Mizusaki, S.C. Singhal, ECS Transactions, 78 (2017) 63-73.
[204] U.M. Damo, M.L. Ferrari, A. Turan, A.F. Massardo, Energy, 168 (2019) 235-246.
[205] T. Horita, Solid State Ion, 127 (2000) 55-65.
[206] S.P. Jiang, J.P. Zhang, K. Foger, J Electrochem Soc, 147 (2000) 3195.
[207] S.P. Jiang, J.P. Zhang, K. Foger, J Electrochem Soc, 148 (2001) C447.
[208] E. Bucher, M. Yang, W. Sitte, J Electrochem Soc, 159 (2012) B592-B596.
[209] S.-N. Lee, A. Atkinson, J.A. Kilner, J Electrochem Soc, 160 (2013) F629-F635.
[210] H. Schichlein, A.C. Müller, M. Voigts, A. Krügel, E. Ivers‐Tiffée, Journal of Applied Electrochemistry, 32 (2002) 875-882.
[211] H. Sumi, T. Yamaguchi, K. Hamamoto, T. Suzuki, Y. Fujishiro, T. Matsui, K. Eguchi, Electrochimica Acta, 67 (2012) 159-165.
[212] H. Sumi, H. Shimada, Y. Yamaguchi, T. Yamaguchi, Y. Fujishiro, Electrochimica Acta, 339 (2020) 135913.
[213] E. Ivers-Tiffée, A. Leonide, H. Schichlein, V. Sonn, A. Weber, Impedance Spectroscopy for High-Temperature Fuel Cells, in: D. Stolten, B. Emonts (Eds.) Fuel Cell Science and Engineering: Materials, Processes, Systems and Technology, Wiley‐VCH Verlag & Co. KGaA, 2012, pp. 441-467.
[214] A. Kromp, H. Geisler, A. Weber, E. Ivers-Tiffée, Electrochimica Acta, 106 (2013) 418-424.
[215] A. Leonide, V. Sonn, A. Weber, E. Ivers-Tiffée, Journal of The Electrochemical Society, 155 (2008) B36.
[216] V. Sonn, A. Leonide, E. Ivers-Tiffée, Journal of The Electrochemical Society, 155 (2008) B675.
[217] C. Endler, A. Leonide, A. Weber, F. Tietz, E. Ivers-Tiffée, Journal of The Electrochemical Society, 157 (2010) B292.
[218] A. Kromp, A. Leonide, A. Weber, E. Ivers-Tiffée, Journal of The Electrochemical Society, 158 (2011) B980.
[219] M. Kornely, A. Leonide, A. Weber, E. Ivers-Tiffée, Journal of Power Sources, 196 (2011) 7209-7216.
[220] Z. Lyu, H. Li, Y. Wang, M. Han, Journal of Power Sources, 485 (2021) 229237.
[221] M. Kornely, A. Neumann, N.H. Menzler, A. Leonide, A. Weber, E. Ivers-Tiffée, J Power Sources, 196 (2011) 7203-7208.

[222] S. Canovic, J. Froitzheim, R. Sachitanand, M. Nikumaa, M. Halvarsson, L.G. Johansson, J.E. Svensson, Surface and Coatings Technology, 215 (2013) 62-74.
[223] M.V. Glazoff, S.N. Rashkeev, J.S. Herring, International Journal of Hydrogen Energy, 39 (2014) 15031-15038.
[224] J.C.W. Mah, A. Muchtar, M.R. Somalu, M.J. Ghazali, Int J Hydrogen Energy, 42 (2017) 9219-9229.
[225] N. Shaigan, W. Qu, D.G. Ivey, W. Chen, Journal of Power Sources, 195 (2010) 1529-1542.
[226] B.A. Pint, S. Dryepondt, M.P. Brady, Y. Yamamoto, B. Ruan, R.D. McKeirnan, Journal of Engineering for Gas Turbines and Power, 138 (2016) 122001.
[227] Z. Lyu, W. Shi, M. Han, Applied Energy, 228 (2018) 556-567.